Improved design bases of welded joints in seawater

Ólafsson, Ólafur Magnús

Publication date:
2016

Document Version
Publisher's PDF, also known as Version of record

Improved Design Basis of Welded Joints in Seawater

PhD Thesis

$$(EIv'')''=q-\rho A\ddot{v}$$

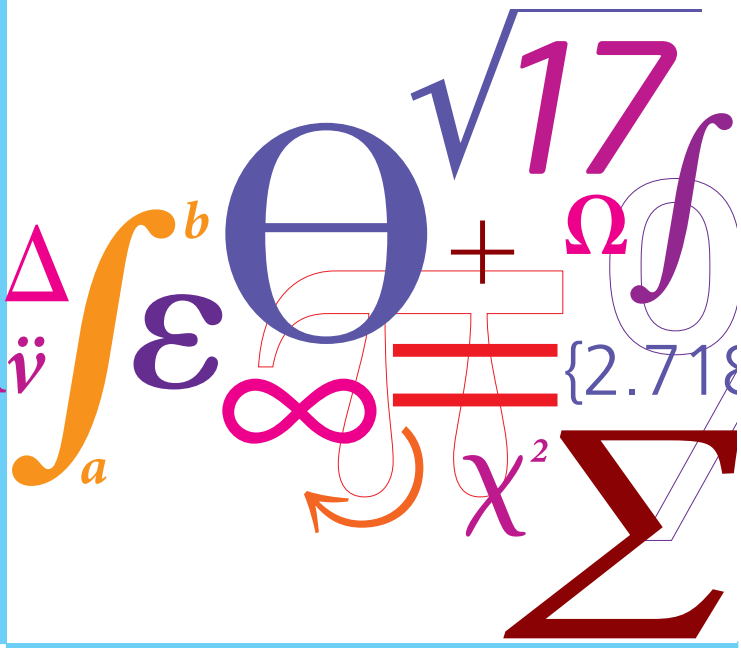

Ólafur Magnús Ólafsson
DCAMM Special Report No. S199
March 2016

DTU Mechanical Engineering
Department of Mechanical Engineering

Improved Design Basis of Welded Joints in Seawater

PhD thesis by
Ólafur Magnús Ólafsson, MSc

Submitted March 2016

Supervisor
Associate Professor Christian Berggreen

Co-supervisor
Professor DSc Jørgen Juncher Jensen

Lightweight Structures Group
Department of Mechancial Engineering
Technical University of Denmark

Published in Denmark by
Technical University of Denmark

Department of Mechanical Engineering
Lightweight Structures Group
Technical University of Denmark
Nils Koppels Allé, Building 403
DK-2800 Kgs. Lyngby
Denmark

http://www.mek.dtu.dk/
Tel: (+45) 45 25 19 60
Fax: (+45) 45 93 14 75
E-mail: info@mek.dtu.dk

Publication Reference Data
Olafsson, O.M.
Improved Design Bases of Welded Joints in Seawater
Ph.D. Thesis
Technical University of Denmark, Mechanical Engineering
January 2016

When you talk, your are only repeating what you already know.
But if you listen, you may learn something new.

- J.P. McEvoy

Preface

This thesis is submitted as a partial fulfilment of the requirements for the Danish Ph.D. degree. The work was performed in the Structural Light Weights Group, Department of Mechanical Engineering, Technical University of Denmark, during the period of August 2011 to March 2016. The project was supervised by Associate Professor Christian Berggreen and co-supervised by Professor DSc. Jørgen Juncher Jensen.

This PhD project was a part of larger joint industry EUDP project, monopile cost reduction and demonstration by joint applied research. The collaborating partners were Vestas Wind Systems A/S, Force Technology and Aalborg University.

Kgs. Lyngby, March 2016

Acknowledgements

I would like to thank my supervisor Christian Berggreen and my co-supervisor Jørgen Juncher Jensen for introducing me to this project and making it possible. Additional thanks to Christian Højerslev (LORC / LWT) for his discussions and tireless work in getting the laser system operational. Additional thanks to Mikkel Melters Pedersen for bringing me up to speed and introducing me to the welding society.

Special thanks go to Laufey Gunnþórsdóttir for her great work in designing the corrosion environment and her collaboration in making it operational. I would like to thank Johan Bartholdy for his contribution in keeping the servo hydraulic testing machines running and always staying positive. I would also like to thank the skilled technicians, in the workshop in building 119, Robert Swan and Keld Plougmann for their contributions in assistance and machining required parts.

I would like to thank all my friends and colleagues at the office for their support, good moments and the outstanding company. Without them, this would not have been possible. Special thanks go to my good friend and colleague Mehrtash Manouchehr for his uplifting spirit, good discussions, and tolerance in listening to all my ideas and predicaments relating to this project.

Then especially I would like to thank my amazing girlfriend, *Anna Fotaki*, for her endless support, important presence and love, even during the caveman days in the end... and my mom, *Katrín Valentínusardóttir*, for her strong words of encouragement, motivation and always calling in times of need.

Thank you!

Kongens Lyngby, March 2016

Ólafur Magnús Ólafsson

Abstract

The presented work aims to investigate and establish a precise, thorough and detailed database from series of experimental testing of submerged arc welded, SAW, specimens of various thicknesses typically applied in offshore structures and foundations. Additionally, the testing was performed in two different environments, i.e. under in-air conditions and in a corrosion environment. Welded structures of all sizes and shapes exhibit fatigue failure primarily in the welded region, rather than in the base material, due to imperfections and flaws relating to the welding procedure. The welded region has therefore received much attention from universities, research institutions along with industry as it is of significant practical importance for all fatigue loaded structures, such as e.g. marine structures.

As-welded SAW specimens of three different thicknesses, manufactured by Lindoe Welding Technology A/S and Bladt Industries A/S, were subjected to uni-axial tension loading at relatively high R-ratios in order to simulate tensile residual stresses of yield magnitude. The main goal was to confirm the thickness effect for the specific case of large butt joints in the as-welded condition as well as to validate whether the thickness correction factor according to recommendations, codes and guidelines is too conservative when it comes to butt-welded joints. A conservative thickness effect factor results in larger, heavier and more expensive structures. The thickness effect considers the influence of the plate thickness on the fatigue resistance of welded joints and is generally included in design rules by scaling the fatigue strength with a recommended factor. The existing database of experiments that relate to the thickness effect is comprehensive and the effect is well proven experimentally and theoretically for various types of welded joints. However, in the case of large butt-welded joints there is room for improvement as details, quality and precise data which can influence the fatigue life of the welded joint is often lacking and severely lacking in truly thick joints.

Additionally, as-welded SAW specimens were tested in a corrosion environment with

cathodic protection. The specimens were subjected to high fatigue loading at the same stress ratio as the tests performed in-air. A direct comparison to the specimens tested under in-air conditions was performed in order to evaluate the effects of the corrosion environment on fatigue resistance.

Furthermore, novelty 25 mm thick steel laser-hybrid welded specimens in the as-welded condition were subjected to experimental testing. A fatigue resistance S-N curve was established for the laser hybrid welded joints in addition to a more detailed analysis. The laser hybrid welded joints were thereafter compared directly to the traditional SAW specimens in order to investigate the two different welding techniques. The laser hybrid welding technique offers great potential in lowering the cost of energy associated with offshore structures.

Keywords:
Welded joints, butt joints, SAW welding, Laser hybrid welding, Fatigue testing of welded joints, corrosion environment, corrosion fatigue, hydrogen embrittlement, cathodic protection, fracture testing, thickness effect, hot spot stress analysis, notch stress analysis, SEM-EDS analysis, hardness testing.

Resumé

Denne afhandling har til hensigt at etablere en præcis grundig og detaljeret database baseret på en serie af eksperimentelle test af svejsesøm under søvandsmiljø. Testene var udført på ubehandlede SAW svejseemner og var udført på forskellige tykkelser stål som er typiske indenfor offshore konstruktioner. Testene er både udført under luft tilstand og i et korrosionsagressivt miljø. Svejste konstruktioner er generelt svækket i forhold til udmattelsesbrud, grundet imperfektioner som følge af svejseprocessen. Der er derfor blevet forsket meget i svejsesøm, i konstruktioner udsat for dynamiske laster, både i industrien og på diverse universiteter.

Ubehandlede SAW prøveemner i tre forskellige tykkelser, produceret af Lindoe Welding Technology A/S og Bladt Industries A/S, blev testet i en-akset træk ved høje stress forhold, R-ratio, for at simulere residualspændinger i størrelse nær flydning. Formålet med testene var at verificere tykkelseseffekten for store ubehandlede butt-svejste emner og at undersøge om tykkelseseffekt faktoren er for konservativ i standarder, anbefalinger og andre guidelines. I givet fald vil dette resultere i større, tungere og dyrere konstruktioner. Tykkelseseffekten medregner effekten af godstykkelsens indflydelse på udmattelsesbæreevnen af svejsesøm og er generelt inkluderet i designregler ved at skalere udmattelsesbæreevnen med en partialkoefficient. Tidligere forsøg og matematiske analyser viser en klar tykkelseseffekt ved forskellige typer af svejsesøm. Men ved særligt tykke butt-svejste svejsesøm er der lavet meget få tests og det er derfor uvist om teorien omkring tykkelseseffekten i sådanne svejsesøm er korrekt.

I projektet blev også udført tests på ubehandlede SAW svejsesøm i korrosivt miljø med katodisk beskyttelse. Forsøgene blev udført ved samme høje udmattelseslaster som forsøgene udført i luft. Disse to testsserier blev sammenlignet for at vurdere effekten af korrosion på udmattelsesbæreevnen af svejsesømmene.

Ydermere blev der også udført forsøg på ubehandlede laser-hybrid svejste stålemner med 25mm godstykkelse. En S-N udmattelseskurve blev udarbejdet for disse svejs-

esøm og resultaterne blev yderlige undersøgt. Resultaterne fra testene af laser-hybrid svejsesøm blev derefter sammenlignet med de tidligere tests af de traditionelle SAW emner for at undersøge forskellen på de to teknikker. Det sluttes at laser-hybrid svejseteknikken har stort potentiale for at sænke omkostningerne indenfor offshore konstruktioner.

Nomenclature

Symbols

The following provides a list of symbols in order of occurrence.

Q	Heat input
V	Welding speed
C_eq	Carbon equivalent
σ_y	Yield strength
σ_{ult}	Ultimate strength
σ_{max}	Maximum strength
σ_{min}	Minimum strength
σ_a	Stress amplitude
$\Delta\sigma$	Stress range
σ_m	Mean strength
N	Number of cycles count
S-N curve	Fatigue resistance curve, stress range with respect to number of cycles
R	Stress ratio

σ_{mem}	Membrane stress
σ_{bend}	Bending stress
$\sigma_{nl} = \sigma_{peak}$	Non linear notch stress
σ_{nom}	Nominal stress
σ_{HS}	Structural hot spot stress
σ_{HS_mem}	Membrane structural hot spot stress
σ_{HS_bend}	Bending structural hot spot stress
ε	strain
E	Modulus of elasticity
F	Force
A	Cross sectional area
M	Bending moment
I	Moment of inertia
y	Distance from neutral axis
t	Thickness
w	Width
L	Length
t_{ref}	Reference thickness
m	negative inverse slope of S-N curve
log$\bar{a}$	Intercept of N-axis by S-N curve
log a	Intercept of mean S-N curve with the log N axis
S_{logN}	Standard deviation of log N
K_m	Stress magnification factor
K_{m_ax}	Axial stress magnification factor
K_{m_ang}	Angular stress magnification factor
e	Eccentricity
α	Angle
K_t	Stress concentration factor
K_t^{mem}	Membrane stress concentration factor
K_t^{bend}	Bending stress concentration factor
k	thickness correction exponent
wt%	Weight percent
E	Electrode potential

List of abbreviations

The following provides a list of abbreviations in order of occurrence.

DTU	Technical university of Denmark
EWEA	European Wind Energy Association
EUDP	Energy Technology Development and Demonstration Programme
SAW	Submerged arc welding
HAZ	Heat affected zone
AWS	American welding society
IIW	International Institute of Welding
DNV	Det Norske Veritas
GL	Germanischer Lloyd
RP	Recommended practice
FAT90	IIW fatigue design curve recommended for butt welded joints
Design curve D	DNV fatigue design curve recommended for butt welded joints
NACE	National association of corrosion engineers
HLAW	Hybrid laser arc welding
LWT	Lindø welding technology
DIC	Digital image correlation
SHM	Servo hydraulic machines
LVDT	Linear variable displacement transducer
ASTM	American Society for Testing and Materials
CEN	European committee for standardization
DS	Danish Standards Foundation
ISO	International organization for standardization

NDT	Non destructive testing
VT	Visual testing
UT	Ultrasonic testing
MT	Magnetic particle testing
ESAB	Elektriska Svetsningsaktiebolaget
WPS	Welding procedure specification
API	American petroleum institute
CP	Cathodic protection
ICCP	Impressed current cathodic protection
UV	Ultraviolet
pH	Power of hydrogen
SCE	Saturated calomel electrode
SHE	Standard hydrogen electrode
SEM	Scanning electrode microscope
EDS	Energy dispersive spectroscopy
GMA	Gas metal arc

Contents

List of Figures

List of Tables

Chapter 1

Introduction

The wind turbine industry is continuously flourishing. The increasing necessity for alternative power production solutions, as outlined by numerous international and national initiatives and policies, combined with the rapid evolution between optimization of wind turbine production and their power output has paved the way to increased research in this field.

According to the Global wind energy council, the annual market growth of the global wind power industry in 2015 represented an approximate 22% growth of new installations. This rapid advancement is led by China, which installed an astonishing 30.500 MW in 2015, surpassing the European Union in total installed capacity. The year 2015 additionally saw the USA, Germany and Brazil set new records of installed wind turbines with markets opening up in Asia, Africa and Latin America [14], [15].

The European Wind Energy Association, EWEA, has announced a growth of installed wind turbines of 6.3% within the EU and notably that wind power was the leading form of newly installed power generation, accounting for 44.2% of the total newly installed power capacity. The capacity installed in 2015 within EU saw the onshore wind turbine market decrease by 7.8%, while the offshore installations more than doubled between years, accounting for 23.7% of the new capacity installed [1], [16]. Figure 1.1 illustrates the annual onshore and offshore wind turbine installations within the EU.

The offshore wind power market is a relatively new and the first offshore wind farm was installed in Denmark in 1991, i.e. the Vindeby offshore wind farm with a 5 MW capacity. In the subsequent years this market has grown almost exponentially and the top 25 largest offshore wind farms were installed from 2009 up till now. The appeal

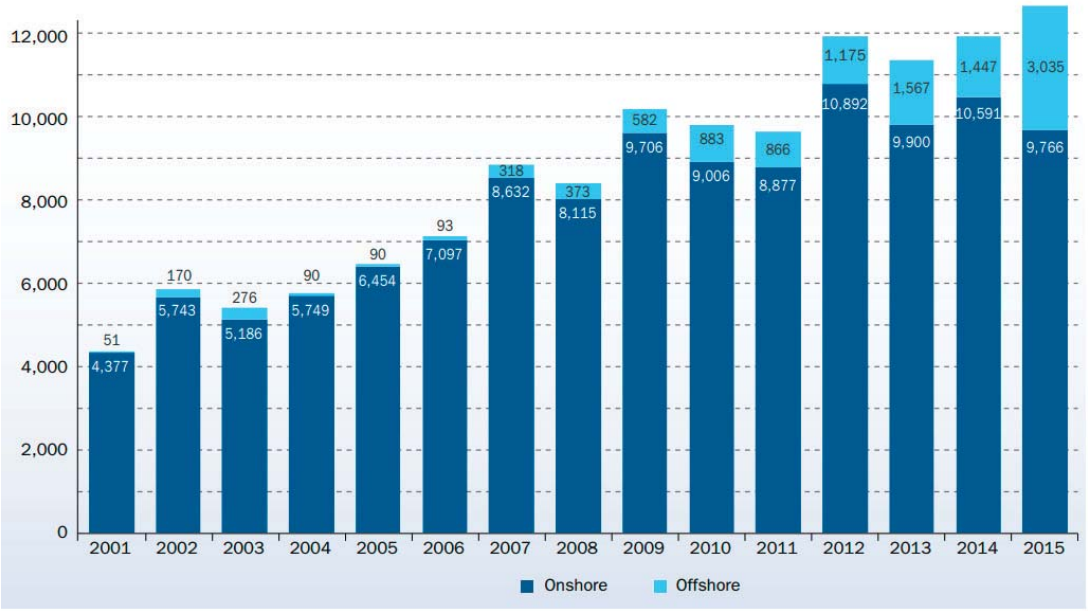

Figure 1.1: *Annual onshore and offshore wind turbine installations in megawatts, [MW] [1].*

of offshore wind turbines compared to onshore lies with higher and more consistent wind speeds over the oceans, which can lead to increased efficiencies of the turbines as it is estimated that the potential energy produced from wind is proportional to the cube of the wind speed. Additionally, the wind speeds tend to increase offshore in the afternoon, contrary to the onshore wind speeds that tend to increase over night. Furthermore, the benefits of offshore wind turbine farms allow for the significant reduction of visual and noise pollution adding to their environmental benefits.

On the other hand, offshore wind turbine structures are associated with a large increase in cost, which can amount up to three times the price compared to an onshore wind turbine. Large foundation structures and transition pieces have to be implemented to the overall structure, which needs to be able to withstand higher environmental loading, such as higher wind speeds as well as additional loads subjected to the structure due to waves and currents. The additional cost relating to the design, manufacturing, transportation and installation of the required support structures ranges between a quarter to a half of the overall cost of the finished structure. Furthermore, operational, inspection and maintenance cost is higher for offshore structures. Thus, the trend in offshore wind turbine structures has been to upscale, i.e. increase the turbine rated power and rotor

sizes in order to achieve increased wind power utilization, in addition to design deeper water foundation solutions in order to exploit the large wind potentials at water depths above 50 meters. [17], [18], [1], [16].

Monopile foundations are by far the most dominant foundation structures applied in the offshore wind industry. Monopiles accounted for 91% of installed substructures in 2014 [16]. These foundations are easier in design and manufacturing compared to other substructure types. They consist of a large welded tube, which is driven into the seabed. Thus, the monopile foundations make calculations, production and transportation to site relatively straightforward with a well known and widely used installation method, i.e. pile driving. However, the immense size of the structures is becoming increasingly problematic with respect to all stages of the wind turbines. For example, the overall weight of an individual offshore wind turbine from the 400 MW capacity Anholt offshore wind turbine farm, the latest and largest installed offshore wind farm in Denmark, surpasses 1000 tons and the wind farm consists of 111 wind turbines.

Taking into consideration the current trends in the offshore industry, wind turbine sizes will continue to increase. The new design concepts for 10 MW turbines are currently on the developing stage and according to initial structural dimensions the estimated base of the foundation should have a diameter of 10 meters. Applying the approximate diameter to wall thickness ratio of 80, i.e. D/t = 80, results in wall thicknesses of 125 mm. These dimensional parameters involved are becoming extremely large, making the corresponding manufacturing process very demanding. The welding associated with the manufacturing process of the foundation structure is a central part of the cost. An increase in the structural parameters could require multiple additional welding passes in order to join the large steel tubes together with longitudinal and circumferential weld seams, along with the associated increased man-hour requirements and material cost.

These extremely large welded structures will be subjected to continuous variable amplitude fatigue loading over their designed lifetime. More specifically, fatigue failure of structures is known to be the most frequent mode of failure in industry [19]. Fatigue failure is the process where a crack or cracks can form and then propagate under repeated loading until complete fracture occurs. The magnitude of the required loads can be considerably less than the required static loads for structural failure. However, when considering welded structures, pre existing cracks, pores and other defects are already present within the welded region. Thus, the fatigue process consists mainly of crack propagation until fracture occurs, as the crack initiation phase is much shorter or entirely absent. Therefore, the fatigue strength of welded structures compared to unwelded structures is significantly lower [6], [5].

The fatigue mechanism of metals is not a fully established field of study and numerous fatigue related topics are still under investigation. The addition of welds does not simplify matters as the weld and neighbouring base material are affected by thermal cycles during the welding procedure which causes heat affected zones, residual stresses, distortions, heterogeneous microstructures along with differing mechanical properties and material compositions. This is accompanied by welding defects such as porosities, slag inclusions, undercuts, overlaps and varying weld profiles with ideal conditions for weld notch crack formations. Furthermore, the large welded offshore wind turbine structure is fixed offshore with an applied layer of protective coating along with cathodic protection. The structure is subjected to complex, sometimes severe, variable amplitude fatigue loading and exposed to the aggressive seawater and microbial life where a number of corrosion processes can severely affect crack initiations, propagations as well as the lifetime of the structure.

Unexpected failures in offshore wind turbines still occur, in spite of over 25 years of experience in turbine structures, utilizing modern and sophisticated tools during the designing process, FEM analysis, large material databases, multiple simulations and live data acquisitions from active structures. Many international and national standards, recommendations and codes have been developed in order to aid the design processes with respect to almost all relevant topics. Additionally, with respect to welded structures, special organizations and research facilities have been established with the sole focus on welds and their behaviour from manufacturing to service operation. Their main objective is to contribute to the field with research and development leading to further design recommendations in order to improve as well as to give reliable estimations of the structure's overall lifetime. In addition, it is worth mentioning that the standards and recommendations are extensive and based upon numerous experimental tests and research. However, they are general and have not been able to follow up with current advances and improvements in the related fields such as, material science, design, manufacturing techniques, inspection techniques and corrosion protection. According to Brennan, [20], the background of the applied fatigue design recommendations for wind turbine support structures is largely inherited from the oil and gas industry and thus several decades old.

There is a general lack of experimental data and literature available concerning fatigue testing of very large welded structures, as these tests can be demanding, challenging and costly. In addition, there is a lack of experimental data and literature concerning large as-welded joints subjected to fatigue loading within a corrosion environment with or without cathodic protection. The present, practical and highly experimental, PhD project will focus on these topics in an attempt to provide much required data to the available literature. Moreover, the validation of a promising, cost efficient, welding

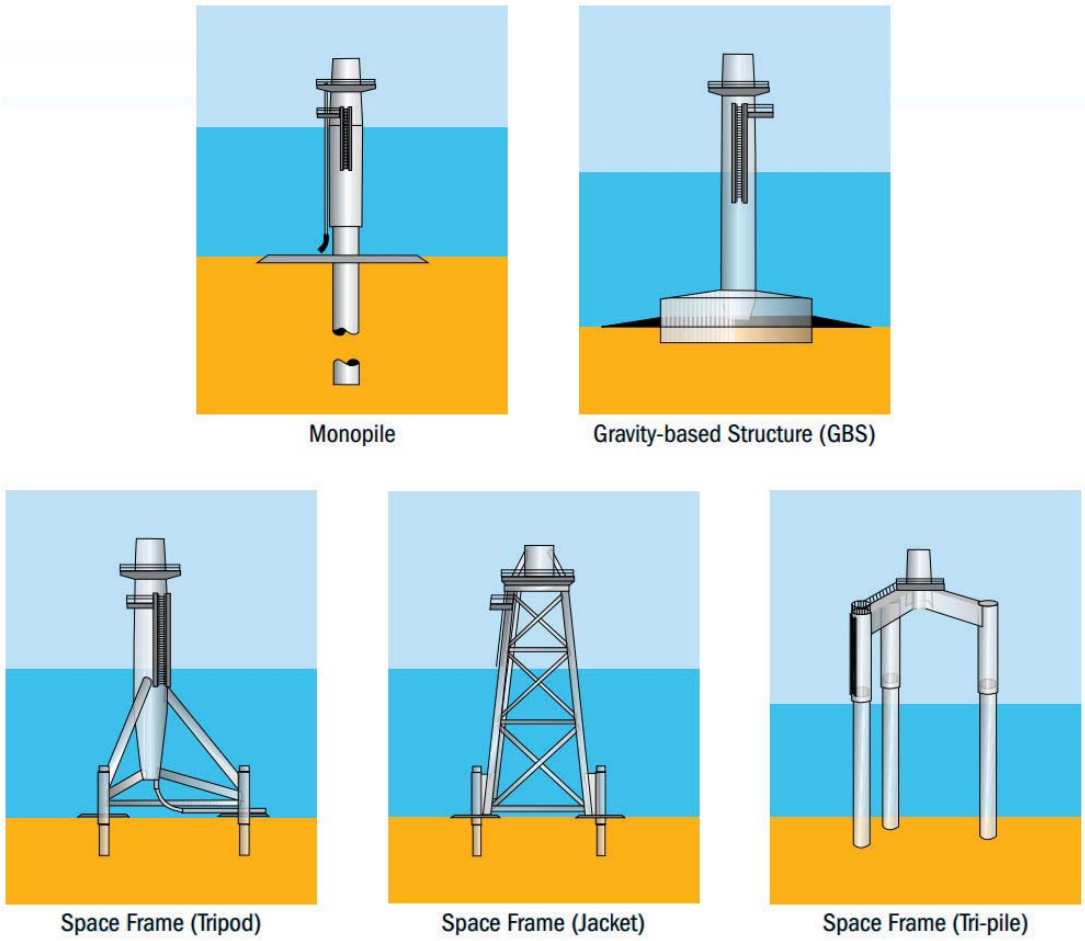

Figure 1.2: *Types of fixed offshore foundations [2].*

technique, which at the time of writing has not been applicable in joining thick steel structures, was subjected to experimental testing.

1.1 Type of structure

The project involves the application of monopile foundations for offshore structures. Monopiles are by far the most common foundation structure for offshore wind turbines. The monopiles are a fixed foundation, contrary to floating foundations which are on the research and development phase. The various types of fixed foundation types are

illustrated in Figure 1.2.

The monopile foundations are reliable and simple. They are easier to manufacture and install compared to rival fixed foundation structures. However, monopiles have been limited to shallow water depths, i.e. up to 25 meters depth. At depths greater than 25 meters, a jacket foundation has been found to be more attractive as they are more adaptable, flexible and lighter. However, jacket foundations are time consuming and expensive to manufacture, assemble, transport and protect against corrosion due to their intricate and multiple welded joints. Thus, monopile foundation concepts have been on the drawing board for deep water installations. These deep water design concepts have been made for monopiles suitable for 45 meter water depth with a bottom foundation diameter of 10 meters, weighing 1200 tonnes and an estimated length of 90 meters, making manufacturing, transporting and installing a formidable challenge [21], [2].

1.2 Project definition and objectives

This PhD project is part of a larger joint industry EUDP project, monopile cost reduction and demonstration by joint applied research. The collaborating partners were Vestas Wind Systems A/S and Force Technology along with Aalborg University.

Two main objectives for the EUDP project were by definition:

- Drive down the cost of energy from monopile based offshore wind turbine generators.
- Stretch monopile foundations to deeper waters and/or bigger wind turbine generators.

The present PhD thesis “Improved design basis of welded joints in seawater” belongs to work package 4.

The PhD project emphasis was based on the validation of the fatigue resistance of submerged arc welded, SAW, joints. SAW is responsible for the majority of the welding performed in joining tubular foundation sections for offshore wind turbines. The welded detail under investigation is butt welded joints in the as-welded condition, i.e. not post treated. Figure 1.3 illustrates an idealized location of a butt welded joint within a large tubular structure.

The main objective and associated challenges were demanding and in order to achieve a step in the right direction in improving the design basis for welded joints in seawa-

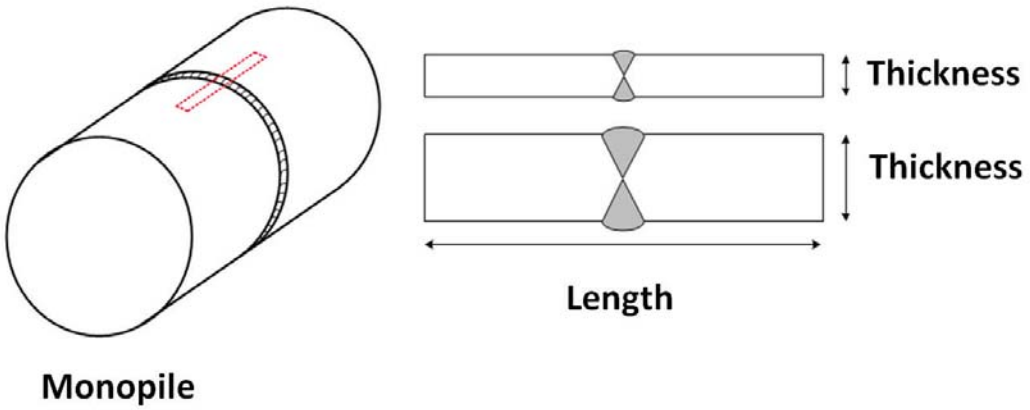

Figure 1.3: *Weld thickness and weld location at the wind turbine.*

ter, the following experimental fatigue test series were defined, established and performed.

Test series 1 - Experimental investigation of the thickness effect for submerged arc welded joints: This test series was performed in order to investigate the thickness effect of welded joints, i.e. whether they are indicating a too conservative approach for design recommendations. In particular this test series, challenges the conservatism in present guidelines and design recommendations, which were inherited from the oil and gas industry. If recommendations are found to be too conservative there is a potential to lower the recommended thickness for a desired fatigue strength and thus reduce material cost which affects most stages of the offshore wind turbine from manufacturing till installation procedure.

Test series 2 - Fatigue resistance of large as-welded SAW joints within a circulating synthetic seawater environment with cathodic protection: This test series was performed in order to build up knowledge and gain experience of performing fatigue tension-tension testing of 20 mm thick SAW butt joints within a circulating corrosion environment with impressed current cathodic protection. There is a notable lack of research in this field, especially concerning corrosion fatigue of large welded joints.

Test series 3 - Fatigue strength of laser-hybrid welded joints and a comparison to submerged arc welded joints: This test series was performed in order to validate the mechanical properties of 25 mm thick laser-hybrid welded joints and establish an experimental fatigue S-N curve. There was an additional comparative study with the SAW butt joints from test series 1. The laser-hybrid welding technique is not new to

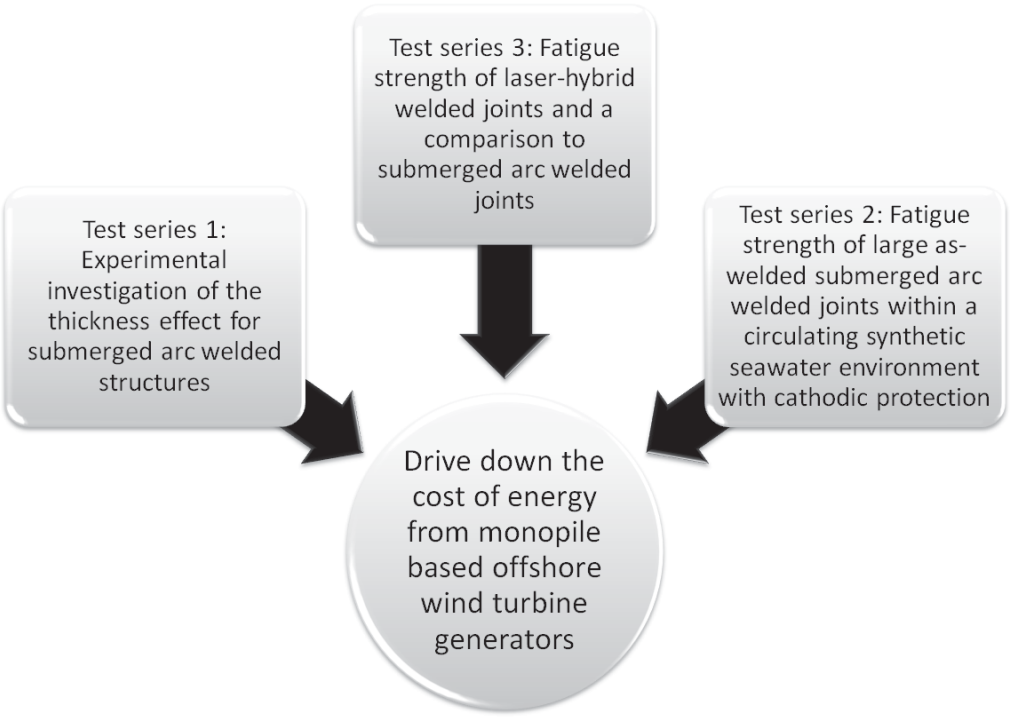

Figure 1.4: *Project paths towards the main goal.*

the market, however it has not, until now, been applicable in joining large steel structures together. The laser-hybrid welding offers a great potential of reducing the cost of energy, as the benefits are plentiful, e.g. automatic, faster, more reliable, consistent weld quality, cheaper and a more eco-friendly welding technique.

To sum up, the objective of driving down the cost of energy associated with the overall procedure of installing an offshore wind turbine was addressed by three different and promising test series. Each particular test series addresses the main objective individually and attempts to present reasonable indications for cost reduction possibilities with the resulting experimental data acquired. Furthermore, the three test series also correlate and compliment each other, i.e. the corresponding results from one test series can and will affect the findings from the other and as a collective they present a more substantial indication towards potential means to reduce the overall cost.

1.3 Scope and limitation

The scope of the project involves different fields of expertise such as materials science and metallurgy, fatigue and fracture, structural connections such as welds, corrosion, corrosion fatigue and cathodic protections. Each distinct field is broad and could independently be a good basis for a PhD project. This project therefore touches upon many aspects and attempts to provide the best and most precise representation of each relevant field.

It goes without saying, that there are naturally many considerations to take into account when performing an extensive experimental Ph.D project, particularly when there are a lot of hands-on man-hours involved. The application of higher load capacity servo hydraulic testing machines proved to be one of the greatest bottlenecks, as it required continuous maintenance and division of running hours between various projects.

Performing extensive fatigue testing according to a pre-defined test plan will accumulate into a lot of hands-on man-hours, in addition to a substantial utilization of machine running hours. In order to build up a reliable S-N curve from fatigue testing, five different stress levels were performed with a minimum of five specimens tested per stress level. This accumulates to a large collection of fatigue test specimens where some may run for less than a day at low-cycle, high-stress level testing, while high-cycle, low-stress level tests may run for over a week at frequencies between 5-10 Hz.

1.4 Thesis outline

The following is a short description of the thesis chapters and their contents. Chapters 4, 5 and 6 are built up separately where the emphasis is on the three separate experimental test series defined for this project.

Chapter 2: Theory

Chapter 2, entitled *Theory*, will in a short and precise way describe and link all the related theory to the project's experimental results and main objectives. The theory section will emphasize on the most relevant topics as the whole project is quite comprehensive and touches upon many different fields of expertise.

Chapter 3: Review of scientific literature

Chapter 3, entitled *Review of scientific literature*, will give an insight into what has been done before, theoretically and experimentally, in fields related to this project. Here an overview of the thickness effect research will be described, as well as the research that has been performed and published relating to experimental corrosion fatigue. Additionally the new and exciting method of laser-hybrid welding of larger sections and the corresponding experimental testing will be summarized and reviewed.

Chapter 4: Test series 1 - Experimental investigation of the thickness effect for submerged arc welded joints

Chapter 4, entitled *Test series 1 - Experimental investigation of the thickness effect for submerged arc welded structures*, is an experimental investigation of the thickness effect, often termed size effect, for SAW butt joints. This section concerns challenging conservatism in the present guidelines and design solutions which were inherited from the oil and gas industry. The basis for this research is the state of the art literature investigation of fatigue resistance of SAW butt joints, which confirmed and demonstrated the trend of thickness effect for larger joints, but also indicated that the thickness correction might be too conservative. The debatable "conservative" thickness effect of welded joints has led to truly thick welded structures, and following the current trend they will only grow even larger in dimension. This increases the already problematic process of manufacturing, transporting and installing the offshore wind turbine structures due to immense sizes. The thickness correction factor is applied in design codes for all welded joints above 25 mm thickness. The influence of thickness on the fatigue resistance of the welded joint is well established theoretically and experimentally, however if proven too conservative implies a great potential to reduce the cost of energy.

Chapter 5: Test series 2 - Corrosion fatigue resistance of large as-welded SAW joints in a circulating synthetic seawater environment with cathodic protection

Chapter 5, entitled *Test series 2 - Corrosion fatigue resistance of large as-welded SAW joints in a circulating synthetic seawater environment with cathodic protection*, relates to fatigue testing of large SAW joints in a corrosion environment in order to investigate the influence of corrosion fatigue on as-welded joints. Corrosion fatigue is another

field of study with great dispute and controversy where the available experimental results sometimes completely contradict one another. Most available articles concerning experimental corrosion fatigue have been conducted on small scale samples which have been post-weld treated to fit perfectly into a test setup, resulting in e.g. compressive residual stresses that have beneficial influences on the results. Experimental testing is therefore significantly lacking for large scale testing of submerged welded joints. An experimental setup was constructed with a circulating seawater environment and a 500 kN loading capacity. The test facility allows control of temperature, circulation speed, pH level with open access to oxygen, making it very efficient for corrosion fatigue testing.

Chapter 6: Test series 3 - Fatigue resistance of laser-hybrid welded joints and a comparison to submerged arc welded joints

Chapter 6, entitled *Test series 3 - Fatigue strength of laser-hybrid welded joints and a comparison to submerged arc welded joints*, concerns validating the fatigue resistance of laser-hybrid welded butt joints and comparing the subsequent results with the conventional and reliable SAW method. SAW is currently accountable for more than 90% of tubular wind turbine welds. The laser-hybrid welding method provides more benefits when compared to the SAW, especially concerning cost optimization, automation, weld quality, weld consistency and energy efficiency. The laser-hybrid welding industry is rapidly evolving, working its way towards truly thick sections. However, there is still necessary progress required until the laser-hybrid method can weld steel sections ranging above 100 mm flawlessly and repetitively for the offshore wind turbine industry. Nonetheless, the possibility of reducing the recommended thicknesses for the structures combined with the introduction of new technology and more powerful lasers, laser hybrid welding would not be an unfeasible endeavour within the wind turbine industry in the near future.

Chapter 7: Summary of experimental results

Chapter 7, entitled *Overall results*, will summarize all the obtained results from the three different experimental test series performed.

Chapter 8: Discussion

Chapter 8, entitled *Discussion*, will combine the findings from the three fatigue test series performed. Thereafter address and discuss the achieved results in order to relate them to the main objectives of the overall project.

Chapter 9: Conclusion

Chapter 9, entitled *Conclusion*, will give the concluding remarks on the experimental test series main findings in addition to suggestions for further research.

This page is intentionally left blank.

Chapter 2

Theoretical background

An essential part of science is to present a complicated notion in the simplest way possible. For some instances this task can be difficult to achieve where the knowledge in the respective field is incomplete, this can lead to simplifications, estimations, assumptions and other approaches which ultimately can influence the obtained results. The following chapter will emphasize on the most relevant theory relating to the objectives for the overall project with an approach to describe in a short and concise manner the theoretical aspects concerning all three performed experimental test series.

As previously mentioned, the project is quite multi disciplinary and touches upon many different fields of expertise. However, emphasis is placed on experimental testing with practical and applicable results.

2.1 Welded connections

Connecting members together is an essential part of assembling large steel structures. There are two common ways of connecting members, i.e. using bolts or welds. In a number of situations welded joints are preferred or they might be the only practical option for joining the steel members, e.g. when dealing with fatigue loading of large structures. Welded connections are permanent, simple in design, require fewer parts and less fabrication operations. Additionally, welded joints are more rigid and can transfer loads more efficiently, especially when concerning groove welds, i.e. two plates connected in the same plane, also known as butt welds. A sound and properly

made weld can be stronger than the surrounding base material, while an improperly made weld, even those that look perfect, are useless.

The main disadvantages of welding are; 1) permanent connections, 2) heat introduction which can disrupt the surrounding base material's microstructure and degrade its mechanical properties and induce residual stresses, 3) causes shrinkage which has to be considered, and 4) requires operator skill in producing a good, sound weld. Furthermore, welding equipment can be expensive [22], [23].

This section will try to provide the most relevant topics related to welded connections in a short and concise manner.

2.1.1 Arc welding

Arc welding is a fusion welding process which joins metals together by introducing immense heat along with a filler metal which causes the surrounding base metal to melt and coalesce. As the metals solidify and cool down they form a metallurgical bond between them.

The Arc welding system consists of a power source, an electrode and the workpiece. An electric arc generates the immense heat required to melt the metal with an electric current between the two electrodes, i.e. the applied electrode and the workpiece, through a heated and ionized gas. The applied electrode can either be a current carrying stick which is non consumable or it can be a stick or a wire which additionally melts and supplies filler metal into the melt between the workpieces.

A shielding gas is applied in order to protect the hot electrode and the reactive high temperature molten weld metal from oxygen, hydrogen and nitrogen present in the atmosphere. The strength and toughness of the molten metal can be affected, in some cases significantly if it comes into contact with air. The shielding gas covers and protects the arc and the molten pool, thus preventing or minimizing the detrimental effects of the surrounding environment. Additionally, the shielding gas can improve the arc's stability as well as the resulting weld by adding e.g. deoxidizers into the molten pool.

The immense heat input from the arc during the welding process, as it moves continuously along the workpiece to form the weld seam, results in material shrinkage and distortion along with the development of mircostructural changes and residual stresses within the metal as it solidifies and cools down. These material alterations depend on multiple parameters, e.g. material composition, workpiece dimensions, thermal prop-

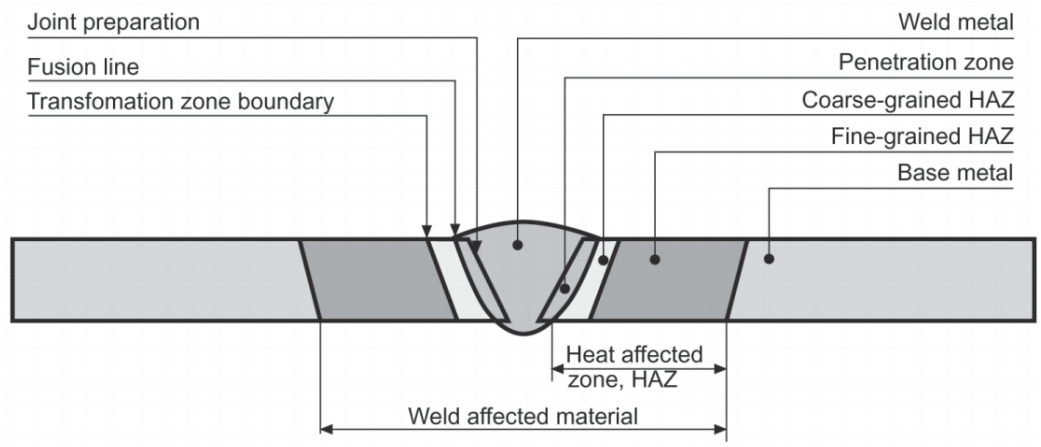

Figure 2.1: *Weld zones and boundaries in the heat affected zone [3].*

erties, preheat temperature, the heat input, the cooling rate, etc. If multiple welding passes are required then the first welding pass will preheat the workpiece, which reduces its cooling rate for the subsequent passes in addition to making it softer. The last welding pass will induce tempering of the filler material from the previous welding passes and the surrounding heat affected zones of the workpiece. The last welding pass remains not tempered [24], [3], [25], [26], [27], [28].

2.1.2 Welding metallurgy

The solidification of a molten weld metal is a complicated phenomenon and dependent on various factors. Three main metallurgically different zones can be determined in relation to fusion welding processes, i.e. 1) the fusion zone, also know as weld zone, which solidifies from the melted weld pool temperature, 2) the heat affected zone, HAZ, which is in between the fusion zone and the base metal, and 3) the unaffected base material, workpiece, at a certain distance from the weld region. The heat affected zone has additionally been divided into a number of sub-zones which are affected differently depending on the welding conditions, thermal cycles as well as the thermal and mechanical history of the base material. Figure 2.1 illustrates the different weld zones in a butt welded joint [3], [29].

The resulting microstructure depends on the respective cooling rates, where faster cooling rates result in finer microstructure and enhanced mechanical properties. The influencing factors on the metal's microstructure are the metal's dimensions, e.g. thickness,

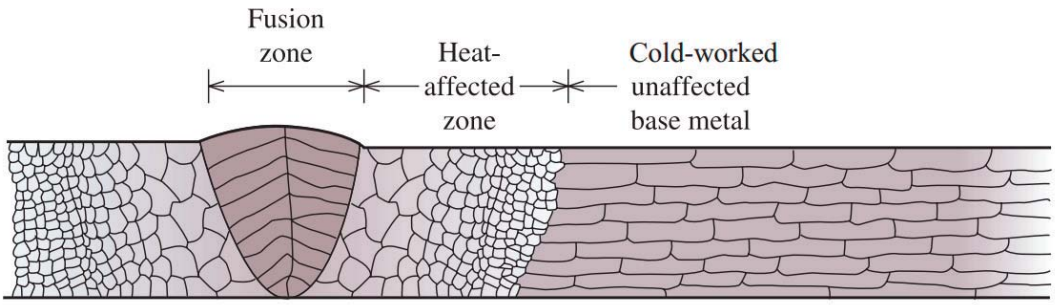

Figure 2.2: *Butt welded joint's recrystallization and grain growth due to welding [4].*

smaller weld fusion zones, low initial metal temperatures and the applied welding technique. Thus, welding techniques with immense heat sources result in faster cooling [4], [29], [24].

Base material

The base material of a welded joint can possess a wide range of mechanical properties depending on the material's thermal and mechanical history. Multiple metalworking processes, e.g. cold working, hot working, rolling and heat treatments, are applied in order to achieve the desired mechanical properties such as strength, ductility, fracture toughness and fatigue resistance. Additional alloying elements in the base material can have significant influence on the material properties [29], [24].

Heat affected zone

The heat affected zone is the region in between the fusion zone and the unaffected base metal which has not been melted. However, it has been affected by the welding process in a way where the region has been heated above the recrystallization and grain growth temperature. This alters the region's microstructure and correspondingly the mechanical properties before the metal cools down again. The properties of the HAZ are mainly based on the base material's composition and the heat introduced during the welding procedure. If the heat input is too excessive the heat affected zone will soften which subsequently reduces the metal's yield and maximum strength in addition to a lowered weld notch toughness. However, if the heat input is too low the heat affected zone will result in hardening. Metals which have been subjected to cold working or

precipitation hardening can effectively reduce the softening effects related to the HAZ [3] [4], [24], [28], [22].

Fusion zone

The fusion zone, the weld metal, is the region which has been subjected to temperatures above the metal's melting temperature. Two main mechanisms occur within the region as the molten metal solidifies, i.e. nucleation and grain growth. The base metal's grains along the fusion line which have not been melted work as a basis for the nucleation. In the absence of filler metal the nucleation takes place by arranging atoms from the molten weld metal upon the non liquefied grains from the base metal with little or no changes made to their crystal structure. This grain growth mechanism is termed eqitaxial growth, forming columnar dendrites. Welding with filler metal of different material composition on the contrary will result in different weld metal crystal structure. Thus, epitaxial growth is inhibited and the new grains from the weld metal have to nucleate at the grain boundaries at the fusion line.

When considering fusion welding, impurities are already present in the molten weld metal and will contribute available surfaces for nucleation initiation. The effects of impurities, such as Sulphur and Phosphorous, within the molten weld metal are known to cause solidification cracking in carbon and low alloy steels, even at low concentrations. This relates to the respective grain sizes and grain boundaries in a way where coarser grain microstructures have less area of grain boundaries resulting in higher concentrations of impurities at the grain boundaries. Consequently, making the metal more susceptible to cracking. Additionally, dilution of the base metal, turbulence from convective forces and possible electrode droplets, and large temperature gradients in the molten metal weld due to continuous input of heat will affect the solidification mechanism of the weld. Furthermore, the welding speed is significantly influential as the width of the HAZ and the corresponding loss of strength is dependent on the ratio between the applied heat input to the welding speed, Q/V. Additionally, the cooling rates are much higher at high welding speeds. However, in order to obtain a good and sound weld the heat input has to be increased correspondingly [24], [28].

2.1.3 Weldability

The integrity of a structure is not solely dependent on the strength of the applied steel, but also on the strength of its welded joints. Thus, weldability of the steel becomes an important consideration. Weldability is used to describe how readily a steel can be

welded as well as to give a measure of the steel's ability to maintain its properties, such as strength and corrosion resistance, after being subjected to welding. Most steels are able to be welded, however they are not always welded with the same amount of effort. Low carbon steels are easy to weld, while medium and high carbon steels become harder to weld due to possible martensite formations in the HAZ, causing a reduction in toughness. This has been countered by various methods, e.g. preheating of the steel or reduce hydrogen absorption of the material as it causes brittleness or possible cracking. The ductility of high strength steels must be sufficient during the cooling down period in order to avoid cracking and be weldable.

The major effect on weldability is the chemical composition of the metal, which has given rise to derivation of numerical expressions in order to assess and evaluate the influence. For this reason, the carbon equivalent content of ferrous materials was determined in order to better comprehend how different alloying elements will influence the welded joints hardness. It compares the relative properties of alloys to carbon steel according to:

$$C_{eq} = C + \frac{Mn}{6} + \frac{Cr + Mo + V}{5} + \frac{Cu + Ni}{15} \tag{2.1}$$

Where a steel is considered weldable if $C_{eq} \leq 0.41$. For $C_{eq} > 0.41$ the steel is considered to have limited weldabilily. Higher carbon content along with a number of alloying elements tend to increase the hardness and brittle behaviour and thus reduce the weldability. This relates to hydrogen induced cracking, also known as cold cracking, which is a frequent defect in welded steel joints [3] [4] [22], [28].

2.1.4 Weld discontinuity

The weld discontinuities can affect the stress distributions in the structure and act as stress raisers by reducing the cross sectional area and thus creating or enhancing the corresponding stress concentrations around them. They additionally become a potential site for a crack initiation as well as a potential site for corrosion and erosion.

The severity of these discontinuities is dependent on the size, shape, sharpness, location and orientation with respect to the loading applied as well as the density of the discontinuities. However, not all discontinuities have detrimental effect on the integrity of the structure. A defect, flaw or an imperfection are definite discontinuities which would lead to the rejection of the welded part or structure as they were unable to

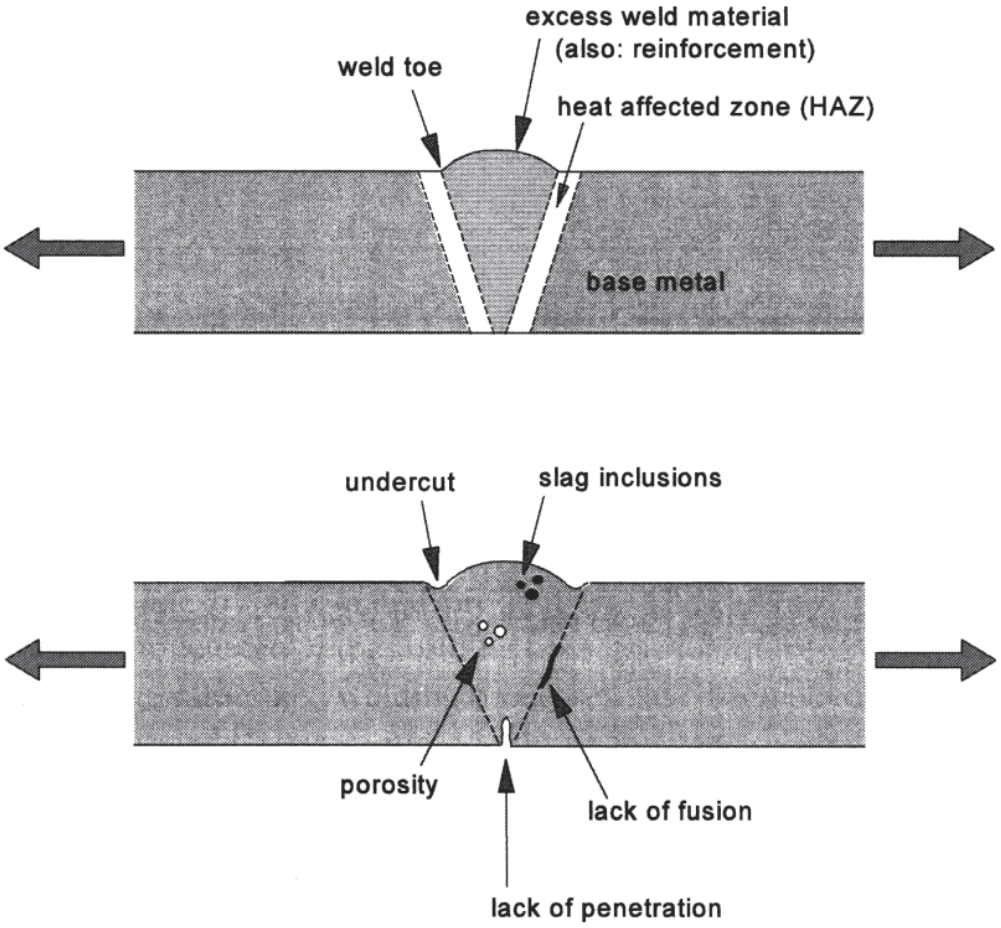

Figure 2.3: *Examples of welding flaws in a butt welded joint, [5]*

meet the minimum acceptance levels from specifications. Figure 2.3 illustrates a butt weld influenced by welding flaws.

The weld discontinuities have been classified into three main groups by the American Welding Society, AWS, i.e. 1) flaws related to the welding technique's procedure and process, 2) the applied material metallurgical behaviour and 3) design related [30], [28], [31], [24]. This discontinuity classification is accordingly:

Weld process and procedure:

- Geometrical discontinuities

  - Misalignment, Undercut, Convexity, Concavity, Excessive reinforcement, Incomplete reinforcement, Lack of penetration, Lack of fusion, Burn through, Overlap, Surface irregularity, etc.
- Others
  - Arc strikes, Slag inclusions, Tungsten inclusions, Spatter, Arc craters, Oxide films, etc.

Metallurgical:

- Cracks or fissures
  - Hot crack, Cold crack, Lamellar tear, etc.
- Porosity
  - Spherical, Elongated, Worm holes, etc.

Design:

- Changes in sections
  - Different thickness, Partial penetration joints.
- Weld joint type
  - Restraints, Accessibility.

The main causes of these discontinuities and their relative density within the welded structure depends heavily on the welding technique, the applied material, the type of weld created, the joint design, the joints fit-up prior to welding in addition to the working and environmental conditions during the actual welding process. Thereafter, the efficiency and accuracy of the applied inspection methods become a vital factor in determining the occurrences of the flaws and their density within the welded joint. Additionally, the results from the inspection decide whether the welded joint is acceptable or not by referring to the available welding codes which contain acceptance levels and specifications [31].

A perfect weld is virtually impossible as all welded structures possess stress concentrations other than the included weld discontinuities and thus it is a matter of consequence whether the defects will lead to the structure's failure or not [6].

Porosity

Porosity or a void is a cavity type discontinuity formed as the result of gas entrapment during solidification due to accessible moisture during the welding process or poor surface treatment prior to welding. The moisture could be on the metal's surface, on the filler metal or simply humid air conditions. The weld pool is also susceptible to contamination from the environment if the shielding gas is not working efficiently. Other sources of porosity formations include, improper electrode coating, length of the arc, speed of the arc, the applied current, the welding technique in addition to the metal compositions selected. Hydrogen is a frequent cause of porosity within high strength steels while oxygen does not usually cause porosity as it can react with most of the metals to form oxides.

Porosity within a welded joint can be uniformly scattered as a result of poor workmanship or poor material quality. Clustered porosity usually implies improper termination or initiation of the weld. Linear aligned set of pores can also form due to contamination.

Porosity does not exhibit the same detrimental effects on structures subjected to static loading while they do have a critical effect on cyclically loaded structures as they can promote crack initiation [30], [28], [24], [25].

Cracks

Cracks are the most detrimental flaw relating to welding. They are severe stress raisers and promote crack growth and thus are not permitted by any welding codes nor specifications. Cracks occur as a result where localized stresses surpass the metal's tensile strength. They tend to occur near discontinuities and notches. Hot cracks occur at high temperatures while cold cracks develop as a results of brittleness and tensile stresses surpassing the fracture stress after the specimen has cooled down. Cracks can additionally form in the weld root, i.e. root cracks, while throat cracks can form at the weld surface and extends towards the root. Longitudinal cracks can develop along the welding direction as a result of high welding speeds.

The main causes of cracks are related to the metal being preheated with a subsequent rapid cooling. Cracks can develop in the vicinity of discontinuities and because of stresses due to shrinkage. The material composition is an additional source of crack formation along with impurities. Additionally, restraints applied to the specimen during welding can induce stresses of high stress levels which form cracks as the welded

region cools down and undergoes shrinkage. These restraints affect and hinder the metal's ability to behave in a ductile manner and leads to brittleness [23, 24, 25, 28, 30].

Other defects

Other critical defects worth mentioning are e.g. slag inclusions where foreign material, such as slag, flux or oxides are trapped within the weld. Slag inclusions only occurs while applying flux shielding and usually occur as a result of poor workmanship due to improper electrode manipulation or lack of cleaning in between passes in a multipass weld.

Lack of fusion is the result of incomplete fusion between the weld and the base metal. The main causes of lack of fusion is poor preparation of the materials or incorrect joint design.

Lack of penetration occurs when the weld penetration is insufficient. This is a result of low heat input, incorrect joint design or poor workmanship.

Undercut happens when part of the base metal is melted away during the welding process with insufficient filler material deposited. Undercut form a groove which can be relatively sharp.

Underfill is due to lack of weld metal. Thus the joint is not filled up and will require an additional welding pass. If left unattended it becomes a severe stress concentration.

Overlap occurs when the weld metal overlaps the weld root or the weld toe due to a slow welding speed or an improper technique [25].

2.1.5 Residual stresses

A metal which has been subjected to non uniform temperature changes, e.g. welding, will develop internal stresses as it solidifies, i.e. residual stresses, and their existence is not dependent on any external forces. They form as a consequence of the weld thermal cycles where the weld and neighbouring metal is heated and cooled, sometimes repeatedly in during multiple welding passes. The corresponding expansion and contraction of the metal is prevented by the restraining effects of the colder base material further away from the weld region which is not subjected to enough heat to expand. These internal stresses are balanced within the welded structure in an equilibrium state, thus

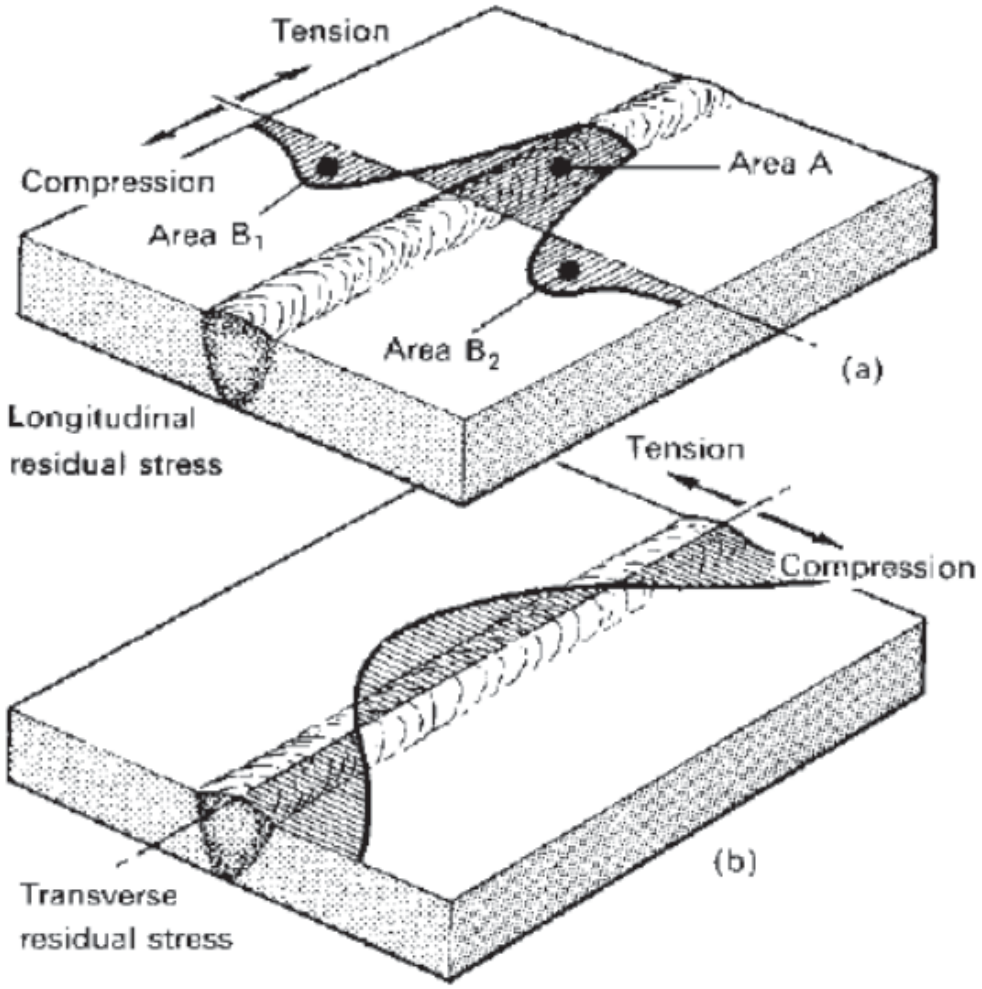

Figure 2.4: *Residual stresses across and along a weld length, [6]*

both high compressive and high tensile stresses are present, which can reach the metal's yield strength in magnitude [6].

Figure 2.4 illustrates the assumed idealized formation of longitudinal and transverse residual stresses. These stresses reach yield strength magnitudes as a result of material shrinkage and due to equilibrium conditions the tensile residual stresses formed

are balanced out with compressive residual stresses further away from the welded region.

The presence of high tensile residual stresses will have a significant effect on welded structures subjected to tensile stresses as the weld metal is already containing stresses up to yield strength, σ_y. Being subjected to external stress the weld will remain at σ_y, with additional local plastic straining. However, when the external stress is removed the residual stresses have been modified due to the maximum stress applied, resulting in lower residual stresses at the weld, corresponding to $\sigma_y - \sigma_{max}$. Thus, if the welded structure is subjected to external cyclic stress range, ranging from an unloaded state up to a maximum value of σ_{max}, the weld will be subjected to a stress range from $\sigma_y - \sigma_{max}$ up to σ_y. The applied stress range, $\Delta\sigma$, at the weld is therefore the same as for the welded structure but the mean stress, σ_m can be significantly higher. This simplified version leads to two significant observations, 1) fatigue failure in welds with high residual stresses can fail under compressive loading conditions, and 2) that the fatigue strength is controlled by the applied stress range, $\Delta\sigma$.

Additionally, the residual stresses resulting from a welding process where the specimen is constrained can lead to crack formations while the corresponding residual strains can lead to the structures global distortion. The residual stresses are dependent on the weld size, the weld penetration, the filler metal applied and the base materials involved as higher yield strength can induce higher residual stresses [6], [28].

Applying post weld heat treatments can reduce the magnitude of residual stresses due to welding. However, it can be extremely costly and impractical for many structural applications [22].

2.1.6 Weld automation

The quality of the welded joint is determined by the weld defects. Thus a considerable difference in welded joints is noticeable when comparing manually performed processes against automated or robotic. To a large extent the manually performed welds are dependent on the qualifications of the welding operator. A qualified operator requires extensive training, knowledge, experience and skill in order to create a sound and good weld. However, the repeatability of the good weld is challenging and demanding for an operator with all the additional influential factors involved. Therefore, semi-automated, fully automated or robotic welding processes have received much attention lately and their ability to perform fast, consistent, repeated, and high quality welds has become attractive. Thus, eliminating the human factor [5].

2.2 Fatigue loading

Fatigue failure of metal structures has been a comprehensive issue throughout history. The first major source for metal fatigue failures has been linked to the railway industry in the 1850's, where railway axles failed frequently at the shoulders. August Wöhler performed a series of research relating to this predicament, developing test machines to carry out axial, bending and torsional tests on notched and unnotched specimens. Wöhler recognized that a repeated load, far below the static strength of a structure, could lead to complete fracture. Additionally, Wöhler demonstrated that higher stress amplitudes reduced the fatigue life of a structure and that there exists a stress amplitude at lower levels where fatigue loading did not lead to fracture [32].

Since then extensive research and experimental testing has been performed concerning this complex failure phenomenon of materials and an estimated 100.000 publications had been published on this topic in the year 2000. Fatigue failure of structures is known to be the most frequent mode of failure in industry [19], and an overwhelming majority of service failures of metal parts is due to fatigue.

A structure or component subjected to a cyclic or an alternating stress is prone to fatigue failure. The failure process starts with the initiation of a microscopic crack nucleus usually around a material discontinuity where stresses can concentrate. This is followed by a crack propagation period until the crack reaches a larger macroscopic size where it will propagate more rapidly until it reaches a critical size where it causes complete fracture. Thus the fatigue life of a structure is commonly split up into two period, i.e. crack initiation period and crack growth period. [5].

Fatigue loading occurs at either constant or variable amplitudes where the stresses may alternate around zero, from zero up to a maximum or a minimum stress range or at stress ranges above or below zero. Multiple fatigue tests have been carried out at varying stress ranges, registering the number of cycles until failure, in order to quantify the respective fatigue resistance of the material. The resulting data is usually presented in a graph illustrating stress ranges $\Delta\sigma$ with respect to the number of cycles until failure, N, also known as fatigue life of the structure.

These fatigue curves, also known as S-N curves or Wöhler curves, are an illustrative representation of the fatigue properties of a material and are commonly presented in a S-N diagram. In order to generate an S-N curve multiple fatigue tests have to be performed at different stress ranges with a number of identical test specimens, which represent the structural detail under consideration. The S-N curves are usually plotted up on a logarithmic scale as the stress range, $\Delta\sigma$, against cycles to failure, N, frequently

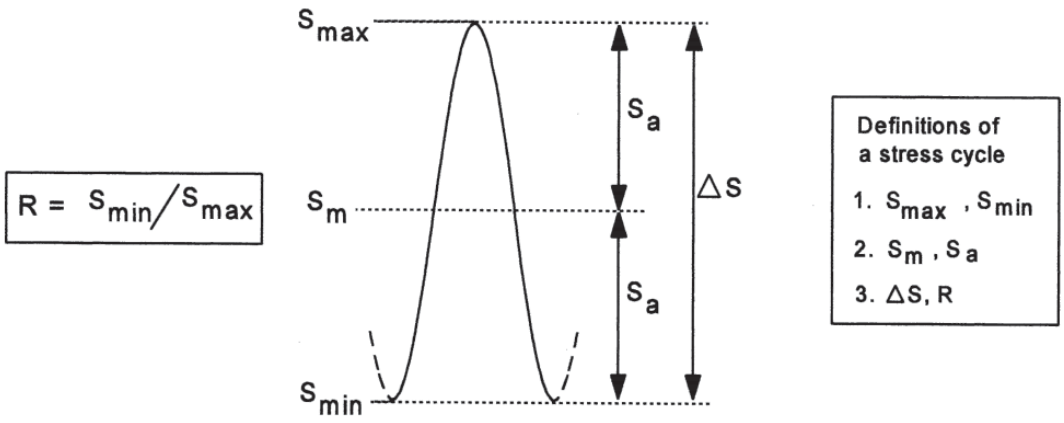

Figure 2.5: *Fatigue load cycle definitions, [5]*

demonstrate a linear relationship for a large range of cycles to failure, N. This linear relationship can be written as:

$$\begin{aligned} \Delta\sigma^m N &= a \\ logN &= loga - m * log\Delta\sigma \end{aligned} \tag{2.2}$$

This equation is called the Basquin relation and the linear slope is equal to $-1/m$, a is a constant and m is dependent on the structural detail involved.

Other terms related to define stresses applied concerning fatigue are:

The mean stress, σ_m defined as;

$$\sigma_m = (\sigma_{max} + \sigma_{min})/2 \tag{2.3}$$

The amplitude, σ_a;

$$\sigma_a = (\sigma_{max} - \sigma min)/2 \tag{2.4}$$

The stress range, $\Delta\sigma$;

$$\Delta\sigma = (\sigma_{max} - \sigma_{min}) = 2\sigma_a \tag{2.5}$$

And the stress ratio, R;

$$R = \frac{\sigma_{min}}{\sigma_{max}} \tag{2.6}$$

Figure 2.5 illustrates the definitions related to a fatigue stress cycle.

The S-N curves can be divided into low cycle fatigue and high cycle fatigue. Low cycle fatigue relates to cyclic loading at high stress ranges with fatigue life up to 10^4 cycles. High cycle fatigue relates to cyclic loading at at lower stress range where the respective fatigue life is above 10^5 cycles. High cycle fatigue can also demonstrate a flattening, or a plateau of the respective S-N curve for some materials, e.g. steels. This plateau represents the material's fatigue threshold limit, or an endurance limit and stress amplitudes below this level should not lead to continuous crack growth nor exhibit fatigue failure. The fatigue tests can demonstrate a lot of scatter in the resulting fatigue life data. Low cycle fatigue demonstrates less scatter than high cycle fatigue, but overall the scatter in fatigue life can range from less than a factor of 2 up to more than 2 orders of magnitude.

Additional considerations which should be stated when considering S-N diagrams are; 1) they are average curves, representing a average number of cycles to failure at the respective stress level, 2) they represent test results performed at constant stress amplitudes, 3) the test specimens applied are usually ideal or machined, therefore not necessarily representing a real structure.

Other factors influencing the fatigue properties of a material are; 1) environmental effects, 2) mean stress effects, 3) residual stresses, 4) notches and stress concentrations, 5) size effects, 6) type of loading, 7) microstructure, 8) post treatments of the specimens, 9) frequency, 10) variable amplitude loading etc [5, 33, 34].

Producing an S-N curve by experimental testing can be extremely time consuming and costly. Thus, running tests at higher frequencies can be beneficial. However, high frequencies can affect material properties and generate heat within the specimens. This effect has been proven to be negligible for most structural metals where frequencies ranging from 1 Hz to 200 Hz had only a small effect on fatigue behaviour [34].

2.2.1 Fatigue loading of welded joints

The aforementioned complex failure mechanism related to fatigue of materials is still not fully understood. Increased research and developments in the field have resulted in a more profound understanding of the phenomenon and methods have been presented in order to prevent fatigue failure of structures. However, the mere complexity and the number of influencing factors involved ensure that fatigue failures, some catastrophic, are still occurring.

Welded connections subjected to cyclic loading contribute additional influential factors to the complexity of fatigue life of structures. Consider the following example, a cycli-

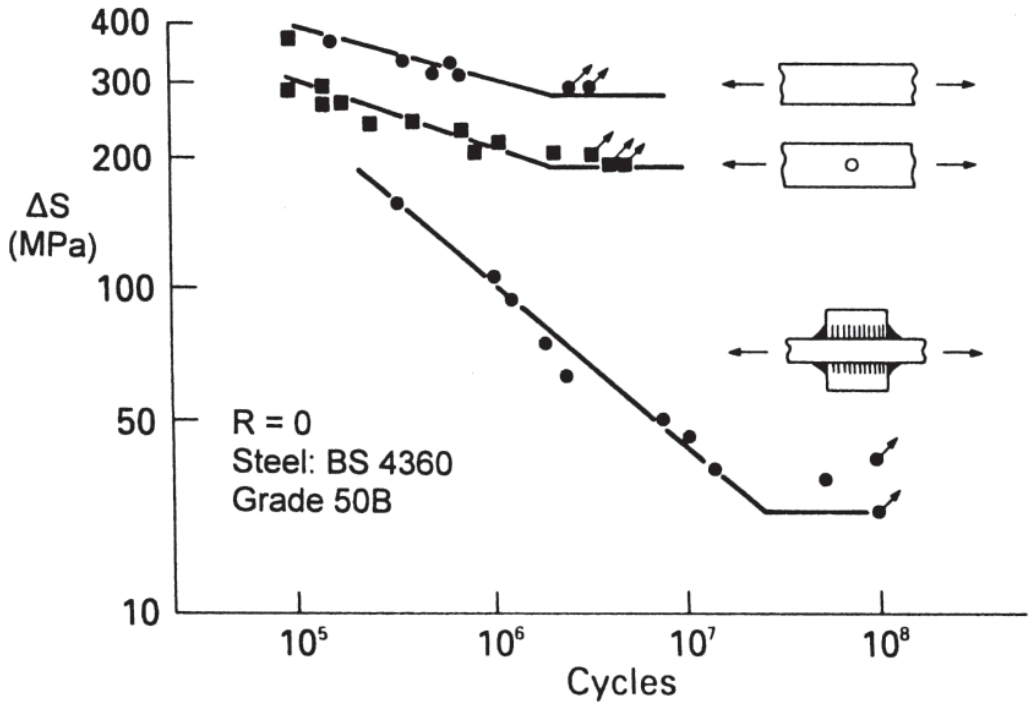

Figure 2.6: *Schematic illustration of fatigue strength for plain steel plate, notched plate, and a plate with fillet weld [6]*

cally loaded distorted welded joint containing residual stresses of tensile yield strength, σ_y, magnitude. The joint has sudden local geometrical features which can introduce severe stress concentrations at critical locations, i.e. the weld region. Furthermore, the inhomogeneous microstructure of the welded region consists of varying mechanical properties and material compositions. Additionally, the welded region comprises of relatively dense clusters of possibly harmful discontinuities of various sizes which act as ideal crack initiation locations. This can be perceived as a common case involving welded structures where all features are within respective tolerance limits.

Figure 2.6 illustrates a comparison of fatigue strengths for a plain steel plate, a notched steel plate and a steel plate with a fillet welded attachment. It illustrates clearly the detrimental effects of weldments. Thus, fitness for service assessments of welded structures has become a widely accepted quality criteria. Fitness for service determines the integrity and fatigue life of a structure which is degraded or defective. Performing detailed stress analysis and defect tolerance assessments to determine the severity of the discontinuities and the remaining service life of the structure. Therefore, a defect as-

sociated with the structure can be considered acceptable as long as it is not detrimental to the structure and its existence does not obstruct the welded joint from fulfilling its intended operation [35].

Current criteria for fatigue design of welded structures has been evolving from uneconomical, impractical infinite life designs to a damage tolerant designs. It is an enhancement of a fail safe design, where the existence of cracks in the structure is acknowledged but periodic inspection should be able to detect the crack before it grows to a critical size which would jeopardize the entire structure. Another important factor of damage tolerant design is the reduction of residual strength as the crack grows under cyclic loading. However, design criteria is always dependent on the application and infinite life designs are still implemented [7].

International and domestic organizations have put forward recommendations and guidelines in evaluating the fatigue life of welded structures. They have established fatigue design S-N curves for a range of structural details, taking various influential aspects of fatigue loading into consideration. In this project the International Institute of Welding, IIW, recommendations for fatigue design of welded joints and components is applied in addition to Det Norske Veritas, DNV, recommended practice for fatigue design of offshore steel structures, RP-C203.

The IIW recommendations specify that the fatigue resistance data is built on published results collected from cyclic testing with constant amplitude loading. The majority of the fatigue test results comes from small welded specimens tested until complete rupture, which is assumed to be close to through thickness cracking. Additionally, all fatigue data is presented as characteristic values, representing a minimum survival probability of 95%, calculated from the populations mean value. Furhermore, the nominal stress range does not exceed the elastic region. Lastly, the design stress values should not exceed 1.5 * σ_y for nominal normal stresses and 1.5 * $\sigma_y/\sqrt{3}$ for nominal shear stresses [7, 36].

Welded detail

The standards give fatigue resistance recommendations for various welded structural details, such as fillet welds, butt welds, etc., which are grouped into classes. Relating to this project then the structural welded detail of interest is a butt welded joint, in the as-welded condition, meaning no post weld treatments have been applied. This corresponds to welded detail number 212 in the IIW recommendations, for a transverse butt weld made in shop in flat position and the recommended fatigue resistance is 90 MPa at 2 million cycles. The butt welded joints have to be fully fused, full penetration welds

No.	Structural Detail	Description (St. = steel; Al. = aluminium)	FAT St.	FAT Al.	Requirements and remarks
200	**Butt welds, transverse loaded**				
211		Transverse loaded butt weld (X-groove or V-groove) ground flush to plate, 100 % NDT	112	45	All welds ground flush to surface, grinding parallel to direction of stress. Weld run-on and run-off pieces to be used and subsequently removed. Plate edges ground flush in direction of stress. Welded from both sides. Misalignment <5 % of plate thickness Proved free from significant defects by appropriate NDT
212		Transverse butt weld made in shop in flat position, NDT weld reinforcement <0.1 A thickness	90	36	Weld run-on and run-off pieces to be used and subsequently removed. Plate edges ground flush in direction of stress. Welded from both sides. Misalignment <5 % of plate thickness
213		Transverse butt weld not satisfying conditions of 212, NDT Al.: Butt weld with toe angle ≤ 50° Butt welds with toe angle > 50°	80	 32 25	Weld run-on and run-off pieces to be used and subsequently removed. Plate edges ground flush in direction of stress. Welded from both sides. Misalignment <10 % of plate thickness

Figure 2.7: *Fatigue resistance values for structural welded details, nominal stress assessment, [7]*

and consisting of base metal not exceeding a yield strength, σ_y, of 960 MPa. Figure 2.7 illustrates the section from the IIW recommendations relating to butt welded joints. Additional considerations for the recommendation is the lack of information concerning the weld reinforcement size, the profile angles, shape and quality [7].

Recommended fatigue curves

Nominal stress range is applied in estimating the fatigue resistance of a categorized structural welded detail. Butt welded joints in the as-welded condition have a recommended design curve of FAT90, illustrated in Figure 2.8, along with other recommended fatigue curves. This curve corresponds directly to the recommended design curve D, according to DNV.

If the evaluation of the fatigue resistance is based on the normal stresses, the slope of the respective S-N curve should be m = 3, unless otherwise specified.

The recommended fatigue resistance curves are based on experimental results that are representing the structural welded detail under consideration. Thus the curves are consequently comprising of the following effects:

- The respective detail's structural hot spot concentrations
- Geometrical local stress concentrations due to the weld
- Fabrication weld imperfections

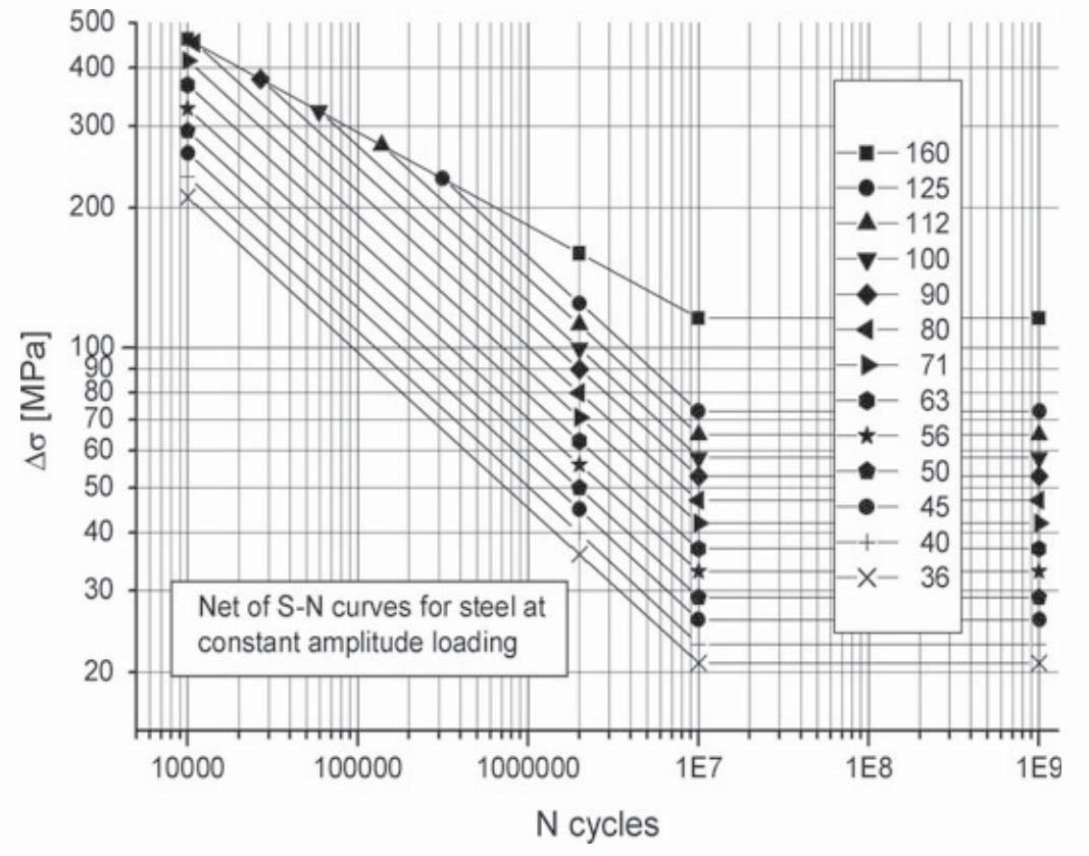

Figure 2.8: *Fatigue resistance S-N curves for welded steel joints at normal stresses, [7]*

- Applied load direction
- The effects of residual stresses
- The effects of the weld metallurgy
- The welding process

Related stresses

Structures are subjected to a wide variety of stresses during the lifetime which occur from sources like wind, waves, currents, ice, snow and temperature changes as well as

the internal stresses and the structure's overall weight.

The involved stress components are; 1) the membrane stress, σ_{mem}, 2) the bending stress, σ_{bend}, and 3) the non linear stress peak or notch stress, σ_{nl}. The membrane stress is the average stress and constant through the thickness. The bending stress is assumed to be linear through the thickness and the notch stress is related to the non linear stress peak at the weld toe.

There are three common stress categories applied in order to investigate fatigue life of welded structures.

- Nominal stress
- Structural stress
- Local notch stress

The difference lies within the level of stress and strain analysis applied, i.e. relating to possible global and local stress raisers in the structural design under consideration [7, 8, 37, 38].

Nominal stress

The nominal stresses can be determined using elementary theories from structural mechanics based on linear elastic behaviour, such as beam theory. The stress is calculated from the applied loads and the cross sectional area of the structure.

$$\sigma_{nom} = \sigma_{mem} = \frac{F}{A} \tag{2.7}$$

where F is the applied load and A is the cross sectional area. This is an ideal beam example where there is no effect of global geometrical changes such as misalignment. Accounting for secondary bending stresses due to misalignment the nominal stress becomes:

$$\sigma_{nom} = \frac{F}{A} + \frac{M}{I} * y = \sigma_{mem} + \sigma_{bend} \tag{2.8}$$

where M is the bending moment, I is the moment of inertia of the cross section, and y is the distance to the neutral axis.

The nominal stress accounts for global geometrical changes of the structure but does not consider the local stress raising effect in the vicinity of the weld [7, 8, 37, 38].

Structural stress

The structural stress, also known as the hot spot stress, enhances the nominal stress by incorporating the stress raising effects of the structural detail. The structural stress is evaluated on the surface of the structure close to a region where cracks are expected to initiate and grow due to fatigue loading, i.e. at the hot spot. The structural stress approach is usually applied where there is no obviously determined nominal stress due to complex geometry.

The hot spot stress of a welded structure can be evaluated by the application of strain gauge measurements where the gauges are positioned at specific distances from the weld toe. The measurement point closest to the weld toe has to be placed at a defined distance away from the weld toe to avoid any influences of the non linear stress peak occurring at the notch. The stress at the hot spot can thereafter be estimated by applying either a linear or a quadratic extrapolation according to:

$$\sigma_{hs} = 1.67 * \sigma_{0.4t} - 0.67 * \sigma_{1.0t} \tag{2.9}$$

$$\sigma_{hs} = 2.52 * \sigma_{0.4t} - 2.24 * \sigma_{0.9t} + 0.72 * \sigma_{1.4t} \tag{2.10}$$

where t is the respective thickness of the applied structure. If the applied stress state to the structure under consideration is close to a uni-axial stress state the hot spot stress can be approximated by the following assumption:

$$\sigma_{hs} = E * \varepsilon_{hs} \tag{2.11}$$

However the structural or hot spot stress does not include the local weld profile with the corresponding non linear stress peak resulting from the local notch at the weld toe [7, 8, 37, 38].

Notch stress

The notch stress involves the non linear stress peak at the weld toe, i.e. at the notch. The notch stress takes into account the effects of global and local structural geometry as well as the parameters related to the weld itself, i.e. the weld profile, weld size, flank angle, and the notch radius along with the corresponding stress concentrations. According to IIW recommendations then the notch stress for butt welded joints in the as-welded condition should be at least 1.6 times the structural stress [7, 8, 37, 38].

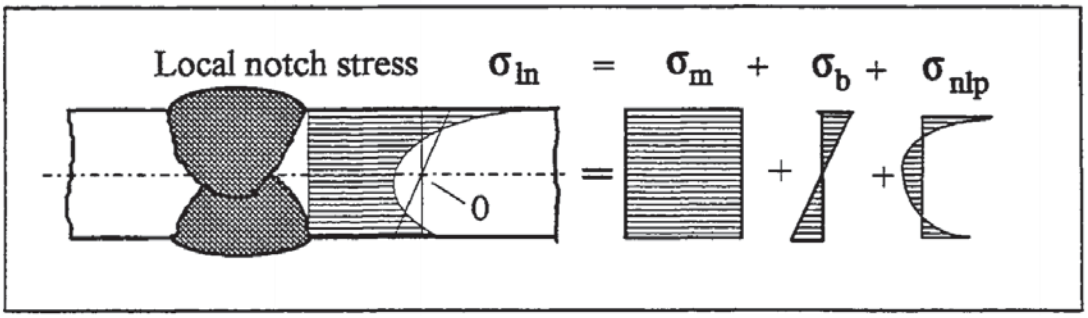

Figure 2.9: *The local notch stress at the weld toe, comprising of membrane, bending and a non linear stress peak, [8]*

Figure 2.9 illustrates the local notch stress at the weld notch, which consists of the membrane stress, the bending stress and the non linear stress peak. The non linear stress peaks at the weld toes on the surface indicate that a crack initiating at the weld toe is much more severe than a crack at the weld root, which is subjected to lower stress [8].

Figure 2.10 illustrates the discussed stress approaches, i.e. 1) the nominal stress furthest away from the weld, 2) the structural stress extrapolated from reference point measurements located at specified intervals towards the weld region, and 3) the computed non linear total stress, i.e. the notch stress at the weld toe.

Thickness correction

The influence of plate thickness is taken into consideration in welded structures if the location of crack initiation is at a weld toe. The fatigue resistance recommended by standards apply for welded joints up to a thickness of 25 mm. However, if the thickness exceeds 25 mm the fatigue strength is lowered due to the detrimental effects of plate thickness on fatigue strength. Thus, the recommended fatigue resistance, or FAT class, from a welded detail is multiplied by a recommended thickness reduction factor according to:

$$f(t) = \begin{cases} 1 & \text{for } t \leq 25\ mm; \\ \left(\frac{t_{ref}}{t}\right)^k & \text{for } t > 25\ mm; \end{cases} \tag{2.12}$$

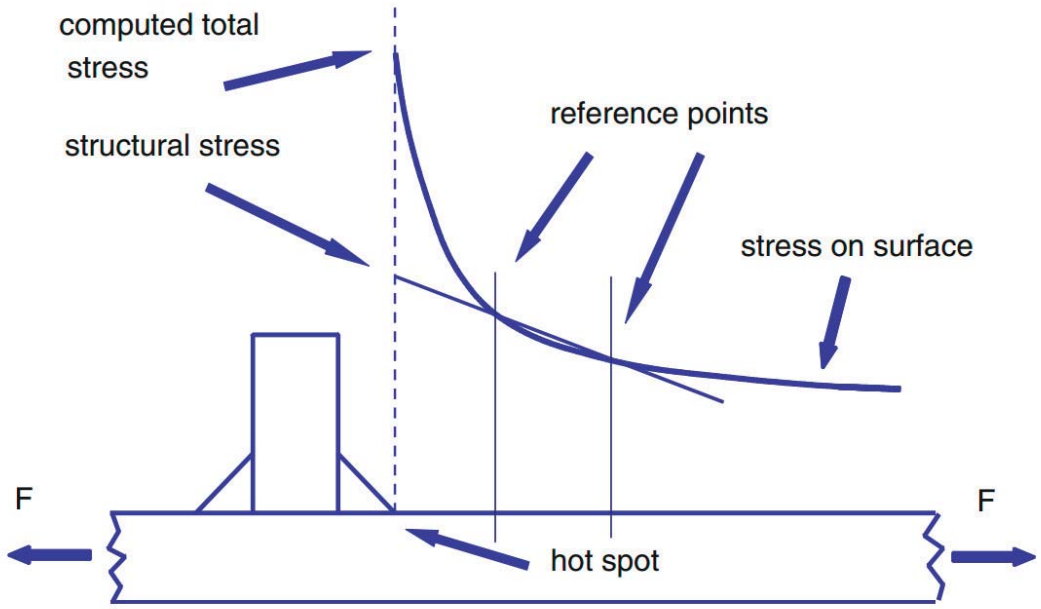

Figure 2.10: *Definition of stresses on a welded structures' surface, [7]*

where t_{ref} = 25 mm and the thickness correction exponent, k, depends on the welded structure's thickness and its corresponding category. The thickness correction exponent for a butt welded transverse joint in the as-welded condition is, $n = 0.2$ while ground flushed butt welds have, $n = 0.1$ [7]. However, there is not a general consistency between the various standards and recommendations concerning the thickness correction [39].

Thus, as the welded structure increases in size, its fatigue strength decreases. The thickness effect is thought to comprise of the following main effects [39, 40, 41]:

- **Statistical size effect:** Considers fatigue of structures as a weakest link process, where a crack nucleates at the most ideal location within structure during loading. The location is most likely where stresses, geometry, metallurgy and discontinuities with the corresponding stress concentrations join to form a ideal situation for a crack to initiate. Thus, increasing the structure's thickness will additionally increase the risk of possible critical locations.
- **Technological size effect:** Considers the manufacturing parameters which emphasizes on the temperature and deformation history of the material. Additionally, different surface treatments lead to dissimilar surface roughness and vari-

ations in residual stresses. Lastly and most importantly is the upscaling, as the weld notch radius is relatively constant for all thicknesses. Therefore, as the thickness increases the stress concentration at the weld notch will increase as well, leading to an obvious thickness effect. Other unaffected factors which require consideration while upscaling are material properties, grain sizes and flaw dimensions.

- **Geometrical size effect:** Also known as stress gradient effect, considers the steeper stress gradient in thinner joints compared to thicker joints. If the two thicknesses are geometrically similar. Then the distribution of stress through the plate is similar, leading to a steeper stress gradient for the thinner joint. Therefore, if the crack initiation is independent of the joint's thickness, then a crack or a notch at the thinner plate will experience lower stress than the same size notch or crack in a thicker joint.

The thickness effect reduction of welded joints fatigue resistance is implemented into the recommended S-N curves according to [36]:

$$logN = log\bar{a} - mlog\Delta\sigma \tag{2.13}$$

where
N = predicted number of cycles to failure for stress range $\Delta\sigma$.
$\Delta\sigma$ = stress range with unit MPa.
m = negative inverse slope of S-N curve.
log $\bar{a}$ = intercept of N-axis by S-N curve.

$log\bar{a}$ is equal to:

$$log\bar{a} = loga - 2s_{logN} \tag{2.14}$$

where
log a = Intercept of mean S-N curve with the log N axis.
s_{logN} = standard deviation of log N.

Which leads to:

$$logN = log\bar{a} - mlog\left(\Delta\sigma\left(\frac{t}{t_{ref}}\right)^k\right) \tag{2.15}$$

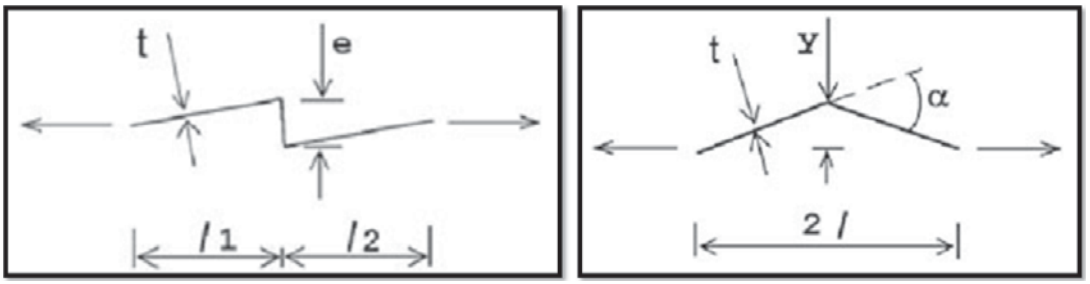

Figure 2.11: *Axial (left) and angular (right) misalignment between flat plates, [7]*

Stress magnification

The effects of misalignment of a butt welded joint under axial loading results in induced secondary bending stresses, σ_{bend}, which increases the stress on one surface in the welded region. For misaligned joints under axial loading, both tensile and compressive secondary bending stresses are induce. Thus, in there are locations where the resulting total stress increases while in others it decreases [38]. In order to incorporate the effects of the global geometrical misalignments of a butt welded joint the axial, e, and angular, α, misalignments are estimated and the following expressions applied [7, 35, 42, 43];

Using the stress relation from equation 2.8, and introducing a stress magnification factor, K_m, according to:

$$K_m = \frac{\sigma_{mem} + \sigma_{bend}}{\sigma_{mem}} = 1 + \frac{\sigma_{bend}}{\sigma_{mem}} \tag{2.16}$$

The axial misalignment, e, for plates of equal thickness, t, subjected to an axial force F is illustrated in Figure 2.11 (left). Treating the overall joint as a beam with a load couple, $F * e$, applied at the center and assuming free rotation which does not affect the load couple results in bending moment on either side of the joint of $(F * e)/2$. The corresponding secondary bending stress is calculated by:

$$\sigma_{bend\_ax} = \frac{\left(\frac{F * e}{2} * \frac{t}{2}\right)}{\left(\frac{w * t^3}{12}\right)} = \frac{3F * e}{w * t^2} \tag{2.17}$$

where, w, is the width of the joint. The applied axial stress equals $\sigma_{mem} = F/(w * t)$ thus:

$$\sigma_{bend\_ax} = \frac{3\sigma_{mem} * w * t * e}{w * t^2} = 3\sigma_{mem}\frac{e}{t} \tag{2.18}$$

and applying the relation in equation 2.16 leads to an axial stress magnification factor, K_{m_ax}:

$$K_{m\_ax} = 1 + 3\frac{e}{t} \tag{2.19}$$

In terms of the angular misalignment, α, of the butt welded joint illustrated in Figure 2.11 (right), can be calculated assuming that the induced bending moment does not change due to the joints straightening under axial loading. Thus, the secondary bending stress is dependent on the fixing conditions at the end. Relating to fixed end conditions and equilibrium where the bending moment is $(F * y)/2$ results in a secondary bending stress of:

$$\sigma_{bend\_ang} = \frac{3 * F * y}{w * t^2} = 3\sigma_{mem} * \frac{y}{t} \tag{2.20}$$

resulting in an angular stress magnification factor, K_{m_ang}:

$$K_{m\_ang} = 1 + \frac{3y}{t} \tag{2.21}$$

which can be expressed in terms of angular change, α, and the respective distance between fixing points, L, according to:

$$K_{m\_ang} = 1 + \frac{3}{4}\alpha\frac{L}{t} \tag{2.22}$$

Due to partial straightening of misaligned butt welded joint under axial loading conditions, a decrease in bending moment is observed as the applied load is increased. To take into account the partial straightening a correction term was derived where:

$$k = \frac{tanh\beta}{\beta} \tag{2.23}$$

where

$$\beta = \frac{L}{t}\sqrt{\frac{3\sigma_{mem}}{E}} \tag{2.24}$$

where E is the elastic modulus and for fixed end conditions, $\beta/2$, is used instead of β.

Thus the resulting stress magnification factor, K_{m_ang} for fixed end condition is:

$$K_{m\_ang} = 1 + \frac{3}{4}\alpha\frac{L}{t}\,\frac{tanh\beta/2}{\beta/2} \tag{2.25}$$

The axial and angular misalignment can subsequently be combined into a general misalignment factor, K_m, according to:

$$K_m = 1 + (K_{m\_ax} - 1) + (K_{m\_ang} - 1) \tag{2.26}$$

The effects of axially loaded joints consisting of axial and angular misalignments do not show a great reduction in fatigue strength unless at relatively large values where $K_m \geq 1.3$ [35]. Additionally, it can be assumed that a majority of butt joints in the as-welded condition subjected to axial loading are affected by secondary bending stresses. Thus the resulting fatigue resistance curves consequently inherited that effect, i.e. secondary bending stresses are taken into account.

Stress concentration

The non linear peak stress at the weld notch can be calculated by first estimating the membrane stresses and the corresponding secondary bending stresses under axial loading acting on the butt welded joint. The secondary bending stresses are calculated by applying the calculated stress magnification factors, K_m, and assuming a linear bending moment through the thickness of the joint. Secondly, the structural hot spot stress which can be determined by the recommended extrapolation procedure, where measured strain values on the specimen's surface are applied in order to estimate the hot spot stress at the critical location, i.e. the weld. Assuming the stress magnification factors, K_m, are constant the hot spot stress can be decomposed into membrane and bending stresses accordingly.

The peak stress can be calculated by the application of the appropriate stress concentration factors by multiplying them with the nominal stress, σ_{nom}, acting on the joint according to [9, 36]:

$$\sigma_{peak} = K_t\sigma_{nom} \tag{2.27}$$

The nominal stress comprises of the corresponding membrane and bending stresses. In the same manner the structural hot spot stress can be applied in order to calculate

the peak stress by using the corresponding hot spot stress concentration factor, K_{t_HS}, according to:

$$\sigma_{peak} = K_{t\_HS}\sigma_{HS} \tag{2.28}$$

The experimentally measured structural hot spot strain values, converted into stresses, σ_{HS}, are a combination of the butt welded joint's membrane and bending stresses present at the surface [9]. The decomposition of the structural hot spot stress into hot spot membrane, σ_{HS}^{mem}, and bending, σ_{HS}^{bend}, in order to calculate the peak stress is performed according to:

$$\sigma_{peak} = \sigma_{HS}^{mem} * K_{t\_HS}^{mem} + \sigma_{HS}^{bend} * K_{t\_HS}^{bend} \tag{2.29}$$

where $K_{t\_HS}^{mem}$ and $K_{t\_HS}^{bend}$ are the appropriate hot spot membrane and bending stresses respectively.

Using the relation that the hot spot stresses under pure axial and pure bending are the same as the calculated nominal stresses [9, 38, 44, 45, 46]:

$$\begin{aligned} \sigma_{HS} &= \sigma_{HS}^{mem} = \sigma_{nom}^{mem} \\ \sigma_{HS} &= \sigma_{HS}^{bend} = \sigma_{nom}^{bend} \end{aligned} \tag{2.30}$$

then the stress concentration factors must also be identical for pure axial and pure bending situations, according to:

$$K_{t\_nom}^{mem} = K_{t\_HS}^{mem} = \frac{\sigma_{peak}^{mem}}{\sigma_{nom}^{mem}} = \frac{\sigma_{peak}^{mem}}{\sigma_{HS}^{mem}} \tag{2.31}$$

the same derivation can be performed for the bending stresses.

By applying these relationships, the peak stress concentration factors for nominal stresses can be applied to derive the peak stress in a situation where both axial and bending loads are involved. Rewriting equation 2.29, results in:

$$\sigma_{peak} = \sigma_{HS}^{mem} * K_{t\_nom}^{mem} + \sigma_{HS}^{bend} * K_{t\_nom}^{bend} \tag{2.32}$$

Published literature provides several stress concentration factors, K_t, applicable in the estimation of the peak stress at the weld notch. However, they vary in complexity and input parameters. The least conservative determination was suggested by Iida and Uemura [47], where they derived the following expressions for, butt welded joints:

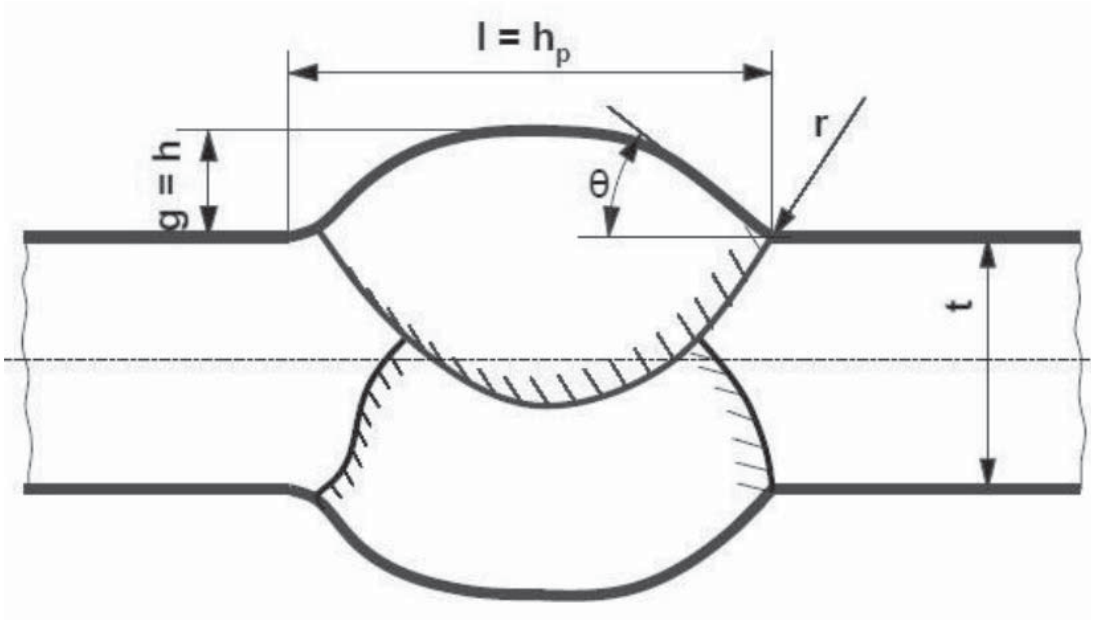

Figure 2.12: *Weld parameters involved in determining the relevant stress concentration factors, [9]*

$$K^m_{t,hs} = 1 + \frac{1 - exp\left(-0.9\theta\sqrt{\frac{W}{2h}}\right)}{1 - exp\left(-0.45\pi\sqrt{\frac{W}{2h}}\right)} * 2\left[\frac{1}{2.8\left(\frac{W}{t}\right) - 2} * \frac{h}{r}\right]^{0.65} \tag{2.33}$$

where the joint is subjected to axial loading, and $W = t + 2h + 0.6h_p$.

And in the case of bending loads.

$$K^{b}_{t,hs} = 1 + \frac{1 - exp\left(-0.9\theta\sqrt{\frac{W}{2h}}\right)}{1 - exp\left(-0.45\pi\sqrt{\frac{W}{2h}}\right)} * 1.5\sqrt{tanh\left(\frac{2r}{t}\right)} \\ * tanh\left[\frac{\left(\frac{2h}{t}\right)^{0.25}}{1-\frac{r}{t}}\right] * \left[\frac{0.13 + 0.65\left(1-\frac{r}{t}\right)^{4}}{\left(\frac{r}{t}\right)^{\frac{1}{3}}}\right] \tag{2.34}$$

The equations proposed by Iida and Uemura have been validated for ratios of notch radius over thickness, r/t, from 0.025 up to 0.4 and for angles, θ, ranging from 20° up to 50°. Figure 2.12 illustrates the weld parameters involved in determining the respective stress concentration factors for axial and bending loads [9, 44, 45, 46, 47].

2.3 Corrosion

Numerous experimental tests and research have been performed in relation to corrosion and the corresponding forms of corrosion. However, the field of corrosion is extremely vast and comprehensive and there are multiple influential factors involved when investigating corrosion. In order to aid inspection and identify corrosion related failures the forms of corrosion have been characteristically defined and categorized. The defined forms of corrosion are the following:

- Uniform corrosion
- Galvanic corrosion
- Thermogalvanic corrosion
- Crevice corrosion, including depost corrosion
- Pitting, and pitting corrosion
- Selective attack, selective leaching, i.e. de-alloying
- Intergranular corrosion, including exfoliation
- Erosion corrosion
- Cavitation corrosion

- Fretting corrosion
- Stress corrosion cracking
- Corrosion fatigue

Additional important and non-negligible factors affecting the corrosion and the subsequent corrosion rate are; 1) temperature, 2) surface deposits, 3) flow rates, 4) hydrogen evolution, and 5) microbial life [10, 13].

Most of the experimental testing which has been performed, focuses on individual effects and not the combination of a few or all related factors together. Additionally, a vast majority of these experiments have been performed in laboratory conditions under ideal controlled circumstances on small scale test specimens. Thus, their applicability in practice has been questioned.

2.3.1 Electrochemical principles

Corrosion is a chemical reaction which occurs due to an electrochemical mechanism. All metal, except gold, in air conditions have an oxide film covering their surface and when the metal is submerged in a liquid solution, this film tends to dissolve. The liquid solution factors, such as pH values and composition, determines whether the oxide film is dissolved completely, partially or not at all.

The corrosion of iron in a liquid environment, i.e. electrolyte, where air is accessible can be written:

$$2FE + O_2 + 2H_2O \rightarrow 2Fe(OH)_2 \tag{2.35}$$

The resulting product, i.e. ferrous hydroxide, can undergo further oxidation and form magnetite, Fe_3O_4, or hydrated ferric oxide, $FeOOH$, i.e. rust.

In considering the involved oxidation and reduction half reactions which occur simultaneously:

$$\begin{aligned} 2Fe &\rightarrow 2Fe^{2+} + 4e^- \\ O_2 + 2H_2O + 4e^- &\rightarrow 4OH^- \end{aligned} \tag{2.36}$$

where the anodic reaction is where electrons are released and the metal consumed, while the cathodic reaction is where the electrons and dissolved species are consumed. Figure 2.13 illustrates the corrosion of iron in a liquid environment [10, 13].

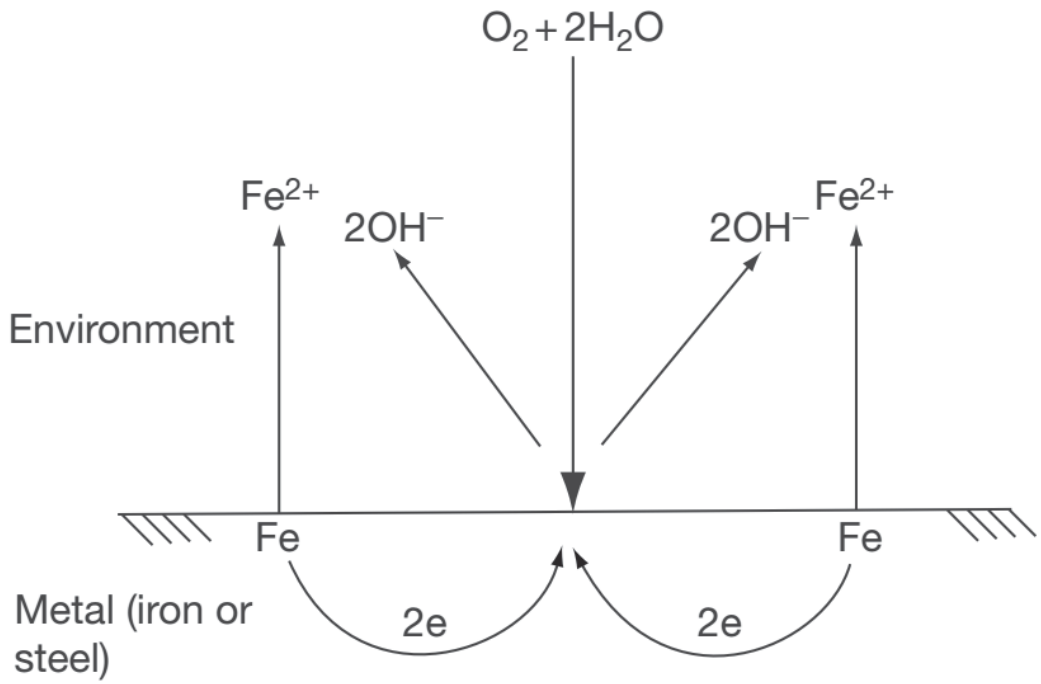

Figure 2.13: *Schematic illustration of the corrosion of iron in a liquid environment [10]*

2.3.2 Corrosion fatigue

Corrosion fatigue is when a structure subjected to fatigue loading is positioned in a corrosion environment. Thus, the detrimental effects from the fatigue loading is combined with the harmful and destructive effects of corrosion. In these situations the environment becomes a significant factor in determining the fatigue resistance of the structure and evaluating its service life. Protection against corrosion must be applied and considered during the design phase of the structure when dealing with an environment where corrosion can occur. Many corrosion prevention and protection methods are available and currently applied in industry, however they can be costly, hard to maintain and their fatigue properties are not always guaranteed. Catastrophic incidents have occurred due to corrosion related fatigue cracking and the related cost of corrosion in industrial applications is immense.

Corrosion fatigue is not the same as fatigue loading of corroded materials. Corrosion fatigue is when the structure is cyclically loading within a corrosion environment

throughout its entire service life.

In performing corrosion fatigue testing the following aspects are of importance and should be considered thoroughly; 1) the type and composition of the applied material as well as its manufacturing history, 2) the type of controlled or non-controlled corrosion environment applied, 3) the influence of the neighbouring environment, and 4) the type, magnitude and frequency of external loads.

Corrosion fatigue of welded structures

The complex phenomenon related to the fatigue loading of welded structures, with all the aforementioned influential factors involved, is intensified and made much more severe as the welded structure is positioned in a harsh, aggressive environment, such as offshore. Furthermore, offshore structures are subjected to higher and more frequent loading conditions with the possibility of extreme scenarios.

Corrosion is a time dependent process and the main damage mechanisms involved with corrosion fatigue are; 1) hydrogen embrittlement, 2) film rupture, 3) dissolution and repassivation, 4) enhanced localized plasticity, 5) interactions of dislocations with surface dissolution, and 6) films or adsorbed atoms. The individual and combined contributions of these mechanisms are controversial and complex. Furthermore, metallurgical composition and the corresponding related environmental factors are of importance.

The corrosion environment is known to have detrimental effects on cyclically loaded structures. It can speed up crack initiation as well as increase the crack propagation period. The detrimental effects of corrosion on the crack initiation period is mostly due to a pure corrosion mechanism at the structures surface, e.g. pitting corrosion. Corrosion pits or grooves form on the surface and lead to possible stress concentrations. Relating to the fatigue crack propagation period the availability of the aggressive environment to the crack and the crack tip determines the growth rate as well as the effect of accumulating corrosion products within the crack [5, 43, 48, 49, 50, 51]. Additionally, plastic local deformations around a crack or the crack tip can induce anodic dissolution [13]. Furthermore, welded structures in a corrosion environment can initiate several crack nucleation sites simultaneously at very low stress amplitudes [5].

The crack nucleation and crack growth velocity becomes an even greater concern when dealing with high strength steels [52, 53, 54].

However, fatigue testing of welded joints in a seawater environment with the application of a cathodic protection can result in fatigue resistance which is similar to that of

welded joints tested in air in the high cycle range [13, 55]. However, the application of cathodic protection in the high stress range still has a large reduction in recommended fatigue resistance due to possible detrimental effects, such as hydrogen embrittlement [43].

It should be emphasized that these tests are performed under laboratory conditions. Not representing a real life structure exposed to non controlled corrosion environment, subjected to variable amplitude loading at different frequencies over a period of many years.

The IIW recommendations do not cover corrosion environments nor do they have any design S-N curve recommendations relating to corrosion fatigue resistance with or without cathodic protection [7]. On the contraty, DNV provides recommended S-N curves for welded structures within a corrosion environment with and without cathodic protection. However, the fatigue resistance, for the respective welded details, have been significantly reduced compared to the in-air recommended fatigue design curves in the low cycle region [7, 36]. Additionally, the recommendations are built on experimental testing of structural steel in the North sea conditions, where temperature ranges from 6 to 10° and the loading frequency is estimated to be 0.17 up to 1 Hz. Furthermore, the standards assume an even distribution from the sacrificial anode corrosion protection. The limits for acceptable corrosion are not well defined as structures are not designed for free corrosion conditions, however there are situations where free corrosion could arise. Lastly, there is a complete lack of information provided concerning internal corrosion protection, which is highly relevant for offshore wind turbines [20, 56, 57].

Cathodic protection

Since the corrosion mechanism of a metal in an electrolyte is based on chemical and electrical processes, a possible manipulation of available electrons on the metal's surface can increase or slow down the consumption of the metal. This is the foundation for cathodic protection where electrons are provided to the metal's surface in order to reduce or bring the anodic reaction to a stop.

Structures subjected to corrosion can be cathodically protected by applying a sacrificial anode or with an impressed current technique. Further prevention of corrosion is addressed by the application of surface coating which also works to reduce the required cathodic protection capacity.

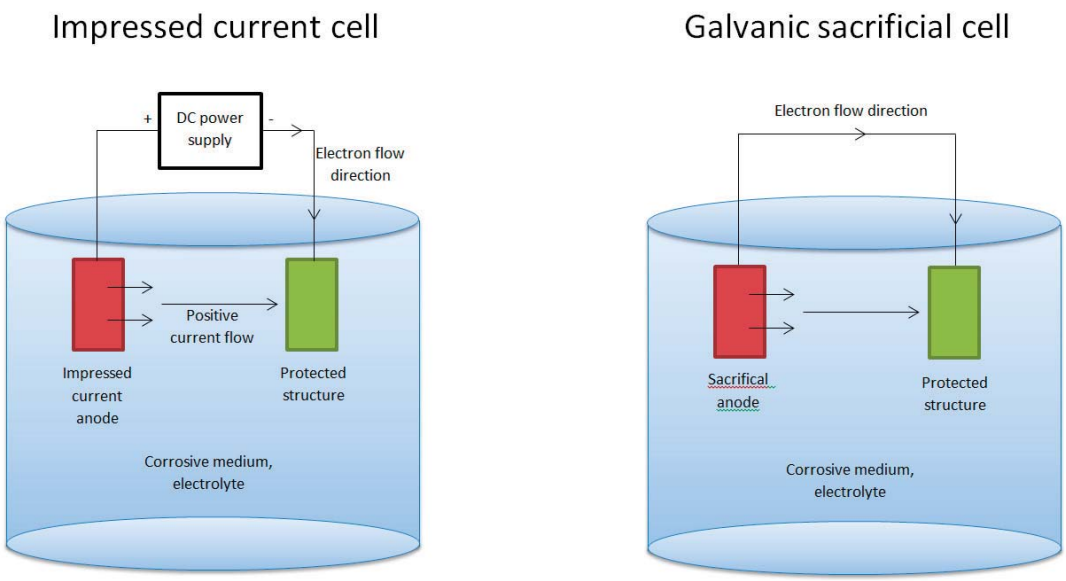

Figure 2.14: *Schematic diagrams of applying cathodic protection using either impressed current technique (left) or a sacrificial anode*

Sacrificial anode cathodic protection

Cathodic protection with sacrificial anodes is based on using the potential differences between different metals within the corrosion environment. The more active metal, i.e. has more negative electrode potential, applied provides electrons and the driving voltage required in order to protect the other metal. Thus the more active anode metal will be consumed over time, hence the name sacrificial anode. The sacrificial anode has to be more negative in the galvanic series for the considered corrosion environment, in relation to the other metal applied. Considering the galvanic series, then for example magnesium, zinc and aluminium are all more negative, i.e. less noble, than steel and thus are applied regularly as anodes for protection of steel structures.

This was first performed by Sir Humphry Davy in 1824, where he demonstrated how zinc and iron anodes prevented the corrosion of copper sheathing of naval vessels hulls [58]. However, his research did not gain momentum and cathodic protection was not applied until approximately 100 years later by oil companies in the USA [10].

Impressed current cathodic protection

Impressed current cathodic protection consists of a power supply, an impressed current electrode, the electrolyte and the structure which is to be protected. The electrons required to protect the structure's surface from corroding are provided by the power supply which drives a positive current from the impressed current electrode, acting as an anode, through the electrolyte. The structure is thus protected from corrosion as its corrosion potential is lowered into the immune region. A table listing values for standard potentials of common metals along with a Pourbaix diagram are shown in Appendix E

The applied impressed anodes can be consumable, semi-consumable or non-consumable. Consumable anodes will be dissolved over a period of time as a consequence of anodic reactions while non-consumable anodes can maintain an anodic reaction which decomposes the electrolyte rather than consuming the metal. Figure 2.14 illustrates the two aforementioned techniques for cathodic protection.

When considering cathodic protections where the potential of the metal is lowered in order to protect the structure the influence of hydrogen evolution cannot be neglected. The hydrogen evolution can affect the structure's coating layer, where it destroys the adhesion between the coating and the base. Furthermore, the hydrogen ions can penetrate into the steel material, reducing its ductility. The hydrogen evolution is dependent on the current which is applied to lower the structure's potential into the immune region. However, the required current to maintain a cathodic protection diminishes over time due to a formation of a protective calcareous deposit layer on the structure's surface [10, 59].

This page is intentionally left blank.

Chapter 3

Review of scientific literature

A lot of research and experimental testing has been performed concerning the fatigue failure phenomenon of metals and welded joints. However, when considering steel welded joints for the following specific cases; 1) fatigue resistance of large butt welded joints, 2) corrosion fatigue resistance of large butt welded joints, and 3) fatigue resistance of large laser hybrid welded butt joints, then the available literature and experimental data is scarce and somewhat lacking.

A plausible cause for the lack of literature and research might lie with the fact that fatigue testing is a time consuming and costly test procedure which is heavily dependent on man-hours and available machine capacity. This is especially true if the desire is to investigate the fatigue resistance of truly large welded structures which require extremely high loading conditions or when trying to simulate ocean loading conditions where the frequency should be ranging from 0.17 Hz to 1 Hz.

The overall objectives of the present PhD project, were investigated by defining and performing three different experimental fatigue testing series. Thus, the following literature review is as well categorized into the three respective test series.

3.1 Test series 1: Experimental investigation of the thickness effect for submerged arc welded joints

Thickness effect

The thickness effect of welded joints has received an increased amount of attention recently and been the subject of a lot of debate, relating to whether it could be too conservative. Thus, it might be leading to overly thick recommendations of welded joints at the design stage in order to obtain the desired fatigue strength. The thickness effect has been proven experimentally and multiple fatigue tests have been carried out in order to verify the effect. The earliest data is from 1950s but it was research published by Gurney [19], which led to the thickness correction factor which enables predictions of fatigue strength of thicknesses other than the suggested reference thickness. Gurney proposed a thickness correction exponent of, k = 0.25.

The thickness correction factors have become more representative nowadays and are available for different welded details of varying qualities in most standards and recommendations. An example is the DNV recommended practice for fatigue design of offshore structures, [36] and IIW recommendations for fatigue design of welded joints and components [7]. DNV and IIW both recommend a thickness correction exponent of k = 0.2 for butt welded joints in the as-welded condition.

Örjasäter [39], put forth a detailed description of the three main arguments relating to the thickness effect on welded components subjected to fatigue loading. They comprise of the statistical, the technological and the geometrical size effects which can have a significant influence on the welded joints fatigue life. The most influential are the geometrical and statistical size effects. Örjasäter additionally proposed a more conservative and general thickness correction exponent of, k = 0.33. Maddox, [6], reaffirms that the most pronounced affect is related to the geometrical size effect where the stress gradient through the specimen's thickness differs between thicknesses. Thus, a thickness independent crack, nucleating at the specimen's surface is subjected to increased stress concentrations when considering larger joints.

As previously stated, then fatigue test results for large welded joints are lacking in available literature, especially for butt welded joints. Stig Berge, [60], carried out tests of large welded fillet joints under axial loading. The thicknesses were ranging from 12.5 mm to 80 mm thicknesses. The results from his research was a reduction in fatigue strength of 40%. Additionally, the results were verified with a fracture mechanical model and the proposed thickness correction exponent by Gurney was found to be ap-

propriate. Contrary to the results provided by Berge, H. von Selle et al., [61], performed fatigue testing of 80 mm thick as-welded butt joints under axial loading conditions with a stress ratio of, R = 0.1. The experimental testing considered a comparison between as-welded joints and post treated specimens subjected to ultrasonic peening. The results relating to joints fatigue resistance indicated a somewhat conservative assessment from the recommendations. This conservatism towards the recommended thickness effect of large welded joints was confirmed by the results obtained by H. Polezhayeva et al, [62]. They performed bending and axial fatigue testing of 22 mm, 66 mm and 100 mm thick butt welded joints where the obtained results demonstrated that the mean fatigue resistance of the thicker joints were somewhat lower than for the 22 mm thick joints. However, in some cases the thicker joints performed better than the 22 mm joints. Additionally, the 100 mm thick joints demonstrated a better fatigue resistance than the 66 mm thick joints.

O. Doerk et al., [63], performed in 2012, a much required extensive experimental fatigue test series on large scale butt welded joints under axial loading. A total of 78 butt welded joints were tested, where the thicknesses were 25 mm, 50 mm and 75 mm. The results confirmed the influence of thickness as the calculated fatigue mean stress range was 130 MPa, 112 MPa and 103 MPa for the 25 mm, 50 mm and 75 mm thicknesses respectively. The corresponding characteristic fatigue resistance was calculated to be 88 MPa, 84 MPa and 75 MPa for the 25 mm, 50 mm and 75 mm thicknesses respectively. By considering the recommended thickness correction factor and a thickness correction exponent of, k = 0.2. The results from the mean stress range confirm that the recommendation is valid and a 79.2% reduction of fatigue strength is obtained when the 25 mm thick joints are compared to the 75 mm thick joints. The recommended thickness correction factor calculated for the same welded joints results in 80.3% reduction. However, when considering the characteristic fatigue resistance the obtained results show a 85.2% reduction for the same thicknesses. This difference between the recommendations and the obtained results becomes even larger when comparing the 25 mm and 50 mm thick welded joints.

Stress range, $\Delta\sigma$

The influence of the mean stress applied during fatigue testing has been subjected to a lot of research and experimental testing. Welded structures contain high tensile and compressive residual stresses as a consequence of the welding procedure where the tensile residual stresses are thought to be of yield strength magnitude within the welded region. Therefore the welded region is subjected to a different stress range during fatigue testing as these stresses are already present. An interesting approach was per-

formed by Ohta et al. [64]. They performed fatigue testing to determine the thickness effect between 9 mm and 40 mm thick butt welded joints as well as analysing the obtained deviation between the tests at different mean stresses. The tests were performed at the same stress ranges, $\Delta\sigma$ but were tested at different stress levels. The first set of tests were performed at $\sigma_{min} = 0$ and $\sigma_{max} = \Delta\sigma$ for both thicknesses. Thereafter, additional testing was performed where $\sigma_{min} = \sigma_{max} - \Delta\sigma$ and the maximum stress level was at the specimens respective yield strength, $\sigma_{max} = \sigma_y$. The test results showed a slight thickness effect when the specimens were tested at the lower maximum stress levels. The obtained results from the higher maximum stress levels, $\sigma_{max} = \sigma_y$, resulted in almost identical fatigue resistance between the two thicknesses.

Additionally, the residual stresses were measured with the strain gauge method. The 9 mm thick welded joints demonstrated compressive residual stresses, up to 200 MPa, away from the welded region, and low tensile residual stresses, close to 30 MPa, in the weld region. The 40 mm thick welded joints demonstrated high tensile residual stresses, above 300 MPa, away from the welded region, and compressive residual stresses, above 200 MPa, in the welded region. These results demonstrate the large differences when dealing with specimens of different geometrical dimensions and indicate that mechanical properties obtained from small scale specimens are perhaps not representative of larger structures by upscaling.

Structural stress, σ_{HS}

The structural stress, also known as the hot spot stress, enhances the nominal stress by incorporating the stress raising effects of the structural detail. According to recommendations from the IIW, [7] and E. Niemi, [37, 38], a surface strain measurement technique can be applied in order to extrapolate the stress at the hot spot. This method incorporates all the stress raising effects of the welded joint, but excludes the local stress concentrations due to the weld parameters.

Notch stress, σ_{peak}

The notch stress involves the non linear stress peak at the weld toe, i.e. at the notch. The notch stress takes into account the effects of the global as well as the local structural geometry. Additionally, it incorporates the parameters related to the weld profile, i.e. the weld length, weld size, flank angle, and the notch radius along with the corresponding stress concentrations. The application of the appropriate stress concentration

factors along with the estimated nominal or structural stress subjected to the joint, enables the determination of the notch stress, i.e. peak stress, at the weld toe. Iida and Uemura, [47], derived a outline from literature on stress concentration factor formulas that are frequently referred to in published literature. The described factors, concern theoretical, elastic stress concentration factors for both axial and bending loads at the weld. They are based on obtained experimental results. Additionally, Iida and Uemura illustrated the relation of stress concentration factor, K_t, as a function of weld notch radius over thickness, ρ/t, ratio for butt welded joints under axial loading conditions. Indicating that if the weld toe radius is assumed to be constant, the increase in thickness of the welded joint will raise the stress concentration factor considerably. Thus giving weight to the geometrical size effect. Additionally, increasing the weld notch radius will increase the fatigue resistance. Other weld parameters, such as length, width, height and flank angle, are also influential on the joint's fatigue resistance. In considering as-welded butt joints, then there are noticeable differences in the weld seam parameters along the joint. Thus, the stress concentration varies by location.

Glinka et al, [44, 45, 46], have performed and published literature where they applied classical stress concentration factors, separating axial and bending stresses, in order to determine the peak stress at the weld notch. The procedure involved decomposing the calculated structural hot spot stress into hot spot membrane and hot spot bending stresses respectively.

3.2 Test series 2: Corrosion fatigue resistance of large submerged arc welded joints in the as-welded condition in a circulating synthetic seawater environment with cathodic protection

IIW, [65], has published guidance concerning large scale testing as well as a suggestion of installing a corrosion fatigue testing facility. The article provides relevant details and considerations of influential parameters involved in establishing an operational corrosion environment. Additionally, the national association of corrosion engineers, NACE, provides standard practices for corrosion related terminology, steel immersion testing and laboratory testing of metals in H_2S environments [66, 67].

However, the published literature on the matter is limited, and especially for large welded joints. Most of the published literature involves corrosion fatigue testing of

ideal, machined, smooth small scale specimens fitted into a corrosion environment facility. M.Z. Shah-Khan et al., [68], performed corrosion fatigue testing on 6.5 mm thick, unnotched and notched specimens in a corrosion environment which was implemented into servo hydraulic testing machines. They indicated that the environment caused a considerable reduction in fatigue strength.

Y. Kumakura et al, [69], performed corrosion fatigue testing in synthetic seawater solution on uncoated and coated steel specimens to evaluate the effect of coated films. The specimens were 10 mm thick steel welded joints subjected to axial loading at R = 0.1 at a frequency of 0.17 Hz. The results demonstrated the effect of the corrosion environment as all tests performed in the corrosion environment showed less fatigue resistance than specimens tested under in-air conditions. Additionally, they found that the uncoated specimens subjected to free corrosion demonstrated fatigue resistance which was less than half of the fatigue resistance obtained for specimens tested under in-air conditions.

Y. Kobayashi et al, [70], performed similar tests on 10 mm thick butt welded joints tested in-air and in a corrosion environment to investigate the influence of the corrosion environment on crack initiation. The specimens were subjected to axial loading at stress ratio, R = 0.1, in natural corrosion conditions with a frequency of 0.17 Hz. The corrosion environment did not affect the crack initiation period and the low cycle, high stress curves are almost identical for both cases. However, the tests performed in the corrosion environment did not demonstrate a fatigue threshold level, i.e. a fatigue endurance limit. Thus, specimens within the corrosion environment initiated cracks at lower stress ranges than the tests performed under in-air conditions.

M.A. Wahab et al., [71], performed a more detailed corrosion fatigue investigation of butt welded specimens. The influence of weld geometry on crack propagation and the corresponding reduction in fatigue resistance was observed for 12 mm thick butt welded joints. The corrosion environment applied in this research was used as a foundation for the design of the corrosion environment applied in the current PhD project.

High cycle corrosion fatigue testing was performed by R. Pérez-Mora et al., [72], on smooth 3 mm thick high strength steel specimens under axial loading conditions. They examined three different types of testing conditions, i.e. 1) smooth specimens tested in-air, 2) smooth pre-corroded specimens tested in-air, and 3) smooth specimens tested in a corrosion environment. The results demonstrated a significant reduction in fatigue resistance between the smooth specimens in-air compared to the specimens tested within the corrosion environment. The reduction of the fatigue resistance was link with noticeable corrosion pits, which were identified from the corrosion testing.

Relating to larger thicknesses and the application of cathodic protection, then Sonsino et al, [54], investigated the corrosion fatigue resistance of welded steel joints with and without cathodic protection. A total of 25 tests were carried out under constant amplitude loading at a frequency of 10 Hz. The applied stress ratio was, R = -1. The results showed a large difference in fatigue resistance between the specimens, where the free corroding specimens demonstrated a fatigue strength reduction by a factor of two. Additionally, the specimens tested with cathodic protection demonstrated similar fatigue resistance as specimens tested under in-air conditions. Thus, the cathodic protection was able to counteract the detrimental effects of free corrosion.

3.3 Test series 3: Fatigue resistance of laser-hybrid welded joints and a comparison to submerged arc welded joints

Laser-hybrid welding, or Hybrid laser arc welding, HLAW, and its application has been under investigation for a number of years. Laser hybrid welding has been utilized extensively in industry, e.g. in automotive and shipbuilding, where it has become the state of the art joining technique. However, the HLAW technique has not been utilized in joining large sections of steel, mainly due to power limitations, beam quality and cost.

In the last two decades, or from the late 1990's major breakthroughs and advancements have been made in laser technology addressing the technique's limitations. M. Grupp et al., [73], demonstrated the future prospects of the HLAW welding technique after investigating the results from a 30 kW laser. S.E. Nielsen, [74], published in late 2015, an overview of the laser hybrid welding challenges ahead concerning a number of development projects. Nielsen emphasizes on the rapid developments in laser technology and proposes the opportunity of joining thick steel section with laser hybrid welding. Nielsen presents results with obtained penetration depths in the range of 15-20 mm for a single laser at 16 kW and penetration depths up to 25 mm at 32 kW. This invites the possibility of joining 50 mm thick steel joints, welded from both sides.

The 32 kW disc laser applied by Nielsen, is among the largest in the world. However, Osaka University in Japan installed a 100 kW fiber laser system. Katayama et al., [75], have demonstrated preliminary results, where a penetration depth of 55 mm has been obtained. Q. Pan et al., [76], published results from Osaka University's laser facility. They investigated the related welding parameters and defects encountered

during Laser-arc hybrid welding of thick high strength steel. The applied thicknesses were 11 mm and 12 mm.

The implementation of the HLAW technique in joining thick steel sections is currently on the research and development stage, where the build up of expertise, experience and knowledge is being established. Installing and tuning the HLAW technique in order to produce sound and high quality welds has proven to be a time consuming and cumbersome process. The formation of imperfections such as solidification cracks is frequently encountered as Højerslev, [77], and F. Vollertsen et al., [78], describe in their results.

H. Remes, [79], performed fatigue testing on three different types of welded joints, i.e.; 1) submerged arc welded, 2) laser arc welded, and 3) laser welded joints. The applied test specimens had thicknesses of 6 mm and 12 mm. The fatigue testing was performed at a stress ratio of, R = 0 and the load frequency varied from 5 Hz to 20 Hz. The results from the fatigue testing indicated a superior fatigue resistance of the laser hybrid welded joints compared to submerged arc welded joints. The increase in fatigue resistance is particularly connected to the beneficial effects of the weld geometry and weld bead.

This page is intentionally left blank.

Chapter 4

Test Series 1 - *Experimental investigation of the thickness effect for submerged arc welded joints*

Investigating the influence of thickness on fatigue resistance of welded joints may shed light on whether the current design recommendations from standards and codes might be overly conservative. As offshore structures themselves are becoming immense in size, all aspects of the process of constructing a wind turbine must be inspected. The thickness effect has been proven in the past both theoretically and experimentally, however there are reasons to believe that the recommended thickness correction factor is too conservative and a reduced factor might result in metric tonnes of material saved. Thus, making manufacturing, assembling, transporting and erecting a relatively easier task.

For the purpose of this project a joint literature study was performed, resulting in an IIW conference paper. Investigation of the thickness effect for butt welded joints [11], and its content is described in the following subsections.

The background and the motivation for pursuing an experimental investigation of the thickness effect is mentioned in Section 4.1.1, where a literature study of available fatigue data from various experimentations was performed. The study combined a

collection of specimens ranging in thicknesses from very small up to very large. There is a great lack of experimental data for very thick joints, especially for large butt welded joints, as the process of testing them is very demanding both technically and financially. However, by manufacturing smaller joints the possibility of overly optimistic results is possible as the joints are usually made perfectly and fitted into the test environment, which does not simulate the true nature of the real structures. This looses its practical value in real life situations, as the test is not representative or replicated outside of a controlled lab environment.

4.1 Motivation for the investigation

The main objective of this PhD project, which is as previously mentioned a part of a larger joint industry research project, was to lower the total cost of energy relating to monopile foundations for offshore wind turbines. For this reason, time was assigned in defining and detecting probable and practical cases where the main objective was feasible.

Focus was directed towards a known and proven aspect which arises when dealing with very thick structures, namely the thickness effect. In short, it states that as structures become larger their fatigue strength is reduced. Since we are investigating the idea of manufacturing, assembling and erecting very large wind turbines offshore, this focus area becomes very relevant. The body of guidelines, codes and recommendations has become of age and simultaneously manufacturing processes, material and mechanical properties and design solution have improved. These reasons make the thickness effect a very promising field to investigate.

4.1.1 Investigation of the thickness effect for butt welded joints

An investigation of the thickness effect, or size effect, of axially loaded butt welded joints of various thicknesses was performed. All available and relevant experimental fatigue data from literature was assembled into a large database and subjected to statistical analysis. A total of 1258 experimental data points were collected from over a hundred test series [62, 80, 81, 82, 83, 84, 85, 86, 87, 88, 89, 90, 91, 92, 93]. The main body of the fatigue test results comes from small scale test specimens. The fatigue tests were all performed at room temperature on fully penetrated butt welded joints in the as-welded condition subjected to tensile loading at a positive stress ratio, $R \geq 0$. The steel material grades ranged from structural S235 up till high strength 960 MPa

steel and the thickness ranged from 8 to 100 mm. The dominant failure reported was fracture at the weld toe.

The thickness effect considers the influence of the plate thickness on the fatigue strength of welded joints. This thickness correction is as stated earlier only relevant for joints of larger sizes. Thus, smaller joints usually around 20 - 25 mm thick are not subjected to thickness correction while larger joints should have a corrected thickness computed according to recommendations. This thickness effect correction is applied in design rules by the multiplying the welded joint's fatigue strength or class with the following factor:

$$f(t) = \begin{cases} 1 & \text{for } t \leq 25\ mm; \\ \left(\frac{t_{ref}}{t}\right)^k & \text{for } t > 25\ mm; \end{cases} \tag{4.1}$$

The reference thickness, t_{ref}, should be 25 mm [7, 30, 36] and the suggested exponent, k, varies between design rules and has values ranging from 0.1 up to 0.3. The exponent, k, is also dependent on the considered weld detail category. In the case of transverse butt welds in the as welded condition, a value of k = 0.2 is recommended [7, 36].

This thickness correction, recommended by the IIW, DNV GL and other standards, codes and guidelines, has been indicated to be conservative when it comes to large butt welded joints, such as for offshore wind turbine foundations.

As mentioned previously in Chapter 2.2.1, The thickness effect is believed to be comprised of several effects, mainly;

- **Statistical size effect:** As the volume of the joint has increased, the probability of severe defect, such as voids, pores or cracks, occurring is higher.
- **Technological size effect:** The manufacturing procedure and conditions applied for thick plate structures is more cumbersome, the structures are subjected to harsher treatment resulting in e.g. different residual stress distribution, surface roughness and micro structure compared to thinner joints.
- **Geometrical size effect:** The stress concentrations and superimposed bending and the resulting stress gradient becomes more gradual for thicker joints compared to thinner joints. Therefore, the combined stress field in the vicinity of a crack will become more intense for thicker joints compared to thinner joints.

All these effects as well as others will lead to the reduction of welded structures fatigue resistance as the structures become larger. However, the last thickness effect mentioned, the geometrical size effect, has been suggested to be the most significant [11].

In general, the theoretical arguments for the thickness effect are well established and the effect is also proven experimentally for plain steel and many types of welded joints, primarily fillet welded joints. Nonetheless, data for butt joints is lacking and severely for thicker joints [64].

The aforementioned effects are put into perspective with the focus on butt welded joints. The statistical size effect is reported to be the least significant, [6], and most difficult to control as it relates to the continuous melting and cooling of the weld and the neighbouring base material. This process of melting and solidifying will result in internal residual tensile and compressive stresses, as well as additional weld defects. Ultimately, with increased thickness the weld has more volume, more defects, more weld passes and more cyclic thermal processes, which will lead to a higher probability of defects. However, as the welding procedure has been "perfected" i.e. the fit-up, consumables, temperature, feeding speed etc., the weld can be performed on a repetitive basis, meaning that the resulting weld is "as good as possible" in terms of quality, given that all other conditions were perfect, such as humidity, applied material, weld operator etc. There is not a practical method to control the occurrence, size and/or density of the defects within the weld nor in the heat affected zone, the weld procedure can only be performed according to the best possible procedure, with known results, where the probability of an accepted certified weld after inspection being relatively high.

Regarding the technological size effect, thicker joints are typically welded today with the SAW technique. Earlier reports indicated that SAW resulted in inferior fatigue resistance [6]. However, modern SAW can produce high quality welds with very high fatigue performance, and it is found to be equal, if not superior, to other welding processes. The level of axial misalignment also tends to decrease as the welded joint increases [61]. Using SAW should therefore lower the effect of the technical size effect.

Lastly, the geometric size effect, which is dominated by stress concentration at the weld toe and the level of superimposed bending stresses. Relating to butt welded joints, the stress concentrations are small when comparing to e.g. fillet and more complex welded joints. Additionally, the level of misalignment is reported to decline with the increase of thickness. Thus, the geometric size effect in butt welded joints is not that decisive.

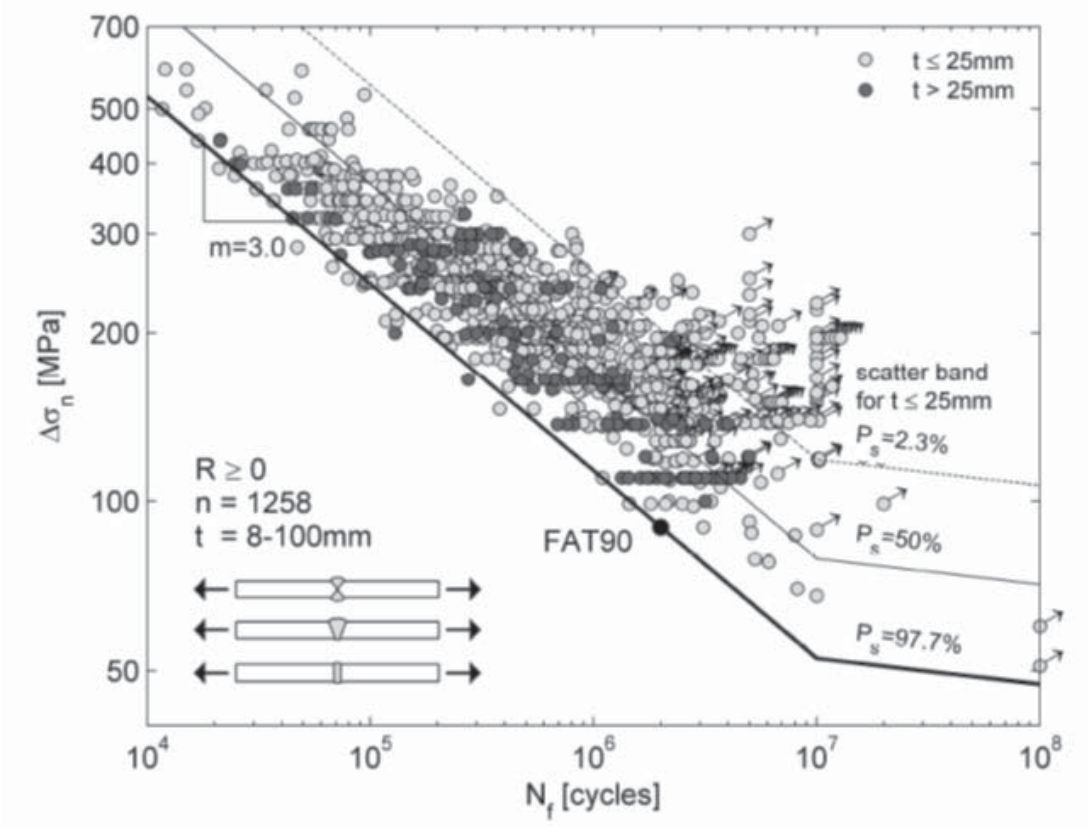

Figure 4.1: *Fatigue data for butt welded joints of all thicknesses [11]*

In summary, the thickness effect dependency for butt welded joints is not expected to be as significant as for other weld details.

Figure 4.1 above illustrates the collected fatigue test database, plotted along with the FAT 90 (IIW) S-N curve which corresponds to design S-N curve D (DNV GL). The plot includes scatter bands for the mean $\pm$ standard deviation ($P_S = 2.8 - 97.7\%$) calculated using a fixed slope coefficient of m = 3.0 and only using the results from specimens less than or equal to 25 mm thickness, i.e. those which are not subjected to thickness correction and excluding the excessive scatter contribution of the run-out tests. The FAT 90 curve coincides almost completely with the lower bound of the fatigue data points, indicating a good agreement and that a slope of $m = 3.0$ is appropriate. Additionally, the plot indicates little difference between thinner (light dots) and thicker joints (dark dots) and they appear to blend acceptably [11].

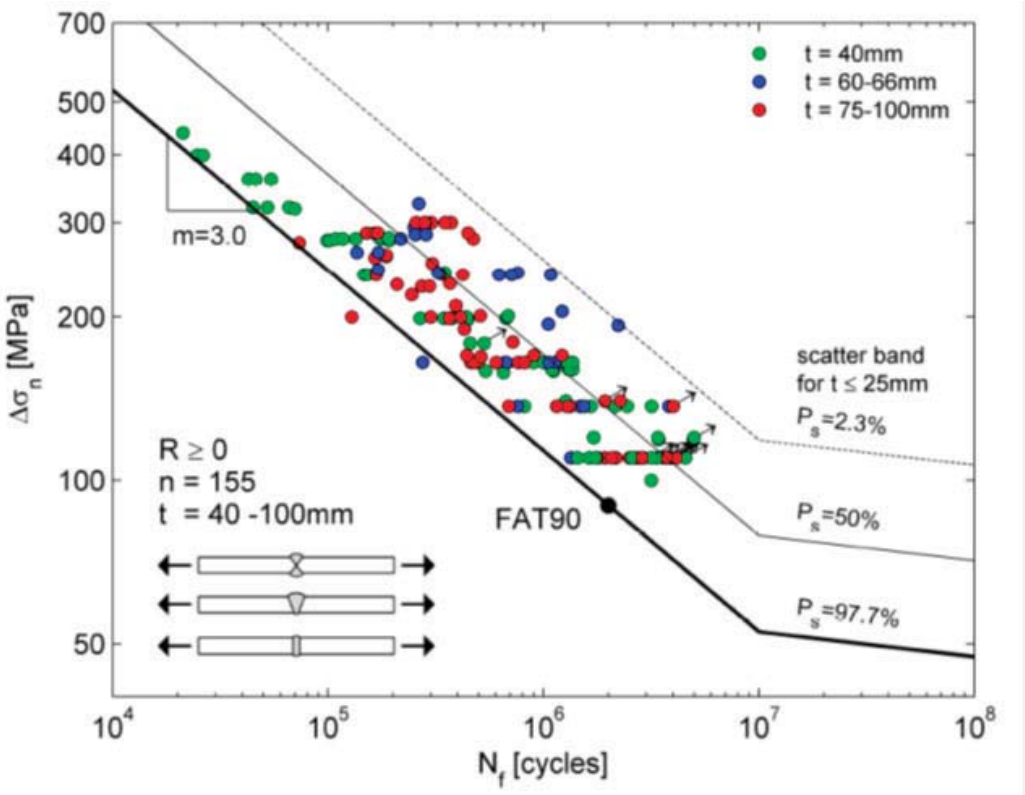

Figure 4.2: *Fatigue data for 40 to 100 mm thick butt joints [11]*

Figure 4.2 illustrates a calculated mean value and scatter bands, after removing the run-outs, as well as the population of test results above the upper scatter band in order to homogenize the population according to [7] to reduce scatter. In addition, the curves, which are calculated from the test results, are not subjected to thickness correction, i.e. 25 mm and lower thicknesses. The resulting curves are more demanding than before, due to decrease in scatter. Thereafter, all specimens with thickness below 40 mm are removed as the focus is on the thicker welded joints, i.e. range of 40 mm to 100 mm thick or those which are subjected to thickness correction. They are grouped into three categories and colour coded, green, blue and red for each thickness range respectively.

Figure 4.2 further illustrates that only two test results from the thicker welded joints lie underneath the lower scatter band for the 25 mm thick joints and the FAT 90 / DNV D curve. Additionally, it is clear that there is a tendency of these thicker joints to lie in the lower half of the scatter band. Moreover, there does not appear to be any

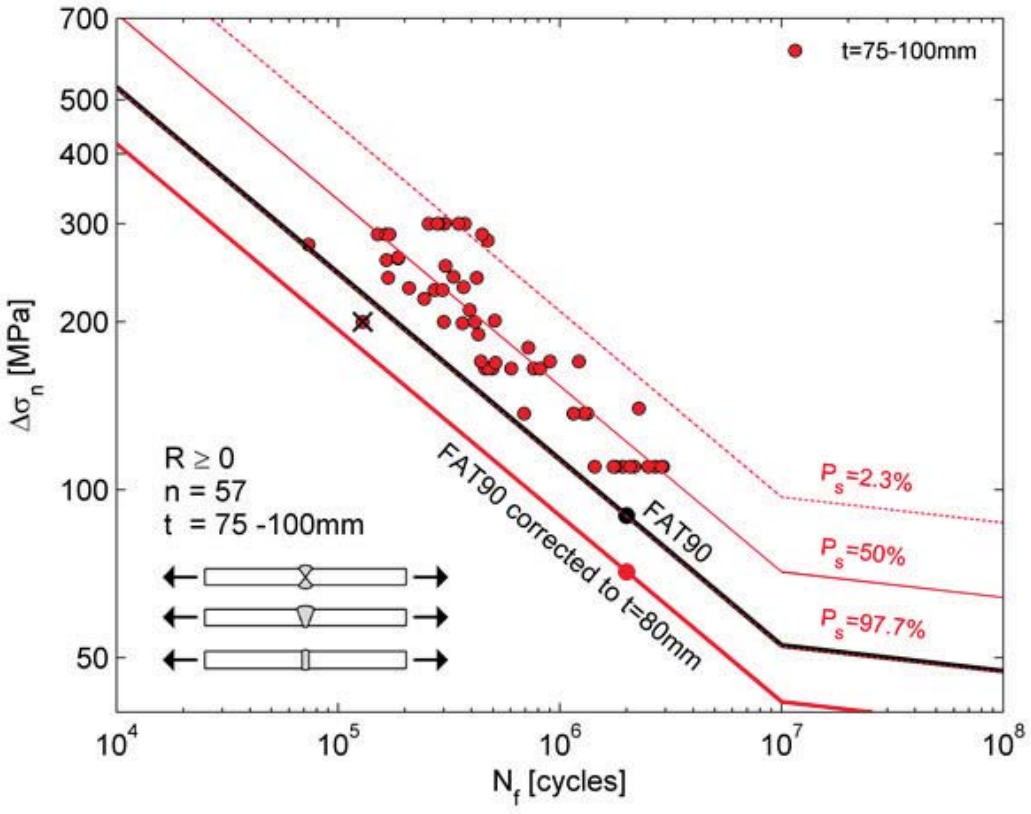

Figure 4.3: *Fatigue data for very thick 75+ mm welded joints with corrected design curve [11]*

obvious difference in the fatigue resistance of these larger welded joints. They appear to perform in a relatively equivalent manner, with many occasions where the 75 - 100 mm thicknesses are outperforming the 40 mm thick joints, and vice versa. Another interesting feature illustrated in the figure is that only a single test specimen in the range of 75 - 100 mm lies below the FAT 90 / DNV D curve, and appears to be an outlier.

Figure 4.3 illustrates the same data for 75 - 100 mm thick welded butt joints along with the corrected FAT 90 / DNV D curve for 80 mm thick joints. Taking into account the effects of the thickness correction; a butt welded joint of e.g. 80 mm thickness is subjected to a reduction from FAT 90 to approximately FAT 71, which is conservative, based on the collected fatigue results presented here.

The results from this investigation demonstrates that most of the collected fatigue data was in good agreement with the recommended FAT 90 / DNV D design curve. Furthermore, the data reveals a thickness dependency from thinner to thicker welded butt joints, however it is less significant than the recommendations from the standards and codes suggest. It was therefore obvious that, the severity of the thickness effect concerning butt welded joints, especially for large welded joints, and the validity of the corresponding recommended thickness correction factor was called into question and a great incentive to continue with the research and pursue in-house experimental study on the matter.

4.2 Experimental test preparation

After performing the aforementioned literature study concerning the effects of thickness on SAW butt joints a straightforward incentive was established to pursue the matter and commence further investigation.

The comprehensive process of ordering material, manufacturing, transporting, inspecting, measuring, cutting, preparing, testing and post processing of the desired test specimens is time consuming and even more so when dealing with larger structures. Thus, after a collaboration was agreed upon introducing Force Technology, a non-profit approved technological service institute, as a project partner, their shareholder company Lindø Welding Technology, LWT, was assigned the manufacturing of the required butt welded plates in the as-welded condition, hereafter termed batch 1.

In order to give more weight the experimental test results, additional three SAW plates of each thickness, batch 2, were ordered. However, the SAW process was no longer available at LWT therefore the manufacturing was performed by another leading welding manufacturer within Denmark. All relevant documentation from LWT's procedure was shared with the manufacturer of the new batch. Thus, a great emphasis was place upon producing equivalent test plates with the same raw material, steel and consumables, applied in the previous welding process.

The selected thicknesses, which were primarily chosen relating to the lab's testing machine capacity, were 20 mm, 30 mm and 40 mm thick SAW butt joints.

4.2.1 Quality control

Descriptions of the influencing factors, sources of error, applied material and testing environment are often limited in available literature. Below the factors known and uncovered while performing this test series are listed, as means to improve the documentation.

In order to achieve satisfying quality and the best attainable results, all factors involved in the process, starting from the initial material selection have to be known and under control. The relevant factors are many, some straightforward, whilst others less obvious with a considerable varying impact on the outcoming results. It goes without saying but the ability to identify more influencing factors and describe the sources of error from the beginning to the end will strongly improve results, the data and ultimately the final structure.

Therefore, while defining the scope of this project, some emphasis was made on the following:

- Steel material consistency and preferably the exact same material as is used in the offshore industry.
- Perfect welding conditions, i.e. temperature, humidity and the same welding operator in order to maintain some consistency in the welds and make them comparable.
- Same welding procedure applied for all welds, with high emphasis on misalignment.
- Same cutting procedure. Waterjet cutting which is extremely accurate and results in low heat distortion.
- Storing and protecting cut samples, keeping them away from environmental effects.
- Detailed description of the welding process.
- Detailed description of the material composition and mechanical properties.
- Misalignment measurements of the finished welded structure.
- Calibrated and verified testing equipment.

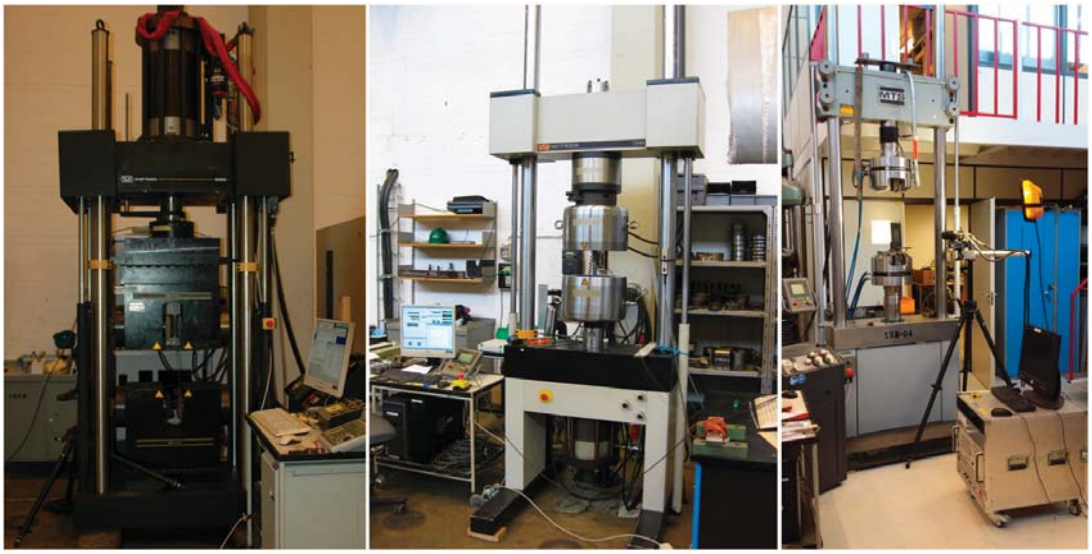

Figure 4.4: *Test series 1 applied testing machines. (left) 1 MN Instron, (center) 500 kN Instron and (right) 500 kN MTS*

4.2.2 Lab capacity

At the start of this experimentally demanding project, the lab capacity available at DTU was significantly limited in dealing with such large test specimens. This was especially highlighted with regards to fatigue testing. The lab was well equipped in servo hydraulic machine testing capacity up to 250 kN, however there were only two options available for loads up to 500 kN and one up to 5000 kN. The 5000 kN machine did not incorporate grips, which would then have to be designed. Additionally, the 5000 kN machine cannot run at high frequencies which would make the required high cycle fatigue tests run for weeks. To put things into perspective, the test specimens with the lowest thickness, 20 mm, required a minimum fatigue load of 250 kN.

However, due to rapid lab improvements and expansions, the capacity was increased significantly and by the end of the project the lab was equipped with three machines of 500 kN capacity (one without hydraulic grips) along with a fatigue rated testing machine up to 1000 kN. Thus, enabling all the desired fatigue tests to be performed, illustrated in 4.4.

Data measurement equipment

The measurement equipment applied in order to acquire the relevant data and pursue the investigation is listed here:

- Vishay general purpose strain gauges, 120 Ω. See Appendix C.
- HBM Spider8, data measurement and acquisition device.
- HBM MGCPlus, data measurement and acquisition device.
- MTS, certified and displacement validated extensometers.
- 4M and 12M Aramis digital image correlation systems.
- SHM controllers acquire the basic load and displacement signals.

All machine load cells and LVDT's were calibrated before commencing with the experimental testing in order to make sure that the machine was performing according to the highest attainable accuracy, see Appendix B.

Additionally, the bending moments were calculated according to the ASTM standard, E 1012 [94]. The computed bending stresses were found acceptable, indicating that the load train alignment procedure when assembling the servo hydraulic testing machine, was done decently.

4.2.3 Material composition

The applied steel for experimental batch 1 was S355 J2 + N, and was selected after following discussions with the collaborating partners relating to the steel applied in offshore structures. It is one of the most common higher strength structural steels for constructions with excellent chemical and physical properties.

The steel for the 20 and 40 mm thick test material was produced in Russia by Ural Steel, and was made according to specifications from DNV rules and EN10029-2010 and normalized. The inspection certification is according to EN 10204:2004/3.1. The tensile testing was performed according to EN 10002/ISO 6892-1. The 30 mm thick steel test material was produced by Arcelor Mittal Galati S.A., Romania. The steel was produced according to EN 10025-2-2004, inspected according to EN 10204-2004-31

and certified by Lloyd's Register. Table 4.1 shows the chemical composition of the steel, while Table 4.2 lists the in-house tested mechanical properties.

Table 4.1: *LWT - Batch 1. Material composition*

Test Series 1 - Thickness effect of SAW butt joints.																
Element	C	Si	Mn	P	S	Al	Cu	Cr	Ni	Mo	V	Nb	Ti	N2	As	C_{eq}
40 mm thick - wt. [%]	0.18	0.35	1.50	0.009	0.006	0.033	0.016	0.015	0.007	0.001	0.002	0.042	0.003	0.0058	-	0.43
30 mm thick - wt. [%]	0.18	0.27	1.30	0.014	0.007	0.036	0.014	0.02	0.017	0.002	0.02	0.035	0.02	0.0062	0,003	0.41
20 mm thick - wt. [%]	0.15	0.43	1.40	0.009	0.005	0.029	0.07	0.06	0.04	0.007	0.003	0.034	0.012	0.009	0.0038	-

Table 4.2: *LWT - Batch 1. Mechanical properties*

Test Series 1 - Thickness effect of SAW butt joints.								
Cast No	Test No	Plate No	Thickness [mm]	Width [mm]	Length [mm]	Yield strength [Mpa]	Tensile strength [MPa]	Elongation [%]
44123B1	-	3315F-1-1	40	3000	10000	381	536	25
Y921121	8488	253240	30	3000	12000	406	558	25
V25848	6860	12	20	2500	8000	370	510	32

Table 4.3: *External manufacturer - Batch 2. Material composition*

Test Series 1 - Thickness effect of SAW butt joints.															
Element	C	Si	Mn	P	S	Al	Cu	Cr	Ni	Mo	V	Nb	Ti	N	C_{eq}
40 mm thick - wt. [%]	0.15	0.52	1.44	0.019	0.003	0.033	0.04	0.04	0.04	0.01	0.00	0.025	0.005	0.0045	0.41
30 mm thick - wt. [%]	0.16	0.49	1.44	0.014	0.002	0.041	0.02	0.04	0.03	0.01	0.00	0.026	0.005	0.0035	0.41
20 mm thick - wt. [%]	0.18	0.31	1.47	0.016	0.003	0.022	0.001	0.05	.01	0.002	0.007	0.022	0.012	0.0023	0.44

Table 4.4: *External manufacturer - Batch 2. Mechanical properties*

Test Series 1 - Thickness effect of SAW butt joints.								
Cast No	Test No	Plate No	Thickness [mm]	Width [mm]	Length [mm]	Yield strength [Mpa]	Tensile strength [MPa]	Elongation [%]
640639	-	715844/1/3	40	2000	12000	371	534	33,5
642799	-	720657/1/7	30	2000	12000	402	545	30,5
011361	-	1258-01248	20	4000	16000	435	575	28,5

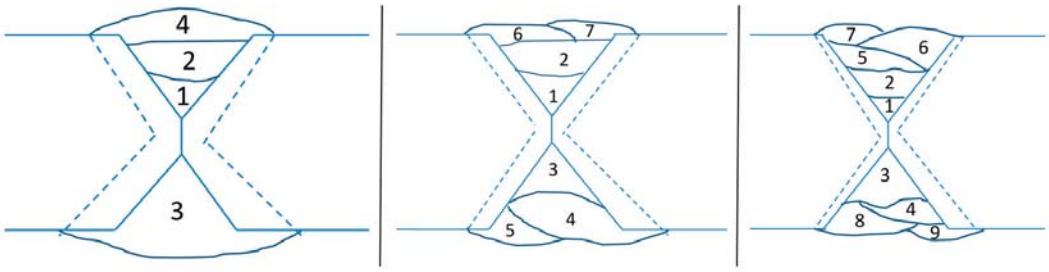

Figure 4.5: *LWT batch 1, the number of passes required to SAW the test thicknesses, 20 mm, 30 mm, and 40 mm thick respectively*

LWT performed the SAW in a tandem electrode/wire configuration, where the leading wire was single and 4 mm thick and the trailing wire was a twin arc of 2 x 2 mm. The same configuration was applied for all welded joints.

The 20 mm thick plate was turned after 2 passes and then again after pass 3 to mitigate thermally induced distortion. The 30 mm plate was turned after 2 passes and then again after pass 3 and pass 5 in order to mitigate the thermally induced distortion. The same weld operator performed the welding procedure for all welded plates.

Relating to batch 2, the steel for the 20 mm thick test material was produced by Jinan Iron and Steel Company LTD., China. The steel was certified by Lloyd Register Industrial and was produced according to EN10025-2.2004 standard. The 30 and 40 mm thick steel test material for Batch 2 was produced by Salzgitter Mannesmann Stahlhandel, Germany. The inspection certificate is according to EN 10204-3.1 while the steel grade is manufactured according to EN 10025-2, AD 2000 W1, EN 10029 and EN 10163-2 in an basic oxygen furnace and normalized. The tensile testing was performed according to ISO 6892.

Table 4.3 shows the chemical composition of the steel from Jinan Iron and Steel Company as well as the Steel from Salzgitter, while Table 4.4 lists the in-house tested mechanical properties.

Both batches of the steel material applied in the project, were normalized, certified and subjected to quality inspection.

N.B. The 20 mm thick test material was produced in double quantity as it was applied for analysis in both the thickness effect validation, test series 1, as well as the investigation of fatigue testing within a corrosion environment, test series 2, described in detail in Chapter 5.

No details of plate shifting was given in the weld procedure log for batch 2. The same welding operator performed all the welding.

Batch 2 did require weld repair on the 30 mm and 40 mm thicknesses as the welded plates did not pass non-destructive testing. After reparation the plates were again subjected to non-destructive testing and this time around both thicknesses passed and were accepted to specifications.

4.2.4 Welding procedure

The welding method applied was semi-automatic submerged arc welding (SAW), as it is accountable for most welds relating to offshore wind turbine foundations. This technique is a very reliable technique with high deposition rate, reduced production time and is either fully or semi-automatic. Instructions were given to the operators, that the welding process should focus with great emphasis on restraining the axial and angular misalignment. Additionally, the operator should make sure that there is no

Table 4.5: *LWT - Batch 1. Welding Procedure*

Test Series 1 - Thickness effect of SAW butt joints.			
-	**20 mm thick**	**30 mm thick**	**40 mm thick**
Process	SAW	SAW	SAW
Weld length	1500 mm	1500 mm	1500 mm
Consumable	ESAB OK 12.22	ESAB OK 12.22	ESAB OK 12.22
Flux	ESAB OK 10.72	ESAB OK 10.72	ESAB OK 10.72
Position	PA Flat	PA Flat	PA Flat
Geometry	X-groove	X-groove	X-groove
Nose	3 mm	3 mm	3 mm
Edges	2 x 37.5°	2 x 37.5°	2 x 37.5°
Polarization	DC+ / AC	DC+ / AC	DC+ / AC
Current	350 - 750 A	400 - 800 A	400 - 825 A
Speed	26 - 53 cm/min	39 - 60 cm/min	35 - 65 cm/min
Arc voltage	24 - 38 V	23 - 38 V	24 - 38 V
Heat input	-	-	-
Preheating	-	-	-
Interpass temperature	20 - 50°C	20 - 110°C	20 - 115°C
Weld passes	4 (3 and 1)	7 (4 and 3)	9 (5 and 4)
Repair	No	No	No
Repair passes	-	-	-

Table 4.6: *External manufacturer - Batch 2. Welding Procedure*

Test Series 1 and 2 - Thickness effect of SAW butt joints.				
-	**20 mm thick (air)**	**20 mm thick (seawater)**	**30 mm thick**	**40 mm thick**
Process	SAW	SAW	SAW	SAW
Weld length	1800 mm	1800	1800 mm	1800 mm
Consumable	ESAB OK 12.22	ESAB OK 12.22	ESAB OK 12.22	ESAB OK 12.22
Flux	ESAB OK 10.72	ESAB OK 10.72	ESAB OK 10.72	ESAB OK 10.72
Position	PA Flat	PA Flat	PA Flat	PA Flat
Geometry	X-groove	X-groove	X-groove	X-groove
Nose	-	-	-	-
Edges	-	-	-	-
Polarization	DC+ / AC	DC+ / AC	DC+ / AC	DC+ / AC
Current	350 - 750 A	350 - 750 A	400 - 800 A	400 - 825 A
Speed	26 - 53 cm/min	26 - 53 cm/min	39 - 60 cm/min	35 - 65 cm/min
Arc voltage	24 - 38 V	24 - 38 V	23 - 38 V	24 - 38 V
Heat input	1,1 - 2,8 KJ/min	1,1 - 2,8 KJ/min	1,5 - 2,9 kJ/min	1,4 - 3,0 KJ/min
Preheating	-	-	-	-
Interpass temperature	20 - 50°C	20 - 110°C	20 - 115°C	20 - 115°C
Weld passes	4	4	8 (5 and 3)	10 (5 and 5)
Repair	No	No	Yes (2)	Yes (1)
Repair passes	-	-	12 and 12	17

stopping and restarting during the welding process.

The butt welded joints were manufactured according to the details in Table 4.5 and Table 4.6. The electrode was used in tandem configuration with a single leading wire, 4 mm diameter, and the trailing wire a twin arc, 2 x 2 mm diameters. Weld joint geometry was an X-groove, nose of 3 mm and edges of 2 x 37.5 deg. ESAB 12.22 was used as the filler material with consideration taken to the base material. Lastly, the flux applied was ESAB OK 10.72. All welds were double sided, without any backing.

The SAW butt joints manufactured by LWT had 4 (3 and 1), 7 (4 and 3) and 9 (5 and 4) passes for the 20 mm, 30 mm and 40 mm thick welds respectively. The SAW butt joints manufactured by the external manufacturer had 4 (no info), 8 (5 and 3) and 10 (5 and 5) passes for the 20 mm, 30 mm and 40 mm thick welds respectively.

The welding repair performed by the external manufacturer on the 30 mm thick welded plate had 12 passes made, 40 mm from the end of the plate and 70 mm long for repair 1 in addition to additional 12 passes, 710 mm from the end and 120 mm long for repair 2. A repair was also performed on the 40 mm thick joints, 17 passes from the end of the plate and 520 mm long were implemented.

4.2.5 Non destructive testing

All SAW butt joints were subjected to non destructive testing in order to verify that the weld quality demands are accepted to specifications. Table 4.7, lists all performed NDT's for batch 1 and batch 2 respectively.

Batch 1 was inspected by Force Technology, the division for inspection and testing. The 20 mm thick welded plate was tested according to ISO 17640-B with quality requirements according to EN ISO 11666-2 as recommended by standards [30, 95]. The plates passed visual inspection, however the ultrasonic testing (UT) identified an indication or defect 40 mm from the end at 10-13 mm depth. Thereafter, the plate was subjected to magnetic particle testing (MT) in-house with test standards according to DS/EN ISO 17638:2009 and acceptance levels according to DS/EN ISO 23278:2009. The MT results complied with acceptance levels. Therefore, as the majority of the plate was of accepted quality and passed inspection according to the NDT, the plate was accepted and the welded region which was defected was scrapped after cutting.

The 30 mm thick SAW butt plate passed visual examination without any remarks. The UT and MT inspection was successful and accepted (100 %) to specifications, applying the same standards as for the 20 mm thick plate.

For batch 2, the NDT of the 20 mm, 30 mm and 40 mm thick welded plates was performed by Nordisk Svejse Kontrol A/S (NSK). Both 20 mm thick joints passed visual examination, MT and UT with all quality criteria fulfilled according to the same test and quality requirement standards as mentioned above.

Table 4.7: *Non destructive testing of all welded joints*

Test Series 1 - Thickness effect of SAW butt joints.				
	Thickness [mm]	Visual inspection	Ultrasonic testing / after repair	Magnetic particle testing
Batch 1	20	✓	Defect 40 mm from edge, depth 10-13 mm / ✓	✓
	30	✓	✓	✓
	40	✓	✓	✓
Batch 2	20	✓	✓	✓
	30	✓	Defected, 40-110 mm & 710-830 mm / ✓	✓
	40	✓	Defected, 0-520 mm / ✓	✓

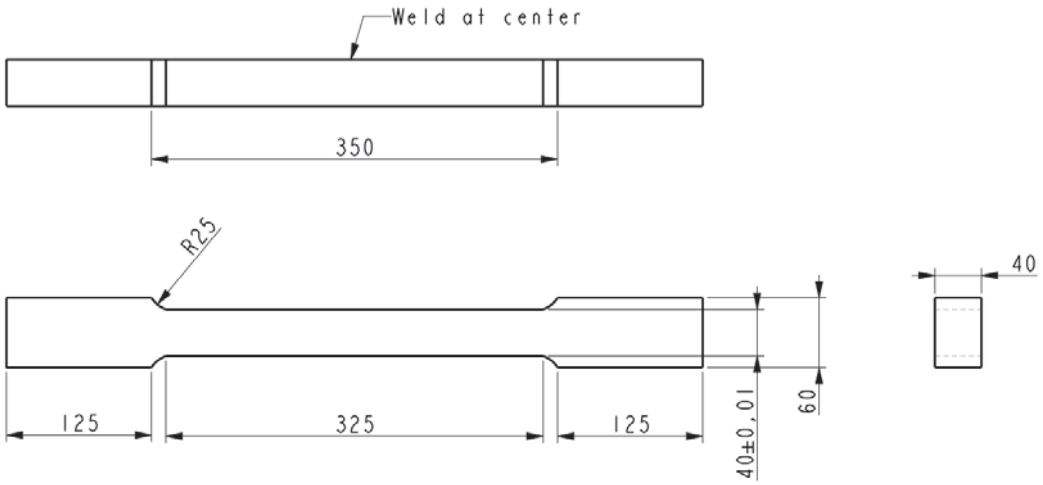

Figure 4.6: *SAW butt joint dimensions*

The 30 mm and 40 mm thick welded joints both passed visual examination and were accepted to specification with remarks that it was as-welded and the surface condition labelled smooth. The applied equipment was a weld gauge, torch and a sliding gauge and the examination was performed on finished welds more than 24 hours after the welding. During UT both the 30 mm and 40 mm thick failed to comply with specifications. The 30 mm thick plate had two regions where repair was required. 70 mm long 40 mm from the starting end and 120 mm long 710 mm from the starting end. The 40 mm thick welded plate required 1 repair as well, a 520 mm long from the starting end. After the reparation, both joints were accepted to all specifications and the visual examination was repeated and accepted without any remarks. Thereafter both joints were subjected to MT and were accepted to specifications. All documentation from the NDT is available in Appendix D.

4.2.6 Cutting procedure

The cutting procedure was performed at DTU, workshop building 427, with a water-jet cutting machine. This cutting technique gives good, smooth and accurate cuts with no heat distortion which can have a significant effect on the specimens, according to ESAB. Figure 4.6, shows the specimen drawing implemented in the water-jet cutting machine software.

Following the cutting procedure, the specimens were cleaned and coated with the avail-

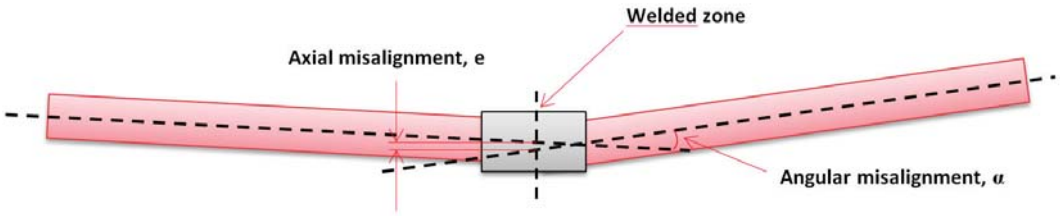

Figure 4.7: *Schematic illustration of the combined angular and axial misalignment*

able oil, grease, varnish or other media to prevent corrosion of the steel material. Additionally, each and every sample was labelled in order to keep track of its location within the original welded plate. Furthermore, special requirements were made concerning their storing, ensuring their safety from environmental effects. Lastly, each specimen was covered and arranged in a way to keep them from getting scratched, chipped and/or indented, as this could be detrimental to their fatigue capabilities.

4.2.7 Misalignment measurements

In order to manufacture a sound and good quality butt welded plate, the fit-up and alignment has to be given special attention as the plate is restrained against bending. The limitation or offset should not exceed 0.1t, while girth weld radial offset is accepted up to 0.2t, where t is the thickness of the plate. Furthermore, the maximum accepted misalignment criteria is 3 mm according to AWS while DNV accepts a maximum of 4 mm. However, the acceptance criteria rises to 6 mm for girth welds [30, 95]. Misalignment measurements of finished structures or parts, should be based upon the centerline. IIW however, has a more strict tolerances towards eccentricity and states that butt welded structure should be below 5% of the plate's thickness [7]. Lastly, according to DS/EN ISO 5817, [96], the quality levels for imperfections states that angular misalignment for welded joints larger than 0,5 mm should not exceed 2°, $\alpha \leq 2°$, for passing inspection, however for higher grades and increased quality the angle, α, should be equal to or below 1°. It is stated in the standard that these values are identical to IIW recommendations. DS/EN ISO 5817, also states that welded joints above 3 mm thicknesses should be $\leq 0.25t$ in relation to angular misalignment for passing but $\leq 0.1t$ for the highest grade. There are however maximum limits of 5 mm and 3 mm for passing inspection with the lowest and highest grade respectively.

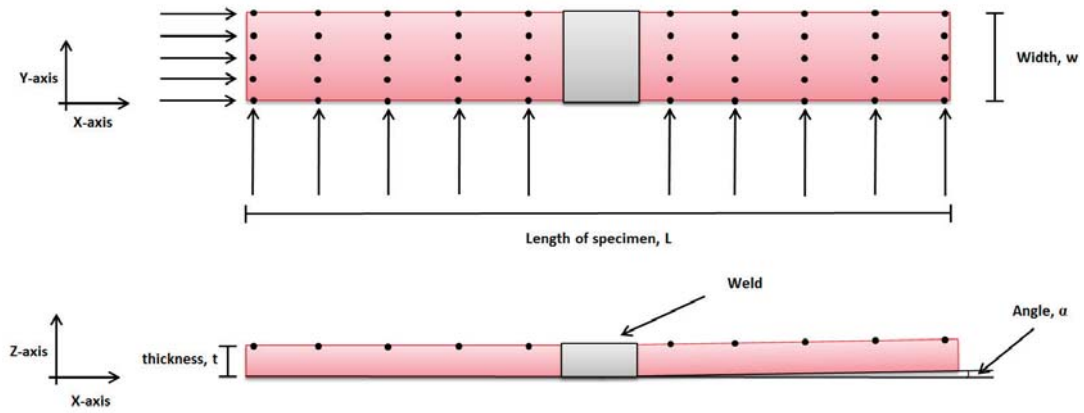

Figure 4.8: *Location of coordinate measurement points and relevant parameters*

The effect of misalignment are considered and implemented in the recommended design S-N curves from DNV and IIW for butt welded joints. However, special considerations needs to be taken into account if the misalignment exceeds the recommended tolerances and appropriate factors applied for analysis.

Batch 1: LWT

A high precision point coordinate machine, Zeiss Calypso, was used to measure the misalignments in the ready made and cut welded specimens. The specimens were positioned within the scope of the machine and from the assigned reference points at the specimens end, five points were subsequently measured at an equal distance along the specimen at fixed intervals of 60 mm, giving exact xyz coordinates in space. The results from the misalignment measurements on SAW butt joints are illustrated in figures 4.9, 4.10, 4.11 and 4.12. The colorbar on the right side, ranges from 0 mm up to the maximum acceptable misalignment recommended by standards, i.e. 10% of the welded joints thickness. The figures demonstrate measurements from each specimen, and the specimens are aligned next to each other to get an overview of the original welded plate. The welded region is located in the center.

N.B. that the measured data solely involves surface planes of joints that are 20 mm, 30 mm and 40 mm thick.

From all the figures it is evident that misalignment is hard to avoid, even with an extra emphasis on the matter and with added precautions. The measurements demonstrate

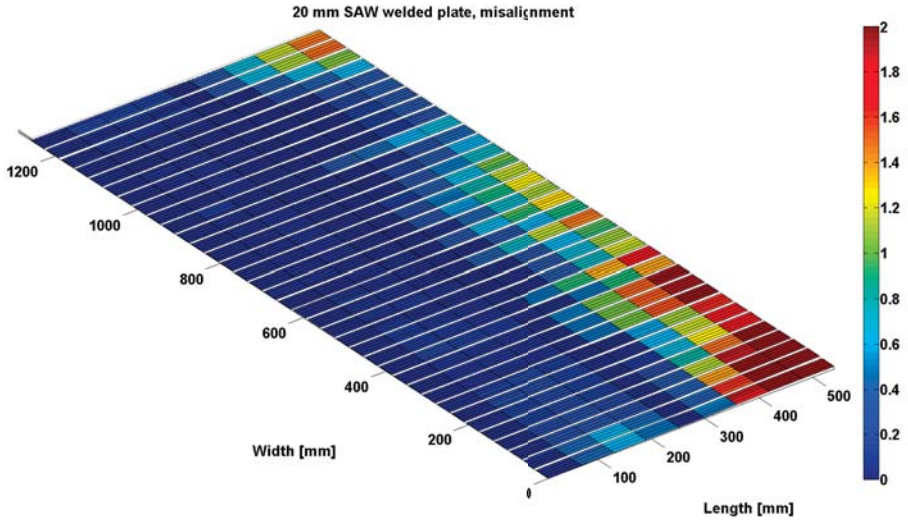

Figure 4.9: *Misalignment measurements of the 20 mm thick SAW butt joints. The figure shows individually measured surfaces for each specimen*

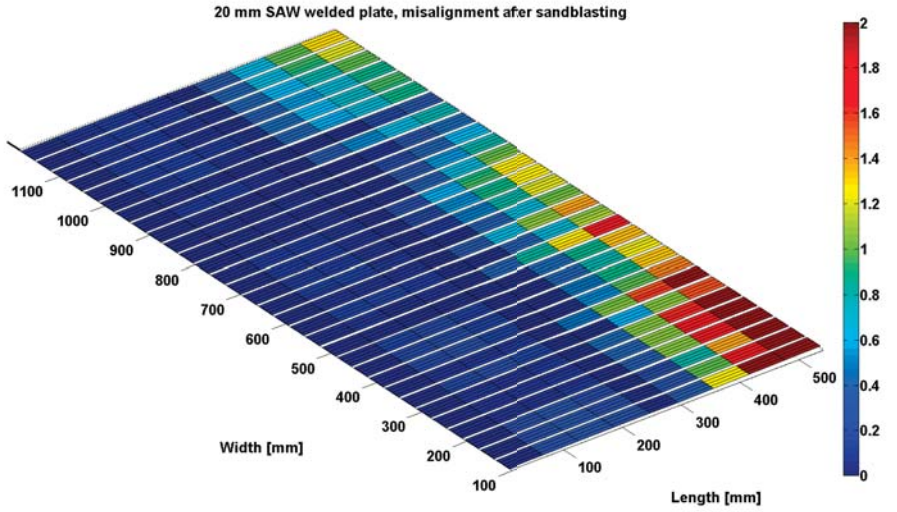

Figure 4.10: *Misalignment measurements of the 20 mm thick SAW butt joints, after sandblasting. The figure shows individually measured surfaces for each specimen*

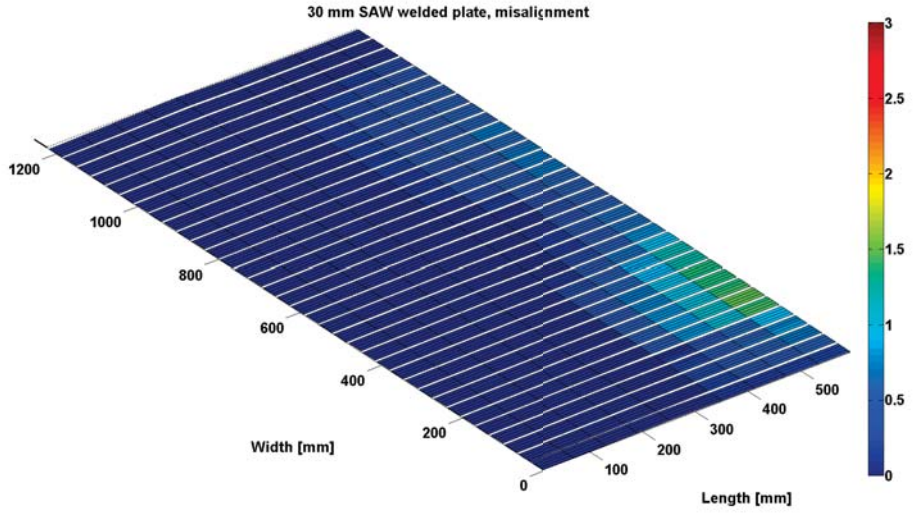

Figure 4.11: *Misalignment measurements of the 30 mm thick SAW butt joints. The figure shows individually measured surfaces for each specimen*

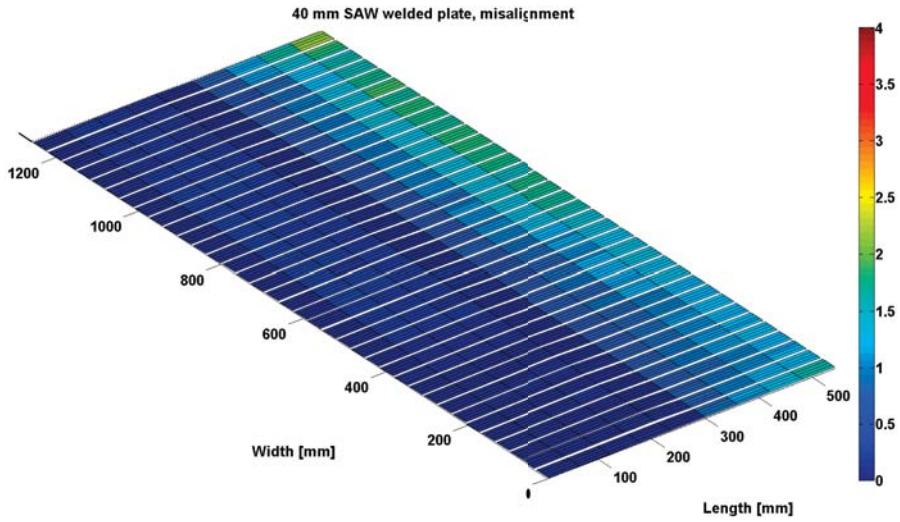

Figure 4.12: *Misalignment measurements of the 40 mm thick SAW butt joints. The figure shows individually measured surfaces for each specimen*

that the top right corner of the 20 mm thick SAW butt joints surpassed the misalignment recommendations in the standards, which results in higher structural stress for those specimens if tested. However, according to standards, the initial and last 50 mm of a welded plate should be discarded.

Additionally, Figures 4.11 and 4.12 show that the 30 mm and 40 mm thick butt welded plates have lower maximum misalignment compared to the 20 mm thick butt welded plate and therefore give added weight to the statement that thicker butt welded joints are less likely to be heavily affected by misalignment. Both the 30 mm and 40 mm thick plates are well below the recommended acceptable misalignment, which is 10% of the thickness of the joint with a maximum value of 3 mm and 4 mm respectively [95].

The maximum end-to-end misalignment measured was 4.40 mm, 1.82 mm and 2.31 mm with the corresponding lowest misalignment measured to be 0.30 mm, 0.04 mm and 1.19 mm. Overall, the measured average misalignment were 1.68 mm, 0.90 mm and 1.71 mm for the 20 mm, 30 mm and 40 mm thick joints respectively. Thus, the difference between the highest and lowest measured values reduces significantly with thickness and was measured as 4.11 mm, 1.85 mm and 1.12 mm for the 20 mm, 30 mm and 40 mm thick respectively, indicating the lowest deviation in the thickest welded joints. Furthermore, it is worth noting that the misalignment of the 40 mm thick butt welded joints are relatively consistent with only a $\pm$ 0.60 mm difference from the average measured value, compared to 0.92 mm and 2.73 mm for the 30 mm and 20 mm thick joints respectively.

4.13 illustrates the two planes of the welded joints which were measured. The first plane measured was used as a reference plane thus it is nearly parallel with the x-axis, while the second plane deviates from the reference plane in the z-coordinate. The sub-figures show measured data from the 2^{nd}, 17^{th} and 35^{th} specimen from each thickness, i.e. 20 mm, 30 mm and 40 mm thick. These images illustrate the out-of-plane coordinate axis, the z-coordinate on the y-axis and the length of the measured specimens along the x-axis. It is evident that the misalignment is a function of the specimen's length. Furthermore, the center dot in every sub-plot represents an "ideal" center point for the welded region. Therefore, if the specimen would only be subjected to axial misalignment, the latter plane would be parallel to the x-axis and offset on the y-axis. However, if the specimen would solely be subjected to angular misalignment then the two planes would ideally intersect in the center of the welded region.

Additionally, Figure 4.13 illustrates the large variation in the measured axial and angular misalignment in a set of sub-images. In some cases it appears to be only angular misalignment, e.g. T20-2, while others are heavily affected by axial misalignment, e.g.

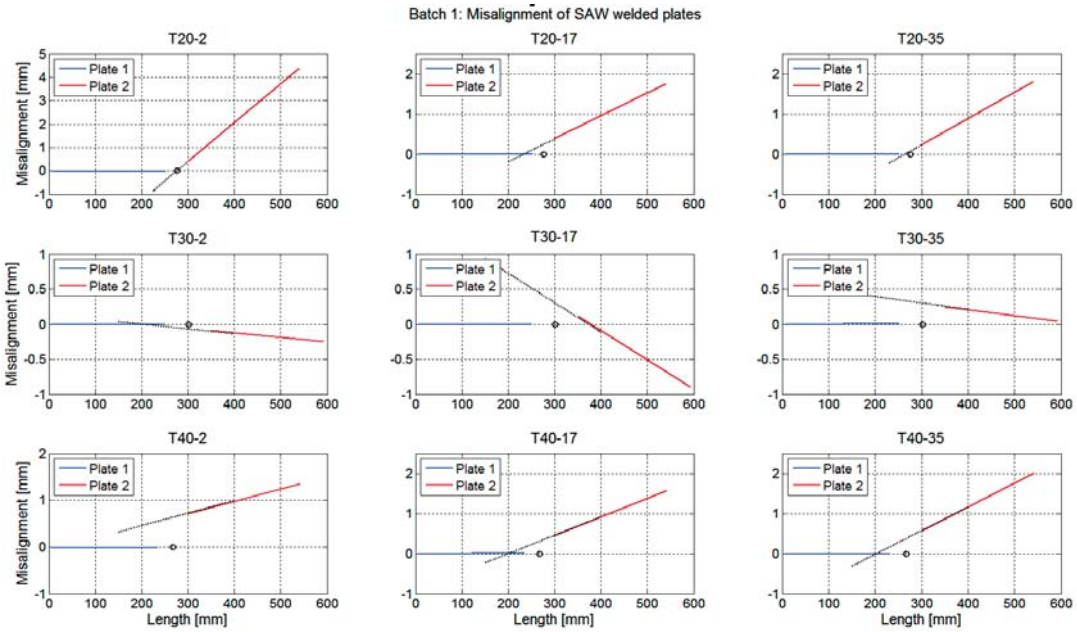

Figure 4.13: *Misalignment measurements from coordinate machine, all thicknesses*

T40-2. Lastly, the measurements for the 30 mm thick butt welded joints show that the second plane is actually inclining in such a way so that the two surfaces would not intersect at all, T30-35. The first plane is relatively parallel with the x-axis while the second plane tilts upwards with a negative slope.

The angular misalignment, α, was computed by applying trigonometry for each specimen of all thicknesses. Averaging of the x-axis and the out-of-plane z-axis was applied which resulted in a maximum angle of 0.96°, 0.32° and 0.38° with the corresponding minimum angle of 0.11°, 0.04° and 0.13° for the 20 mm, 30 mm and 40 mm thicknesses respectively. Furthermore, the average angle for each thickness was computed to be 0.37°, 0.19° and 0.27° for the 20 mm, 30 mm and 40 mm thicknesses respectively.

Figure 4.10, illustrates the misalignment measurements of the 20 mm thick butt welded plate after the surface had been sandblasted. The sandblasting was at very low pressure and only used to clean the base material surface, in order to examine whether the thin contaminated oxide layer on the steel's surface was responsible for increasing the deviation in the alignment measurements. Thus, as Figure 4.10 shows, the trend in the measurements is almost identical, indicating that the layer formed at the surface of the steel is relatively uniform. However, comparing the angular differences between

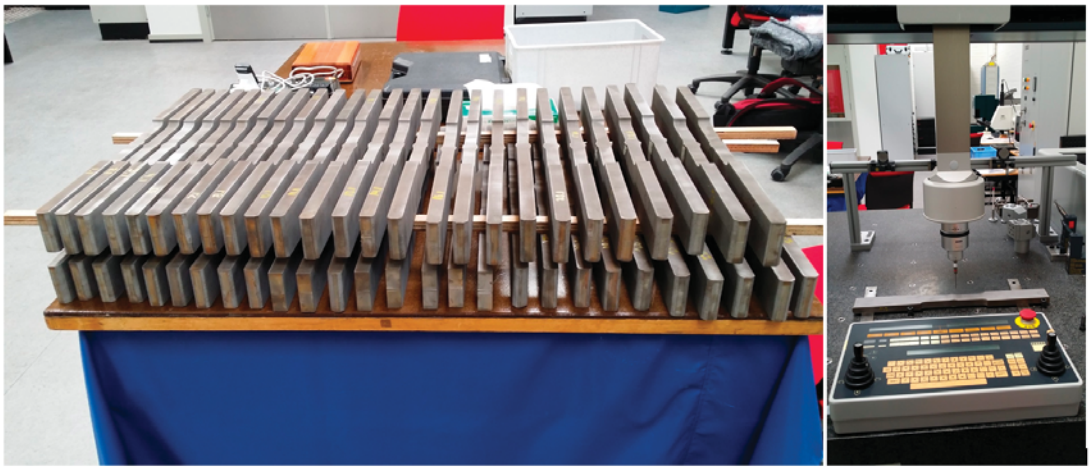

Figure 4.14: *(Left) 20 mm thick butt welded specimens from Batch 2 and (right) Coordinate measurement machine*

the two measurement processes, resulted in an increase of 2.63°, 7.82° and 6.14° from specimens at the start, middle and end of the butt welded plate. Applying the maximum angular difference would therefore increase the average measured angle for the same plate with the oxide layer from 0.37° up to 0.40°. Although this increase is noticeable, the lack of capacity, man-power and possible sources of error associated with the misalignment measurements, the remainder of this test series, batch 1, and related calculations were performed on specimens as-welded without removal of the surface layer.

The axial misalignment of the butt welded joints were measured according to Figure 4.7, where the base material is considered to be consistent of equal thickness. Thus the centerline can be moved upwards to the surface and the two surfaces will intersect similarly as the two centers would. Therefore, by offsetting the second plane by a factor in order for it to intersect with the first plane at the weld center, see figure 4.13, an indication of the axial misalignment can be derived. Tables with axial and angular misalignment as well as measured values for each specimen are presented in Appendix A.

Batch 2: External manufacturer

The same misalignment measurement procedure was applied to batch number 2, i.e. the 20 mm thick test specimens, see Figure 4.14. This batch was larger then the previous

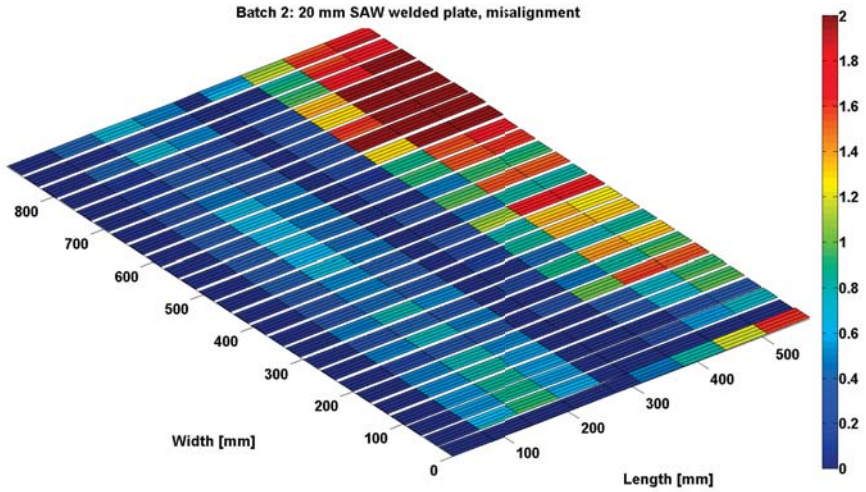

Figure 4.15: *Misalignment of the 20 mm thick butt welded joint from batch 2, plate 1*

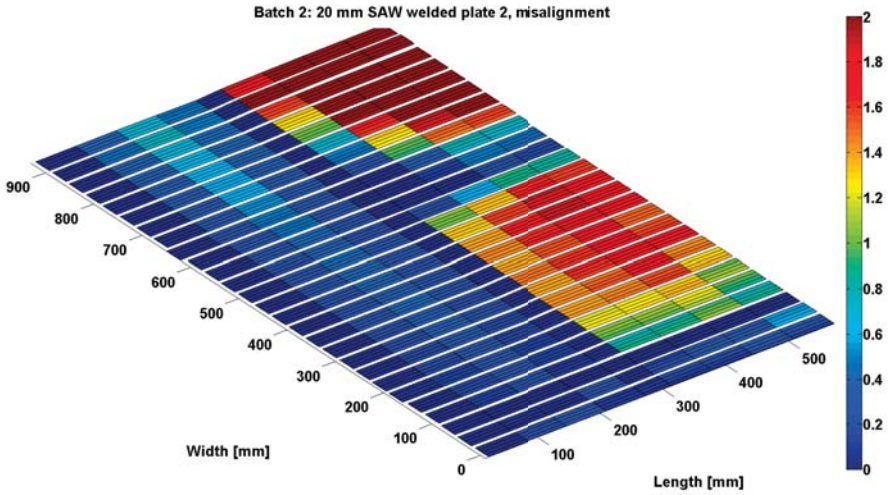

Figure 4.16: *Misalignment of the 20 mm thick butt welded joint from batch 2, plate 2*

20 mm thick butt welded plate, since half of these specimens were applied in Test Series 2, see Chapter 5, for a direct comparison to specimens tested in fatigue within a corrosion environment.

Before proceeding with the misalignment measurements, the oxide surface layer was removed completely from all samples. Figures 4.15 and 4.16 illustrate the measurement results with the colorbar on the right indicating recommended maximum allowed misalignment according to standards.

It is clear that there is a large difference between the butt welded plates from Batch 2 compared to Batch 1 as a large portion of the measured specimens surpasses the recommended limit, i.e. 10% of the welded detail's thickness. Thus, in this way, these specimens will be affected by the local stress increase due to the secondary bending during their axial testing. However, this is combined out of plane deviation which is illustrated, i.e. the axial and angular misalignment, relating to Batch 2. According to the measurements, the out of plane deviation measured next to the weld and towards the specimen's shows a definite increase.

The maximum end-to-end misalignment measured was 5.26 mm and 6.90 mm with the corresponding lowest misalignment measured to be 0.45 mm 0.08 mm for plate 1 and 2 respectively. Furthermore, the average misalignment was 1.76 mm and 1.65 mm for plate 1 and 2 respectively. The angular misalignment, α, resulted in a maximum measured value of 1.10° and 1.06°, with a minimum value measured to be 0.02° and 0.01° for plate 1 and 2 respectively. Additionally, the average angle measured for both plates from batch 2 was 0.37° and 0.21°.

These results show that the axial misalignment for batch 2 are not as good when compared to batch 1 as the average angular misalignments are either equal or lower than the measured values for the 20 mm thick specimens in batch 1. This may be a consequence of a poor fit-up before the plates were welded.

Misalignment is unavoidable when it comes to welded joints, and for butt welded joints the axial and angular misalignment due to material parameters, manufacturing inaccuracies and the applied welding process are particularly large and result in secondary bending stresses when tested axially. An estimation according to [35], states that a local increase of stress can rise up by 30%, and this local stress increase due to bending becomes even more significant for thinner welded specimens [97].

4.3 Experimental test results

The following section will describe the experimental test procedure and include a discussion relating to the obtained test results.

Figure 4.17: *(Left) Strain gauges location and preparation, (center) prior to static testing, measurement equipment setup and (right) visible surface pattern for the DIC system and necking of the specimen occurring above the weld*

4.3.1 Static testing

The butt welded joints were subjected to axial static testing in order to retrieve mechanical properties, verify the manufacturer's yield strengths and most importantly estimate a reference load level for the subsequent fatigue testing. The static tensile testing was performed in accordance to ASTM E8, ASTM E111 and DS/EN ISO 6892 [98], [99] [100]. The testing machines applied were described in section 4.2.2. Before initiating the test sequences all machines were calibrated and load cell readings verified, relevant load calibration and verification data are listed in Appendix B. No testing was performed in a machine if the load signal surpassed 1% error, measured against an Interface certified reference load cell.

The strain gauges applied were "general purpose", EP-08-250BG-120 ohm strain gauges from Vishay with an active gauge length of 6.35 mm. These gauges are intended for high elongation and post yield strain measurements. In addition, extensometers were applied for the computation of the elastic modulus and lastly a digital image correlation system was used in order to receive a full field three dimensional displacement field of

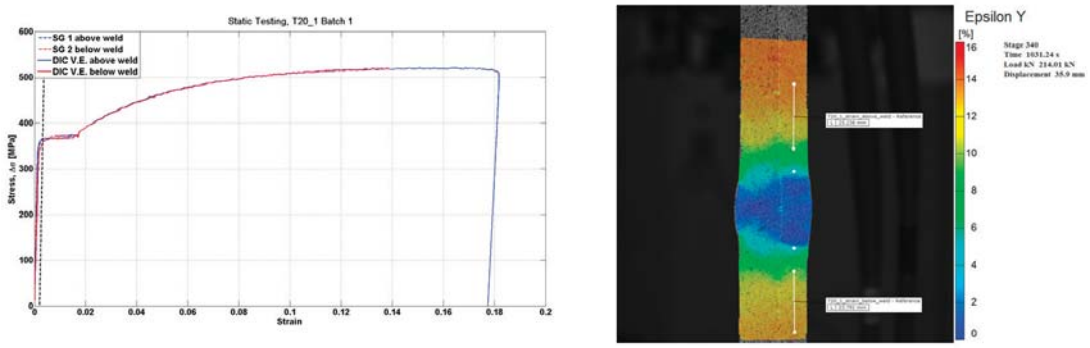

Figure 4.18: *20 mm thick butt welded specimens from Batch 1. (Left) Stress-strain curves and (right) full field axial strain distribution over the welded zone*

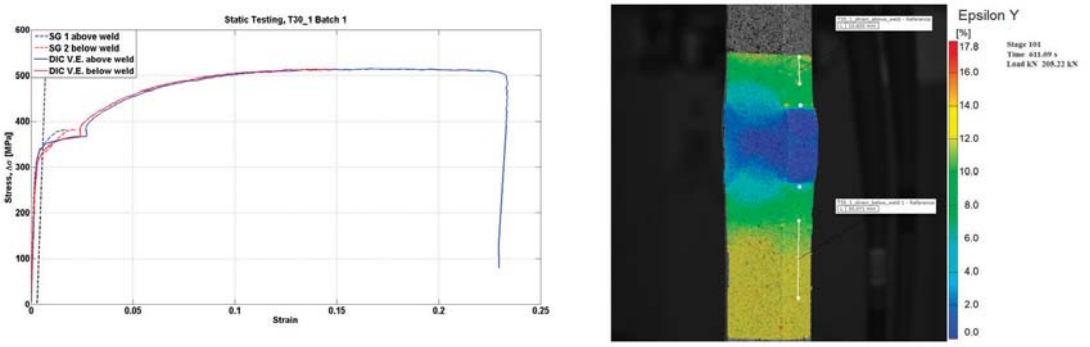

Figure 4.19: *30 mm thick butt welded specimens from Batch 1. (Left) Stress-strain curves and (right) full field axial strain distribution over the welded zone*

the area of interest.

The location of the strain gauges varied between tests, a few static tests were used to investigate the hot spot stress close to an as-welded discontinuity. For those specimens the gauges were located as recommended by the IIW at a distance of 0.4, 0.9 and 1.4 times the thickness of the joint, the specimens not used in this investigation had strain gauges mounted at a distance of >1.4t in order to avoid stress concentrations due to the weld. As strain gauges solely provide a local strain result, the DIC system Aramis was also utilized in order to obtain a more clear picture of the welded region and to visualize the strain distribution around the welded region. The DIC camera system was orientated at an angle so both the surface of the specimen as well as the thickness were

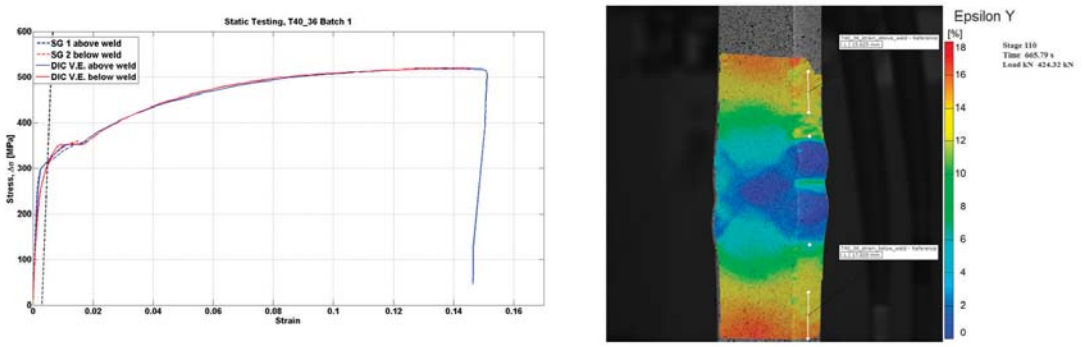

Figure 4.20: *40 mm thick butt welded specimens from Batch 1. (Left) Stress-strain curves and (right) full field axial strain distribution over the welded zone*

recorded during the tensile test. The DIC system allows you to track with high precision (approximately 2 microns for these tests) a pattern on the surface of the specimen after being calibrated to a certain measurement volume. The system compares a defined region or a facet on the initial image to every subsequent recorded image in order to track the displacements with a reliable algorithm. Thus, in the system a strain gauge or an extensometer is relatively easy to create, as two aligned points are selected with a specified known distance between them and the subsequent change in displacement due to the load introduced will result in deviations between the two selected points.

Figures 4.18, 4.19 and 4.20 illustrate a specimen under tensile loading at maximum load with two virtual extensometers, one located above the weld and the other below. The corresponding stress-strain curve for the selected tests are shown on the left side. The DIC system is very beneficial in retrieving a clear full field displacement overview of the entire area of interest and being able to track the displacements all the way to fracture at various locations, contrary to strain gauges that give you a precise local strain reading until they fall off as the specimen undergoes plastic deformation.

In total, five static tests were performed for each thickness for both batches, with the exclusion of the 30 mm thickness in batch 2 due to lack of specimens, where three static tests were performed. Additionally, the two specimens cut from the ends of the welded plate were used as pilot specimens as it is recommended to discard the first and last 50 mm of a welded plate. The rate of displacement varied also from 2 mm/min up to 4 mm/min. The measurement systems were synchronized with a common load signal. Unfortunately the DIC system was not able to operate at a high data acquisition frequency which resulted in only a few measurement intervals during the elastic region and the subsequent yield plateau of the material.

All statically loaded specimens fractured in the base material, as the welded region was over-matched, i.e. made of a material of higher strength. Furthermore, all specimens broke far from the weld and the heat affected region. The mechanical properties are listed in tables 4.8 and 4.9. The yield levels were estimated by applying a 0.2% offset curve and some intuition as the testing resulted in some scatter, which is to be expected as the specimens were not post-processed, misaligned and included a welded region which will have an influential affect on the results. However, as mentioned previously, these static tests were mainly performed in order to retrieve adequate load levels for the subsequent fatigue testing of the same butt welded joints, as well as to verify and validate that the material is of the desired strength and the weld of specified quality to withstand these high tensile loads.

The tables show the results of the static testing and portray the scatter between the test

Table 4.8: *LWT - Batch 1. Mechanical properties, engineering*

Test Series 1 - Thickness effect of SAW butt joints.							
Specimen #	Width [mm]	Thickness [mm]	Area [mm^2]	Length [mm]	σ_y [MPa]	σ_{ult} [MPa]	E modulus [GPa]
T20.1	20.11	20.65	415.27	500	361.37	524.81	211.65
T20.2	20.10	20.64	414.86	500	377.93	518.16	208.58
T20.3	20.13	20.67	415.88	500	378.02	520.99	206.18
T20.35	20.07	20.36	408.63	500	376.32	521.17	202.91
T20.36	20.13	20.38	410.25	500	373.78	523.91	205.78
T30.1	20.12	30.29	609.43	500	350.23	517.36	205.43
T30.2	20.31	30.35	616.41	500	374.19	511.04	197.76
T30.3	20.29	30.38	616.31	500	377.83	510.32	201.59
T30.35	20.33	30.37	617.42	500	379.93	509.16	211.88
T30.36	20.17	30.39	612.97	500	375.29	512.88	190.71
T40.1	20.11	40.52	814.05	500	355.30	534.50	203.82
T40.2	20.17	40.58	818.50	500	367.92	526.50	209.34
T40.3	20.15	40.52	816.38	500	371.52	527.27	189.40
T40.35	20.19	40.53	818.20	500	368.07	526.74	188.24
T40.36	20.17	40.53	817.49	500	345.81	525.60	195.26

specimens in terms of yield and calculated elastic modulus. The resulting strengths are lower than those listed from the manufacturer. Nonetheless they are above the desired strength levels. Compared to the data provided by the manufacturer, i.e. the mechanical strengths of the material, the same trend in strength is noticeable. Relatively consistent yield strengths for all thicknesses in batch 1, delivered by LWT, and the reduced yield strengths in relation to thickness for the joints delivered from the external manufacturer.

4.3.2 Fatigue testing

Axial loaded tension-tension fatigue tests were performed in several servo hydraulic testing machines (SHM), located in building 119 at the Technical University of Denmark, DTU. All SHMs were calibrated and load verified as well as the measurement equipment before initiating a test sequence. All tests were carried out in laboratory air

Table 4.9: *External manufacturer - Batch 2. Mechanical properties, engineering*

Test Series 1 - Thickness effect of SAW butt joints.							
Specimen #	Width [mm]	Thickness [mm]	Area [mm^2]	Length [mm]	σ_y [MPa]	σ_{ult} [MPa]	E modulus [GPa]
T20.1.1	39.82	19.87	791.22	600	407.88	543.57	198.37
T20.1.2	39.86	19.89	792.65	600	406.27	548.05	194.14
T20.26.1	39.72	19.78	785.47	600	416.15	548.15	190.90
T20.26.2	39.79	19.78	787.19	600	391.39	-	214.87
T20.27.2	39.77	19.79	787.05	600	410.30	-	216.29
T30.1.2	39.82	30.17	1201.70	500	365.70	519.64	210.77
T30.2.2	39.73	30.16	1198.06	500	372.82	515.98	210.88
T30.3.2	39.65	30.31	1201.59	500	375.68	538.30	206.91
T40.19.2	39.77	40.19	1598.36	500	358.36	522.24	194.90
T40.20.2	39.67	40.39	1601.87	500	354.55	522.60	191.69
T40.22.2	39.70	40.26	1597.92	500	354.80	522.45	192.32
T40.23.2	39.80	40.31	1604.14	500	358.40	522.56	183.07
T40.24.2	39.65	40.25	1595.71	500	357.66	526.07	189.44

conditions at room temperature, +20°C.

Pilot testing

Initial pilot testing was performed on SAW butt joints in order to verify the test procedure, investigate the effect of stress ratio, R, and validate whether the test specimens could be tested as straight beams instead of in the recommended dog-shaped form. The tests were performed in collaboration with Laufey Gunnþórsdóttir, a master student of DTU mechanical engineering [12]. All the fatigue tests were monitored by a high resolution camera in order to observe the visual crack initiation and estimate its propagation across the weld.

The tests resulted in a substantial effect of the stress ratio, R, altering the stress amplitude σ_a and mean stress, σ_m, while cycling down from the yield strength, σ_y of the specimens. The test frequency varied from 6 - 12 Hz, depending on the stress amplitude. The average fatigue resistance until fracture for these tests were 173.563, 842.564 and run-outs at 2.000.000 cycles for R = 0.25, 0.5 and 0.75 respectively. All of the test specimens fractured in the welded region. The crack propagation started at the weld toe for the majority of the specimens while two test specimens demonstrated a crack across the entire length of the weld without having demonstrated a surface crack "initiation", i.e. the crack had propagated from end to end without a noticeable crack growing on the surface. That may be indicating that the crack was either very minuscule so that the camera system was unable to pinpoint the origin, or that the crack was growing sub-surface. The run-outs did not contain any visible cracks on the surface.

Test series 1 - thickness effect

The thickness effect investigation, Test Series 1, followed directly after the pilot testing was completed, i.e. tension-tension fatigue testing of SAW butt joints, as-welded, under in-air conditions. Three different thicknesses were evaluated, i.e. 20 mm, 30 mm and 40 mm thick butt welded joints, with a constant width of 40 mm. The specimens were subjected to constant amplitude sinusoidal waveform at a frequency ranging from 6-10 Hz. Testing was based on the estimated yield strength of the SAW butt welded joints from the static testing results. The cyclic loading was performed at a stress ratio of R = 0.5, with stress levels computed as a percentage of the specimens average yield strength, σ_y. Also, in order to generate a more reliable S-N curve, the welded joints were tested at a minimum of five different stress levels and with a minimum of five specimens tested at each stress level. The maximum stress, σ_{max}, equalled 120% of the

yield strength while the minimum stress applied, σ_{min}, equalled 60% of the material's yield strength.

The main test parameters for this test series is therefore:

$$R = \frac{\sigma_{min}}{\sigma_{max}} = 0.5 \tag{4.2}$$

Thus,

$$\begin{aligned} \Delta\sigma &= \sigma_{max} - \sigma_{min} \\ &= \sigma_{max} - \frac{\sigma_{max}}{2} \\ &= \frac{\sigma_{max}}{2} \end{aligned} \tag{4.3}$$

Where σ_{max} is a function of the yield strength, ranging from [0,6 to 1,2] of σ_y.

The definition of failure in all fatigue tests was complete rupture, which is commonly very near the through thickness cracking. This is mentioned as fatigue failure in large structures which is generally considered to be when a crack has propagated through the thickness or a large crack has propagated at or below the surface.

The testing at stress levels computed as a percentage of the specimen's average yield strength was chosen in order to minimize the potential differences of residual stresses, which varies quite significantly with the thickness of the components.

The choice of R = 0.5 was taken after considering the affects of residual stresses, in order to better simulate the high tensile residual stresses experienced by welded joints in real large structures. In this way, it would be possible to mimic as close as to possible the actual loading conditions experienced by a monopile structure and maximizing the possibility for comparison to existing structural results. Taking into account the recommendations from IIW, [7], for generating a proper S-N fatigue curves, close attention has to be brought on to the fact that internal residual stresses are usually lower in small scale specimens. IIW states that results from these small scale testing should be rectified in order to take into account the greater effects of residual stresses in structures, therefore representing the real situation at hand. In order to achieve these more realized values, IIW recommends testing at high stress ratios, R, e.g. R = 0.5, or by applying a stress ratio of R = 0 followed by a 20% reduction of fatigue strength at 2 million cycles. Additionally, there is a notable lack of experimental test results in literature of butt welded joints tested at R = 0.5.

With these considerations in mind, it follows that by increasing the specimen's width and thickness the more representative of the real structural residual stresses it becomes,

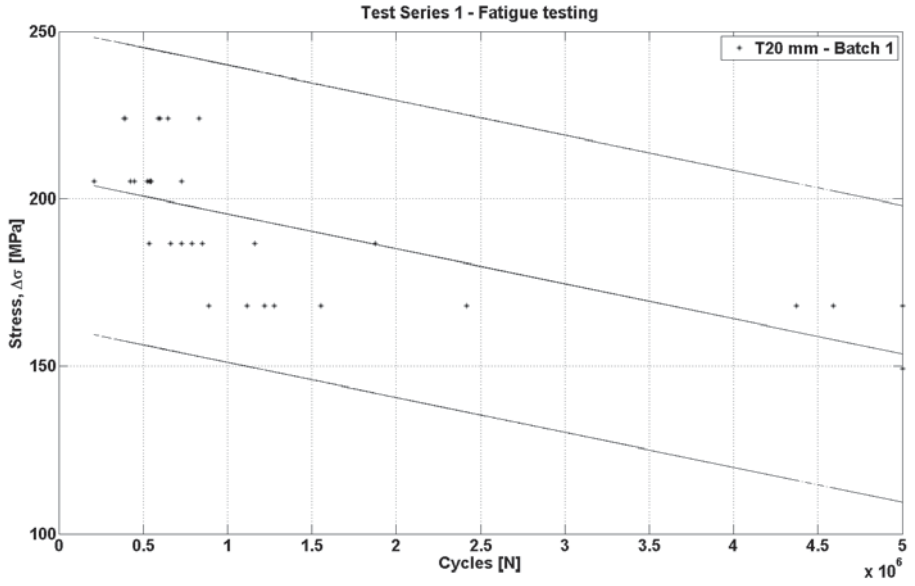

Figure 4.21: *Fatigue results for the 20 mm thickness from batch 1. Stress range, $\Delta\sigma$, as a function of cycles, N*

as the internal stresses are allowed to build up. However the bottleneck or ruling factor becomes the lab facility's test capacity.

Batch 1

The test series started with the axial tension-tension testing the 20 mm thick, as-welded, SAW butt joints. The results from these initial tests were applied as a reference for this investigation, as welded structures with less than 25 mm of wall thickness are not subjected to thickness correction according to standards and guide recommendations.

The fatigue test sequence started with testing the specimens with stress ranging from $\sigma_{max} = \sigma_y$ at R = 0.5. Thereafter the stress level was calculated as a percentage of yield until a threshold limit was reached. The threshold limit for all test series was set to be at 5 million cycles. The entire data collection for the 20 mm thick fatigue tests from batch 1 are illustrated in Figure 4.21. The plot demonstrates the results with the stress range, $\Delta\sigma$, on the ordinate and cycles to failure on the abscissa. A mean curve is as well shown along with $\pm$ two standard deviations, which corresponds to a survival

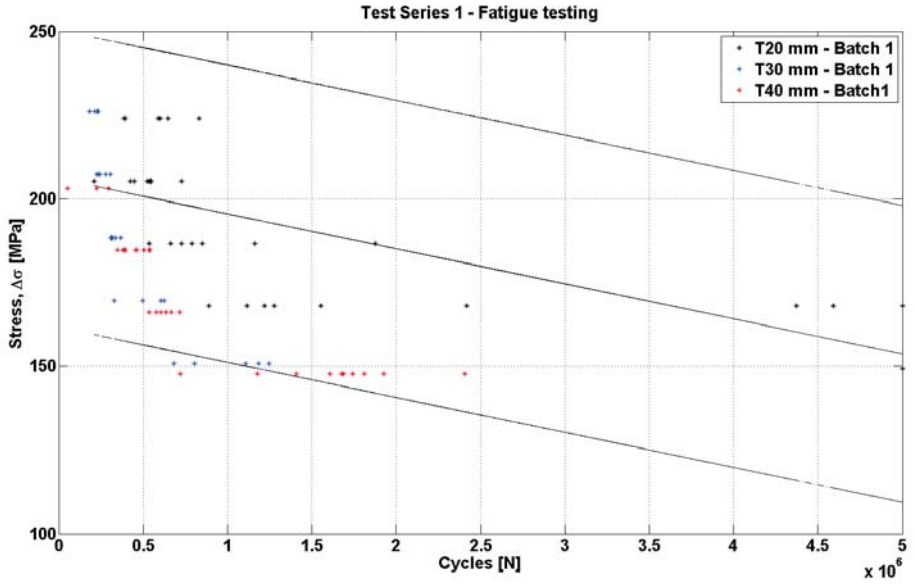

Figure 4.22: *Fatigue results for all three thicknesses from batch 1. Stress range, $\Delta\sigma$, as a function of cycles, N*

probability of 97.7%.

The figure shows clearly the five different stress levels, with a handful of specimens running out. All test results lie within the $\pm$ two standard deviations from the mean.

Figure 4.22, demonstrates a combined plot after adding all the fatigue test results from the 30 mm and 40 mm thick SAW butt joints from batch 1.

Already it is clear that there are, some indications towards the thickness correction of larger joints that come into question. It can be seen that the 20 mm thick joints have superior fatigue resistance compared to the 30 mm and 40 mm thick welded joints. However, the majority of the 30 mm and 40 mm thick joints lie within the $\pm$ 2 standard deviation scatter bands of the mean calculated for the 20 mm thick joints. The thicker joints tend to lie in the lower half of the scatter band with a total of four outliers. Another interesting indication from Figure 4.22 is that the 40 mm thick joints demonstrate a higher fatigue resistance than the 30 mm thick joints.

As the investigation is emphasized on analysing fatigue resistance of SAW butt joints in the as-welded condition. The specimens which failed in the grip region are removed from the analysis. There was a portion of specimens that initiated a crack within the

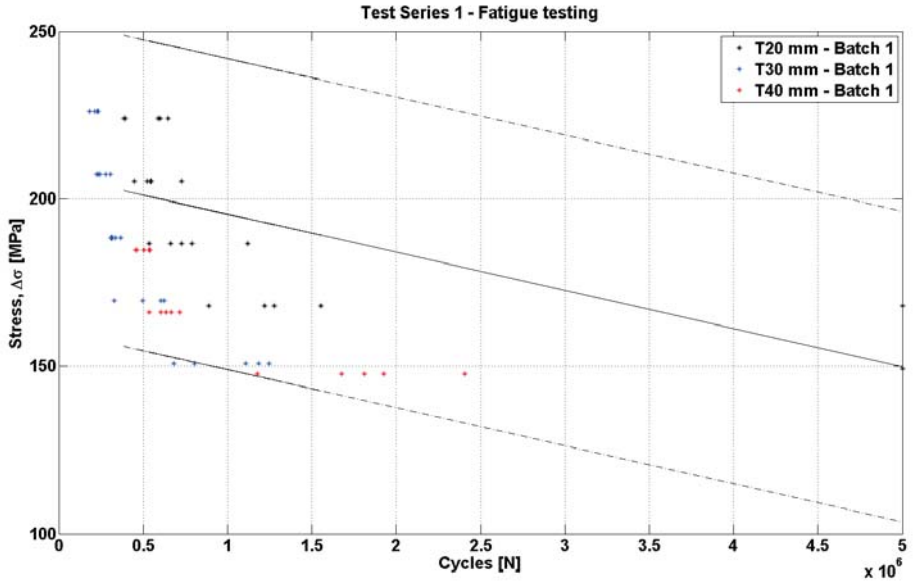

Figure 4.23: *Fatigue results for all three thicknesses from batch 1, excluding specimens that fractured in the grip region. Stress range, $\Delta\sigma$, as a function of cycles, N*

grip region which lead to fracture. Poor test specimen design, cutting and clamping force are sources of error, which may have contributed heavily. These specimens were in the 20 mm and 40 mm thicknesses, the 30 mm thickness was unaffected and all specimens fractured in the weld region. Figure 4.23 shows the fatigue test results after excluding those specimens from the analysis. The mean curve and the scatter bands were adjusted to the 20 mm thick specimens which fractured in the weld region. In order to get a better estimation of the curve, the run-outs were excluded from the mean curve computation as they show superior fatigue resistance and therefore contribute extensively to the scatter of the data.

These results are to be compared to recommended design S-N curves, also known as Wöhler curves, and according to standards, the S-N curves should be presented graphically as a log-log graph where the endurance in cycles is plotted on the abscissa and the range of fatigue actions on the ordinate, as described in section 2.2. The structural detail of a SAW butt joint corresponds to design curve FAT90 in the IIW guideline which relates to design curve D in the DNV recommendations and UK Class D, which is interpreted as the allowable design stress equals 90 MPa at 2 million cycles. The fatigue test results are shown in Figure 4.24 along with the recommended design curve. The mean curve for the 20 mm thick fatigue test results is based on a recommended

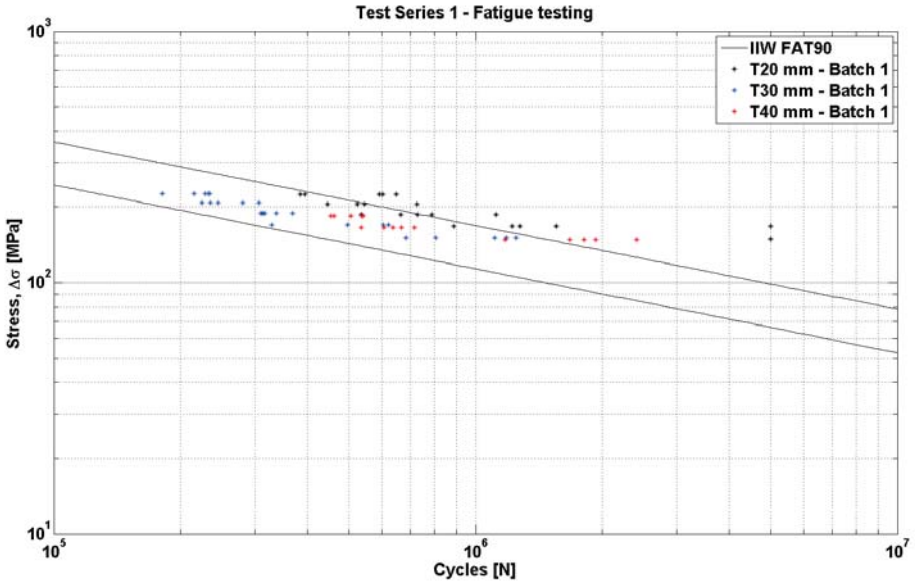

Figure 4.24: *Fatigue results for all three thicknesses from batch 1, including the recommended fatigue design curve, FAT90. log-log plot with the stress range, $\Delta\sigma$, as a function of cycles, N*

fixed slope of 3, this was discussed in section 2.2.

As is illustrated by the figure, all fatigue specimens tested lie above the recommended design curve. The design curve itself also appears to be a good guide to fatigue resistance as all specimens are scattered above the line. There is a single test specimen of the 30 mm thick joints, which comes close to the design curve, while all the 40 mm thick test results are located safely above the design curve. However, the 30 mm and 40 mm thick joints are to be subjected to thickness correction, which means that the design stress range is lowered for the same number of cycles endured, i.e. their fatigue resistance is reduced. This thickness correction for the 30 mm and 40 mm thick joints is illustrated in Figure 4.25.

The corrected design curve for the 30 mm thick butt welded joints in relation to the results acquired from this investigation appears to be a decent recommendation as there is a data point close to the FAT90 curve and the correction corresponds to a stress range reduction of 6 MPa or approximately 3.66%. However, more interestingly the corrected curve for the 40 mm thick joints appears to be an overly conservative measure, reducing the recommended design fatigue strength by 13 MPa or approximately 9.29%. Addi-

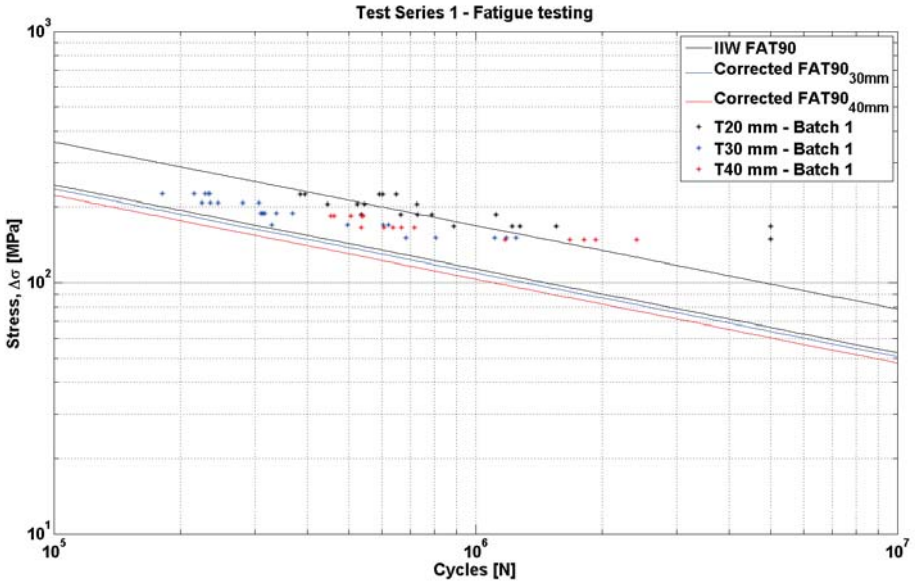

Figure 4.25: *Fatigue results for all three thicknesses from batch 1, including the original and thickness corrected recommended fatigue design curves, FAT90. log-log plot with the stress range, $\Delta\sigma$, as a function of cycles, N*

tionally, the fractured 40 mm thick butt welded joint which is closest to the original FAT90 curve is 26.1 MPa above or approximately 18.64%. Comparing the same 40 mm thick specimen to the corrected FAT90 design curve for 40 mm thick joints, it lies 39.1 MPa above or approximately 30.79%, corresponding to 217.400 additional load cycles.

Batch 2

To give this investigation increased weight and more validity, an additional SAW butt plate was manufactured. Unfortunately, LWT's capacity to produce SAW plates was no longer available. Therefore, another third party vendor, was contacted in order to manufacture the required welded plates. Three thicknesses were ordered and the welding procedure specification, WPS, was handed over to the new manufacturer, in order for them to achieve an "as close as possible" repetition of the previous welded batch from LWT, this was described in section 4.2.3.

All specimens were cut into a "dog-bone" tensile test shape in order to avoid the

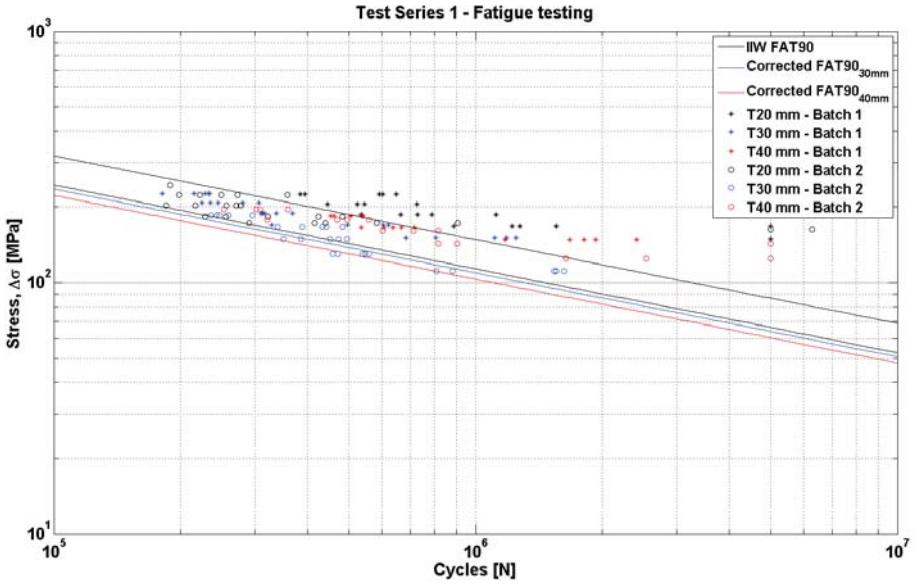

Figure 4.26: *Fatigue results for all three thicknesses from batch 1 and batch 2, including the original and thickness corrected recommended fatigue design curve, FAT90. log-log plot with the stress range, $\Delta\sigma$, as a function of cycles, N*

predicament of crack propagation and fracture in the grip region. Subsequently, all specimens broke in the weld region.

Figure 4.26 illustrates the total test population after adding the additional fatigue tension-tension testing from batch 2 into the previous log-log plot from batch 1 along with the original and corrected design S-N curves. The mean curve was adjusted to the additional population of 20 mm thick specimens.

Figure 4.26 shows that the SAW butt joints for batch 2 have an overall lower fatigue resistance compared to the batch 1, even though the previous WPS was replicated. This demonstrates to a high degree the variability of the welding procedure and the difficulty of manufacturing a welded joint with high quality and repeatability. Therefore, another angle concerning the weld quality and its effects was added to this investigation of the thickness effect.

As described in 4.2.4. The welded plate from the external manufacturer followed the WPS from the previous batch and the 30 mm and 40 mm thick welded plates had to undergo repair where the weld had to be remelted and the material had to be subjected to additional heating and cooling solidification processes which could have significant

effects, since only a small variation in the weld toe can lead to differences in fatigue strength. The location of the repaired specimens in the 30 mm thick butt welded plate corresponds to specimens $T30\_12\_2, T30\_13\_2, T30\_14\_2$ which were tested at $\Delta\sigma = 185,7MPa$ and $T30\_2\_2$ tested at $\Delta\sigma = 148,56$. These specimens all demonstrate the lowest cycle count for the respective stress range. However, relating to the 40 mm thick butt welded plate from batch 2, the misalignment of the plate at the location of the repair (end) was too excessive and thus the specimens were not tested, which also explains why there are fewer test specimens for the 40 mm thick fatigue test sequence from batch 2.

Figure 4.26, illustrates a similar trend as before, where all but a single specimen for the 20 mm thickness lie above the recommended design S-N curve. The 30 mm thick specimens demonstrate less fatigue resistance and a total of nine specimens lie below the recommended as well as the corrected S-N curve for 30 mm thickness. However, in the case of the 40 mm thick specimens, they exhibit higher fatigue strength than both the 20 mm and the 30 mm thick specimens and lie comfortably above the recommended original design S-N curve for specimens unaffected by the thickness correction. The specimen from the 40 mm thick joints, which is closest to the original curve is 12.4 MPa above or approximately 7.47%, corresponding to approximately 62.500 additional load cycles. Additionally this specimen is 27.4 MPa above the thickness corrected design curve for the 40 mm thick joints or approximately 18.15%.

The thickness correction has no limits and continues to reduce the fatigue resistance of the joints as the structural designs become ever larger. If the current proposals of new XL monopile designs come into practice then foundations with diameters of up to 10 m will be installed. The thickness to diameter ratio of 70-80 is common for the larger monopiles and assuming a ratio of 80 would result in a wall thickness of 125 mm. Thus, a butt welded joint, which would have had a fatigue strength of 90 MPa at 2 million cycles according to the original FAT90 curve, will be reduced to 65.2 MPa given the same number of cycles. Figure 4.27 illustrates the recommended reduction in fatigue strength for a SAW butt joint of 125 mm thickness.

This reduction of strength lowers the large welded joint from the recommended IIW design curve of FAT90 to FAT63, i.e. fatigue strength of 63 MPa at 2 million cycles. Taking into consideration the aforementioned literature review of compiled data showing that the extremely thick specimens were not lying outside the lower scatter band for the $\leq$ 25 mm thick specimens and distributed evenly in the lower scatter band from the mean curve. That trend was replicated in this experimental study for the 40 mm thick specimens. This gives an indication that the thickness correction factor might be on the conservative side and giving rise to the need of experimental testing of extremely thick

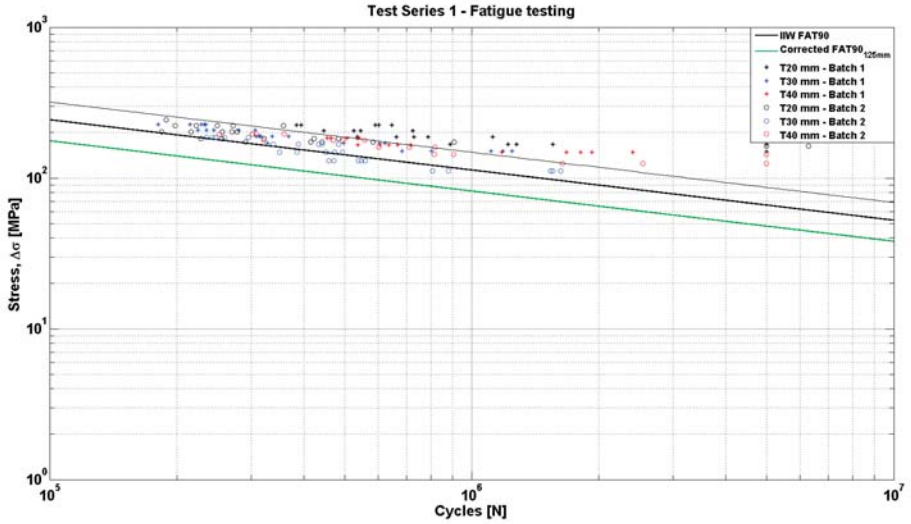

Figure 4.27: *Fatigue results for all three thicknesses from batch 1 and batch 2, including the original fatigue design curve, FAT90 along with the corrected design curve for 125 mm thick welded joints. log-log plot with the stress range, $\Delta\sigma$, as a function of cycles, N*

welded joints as those experimental test results are truly lacking in literature.

Statistical analysis

A statistical analysis was performed on all the fractured fatigue tested specimens in order to make a more reliable investigation of the fatigue strength from the experimental data. Additionally, this was performed to reduce the obtained scatter. According to IIW recommendations, [7], the most common approach is to fit the S-N curves by regression analysis, using Log(N) as the dependent variable. The test results should be analysed in order to derive characteristic values, k, which are the values that represent a 97.7% survival probability, calculated from the mean. The fatigue results from all test specimens are listed in Appendix, E.

In order to reduce scatter the run-outs were excluded from the analysis as those results show increased fatigue performance and contribute extensively to the scatter of the data, in most cases shifting the curves upwards, in such making the findings more optimistic. To a further extent, all data with fatigue capacity outside of the $\pm$ 2 stan-

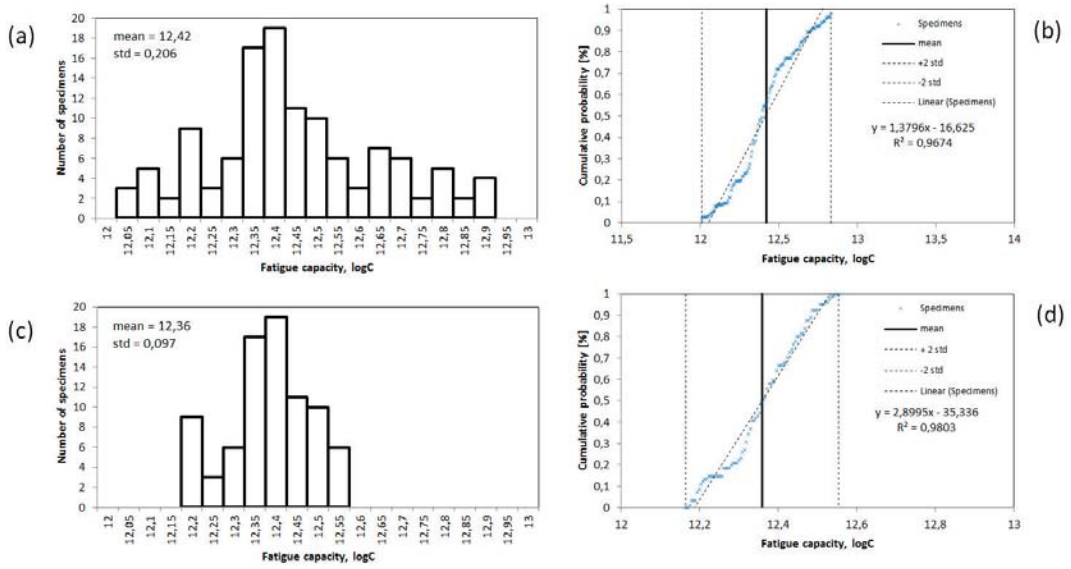

Figure 4.28: *Statistical analysis of the entire test population*

dard deviations from the mean were removed. This reduced the population from 120 specimens to 81, which is illustrated in Figure 4.28. This was necessary in order to make the population more homogeneous (d) compared to initial population (b) where the data is relatively heterogeneous.

Naturally, there are the effects of weld quality, having joints from two different batches, manufactured in different workshops involved, where the weld quality comes into question, especially with batch 2. However, the recommended S-N curves are general and should apply for most cases, in other words where the weld passes NDT.

After iteration the resulting scatter in the fatigue capacity was reduced and the data looks more homogeneous. The mean of the fatigue capacity was reduced from 12.42 to 12.36 and the standard deviation decreased from 0.21 to 0.10 after the data was homogenized. However, excluding the run-outs, the mean fatigue strength of the total population at 2 million cycles, before homogenizing, was 109.59 MPa. The characteristic fatigue strength, i.e. the lower part of the scatter band with 97.7% survival probability, was 82.56 MPa at 2 million cycles. After homogenizing the population, the mean fatigue strength at 2 million cycles was computed to be 104.58 MPa and the characteristic fatigue strength equal to 91.24 MPa, i.e. the lower part of the scatter band coincides with the IIW recommended fatigue design curve FAT90. All these computations where performed by maintaining a fixed slope of m = 3, same as the

recommended design curves.

Secondary bending under axial testing

All the aforementioned analysis and data processing of the performed fractured fatigue test results are based on test machine readings from a verified load cell mounted in an uni-axial servo hydraulic testing machine. Therefore the calculated stresses are based on the combination of the applied load range, ΔF, the specimens width and the thickness in mm, which corresponds to the nominal or membrane stress for welded detail. In this way, there is no effect of secondary bending stresses with the corresponding stress magnification on the specimen's nominal stress. Taking equations 2.19 and 2.25 into account the stress magnification factors due to geometrical features such as misalignment can be derived at the specimens critical location, i.e. the welded region. The stress concentration factors due to axial and angular misalignments are calculated separately and used in conjunction with the measured nominal stress to derive a modified nominal stress, σ_{nom_mod}, in the region of the weld toe, i.e. the including the stress introduced due to the joints misalignment. However, this does not include the stress concentration due to the weld profile and the weld notch. In cases where there is a combination of axial and angular misalignment under uni-axial testing, the derived modified nominal stress for both cases can be added together according to equation 2.26. This magnification is accountable for a significant increase in stress applied to the joint, at critical locations.

It is important to keep in mind that all the fatigue tests, were performed with the combined secondary bending, axial and angular, therefore affecting the total cycle count as the secondary bending can have severely detrimental effects on the fatigue resistance of welded joints. As described in section 2.2.1, the nominal stress, can be computed for each tested specimen, taking into account the secondary bending which the specimens were subjected to during the fatigue test procedure which eventually resulted in the aforementioned number of cycles endured before fracture.

The graphs, shown in figure 4.29, contain all the measured axial and angular misalignment results from the coordinate measurement machine, plotted up along the allowable misalignment recommendations from the standards, [7], [36] and [96]. The axial misalignment limit increases with thickness, 0.1t, while the angular misalignment is constant for all thicknesses. The 30 mm and 40 mm thick SAW butt joints from batch 2 could unfortunately not be measured.

Figure 4.29 above, shows that all specimens measured were below the recommended axial misalignment limits. However, the 20 mm thick specimens from batch 2 result

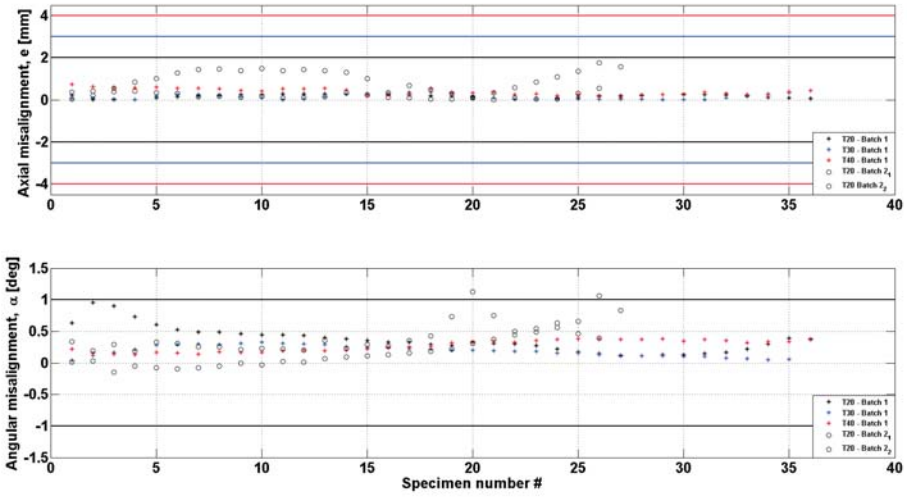

Figure 4.29: *Misalignment measurements of all batch 1 specimens and the 20 mm thick joints from batch 2. (Above) Axial misalignment, e, and (below) angular misalignment,* α

in higher axial misalignment values. Figure 4.29 below, shows the measured angular misalignment, where again the lower thicknesses show more misalignment. The 20 mm thick joints from batch 1 had a few specimens close to the recommended maximum limit, while the 20 mm thick specimens from batch 2 have 2 specimens above the maximum limit. The thicker welded joints also tend to show less variation in axial and angular misalignment, if the material fit-up and manufacturing procedure is adequate. The values indicate that the fit-up was worst for the 40 mm thick joints compared to the 20 mm and 30 mm thick joints from batch 1. Additionally, the second plate in the 20 mm thick joints from batch 2 demonstrated the worst axial misalignment.

Applying these axial and angular measurement results along with equations 2.19, 2.25 and 2.26, the axial and angular bending magnification factors can be combined to derive a bending magnification factor, K_m, and subsequently the secondary bending stress at the critical location can be computed for each specimen according to:

$$K_m = \frac{\Delta\sigma_{nom} + \Delta\sigma_b}{\Delta\sigma_{nom}} = 1 + \frac{\Delta\sigma_b}{\Delta\sigma_{nom}}$$
$$\Delta\sigma_b = (K_m - 1) * \Delta\sigma_{nom} \tag{4.4}$$

Figure 4.30, illustrates the influence of the secondary bending under axial testing and

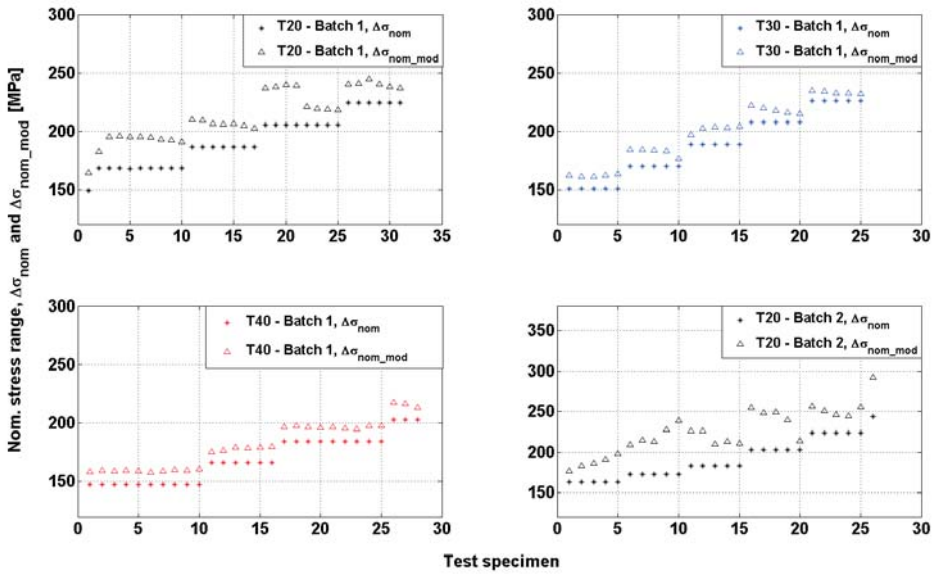

Figure 4.30: *Influence of the secondary bending stresses under axial loading, modified nominal stress*

the resulting computed modified nominal stress at the critical location.

It is evident that the influence of misalignment is significant and its detrimental effects on fatigue under axial loading has been established by multiple fatigue experiments. The SAW butt plates for this test series were manufactured with a high emphasis on misalignment and material fit-up, showing how challenging and problematic it can be to produce a sound, high quality welded joint. However, there are multiple sources of literature which do not take any misalignment measurements into account, many of which are testing welded joints in the as-welded condition, others with post-treated weld seam, which does not alter the axial and angular misalignment of the entire joint. Then there are reports where the entire welded joint is post-treated, which could lead to overly optimistic results.

Figure 4.30 additionally shows that the 30 mm and 40 mm thick SAW butt joints are subjected to less stress magnification at the critical location due to less misalignments. The thicker joints also show more consistency and almost a uniform stress magnification throughout the entire welded plate, whilst the stress magnification for the 20 mm thick welded plates varies substantially.

Table 4.10, lists the average measured axial, $\bar{e}$, and angular, $\bar{\alpha}$, misalignment and the

resulting computed stress magnification factors for each thickness. The maximum and minimum values for each thickness are also listed, to demonstrate the variation in the welded plates.

Comparing these results to the standards, then IIW recommends and already implements in the FAT class a K_m = 1.15 for butt welded joints welded in shop in the flat position and K_m = 1.3 for other cases. Thus, the average results for batch 1 are demonstrating relatively decent measurements with, K_m = 1.12 for the 20 mm thick butt welded joints and K_m = 1.06 and 1.07 for the 30 mm and 40 mm thick joints respectively. However, the 20 mm thick joints from batch 2 show results that are marginal for being in the same category as batch 1, i.e. k_m = 1.14 and 1.20. It is as well interesting to compare the range of the measured stress magnification factors, where the 20 mm thick joints from batch 1 range from max. K_m = 1.19 to min. K_m = 1.06 or ΔK_{m_20mm} = 0.13. The two additional 20 mm thick SAW plates show $\Delta K_{m\_20mm\_batch2}$ = 0.25 and 0.53 for plate 1 and 2 respectively. The thicker welded joints, 30 mm and 40 mm thick joints from batch 1, show ΔK_{m_30mm} = 0.07 and ΔK_{m_30mm} = 0.04 respectively.

It should be highlighted that the stress magnification factor does not include the non-linear stress behaviour in the vicinity of the weld, i.e. hot spot stress, due to the structural and/or geometrical profile of the detail nor the local effects of the discontinuity, i.e. the stress concentration at the weld notch. The stress concentration of the weld toe is very dependent on the weld seam and its profile angle towards the base material in addition to the notch radius, which is the critical factor. reducing the size of the weld profile, or reinforcement, as well as increasing the notch or weld toe radius will

Table 4.10: *Stress magnification factors due to misalignment under axial loading*

Test Series 1 - Thickness effect of SAW butt joints.							
Plate #	$\bar{\alpha}$ [deg]	$\bar{e}$ $[mm]$	$\bar{K}_{ang\_m}$	$\bar{K}_{ax\_m}$	Combined, $\bar{K_m}$	Max. K_m	Min. K_m
T20 Batch 1	0.3700	0.1718	1.0994	1.0250	1.1244	1.1929	1.0589
T30 Batch 1	0.1905	0.1461	1.0418	1.0149	1.0567	1.0874	1.0138
T40 Batch 1	0.2714	0.3883	1.0441	1.0292	1.0733	1.0946	1.0511
T20_1 Batch 2	0.3819	0.2099	1.1024	1.0335	1.1359	1.3248	1.0720
T20_2 Batch 2	0.2061	0.9452	1.0539	1.1417	1.1956	1.5410	1.0106

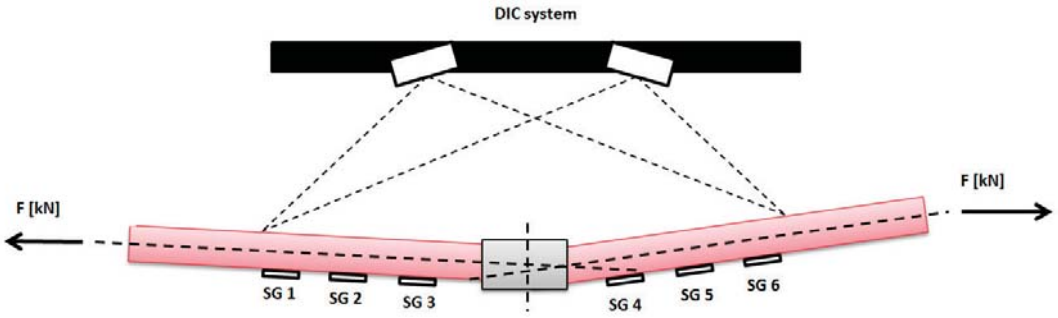

Figure 4.31: *Schematic illustration of the measurement equipment setup. DIC on one side and strain gauges mounted on the other side*

enhance the fatigue performance of the welded structure significantly.

Hot spot stress analysis

The previous calculation of the magnification factor, k_m, due to the specimen's axial eccentricity and angular distortion can give a reasonable estimate of the bending stresses affecting an ideal misaligned beam without taking into consideration the effects of the weld itself nor the weld notch and the corresponding stress concentrations and non-linear stress distribution towards the stress peak at the notch. The sudden and sharp change in geometry at the weld seam will affect the stress distribution and the weld notch, also called weld toe, can give rise to critical stress concentrations, that can be dominating in the joints fatigue life.

In the interest to determine these stresses at the weld of the SAW butt joints, a hot spot stress analysis was performed for each thickness. According to recommendations, [7], strain gauges were mounted on the specimen's surface at specific reference points at known distances from the weld toe and the exact locations were dependent on the joint's thickness. From the resulting strain readings, a hot spot stress at the weld notch can be extrapolated by applying equations 2.9 and 2.10.

In order to avoid the significant impact of the non-linear stress singularity of the weld notch the first gauge has to be positioned at a defined distance away from the weld. An illustration of the measurement equipment test setup is shown in Figure 4.31, where the gauges are aligned along the surface towards the weld on one side and on the other

side a 12 mega-pixel digital image correlation system. The application of the 3D DIC system was to be able to compare the measured strains from the gauges to the observed displacements measured from the DIC. Additionally, as the DIC system results in a full three-dimensional displacement field enabling a visual examination of the whole surface. The system can additionally be used to monitor individual 3 dimensional points in space within the calibrated 3D measurement volume and by tracking the change in displacements between two assigned points with a specified known distance between them, a virtual extensometer is generated. The application was applied in order to monitor the local strain concentrations up towards the weld notch with reduced spacing between measurement intervals and thus being able to approach the proximity of the notch influential region even closer to the borderline.

However, the 3D DIC system did not work as it was intended to, because of the spatial and strain resolution was too high, meaning that the observed displacements within a "small" defined gauge length, mimicking the size of the strain gauges, had noise levels of similar magnitude. The magnitude of the observed displacements and noise were however minuscule, i.e. in the range between 1-2 microns. In this way, by increasing the gauge length between measurement points in the 3D DIC measurements the influence of the noise could be reduced significantly. However, because of this reduction, a direct comparison to the measured strains from the gauges then becomes unrealistic, as they are measuring local strains and not averaged over a large area. Therefore, a new approach was adopted. Knowing the measured local strains from the gauges and their location on the specimen's surface a "strain-gauge" extensometer was derived. By integrating the polynomial curve resulting from the strain gauge measurements towards the weld and dividing by the change in distance, an average strain was derived from the strain gauges. This derived strain average was then compared to the computed strains from the 3D DIC system, which had the approximate same gauge length.

Figure 4.32, illustrates the results from both measurement techniques. The average strains measured were converted into stresses by applying the computed average E-modulus from the static testing for each thickness respectively. The specimens were subjected to axial loading up to 80% of their respective yield limit and the computed nominal stress at 80% is included in the figure as the dotted line. The Figure demonstrates the effect of misalignment quite clearly, however there are a number of items that require further clarification. First, the DIC system constructs a 3D coordinate model of the specimen during measurements and from the model it indicated that the 3D DIC system was monitoring the tension side, as illustrated in Figure 4.31, for the 20 mm and 30 mm thick specimens but the compression side for the 40 mm thick specimen. The Figure shows a tension and compression label on opposite sides of the nominal computed stress. Secondly, the three thicknesses which were tested had dissimilar mis-

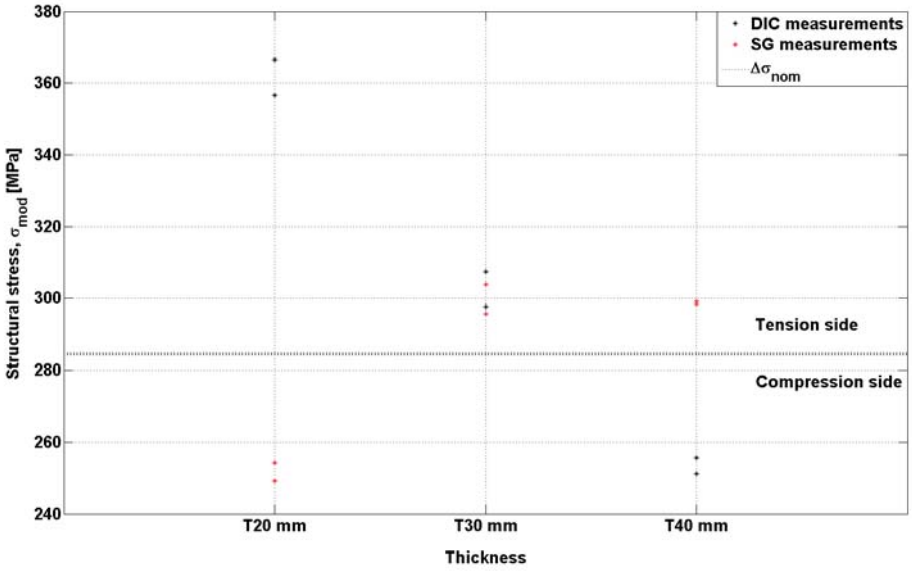

Figure 4.32: *Schematic illustration of the measured average strains from the strain gauges and 3D DIC system converted into stresses for each thickness*

alignments, i.e. the 20 mm thick joints had the largest misalignment with K_m = 1.16, then the 40 mm thick joints, K_m = 1.15 while the 30 mm thick joints had almost no misalignment, with a computed K_m = 1.025. Lastly, the two measurement points from each technique for each thickness, x-axis, show the measured strain averages above and below the weld. For example, for the 20 mm thick joints in the figure, the 3D DIC system resulted in computed stresses of 356.5 MPa above the weld and 366.5 below the weld while the strain gauges from the same test resulted in 254.23 MPa above the weld and 249.18 MPa below.

Figure 4.32, displays that the influence of a slight misalignment severely affects the strain measurements, and strain gauges located at the compression side will result in a hot-spot stress which is below the nominal stress while on the tension side the hot-spot stress is higher than the nominal stress. The influence of the weld parameters and weld notch is as well indicated as the relationship between the tension and compression surfaces are not equal, the welded joints tendency to straighten out as it is axially loaded adds more complication and will affect the measured strains.

For the ideal situation of a straight joint with a completely symmetrical weld profile, weld notch, heat affected zone, defect distribution and internal stresses, etc., the hot-

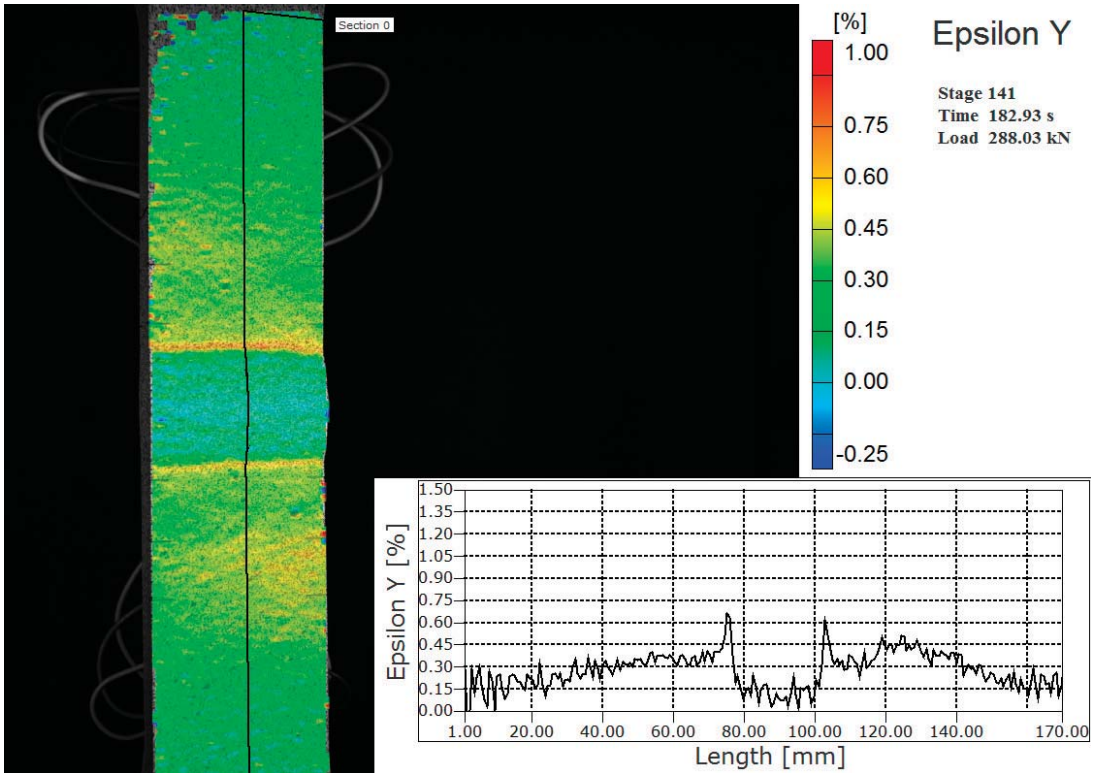

Figure 4.33: *Weld notch stress concentration, aramis 3D DIC image of the 20 mm thick specimen under static testing*

spot stress should be equal. In order to compare computed hot spot stresses between the three thicknesses an idealized case of a straight beam with symmetrical weld parameters was assumed with a linear relation of the bending stress, σ_b, between the two surfaces. In this way, maintaining that linear relationship between the surfaces, the measured strains on the compression side can be converted into the corresponding strains on the tension side. This was only required for the 20 mm thick specimen. The 30 mm thick specimen was not heavily influenced by misalignment and the 40 mm thick specimen had the strain gauges mounted on the tension side.

The computed hot spot stresses for each thickness is illustrated in Figure 4.34, plotted up against the distance from the weld notch, i.e. the critical location. All three thicknesses were subjected to approximately 284 MPa axially loaded stress, around 80% of σ_y, shown as the nominal stress, σ_{nom}, in the figure. All specimens show an increase in stress in relation to the nominal stress as the measurement points approach the weld

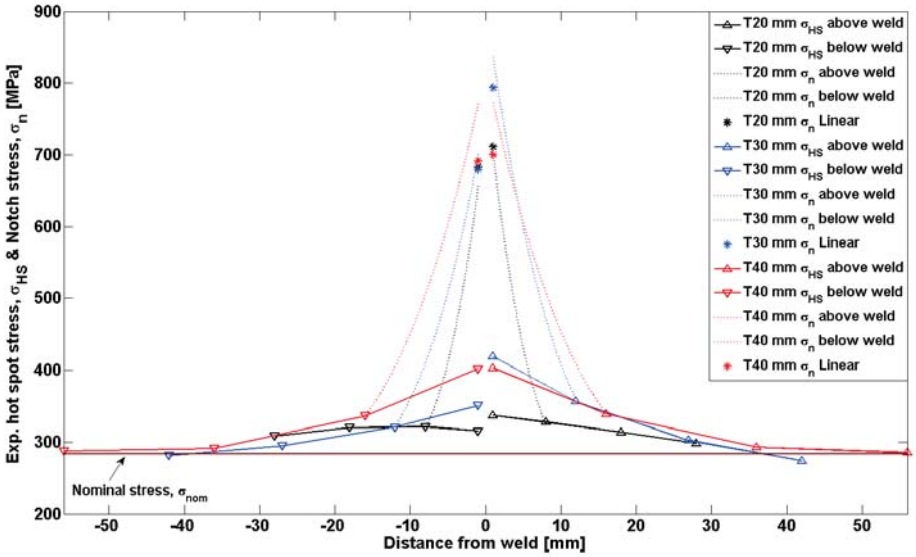

Figure 4.34: *Hot spot stress analysis along with an estimation of the notch stress as a function of the distance from weld*

notch. The measurements for the 20 mm thick specimen are showing an increase of stress compared to the nominal value, however there appears to be a minor relation to the reduced distance towards the weld and the values are similar from each gauge. The influence of the strain gauge grid size could be the influential factor here as it is recommended that the strain gauges do not exceed 0.2 times the thickness of the specimen. The strain gauges mounted on the 30 mm and 40 mm thick specimens show on the other hand a relatively large increase in stress as the measurement points approach the weld notch and the strains measured at the distance of 0.4 times the thickness of the specimen show an increase of $\Delta\sigma$ = 25.3% and $\Delta\sigma$ = 19.0 %. Applying the recommended equation to implement the measured strains in order to interpolate the stress at the hot spot, weld notch, results in stress increases of 18.7%, 47.2% and 41.6% for the 20 mm, 30 mm and 40 mm thick specimens respectively assuming the higher measured value.

Figure 4.34, also illustrates the location of the computed hot spot stresses, based on the nominal stress and the aforementioned computed bending stresses according to the misalignment measurements. As discussed in section 2.2.1, Iida and Uemure, [47], derived empirical expressions in order to determine the peak stress concentration factors for welded joints in relation to the weld reinforcement, or profile, parameters as well as

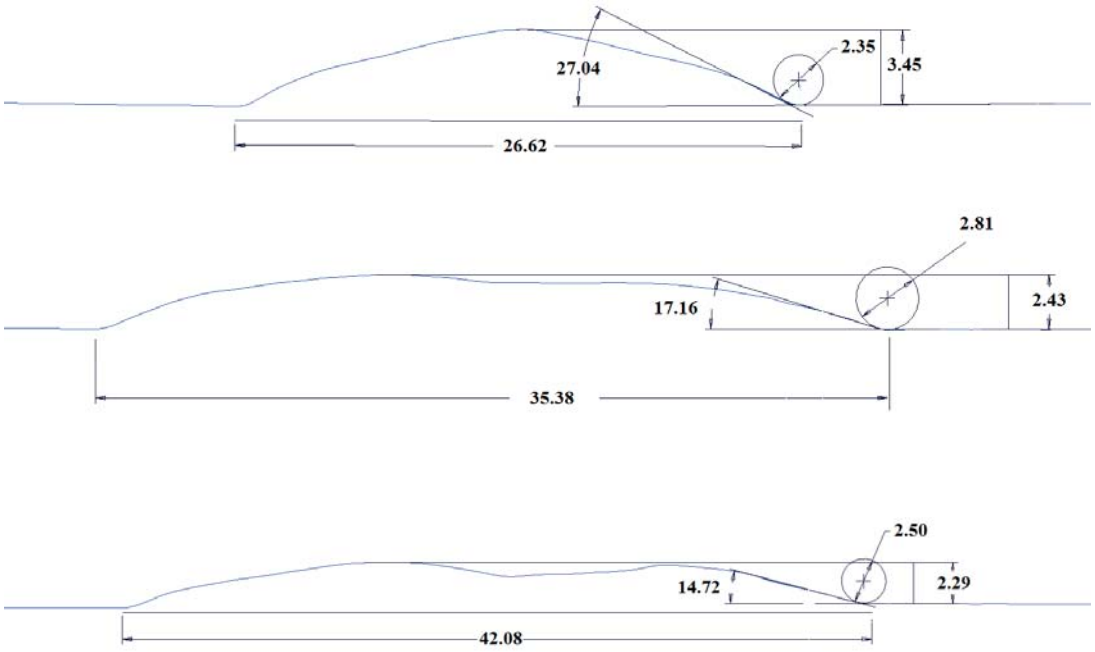

Figure 4.35: *Schematic illustration of the weld profiles and weld parameter measurements for the 20 mm, 30 mm and 40 mm thick specimens*

the notch radius. The equations are applied to compute the notch stress concentration factors, K_{t_HS}, for axial and bending loading conditions. The required parameters for each test specimen were estimated from the 3D model constructed by the DIC system, illustrated in Figure 4.35, for the 20 mm, 30 mm and 40 mm thick specimens. The 20 mm thick joint had by far the largest weld profile angle, which is detrimental to its fatigue strength. The weld profile angle thereafter reduces with respect to the specimen's thickness. The other critical factor is the weld notch or radius. The radius can be very cumbersome to estimate, thus the standards and guidelines recommend a notch radius of 1 mm which was applied in this study. The computed notch stress, σ_n, is illustrated as a peak point for each thickness at the weld notch in Figure 4.34.

Applying the same notch stress concentration factors, $K_{t\_ten\_HS}$ and $K_{t\_bend\_HS}$ for the hot spot strain results from the strain gauges an experimental peak stress, σ_{peak}, was derived at the weld notch, illustrated as a dotted line for each thickness above and below the weld in Figure 4.34. This assumes that the strain gauges are located at a

distance which is sufficient to avoid the influence of the non-linear stress singularity. The resulting hot spot stresses computed are significantly higher than the applied nominal stresses. These computed notch stresses have a stress concentration factor with respect to the nominal stress of K_t = 2.47, 2.94 and 2.72 for the 20 mm, 30 mm and 40 mm thick specimens respectively. This shows as expected due to a large weld profile angle that the 20 mm thick joint is more affected by the weld reinforcement parameters compared to the 30 mm and 40 mm thick joints, which gives an indication to the low fatigue resistance of the 20 mm thick joints from batch 2.

This page is intentionally left blank.

Chapter 5

Test Series 2 - *Corrosion fatigue resistance of large as-welded SAW joints in a circulating synthetic seawater environment with cathodic protection*

The second experimental test series, Test series 2, *"Fatigue strength of large submerged arc welded joints within a circulating synthetic seawater environment with cathodic protection"*, was performed in order to establish a practical foundation for experimental fatigue testing of large welded joints in a synthetic seawater environment. By doing this, valuable experience and knowledge is gained about ways to approach and pursue the topic to a further extent and implement even larger welded joints.

This type of test sequence therefore involves the combined effect of axially induced fatigue loading, along with the effects of the corrosive medium, where all factors of influence have to be accounted for and taken under consideration. There is a severe lack of experimental data relating to corrosion fatigue testing of larger scale submerged arc welded butt joints, i.e. thicknesses above 10 mm, and the detrimental effects of corrosion under cyclic axial loading. The majority of experimental data available has been performed on ideal, small scale specimens, i.e. specimens which have been machined

to fit perfectly into the test environment which might lead to overly optimistic results. The experimental testing concerns immersion tension-tension testing of welded joints within a corrosion environment with or without corrosion protection, not pre-immersed fatigue testing of welded joints which have been subjected to corrosion prior to testing in order to investigate the effects of the corrosion on the specimen's mechanical properties.

The test specifications entail the design, manufacturing and construction of a circulating controlled ASTM standardized synthetic seawater solution environment installed within the frame and capacity of a servo hydraulic testing machine. This process was performed in collaboration with Laufey Gunnþórsdóttir, a MSc. student at DTU Mechanical Engineering [12].

5.1 Background

The global energy consumption and demand is gradually increasing per year and correspondingly the global electricity generation follows. In 2014, an estimated 3% of the global electricity was generated from wind energy, demonstrating a 16.2% growth between years. Within Europe the installed wind power capacity in 2015 was 5.4% higher than the previous year, where 23.7% of the installed wind farms were offshore, demonstrating a more than 100% increase between years. The annual wind power installation within the European Union has been steadily growing over the past 15 years, from 3.2 GW in the year 2000 up to 12.8 GW in 2015. The year 2015 had more wind power installed compared to any other form of power generation and it has surpassed hydro as the third largest source of power generation within the European Union [101], [16].

This rapid growth of wind energy generation, especially from offshore installations, appears to continue and even increase in the coming years with Europe's target to source 20% of final energy consumption from renewables along with the additional regulations concerning reduction of global CO_2 emissions, this increase could become even greater. In the past 5 years, 21 out of the 25 largest, i.e. power capacity, installed offshore wind farms were made operational.

The offshore wind energy industry is addressing the increased demand from the global energy market by continuing growth and upscaling, i.e. developing larger, more efficient wind turbine structures with increased power production capacities further away from shore at deeper water depths.

In order to construct ever larger wind turbines offshore with increased power capacity gives rise to many demanding and complicated challenges. The overall size of the whole structure, i.e. foundation, transition piece and the wind turbine tower, has to be enlarged which demands an increase in required material use with the corresponding material cost. Larger structures become exceptionally problematic and labour intensive to manufacture, post treat and inspect, especially concerning welding and joining. Transportation and on site installation will additionally become more difficult. Additional major concerns relating to offshore wind farms are the limited and weather dependent access for inspection and maintenance. The hydrodynamic loads from currents and waves subjected to the structure with the possibility of extreme weather conditions and ice impact. The effects incorporated with the exposure of an aggressive salty environment, i.e. corrosion and marine life, which may reduce the fatigue resistance and the corresponding design class for the structure in addition to the reduction or complete removal of the fatigue threshold limit.

The standards, codes and guidelines all recommend the application of design S-N curves specially derived for the exposure of the structure to corrosive seawater environment, with or without cathodic protection. The recommended fatigue resistance is not consistent between the standards with a slope change recommended by some standards when considering joints with cathodic protection. Free corrosion has a limited section within the standards and is accounted for by IIW and API by reducing the recommended in-air S-N curves by a factor. DNV recommends using the seawater design S-N curves with cathodic protection for joints in the splash zone in addition to implementing a larger design fatigue factor. However, all recommendations omit the fatigue endurance limit for structures in seawater conditions [36], [7], [102], [95], [103].

Additional research and development is severely lacking but highly necessary in order to keep up with the offshore industry's growth [56]. Universities, research facilities as well as industry have been investing more time and funds on the topic in recent years as there is limited amount of literature and experimental data available concerning this multidisciplinary field of study. The fatigue behaviour of steels and welded joints within a corrosion environment is not scientifically nor practically complete as there are many unknowns still remaining in addition to contradictory and debatable published results.

5.2 Experimental design, setup and preparations

The following section describes the process of designing, constructing and making a functional corrosion environment for static and fatigue testing of large scale butt welded joints. The inspiration for the setup was based on previous fatigue testing within a corrosion environments found in literature [65], [104], however the number of articles and experimental test results were limited and severely lacking when concerning larger scale testing of as-welded steel butt joints.

In order to establish a operational corrosive testing environment the following objectives were highlighted:

- A suitable servo hydraulic testing machine.
- A practical mechanical design for specimen gripping.
- A large, spacious and water tight test cell in order to submerge the test specimen in corrosive medium.
- A pump in order to obtain a seawater circulation loop.
- A sufficient cooling system.
- Equipment in order to monitor temperature and pH values.
- Equipment to provide the specimen with an impressed current cathodic protection.

In addition the corrosion environment test facility had to provide open access for specimen change, maintenance and monitoring of the specimens subjected to testing.

5.2.1 Lab capacity

The corrosion fatigue testing was performed in a four column servo hydraulic testing machine, Kyung Do, ideally meant for bend testing of large specimens. The machine is equipped with an actuator installed on top with a loading capacity of 650 kN and a spacious 1500 mm x 2500 mm steel base. The spacious base area underneath the actuator was ideal for the implementation of the required parts for the corrosion environment. The testing machine along with the corrosion environment setup is illustrated in Figure 5.10.

5.2.2 Design of the corrosion environment

The following section will provide a detailed description of the design and construction of the corrosion environment. The definition of the problem involved multiple influencing and critical parameters, which needed to be accounted for in order to establish a functional facility for corrosion fatigue testing. Several concepts and ideas were considered prior to proceeding with the manufacturing of the required parts and the construction of the testing environment. Figure 5.3 illustrates the changes performed on the applied testing machine with the implementation of the corrosion environment.

The application of hydraulic grips was not feasible as the environment contains damaging aggressive medium. Thus, all scenarios concerning possible leaks had to be accounted for.

Test machine alterations

The test machine was not equipped with grips and no option for mounting a grip in the steel base. Thus, a concentric threaded hole pattern, 12 x M20, was drilled, with a magnetic drill, into the base plate. The hole pattern was aligned with the the center of the actuator on top.

Gripping mechanism

The gripping mechanism had to be able to provide enough clamping pressure to counteract the high tensional forces to ensure no slippage of the test specimen during static or fatigue axial loading.

The designed and manufactured pieces required for the gripping mechanism consisted of:

- A large base plate adapter piece.
- 2 x threaded grip stud pieces.
- 4 x grip-specimen clamping plates.
- 4 x rough surfaced wedge plates.

Furthermore, existing spiral washers and lock components with bolts were applied in the overall assembly. All items manufactured were of high strength, pre toughened steel, 2738 from Meusburger Georg GmbH & Co KG, with a strength of σ = 1080

MPa. The manufacturing of the designed pieces was performed by THK maskinfabrik. The assembly is illustrated in Figure 5.1.

An adapter piece was manufactured to fit the concentric hole pattern in the machine's base plate. The 12 x M20 holes, drilled through the piece had additional diameters of 2 mm relating to the bolt pattern in the base plate in order to accommodate and ensure the actuator's load trains' vertical alignment.

The two threaded stud pieces were designed to fit into the adapter piece in the base plate and the load cell connected to the actuator's piston from the top. Enough spacing was ensured in order to fit existing spiral washers in between for pre-tensioning of the mechanism. Additionally, the stud pieces were manufactured with a groove in order to fit and hold the clamping plates in place. Four clamping plates were manufactured in order construct a fork clamping scenario, where the specimen would be constrained in between. The clamping plates were designed with a centering hole in order to align and hold the manufactured wedges in place.

Specially designed wedges were manufactured with rough surfaces in order to increase friction and constrain the test specimen. The wedges were made from high strength, hot worked steel alloy susceptible to corrosion, 2343 ESU from Meusburger Georg GmbH & Co KG, with a strength, σ = 780 MPa. The wedges were additionally heat treated by Bodycote Varmebehandling A/S in order to increase hardness and nitrided to enhance wear resistance and durability. The wedges were designed with a hole in the center in order to align them with the clamping plates.

Existing lock components, consisting of eight thick high strength steel blocks with drilled holes in the opposing ends and eight long steel bolts with end threading were applied in the overall assembly. The eight blocks go on opposite sides of the manufactured clamping plates with the steel bolts going through the holes and nuts on all ends fixing the components together.

A hydraulic hand pump along with a pre-tensioning unit was applied in order to provide the required clamping pressure. The device encompasses the threaded bolts on both sides with the nuts screwed on and pulls the bolt as the pressure is manually increased by pumping. When the desired pressure is reached the nuts are tightened and the pressure is released.

For additional friction, the grip plates were sandblasted and a thin coating of silicon carbide, SiC, was applied to the surfaces.

To sum up, description of the procedure relating to the mechanical gripping mechanism's assembly: 1) The adapter piece was bolted and pre-tensioned into the machine's

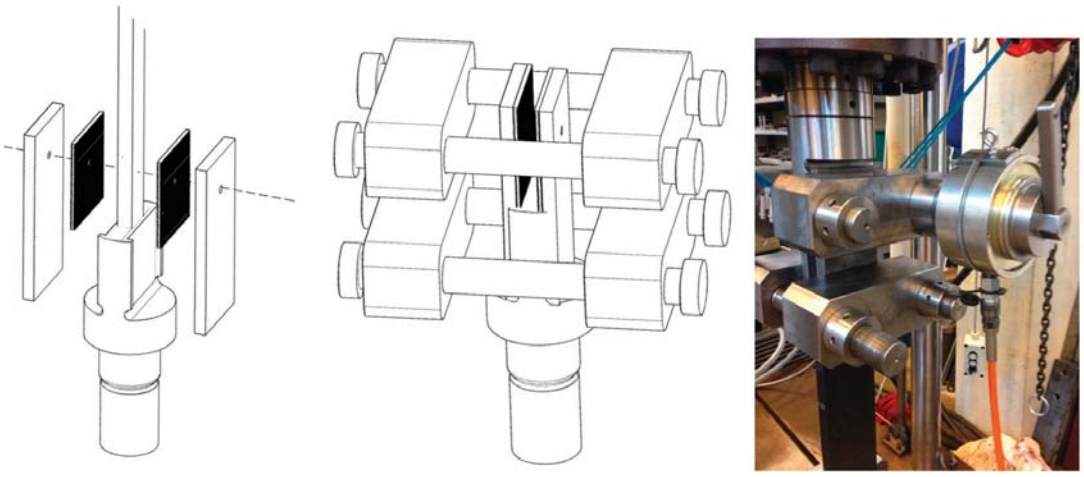

Figure 5.1: *Corrosive environment grip mechanism [12]*

base plate. 2) The two threaded stud pieces were inserted into the adapter piece and load cell with spiral washer in between for pre-tensioning. 3) the clamping plates were positioned into the machined groove in the stud pieces. 4) The wedges were inserted and aligned with the clamping plates with a pin which fitted through the wedge into the clamping plates. 5) The specimen was inserted in between the rough surfaces of the wedges. 6) The lock components were assembled on both sides to clamp the fixture together. 7) The hydraulic pump and pre-tension unit were applied in order to provide the necessary clamping pressure and released once the desired pressure level was reached.

Test cell

Fully immersed corrosion fatigue testing requires the test cell to encompass the whole area of the test specimens which is of the highest interest, i.e. the welded region. The test cell was manufactured by Brønnum Plast A/S out of Plexiglass, which is an ideal solution as it allows monitoring of the specimen during testing, it is durable, corrosion resistant and wards off unwanted galvanic coupling.

The test cell consisted of three pieces of Plexiglass along with a rubber O-ring. The cylindrical test cell was 200 mm in height, with an outer diameter of 200 mm and a wall thickness was 10 mm. This allows the tank to contain roughly five L of seawater and the cylindrical geometry removes glued connections. A 20 mm thick Plexiglass

Figure 5.2: *Cooling system for the corrosion environment, [12]*

round ring plate with outer and inner diameter of 260 mm and 180 mm respectively was glued directly to the test cell. It contained a groove for an O-ring and a circular hole pattern with eight holes. An additional external bottom plate was manufactured with the same diameter and thickness as the glued bottom ring, containing the same circular hole pattern as well as a 22 mm x 42 mm cut section in the center in order to fit the specimen through. The additional 1 mm gap around the specimen was filled up with elastic water resistant silicone. This plate also contained a threaded hole for a drain pipe. The two pieces can thus be assembled by bolts where the O-ring is squeezed in between to block potential leakage.

A PVC drain pipe was applied in order to maintain the water level at the desired height during testing as well as drain the cell after testing. The drain pipe consisted of a main drain opening at the top and smaller drain holes in the bottom and it was assembled to the bottom plate of the test cell.

Cooling system

The corrosion environment was implemented with a 2kW capacity cooling system in order to achieve desired temperature levels of the seawater. Thybo Køleteknik A/S was hired for the detailed design and construction of the cooling system. The system itself had a 20 L reservoir tank. Capacity to cool the seawater down to 2°C, with a stainless steel cooling coil as well as a thermal tube for the control unit. Contained refrigerant

Figure 5.3: *Corrosion environment test facility before and after construction*

R134a. It was equipped with a fan cooled condenser and an oil circulating compressor. The system was well isolated and had an external control unit with a digital display. The cooling system is illustrated in Figure 5.2.

Corrosive medium circulation loop

The corrosion environment's water circulation loop from the cooling system's reservoir tank to the test cell is connected with ordinary hoses to PVC plastic piping units. The circulation loop was driven by a Grundfos Alpha2 pump which is used for applications with low flow rates. A string regulation valve was applied to regulate the flow from the pump. Two ball valves were inserted in order to isolate the flow from the cooling system to the pump and the other towards the test cell. A check valve was used to maintain the flow in one direction.

The circulation loop ran through a T-union with an implemented pH sensor which displays continuous readings of pH values and temperature on a digital display.

An ultraviolet, UV, disinfection system was implemented in order to prevent the accumulation of undesired bacteria, without effecting the composition of the synthetic

seawater solution.

A net filter was additionally placed within the reservoir tank in order to avoid large particles coming from the test cell from entering the circulation loop.

Cathodic protection

Impressed current cathodic protection was implemented into the corrosion environment's circulation loop. The complete circuit consisted of an external DC power source in order to provide the cathodic polarization of the specimen being tested. Cylindrical platinised titanium net, working as a non consumable anode and thus in principle does not require a replacement throughout the entire test series procedure. Additionally, the corrosive medium, i.e. the seawater, and the specimen itself, which is to be protected, are vital parts of the setup in order to complete the circuit.

To achieve the cathodic protection, the titanium net, i.e. impressed current electrode, and the specimen have to be in both electrolytic and electronic contact. The power source provides a positive current to the impressed current electrode which goes through the corrosive seawater medium and onto the test specimen. Thus, the potential of the specimen is lowered and it becomes cathodically polarized. The positive current thereafter returns to the power source through the circuit.

The voltage applied was approximately 2.5 V, which resulted in an approximate -1.22 V potential at the cathode measured against a SCE electrode, which corresponds to -0.98 V against a SHE reference electrode. The recommended potential accepted as a design protective potential for low-alloy steels lies between -0.80 V and -0.90 V, depending on the environment, to provide sufficient protection, according to DNV [57]. Thus, the specimen's potential during testing was slightly more negative than the recommendation, within the immune region of iron.

ASTM synthetic seawater

ASTM standardized substitute seawater, according to [105], was applied as the corrosive medium for the corrosion fatigue testing in this test series. The standard covers the medium preparation which contains inorganic salts in proportions and concentrations in order to serve as synthetic seawater.

The chemical composition of the substitute seawater is listed in Table 5.1.

5.2.3 Validation of the test facility

The test machine and the corrosion environment required validation and verification prior to testing. In order to align the machine's load train with the manufactured adapter piece in the base plate, a centerless ground solid cylindrical bar with low tolerances was applied. The bar was manufactured with threads to fit the upper load cell as well as the adapter piece. With the bar screwed in at both ends the actuator's piston was lowered until it touch the steel base, thereafter the adapter piece was bolted tight.

The machine's load cell was calibrated and verified against a 900 kN interface reference load cell, with a maximum percentage error of 0.541 %.

The gripping mechanism was tested up to a maximum of 500 kN load, with a clamped high strength steel beam, where the spiral washers were tightened.

Several leak tests were performed for all pieces involved in the circulation loop in order to make sure that the aggressive synthetic seawater did not leak. Special care was ensured for the lower gripping mechanism as it was directly underneath the test cell.

Table 5.1: *ASTM substitute ocean water, chemical composition*

Test series 2 - substitute ocean water			
Element	Concentration [g/L]	Element	Concentration [g/L]
$NaCl$	2.453E+01	$SrCl_2$	2.500E-02
$MgCl_2$	5.200E+01	NaF	3.000E-03
Na_2SO_4	4.090E+00	$Ba(NO_3)_2$	9.400E-05
$CaCl_2$	1.160E+00	$Mn(NO_2)_2$	3.400E-05
KCl	6.950E-01	$Cu(NO_3)_2$	3.080E-05
$NaHCO_3$	2.010E-01	$Zn(NO_3)_2$	9.600E-06
KBr	1.010E-01	$Pb(NO_3)_2$	6.600E-06
H_3BO_3	2.700E-02	$AgNO_3$	4.900E-07

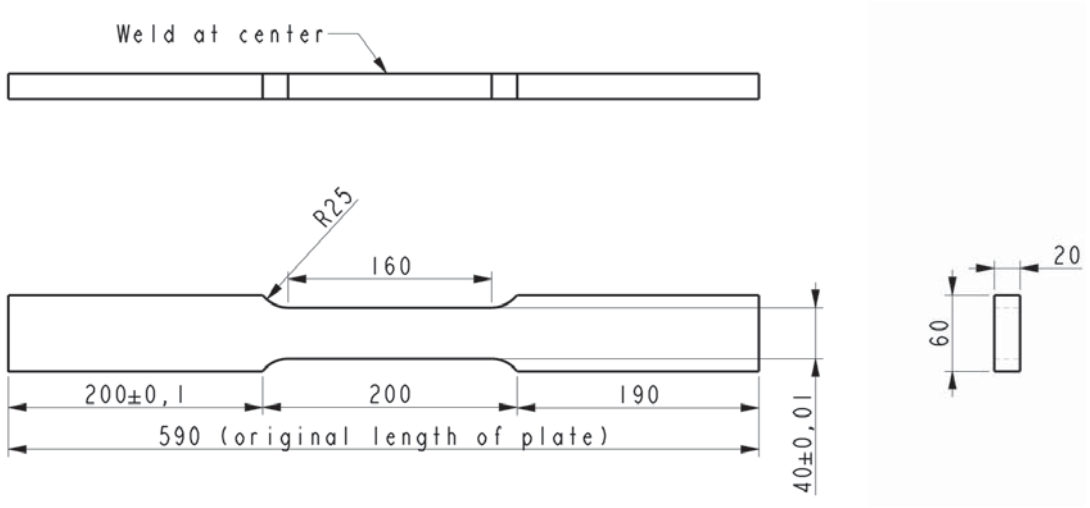

Figure 5.4: *Corrosion environment, specimen dimensions*

5.2.4 Test specimen preparation

The applied test specimens were made out of S355 J2 + N steel and submerged arc welded. The welded plate, noted batch 2, was manufactured along with the test specimens described in Chapter 4, section 4.2.3 where information about the material and mechanical properties of the test specimen is listed in Tables 4.3 and 4.4 respectively. The test specimens dimensions for the fatigue test series are illustrated in Figure 5.4, where the length of the specimens gripping area was increased to fit into the corrosion environment gripping mechanism.

Welding procedure

A description concerning the SAW procedure is found in section 4.2.4 and in Table 4.6.

Non destructive testing

All the applied test specimens passed NDT inspection and were accepted to all specifications. The procedure is discussed in detail in section 4.2.5.

Misalignment measurements

The test specimens were subjected to misalignment measurements in order to obtain the axial, e, and angular, α, misalignments. This is described in detail in section 4.2.7 and an illustration of the overall specimen misalignments for this test series is presented in Figure 4.16.

5.3 Experimental testing

The following section accounts for all the experimental testing performed that relates to the this test series of 20 mm thick SAW butt joints within the circulating corrosion environment with standardized synthetic seawater medium.

5.3.1 Static Testing

As previously mentioned, the test specimens applied in this test series were manufactured, cut and misalignment measured along with the test specimens applied in test series 1, Chapter 4. The static testing was also done simultaneously and the results from the static testing for the specimens applied in this test series, 20 mm thick SAW butt joints, batch 2, are presented in section 4.3.1 and listed in Table 4.9.

The computed average yield strength, $\bar{\sigma}_y$, from the static testing was applied in determining the required load ranges for the subsequent fatigue testing.

5.3.2 Corrosion testing

Prior to implementing the cathodic protection to the corrosion environment a few investigative corrosion tests were performed on butt welded SAW specimens from the same batch, in order to assess the electrochemical process relating to the corrosion of the SAW butt joints in addition to verifying the effectiveness of the impressed current cathodic protection.

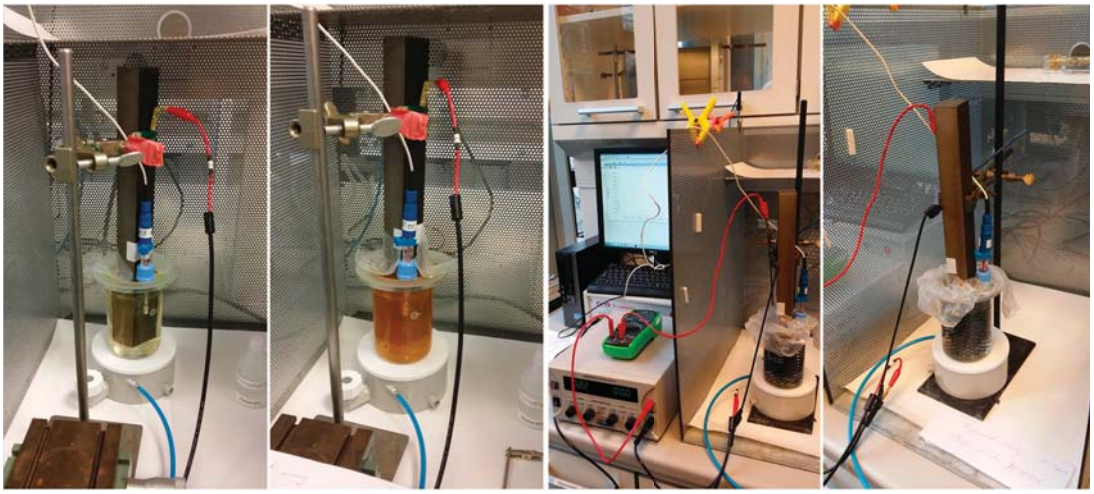

Figure 5.5: *Corrosion environment trial testing*

Corrosion gel testing

The corrosion of metal within a corrosion environment is an electrochemical process. This comprises of an electrolytic and electronic conductors, e.g. seawater and steel joint and the anodic and cathodic formation.

An accelerated gel corrosion test was performed in order to visualize the corrosion reactions involved when submerging the butt welded joint in a corrosive seawater solution. The gel, working as an electrolytic conductor, consisted of agar powder, an universal pH indicator and the ASTM seawater solution. The universal pH indicator turns blue in the presence of iron, Fe^{2+}, ions and red in the presence of hydroxide, OH^{-}, ions.

A thin layer of gel was applied over the enclosed welded joint's surface and special care was ensured of limiting the oxygen access coming under the gel from edges. This test is very rapid and the corrosion reactions were identified within a couple of hours.

Impressed current cathodic protection

Trial testing of the impressed current cathodic protection, ICCP, was performed prior to installing the corrosion protection technique and corresponding setup into the corrosion environment. Two SAW butt joints were placed in the same ASTM standardized

seawater solution and their respective potential change was measured against a reference SHE electrode. The one specimen was allowed to corrode freely, while the other specimen was subjected to impressed current of 2.2 V magnitude. The two test glass containers were additionally covered with plastic to limit the access of oxygen. The two tests were left untouched over a period of 3 days. Figure 5.5 illustrates the two tests, where the two subfigures on the left illustrate the non protected specimen and the two subfigures on the right illustrate the cathodically protected specimen.

5.3.3 Fatigue testing

Axially loaded tension-tension fatigue testing was performed in the constructed and verified corrosion environment, located in building 119 at the Technical University of Denmark, DTU. All tests were carried out in laboratory air conditions at room temperature, $+20^{\circ}$.

20 mm thick SAW butt joints were subjected to fatigue loading in the as-welded condition, i.e. no post weld treatment was applied. All test specimens were positioned within the corrosion environment's test cell with the welded region completely submerged throughout the entire span of the test. The synthetic seawater medium was maintained at 10°C by the cooling unit. The pH level was approximately between 7.5 to 8.0 at the start of every fatigue test. The seawater solution was changed if needed, and an average of 2 specimens were tested per 15 L of seawater. A galvanic tape was applied in the region of the splash zone in order to shield the specimen from the significant drop in pH resulting from gas formation.

The impressed current cathodic protection was driven by a 2.5 V signal from the power source, resulting in a lowered potential of the steel welded joint, measured to be -1.22 V against a SCE. This according to the Pourbaix diagram positions the specimen within the immune region, i.e. the specimen should not be subjected to corrosion.

All test specimens were subjected to a constant amplitude sinusoidal waveform at a frequency of 8 Hz. The cyclic loading was performed at a stress ratio of R = 0.5, with stress levels computed as a percentage of the specimens average yield strength, $\bar{\sigma}_y$. The stress ratio of R = 0.5 was maintained constant throughout the test sequence in order to achieve a direct comparison to 20 mm thick SAW butt joints from the same batch tested under in-air conditions. These specimens were additionally applied in test series 1, Chapter 4.

Five different stress levels were tested with at least three specimens tested per load level, except for the lowest load level, $\Delta\sigma = 0.6 * \sigma_y$, due to a shortage of specimens.

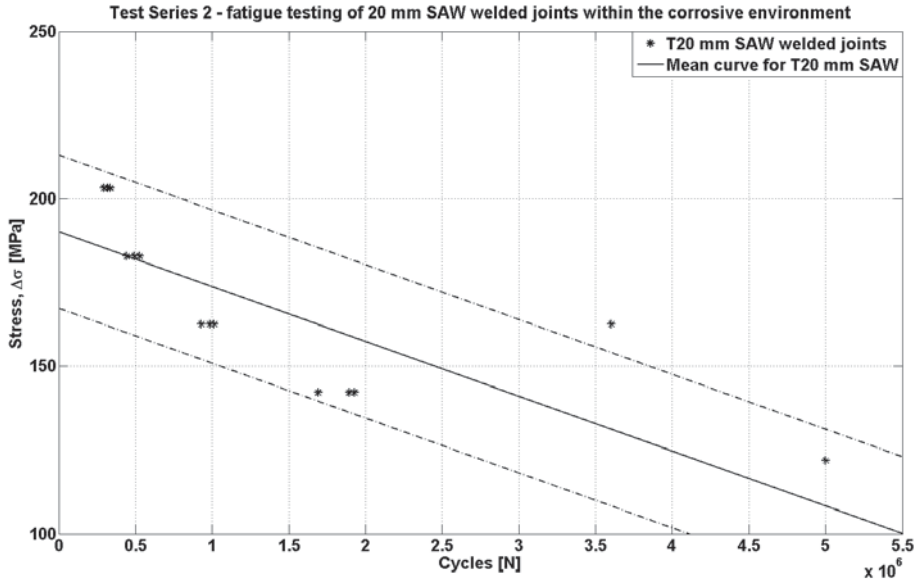

Figure 5.6: *Fatigue results for the 20 mm thick SAW butt welded joints tested within the corrosion environment. Stress range* $\Delta\sigma$ *as a function of cycles to failure, N*

The maximum applied stress, σ_{max}, equalled 100% of the average yield strength of the SAW butt joints while the minimum stress applied, σ_{min}, equalled 60% of the respective average yield strength. The definition of failure in all fatigue tests was complete rupture.

All relevant test data applied in the post processing was acquired from the SHM's controller.

The fatigue test sequence within the corrosion environment started with performing tests at 80% of the yield strength, $\Delta\sigma = 0.8 * \sigma_y$, with the corresponding maximum and minimum applied loads of 256.7 kN and 128.3 kN. The subsequent stress levels were reduced in order to reach the fatigue threshold stress level, i.e. an endurance limit for the test series. Thereafter, the stress level was increased with respect to the average yield strength for short cycle, high stress level results in order to derive an experimental S-N curve for the test series. The results from the fatigue testing are illustrated in Figure 5.6.

Figure 5.6 illustrates the fatigue strength of the 20 mm thick SAW butt joints tested within the corrosion environment as a function of cycles to failure, N. The figure additionally shows the mean $\pm$ two standard deviation from the whole test population,

excluding the run-outs.

5.4 Experimental test results

This section will analyse the relevant results from the 20 mm thick SAW butt joints tested within the corrosion environment with a circulating ASTM standardized seawater medium.

5.4.1 Static testing

The static testing was performed in conjunction with the static test specimens from test series 1, Chapter 4. The results from the static testing is presented in Table 4.9. The main findings is the average computed yield strength of the specimens and for the 20 mm thick SAW butt joints from batch 2, $\bar{\sigma}_y$ = 406.4 MPa.

5.4.2 Corrosion testing

The results from the two corrosion trial tests, accelerated corrosion gel test and trial impressed current cathodic protection testing are described below.

Corrosion gel testing

The accelerated corrosion gel testing demonstrated the electrochemical anodic and cathodic reactions of the SAW butt joint. The formation of anodes and cathodes depended on the availability of oxygen in the different regions of the welded joint and the cathode will form where there is more oxygen available. Figure 5.7, illustrates the gel test method. First the bare specimen was covered with the agar gel mixture. One hour after applying the gel, the cathode became visible with the corresponding reactions as local red regions in the weld. Four hours after application, the chemical reactions were apparent and the anode, i.e. the base material, demonstrated a dominant blue color, as there were iron, Fe^{2+}, ions being dissolved in an oxidation reaction, while the weld is shown as being cathodic, i.e. reduction reaction. This could give some indication of a potential difference and thus a galvanic corrosion between the base and weld metal, i.e. the weld being less corrosive.

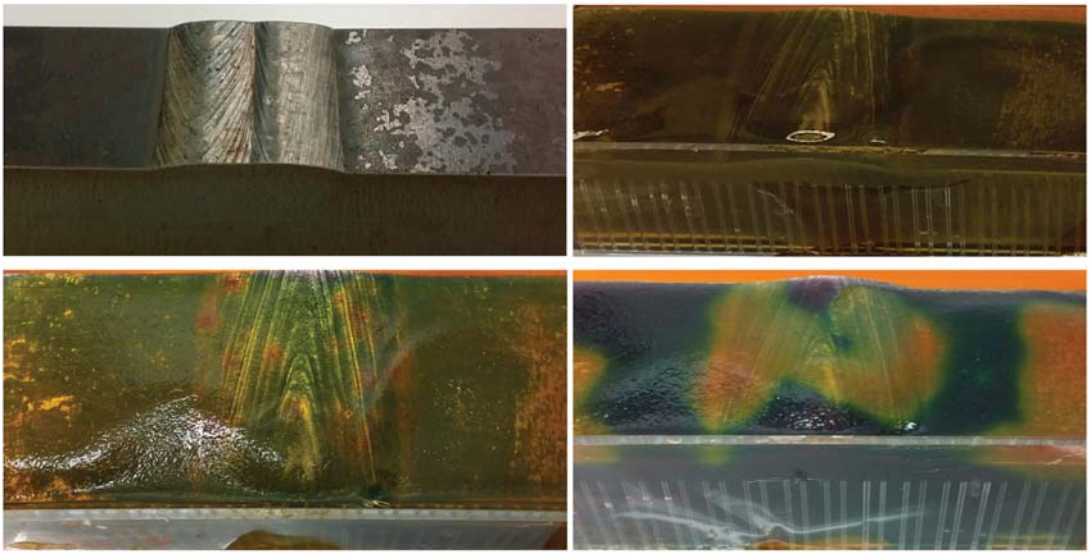

Figure 5.7: *Accelerated corrosion test of butt welded joint with agar gel*

Impressed current cathodic protection

The trial case with the impressed current cathodic protection was performed in order to gain knowledge and experience with the technique as well as verify that the SAW butt joint would be protected within the ASTM seawater solution. The test specimen subjected to free corrosion started already within the first day to corrode and the surrounding solution became opaque and brown-reddish coloured. However, the test specimen with the ICCP did not show signs of corrosion and the solution remained transparent. Additionally, concerning the test specimen subjected to ICCP a noticeable gas formation was observed, indicating the decomposing aqueous environment forming hydrogen gas.

Figure 5.8 illustrates the results from the potential measurements, where the SAW butt joints change in potential is shown on the y-axis with respect to time. Figure 5.8 (right) illustrates the free corrosion test specimen where the initial potential drop is rapid due to the dissolution of iron ions, Fe^{2+}, then the rapid decrease reduces as a result of oxide and/or the formation of corrosion product layers on the specimens surface at roughly -700 mV. However, for the ICCP specimen there is a sudden drop in the beginning as the specimen's potential is severely lowered by the cathodic protection. The ICCP is supplying the specimen's surface with additional electrons and thus speeding up the cathodic reaction and hindering the anodic reaction, thus slowing down the dissolution

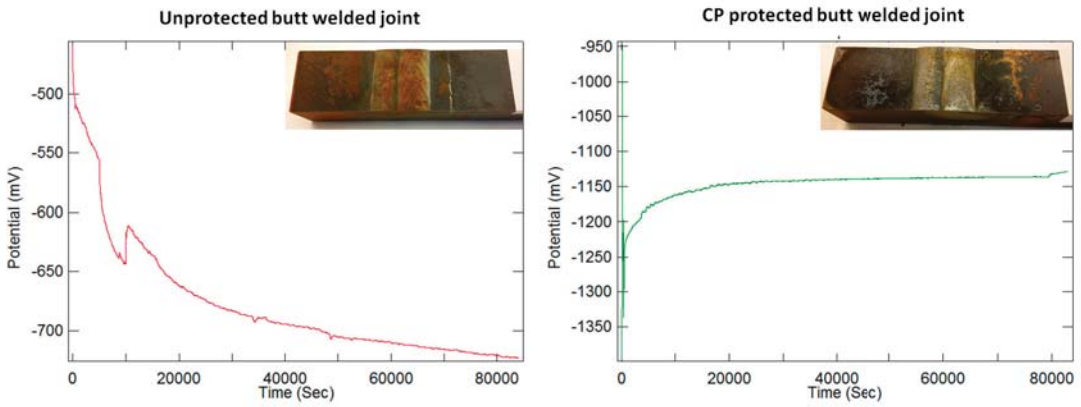

Figure 5.8: *Change of the open circuit potential with time for a SAW butt joint with and without cathodic protection*

of the metal and protecting the specimen. This is illustrated in Figure 5.8 (right), where the specimens potential is kept almost constant at -1140 mV, within the immune region for iron, by the introduction of electrons from the power source.

The pH level of both ASTM seawater solution were estimated after testing with a pH universal indicator stip, which resulted in a pH level between 3 and 4 for the free corrosion solution while the ICCP solution demonstrated a pH between 7 and 8, i.e. the effect of the ICCP and the specimen was minuscule.

5.4.3 Fatigue testing

Figure 5.6 illustrates the experimental fatigue test results from test series 2. The results are displayed in the form of stress range, $\Delta\sigma$, against the number of cycles to failure. From the figure it is demonstrated that all specimens tested within the corrosion environment lie within the $\pm$ two standard deviation of the mean for the whole population, excluding the run-outs at 5 million cycles. Figure 5.10 gives an illustration of the testing machine with the implementation of the corrosion environment where a specimen has been clamped in the lower grip.

Figure 5.9 illustrates the test results from the fatigue testing within the corrosion environment when compared to the fatigue testing of the same 20 mm thick SAW butt joints tested under in-air conditions on a loglog plot. The respective mean curves for the two different test environments are additionally added to the figure along with the

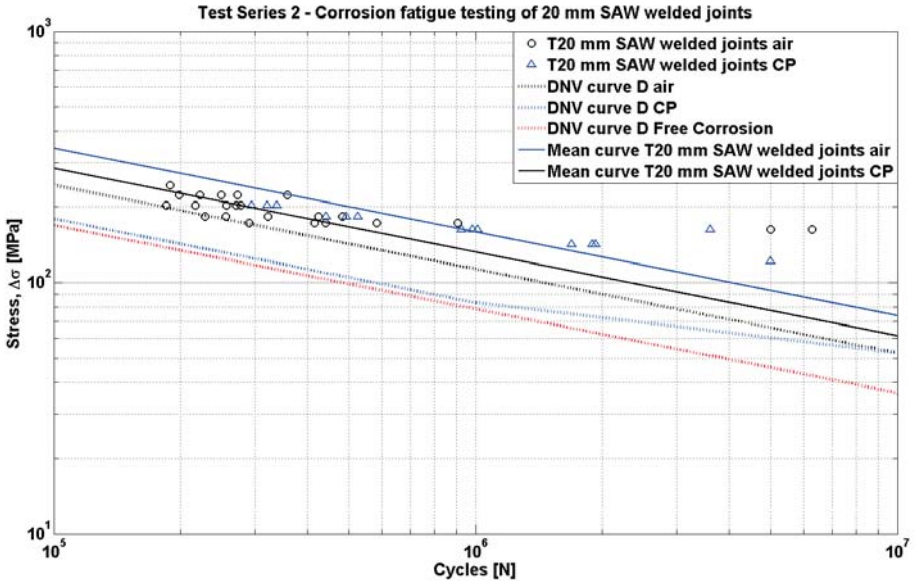

Figure 5.9: *S-N plot showing the fatigue resistance of the 20 mm thick SAW butt joints in the corrosion environment as well as under in-air conditions against the recommended DNV design curves D with respect to testing environments*

DNV recommended designs curves, curve D for butt welded joints under in-air conditions, curve D for butt welded joints with cathodic protection and lastly a curve D for free corrosion.

Figure 5.9 shows that the average fatigue resistance of the 20 mm thick SAW butt joints tested in the corrosion environment is slightly higher than the compared average fatigue resistance of the same joints tested under in-air conditions. This slight increase is however in the range of the overall scatter from the fatigue results. Ideally, there should not be any expected change between the two if the cathodic protection is working efficiently but another more important aspect is that corrosion is a time dependent process and the applied high test frequency, i.e. 8 Hz, of the fatigue tests performed within the corrosion environment is roughly 40 times higher than expected load frequency of ocean waves. Thus, the test series is not representing the expected corrosion process relating to offshore structures and the corresponding wave loading. Instead the test series is comparing the influences of the testing environment.

For this test series, the longest runtime for a single fatigue test specimen within the corrosion environment was roughly seven days and five hours, while the shortest run-

Figure 5.10: *Corrosive environment test setup*

time was roughly ten hours. Thus the high stress range, short cycle tests are not heavily affected by any corrosion reactions, while on the contrary an effect should be observed for the low stress, high cycle tests. As the previously described corrosion trial testing indicated, a specimen subjected to free corrosion was already forming an iron oxide layers within the first day when submerged in the ASTM standardized synthetic seawater solution.

Figure 5.9 shows that the high cycle fatigue test results from the corrosion environment are fracturing at stress ranges below the established fatigue threshold level from the fatigue tests performed under in-air conditions. The fatigue threshold limit for the tests performed under in-air conditions was established at 80% of the average computed yield strength of the manufactured welded batch, i.e. $\Delta\sigma$ = 162.56 kN, with five specimens running out at 5 million cycles and one of those ran up to 6.3 million cycles without failure or noticeable cracks. The fatigue tests performed within the corrosion environment all fractured at 80% of the respective static yield strength with an average cycle count of, N = 1.632.135 cycles. Additionally, all specimens tested in the corrosion environment at 70% of the respective static yield strength fractured with an average cycle count of, N = 1.837.378 cycles. The fatigue threshold for the tests performed within the corrosion environment was reached at 60% of the respective

static yield strength with 2 specimens running out at 5.000.000 cycles without failure and without any visual indication of cracks. Thus, indicating that the specimens tested within the corrosion environment were subjected to stress corrosion cracking, by the lowering of the fatigue threshold level, i.e. the endurance limit.

5.11 illustrates the ICCP circuit applied in the corrosion environment fatigue testing.

Figure 5.9 additionally illustrates the recommended design S-N curves according to DNV for as-welded butt joints, IIW does not have specific recommended design S-N curves for corrosion environments available. The three curves added to the figure are recommended design S-N curves for tests under in-air conditions, with cathodic protection and lastly with free corrosion, from top to bottom respectively. The figure illustrates the significant influence of the corrosion environment. The recommended fatigue strength at 2 million cycles according to the in-air design curve D is, $\Delta\sigma$ = 90 MPa. However, considering the same defined structural detail, i.e. butt joints, within a corrosion environment with cathodic protection, the reduction of recommended fatigue strength is reduced to 72.61 MPa, or almost 20% reduction. Furthermore when considering free corrosion the fatigue strength at 2 million cycles results to 62.42 MPa.

The resulting fatigue strength from the fatigue tested specimens within the corrosion environment at 2 million cycles was 126.67 MPa with a characteristic fatigue strength of 89.96 MPa, i.e. the lower half of the $\pm$ two standard deviation scatter band, coincides with the recommended design S-N curve D. The corresponding values for the test specimens under in-air conditions was 105.32 MPa and 68.36 MPa respectively at 2 million cycles.

5.4.4 Test analysis

Secondary bending under axial loading

The presented fatigue data measurements from the 20 mm thick SAW butt joints test within the corrosion environment are based on the respective test machine's controller readings from a verified load cell mounted in the SHM. The resulting acquired stresses are calculated from the applied load range, ΔF [kN], and the specimens cross sectional area [mm^2], which corresponds to the nominal stress, σ_{nom}, for the welded detail, not taking into account the stresses induced by secondary bending as a result of global geometrical misalignment of the specimens.

Applying equations 2.19, 2.25, and 2.26 a stress magnification factor, K_m, for axial

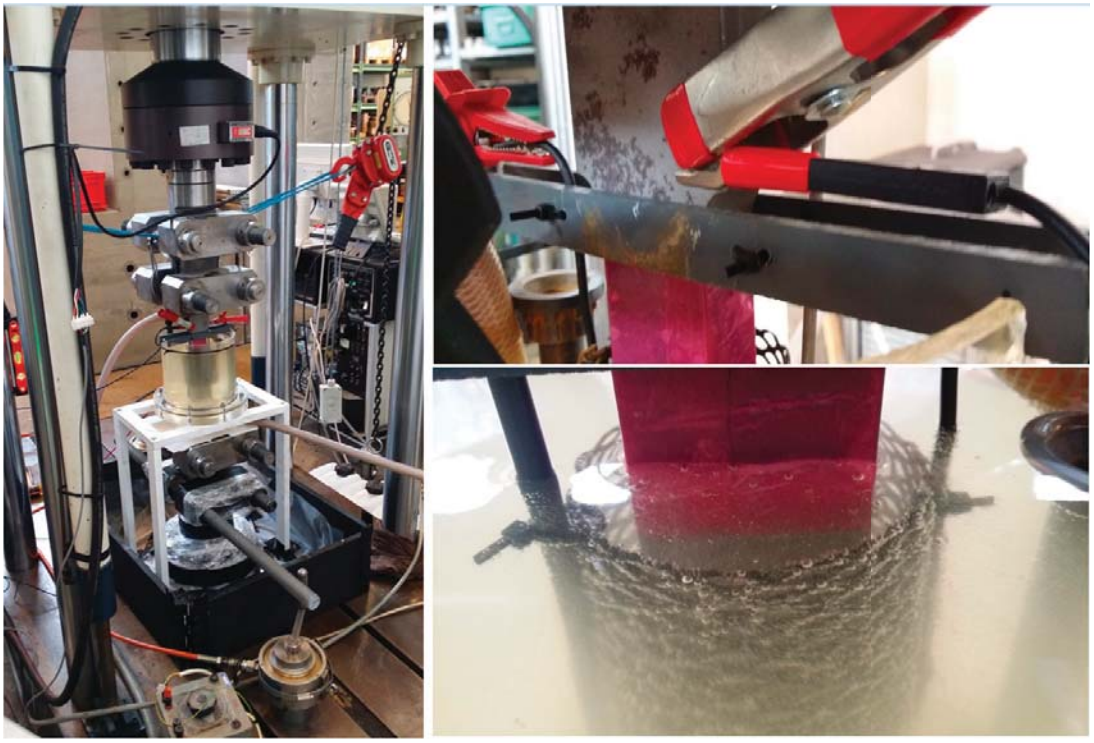

Figure 5.11: *Corrosive environment test setup, impressed current cathodic protection*

and angular misalignment can be derived and subsequently the bending stress can be computed at the critical location, i.e. at the welded region. The stress magnification factors are computed separately and used in conjunction with the measured nominal stress to derive a modified nominal stress, σ_{nom_mod}, for the joints. Thus, the secondary bending stress introduced by the joint's geometrical misalignment under axial loading is taken into consideration.

Figure 5.12 illustrates the increase in stress due to the secondary bending under axial loading derived by the application of the computed axial and angular magnification factors for each of the respective 20 mm thick SAW butt joints fatigue tested in the corrosion environment.

Table 5.2 lists the computed average axial, $\bar{e}$, and angular, $\bar{\alpha}$, misalignments derived from the measurement coordinate machine's values for the 20 mm thick SAW butt joints. Additionally, the average stress magnification factors for angular and axial misalignment, $\bar{K}_{ang\_m}$ and $\bar{K}_{ax\_m}$ are presented along with the combined stress magnification factor, $\bar{K}_m$ and the maximum and minimum computed values for the test

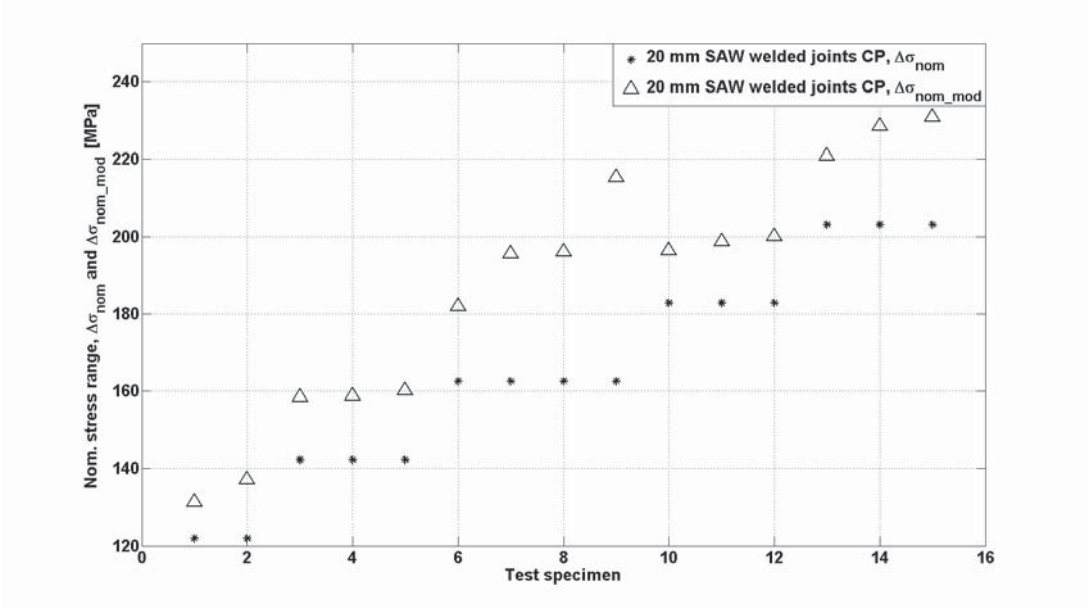

Figure 5.12: *Influence of the secondary bending stresses under axial loading, computed modified nominal stress* σ_{nom_mod}

series.

Table 5.2 shows that the measured misalignments were rather significant for the test specimens and the maximum induced secondary bending stress range under axial loading was computed to be $\Delta\sigma_{bend\_max}$ = 52.8 MPa. The average computed secondary bending stress range due to global geometrical misalignments equalled, $\Delta\bar{\sigma}_{bend}$ = 22.10 MPa.

Table 5.2: *Stress magnification factors due to misalignment under axial loading*

Test Series 2 - 20 mm thick SAW butt welded joints.							
Plate #	$\bar{\alpha}$ [deg]	$\bar{e}$ [mm]	$\bar{K}_{ang\_m}$	$\bar{K}_{ax\_m}$	Combined, $\bar{K_m}$	Max. K_m	Min. K_m
T20 SAW - CP	0.3988	0.1751	1.1078	1.0265	1.1344	1.3248	1.0738

Hydrogen evolution

The fatigue testing of 20 mm thick SAW butt joints within the corrosion environment, with impressed current cathodic protection, demonstrated a noticeable amount of gas formation during the span of each test.

The corrosion of iron, Fe^{2+}, within a corrosion environment with access to air can be written:

$$2Fe + O_2 + 2H_2O \rightarrow 2Fe(OH)_2 \tag{5.1}$$

The resulting corrosion product, i.e. the ferrous hydroxide, is usually oxidized further to magnetite (Fe_3O4) or to hydrated ferric oxide ($FeOOH$), also known as rust.

When considering the related half reactions separately, yields:

$$\begin{aligned} 2Fe &\rightarrow 2Fe^{2+} + 4e^- \\ O_2 + 2H_2O + 4e^- &\rightarrow 4OH^- \end{aligned} \tag{5.2}$$

As mentioned previously the anodic reaction, i.e. the consumption of the metal and the release of electrons, can be inhibited by introducing additional electrons to the specimen's surface and if sufficient amount of electrons are supplied the rate of dissolution ceases completely.

The introduction of the additional electrons by the application of the cathodic protection becomes important when dealing with steel, especially when considering the evolution of hydrogen. The electrolyte, in this case ASTM seawater, is able to act as a cathodic reactant and thus enabling the formation of molecular hydrogen according to:

$$2H_2O + 2e^- \rightleftharpoons H_2 + 2OH^- \tag{5.3}$$

This reaction is thermodynamically possible, however in practice it is barely significant as the reduction of oxygen is both thermodynamically favoured and kinetically easier. However, in the process of lowering the specimens potential into the immune region in order to achieve cathodic protection, the current supplied from the power source must be sufficient in order to sustain the cathodic reactions, i.e. both the oxygen reduction and hydrogen evolution. Thus, by lowering the potential of the specimen far below the electrode potential, E, of where the rate of the anodic reaction is zero, $E_a = 0$, could result in an increased current and bolster the hydrogen evolution. Furthermore,

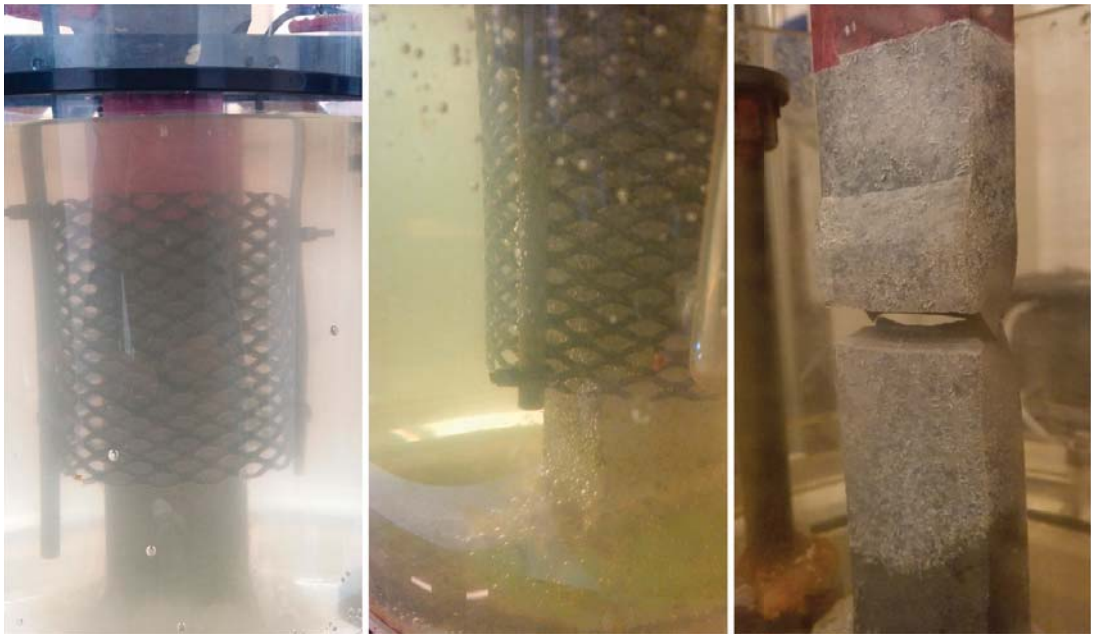

Figure 5.13: *Calcareous coating formation on the corrosion fatigue specimens*

applying a non consumable ICCP, such as platinized titanium in this test series, sustains an anodic reaction which decomposes the electrolyte, i.e. ASTM seawater, rather than dissolving the anode's metal with the possible reaction [10]:

$$2H_2O \rightarrow O_2 + 4H^+ + e^- \tag{5.4}$$

This process is capable of operating at high current densities without damaging the anode, but correspondingly it will produce high levels of acidity and increase the formation of gas.

By lowering the potential of the specimen, the oxygen reduction reaction, eq. 5.2 reaction is overtaken by the dissociation of the ASTM seawater and the evolution of hydrogen gas, H_2, according to eq. 5.3 [106]:

The effects of the hydrogen evolution by applying the ICCP can be detrimental to the specimens being tested and more significantly if the potential is lowered far below the, E_a, i.e. causing the specimen to be overprotected. The small hydrogen atoms and even smaller hydrogen ions are able and capable of penetrating the steel material, especially in the welded region where a number of defects are pre-existing, making it brittle,

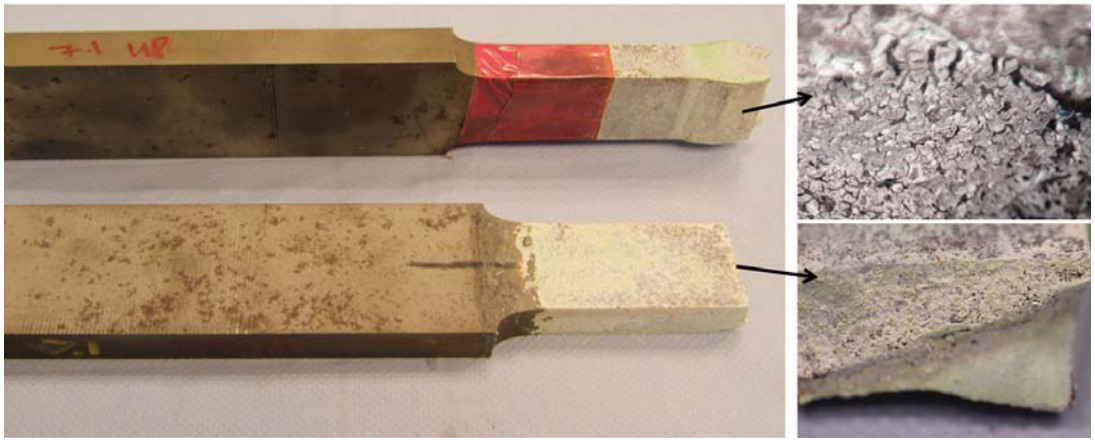

Figure 5.14: *Calcareous layer examination*

and thus reducing its ductility. The hydrogen absorption of steel is also believed to cause a reduction in true stress at fracture, i.e. not significantly influencing the yield and ultimate strength, but leading to fracture at lower levels of true strain and true stress. This becomes particularly significant when considering stress concentrations and notches such as weld toes, as the notch fracture strength decreases [59].

Another important aspect to consider concerning the hydrogen absorption of steel and welded joints subjected to tensile stresses relates to the increased pressure formation due to the accumulation of hydrogen gas within the material's cavities and defects. The hydrogen diffuses preferably at notched locations and crack openings which can cause crack propagations, as well as affect the crack growth, especially when dealing with high strength steels, as their susceptibility to hydrogen embrittlement is greater due to a reduced amount of allowable diffusible hydrogen [5], [59], [107], [108], [109], [110]. The severity then increases when dealing with welded joints as they are associated with trapped hydrogen within the welded region from the welding process, high internal residual stresses, pre existing defects within the weld and a weld toe notch, in the non post treatment situations.

Calcareous coating

The fatigue tested 20 mm thick SAW butt joints tested in the corrosion environment with the ICCP demonstrated a formation of a calcareous coating on the specimen. This coating or layer reduces the current demand and inhibits oxygen transport to the specimen's surface.

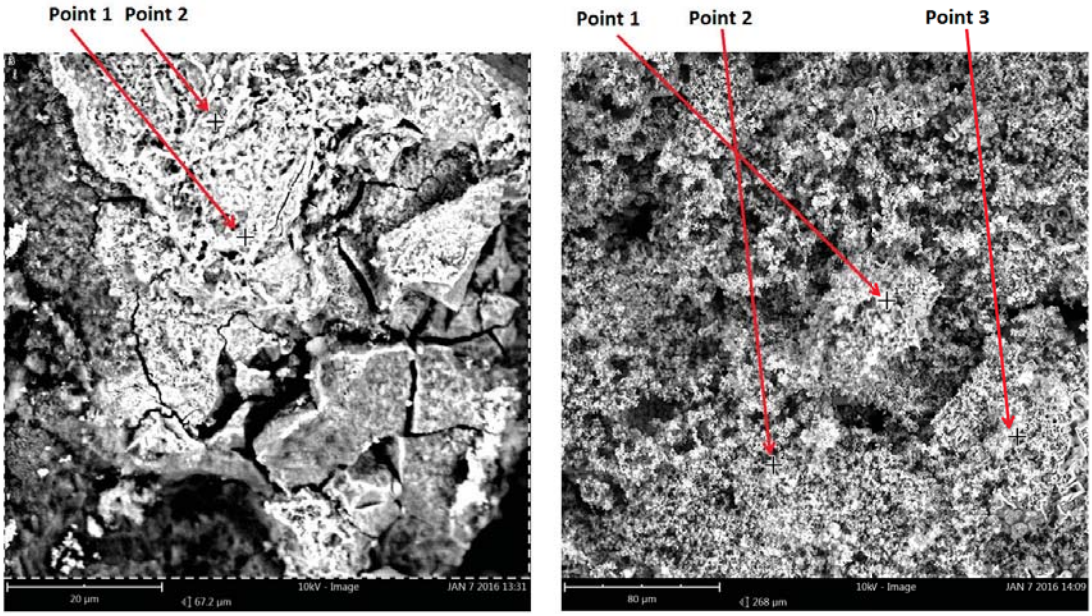

Figure 5.15: *Calcareous layer examination, SEM microscope*

The formation of hydroxyl ions, OH^-, from reactions 5.2 and 5.3, increases the pH level at the specimen's surface which results in the following precipitation of coating layers from the reactions in the ASTM seawater:

$$\begin{aligned} OH^- + HCO_3 &\rightarrow H_2O + CO_3^{2-} \\ CO_3^{2-} + Ca^{2+} &\rightarrow CaCO_3 \\ Mg^{2+} + 2OH^- &\rightarrow Mg(OH)_2 \end{aligned} \tag{5.5}$$

The possible deposition of these layers is dependent on the pH level of the ASTM seawater in addition to the potential applied, the temperature and the flow rate.

Figure 5.14 illustrates the the post examination of a test specimen subjected to corrosion fatigue loading. The specimen fractured at the lower weld toe region. The fracture region was cut into smaller sized samples in order to perform material identification by Fourier transform infrared spectroscopy, FTIR. The Material analysis of the calcareous layer deposited on the sample's surface indicated after a database search a possible match with the formation of magnesium oxide, $Mg(OH)_2$, also known as Brucite. Brucite coating has the beneficial effects of lowering the required current density to protect the specimen, on the contrary Brucite is being subjected to much attention in

1st Specimen (Left)					
	Element Number	Element Symbol	Element Name	Confidence	Concentration Weight Percent [%]
Point 1	8	O	Oxygen	100	62.7
	26	Fe	Iron	100	27.7
	17	Cl	Chlorine	100	4.1
	7	N	Nitrogen	100	5.5
Point 2	8	O	Oxygen	100	100
Total Area	8	O	Oxygen	100	50.0
	12	Mg	Magnesium	100	22.0
	26	Fe	Iron	100	28.0
2nd Specimen (right)					
Point 1	8	O	Oxygen	100	50.1
	12	Mg	Magnesium	100	19.0
	17	Cl	Chlorine	100	7.3
	30	Zn	Zinc	50	17.6
	7	N	Nitrogen	100	4.6
	16	S	Sulfur	100	1.4
Point 2	17	Cl	Chlorine	100	20.7
	12	Mg	Magnesium	100	23.1
	8	O	Oxygen	100	56.2
Point 3	8	O	Oxygen	100	45.2
	12	Mg	Magnesium	100	21.8
	17	Cl	Chlorine	100	12.3
	30	Zn	Zinc	50	20.7

Figure 5.16: *Calcareous layer examination, tabular data*

recent research in the validation of the coated layer and whether it actually reduces or increases hydrogen uptake [106], [10], [111].

The calcareous layer was additionally inspected in a tabletop SEM microscope. A scalpel was used to scathe powder, i.e. the oxides, from the sample's surface onto a carbon tape, which was then measured directly. Figure 5.15 illustrates the results from the SEM material analysis from the SEM microscope, the magnification on the left was 4000x while the magnification on the right was 1000x.

Figure 5.16 shows the tabular data from the tabletop SEM. The figure lists the material

composition from the selected points illustrated in Figure 5.15. The points show some variation between them, identifying Zinc at point 1 and point 3 from the figure on the right, with a 50% confidence. The composition for the total area in Figure 5.16 (left) shows a concentration of 50% oxygen, 22% magnesium and 28% iron.

This page is intentionally left blank.

Chapter 6

Test Series 3 - *Fatigue resistance of laser-hybrid welded joints and a comparison to submerged arc welded joints*

The third experimental test series, Test series 3, "fatigue strength of laser-hybrid welded joints and a comparison to submerged arc welded joints", was a novel and exciting approach towards the overall goal of the project, reducing the cost of energy for the manufacturing process relating to large structures, such as offshore wind turbines. This was a joint collaboration with Force Technology's subsidiary Lindoe Welding Technology, LWT, in developing and producing "larger" scale laser-hybrid welded joints for experimental testing and a comparative study with the industry's dominant welding technology of today, i.e. submerged arc welding.

The laser-hybrid welding technique demonstrates huge potential and could be extremely beneficial in the future development and manufacturing of large structures.

There is still quite a long way to go until the laser-hybrid welding technique is ready for mass production of large constructions. The challenges are considerable, however the possible gains are much greater and the industry is already involved with a growing interest. The development of this welding technique has grown rapidly in recent years and already today, joints of 100 mm have been welded and passed non destructive

testing at research institutions.

6.1 Background

This test series focuses on investigating and comparing the mechanical and material properties of the traditional submerged arc welding (SAW) technique against a laser-hybrid based welding technique. The main goal is to investigate the fatigue performances of laser-hybrid welded joints in comparison to the SAW specimens.

Increased competitiveness and cost optimization are two significant objectives in industry today, especially concerning production and manufacturing processes. In order to uphold competitiveness, the finished product requires either; 1) a reduction in total cost, where a compromise is often necessary between several conflicting requirements, or 2) the finished product is structurally enhanced with increased strength and durability associated with the corresponding increase in cost. Ideally both options are desirable however that is generally impossible without an implementation of a technological or industrial breakthrough.

Laser-hybrid welding is not new to the market and is well established in industries such as the automotive, medical, shipbuilding, electronics and aerospace industry. The main application in these industries for laser based welding is joining parts of small thicknesses at high speeds with excellent reproducibility of strong welds in a fully robotic/automatic, robust and flexible manner. At the present, laser-hybrid welding of large heavy structures, thick joints from 40 to +80 mm thicknesses, still persists solely within the research and development stage and not generally applicable in practice.

A major laser welding facility (Lindoe Welding Technology, LWT) has been established at Lindoe Industrial Park for the offshore wind energy sector. LWT will test and develop new production methods, with an emphasis on the new and powerful 32 kW laser consisting of two 16 KW laser systems. The founders are Force Technology and LORC, both of who are invested in the potential in welding with laser based technology for heavy structures, such as wind turbine towers and foundations. Between a fourth up to half of the total cost of offshore wind turbine installation process relates to the welded towers and substructures. An opportunity to optimize this part of the manufacturing process in order to minimize the cost is thus quite attractive. The focus of new and green sustainable energy is also highly relevant in implementing the laser-hybrid welding technology into the heavy structured industry, according to a study from Trumpf Laser GmbH, which states that laser based welding can run up to

24 m/kW compared to conventional welding processes that run approximately 4 m/kW, that is six-fold the efficiency.

Laser-hybrid welding can perform at high speeds with the capability of fully automated production of consistent, sound and high quality welded joints. Compared to conventional welding processes, the laser-hybrid welding is faster, requires fewer passes and with little or low use of welding consumables such as filler material. The efficiency is high as it can be fully robotic or automatic and the maintenance cost is minimal. Additionally, there is a very low thermal exposure of the bulk material as the welding melt pool is very local. Therefore, minimizing deformations, distortions and weld reinforcement parameters which reduces the need for post processing. In the last few years the achievable thickness of laser-hybrid welded joints has increased, especially in the last five years.

6.2 Experimental test preparation

6.2.1 Lab capacity

Two uni-axial servo-hydraulic testing machines (SHM) were applied in this test series, a 500 kN MTS machine and a 500 kN Instron machine. Both were readily available and prior to testing the machines load cells were calibrated and verified. The maximum allowable error in the load cell's voltage signal with respect to a certified reference load cell is 1% and both machines were below the maximum limit with respect to the entire tensile load capacity of the machines.

The SHMs load train alignments were examined with an alignment transducer according to the ASTM standard, E 1012 [94]. The resulting computed bending strain for both machines did not exceed the maximum calculated bending strain classification, i.e. 5% bending.

Data measurement equipment

The following measurement equipment was used in order to acquire the relevant data and to determine the mechanical properties and pursue in order to pursue the investigation.

- Vishay general purpose strain gauges, 120 Ω resistance.

- HBM MGCPlus, data measurement and acquisition device.
- MTS, certified and displacement validated extensometers.
- 4 mega-pixel and 12 mega-pixel Aramis digital image correlation system.
- SHM controllers acquire the basic load and displacement signals.

6.2.2 Material composition

The steel material applied in this test series for the specimen production was steel S355 J2 + N, i.e. the same steel material grade as was used in test series 1, for the thickness effect investigation.

Six 800 x 600 x 25 mm steel plates were ordered in order to laser-hybrid weld 3 plates for testing. The material composition is listed in Table 6.1.

6.2.3 Welding procedure

As the welding technique is still within the research and development stage, there was no detailed information provided about the welding procedure or setup from the collaborating partner. However, the 25 mm thick plates were bevelled into a double-Y joint by machining and thereafter laser-hybrid welded in a PA flat position. The plate was welded in two passes, i.e. one from the top and the latter from the bottom, where a GMA welding technique was used in conjunction with the 2 x 16 kW laser to form the welded seams in the machined bevel on the top and bottom while the laser penetrated deeper and welded the adjacent flat surfaces of the material. Figure 6.1 illustrates the welding preparation along with a fully penetrated welded specimen from this test series.

Table 6.1: *LWT Laser-hybrid welded plates. Material composition*

Test Series 3 - Laser-hybrid welded joints.																
Element	C	Si	Mn	P	S	Al	Cu	Cr	Ni	Mo	V	Nb	Ti	Co	Sn	Mg
25 mm thick - wt. [%]	0.18	0.39	1.51	0.017	0.009	0.032	0.018	0.028	0.015	<0.001	0.002	0.023	0.017	0.003	0.007	0.0003

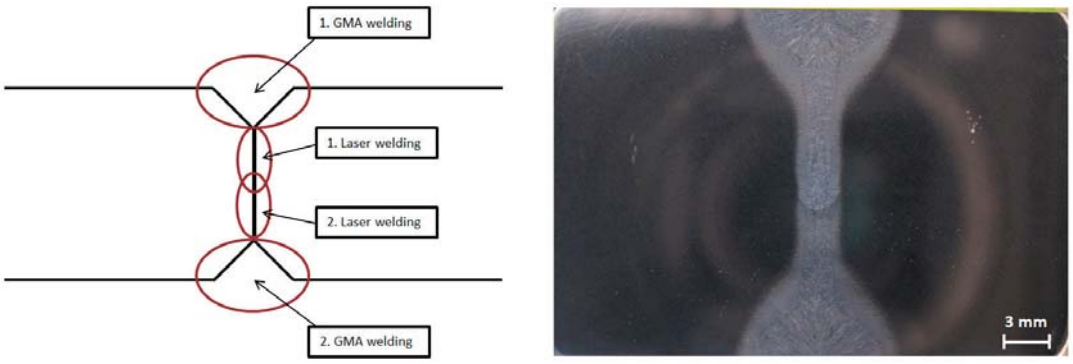

Figure 6.1: *Laser-hybrid welding joint preparation (left) and a completed laser-hybrid weld section (right)*

6.2.4 Non destructive testing

As previously mentioned, the laser-hybrid welding technique introduces cooling rates of very high magnitudes or in the range of thousands of degrees per second which causes high thermal gradients in the structure during the welding procedure. Thus, this extreme cooling rate is likely to induce defect formations, such as cracks, pores, lack of fusion etc. For this reason, a lot of time is invested and required in fine-tuning the welding setup in order to find the proper welding procedure to avoid this predicament. However, once the setup is ready, multiple repetitions of similar sound and high quality welds can be performed.

The laser-hybrid welded joints passed visual inspection according to EN 970 and with EN/ISO 5817 with a quality demand without any remarks. The ultrasonic testing was performed according to ISO 15614 and the quality demand was set by ISO 12932:2013. No defects were detected and the entire weld seam was accepted according to specifications. Lastly the laser-hybrid welded joints were subjected to magnetic particle testing according to ISO 15614 with the quality demand set by EN/ISO 23278,1. Both sides were examined and the welded plates were accepted according to specifications.

6.2.5 Cutting procedure

The cutting procedure was performed at DTU, workshop building 427, with a water-jet cutting machine. This cutting technique gives good, smooth and accurate cuts with no heat distortion, which can have a significant effect on the specimens, according to

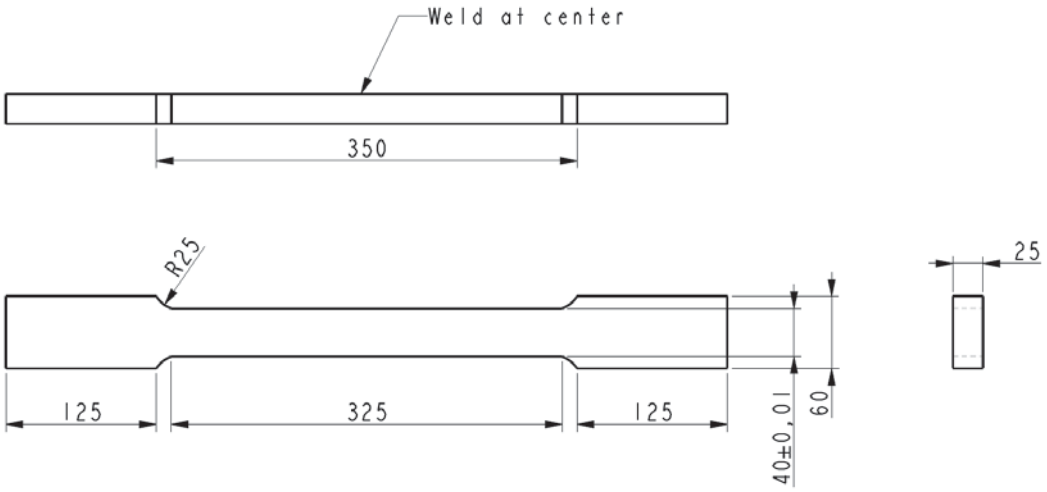

Figure 6.2: *Test series 3, laser-hybrid welded joints dimensions*

ESAB. The cutting procedure involves cutting the welded plates across the weld into tensile test specimens of "dog-bone" shape. The specimens located at the ends of the welded plates were used for static testing as it is recommended to discard the first and last 50 mm of a welded plate.

A total of 39 specimens were cut out of the welded plates. After the cutting procedure, all specimens were cleaned and coated with the available oil, grease, varnish or other media to prevent corrosion of the steel material. All specimens were labelled in order to keep track of where they were located within the respective original welded plate. Additionally, all specimens were wrapped in cloth and special requirements were made concerning specimens storing, to minimize the risk of environmental and/or accidental detrimental effects. Figure 6.2, illustrates the specimens dimensions.

Table 6.2: *Non destructive testing of laser-hybrid welded joints*

Test Series 3 - Laser-hybrid welded joints.			
Thickness [mm]	Visual inspection	Ultrasonic testing	Magnetic particle testing
25 mm plate	✓	✓	✓

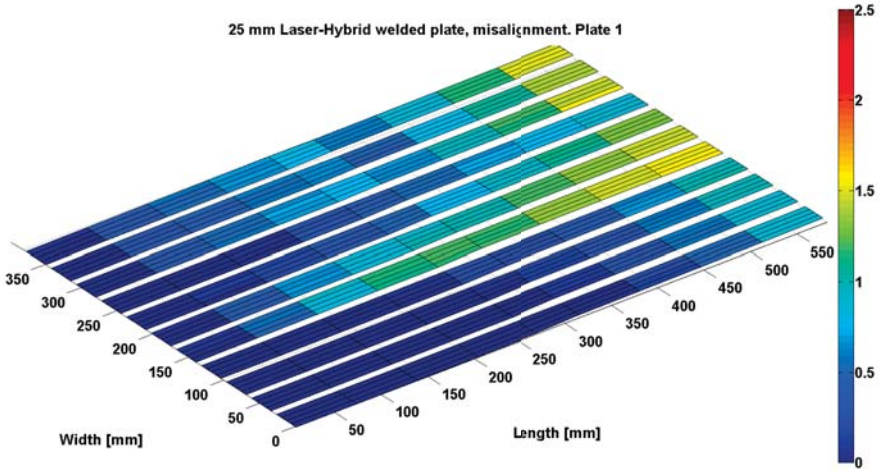

Figure 6.3: *Misalignment measurements of the 25 mm thick laser hybrid welded joints, plate 1. The figure shows individual measured surfaces for each specimen which are thereafter aligned together in their original location*

6.2.6 Misalignment measurements

Misalignment measurements were performed on the laser-hybrid welded joints after they were cut down to specimen dimensions. High precision point coordinate machine, Zeiss Calypso, was applied to measure the misalignment and tolerances. The acceptance criteria for allowable misalignment for butt welded joints was discussed in section 4.2.7. Figures 4.7 and 4.8 give an illustration of the axial and angular misalignments as well as the location of the measured coordinate points on the specimen's surface respectively.

Figures 6.3, 6.4 and 6.5, illustrate the measurements of the welded joints from the coordinate machine. Each stripe in the figure represents the surface of a test specimen. The measured surfaces are then aligned together in order to get an overview of the original welded plate. The colorbar on the right ranges from 0 up to the maximum allowable axial misalignment, e, according to standards. The axial misalignment is where the two surfaces on opposite side of the weld would ideally intersect. In addition, the figures also include the angular misalignments. The figures show that the laser-hybrid welded specimens are not heavily affected by misalignment, although it is a considerable challenge to avoid it completely when dealing with welded joints.

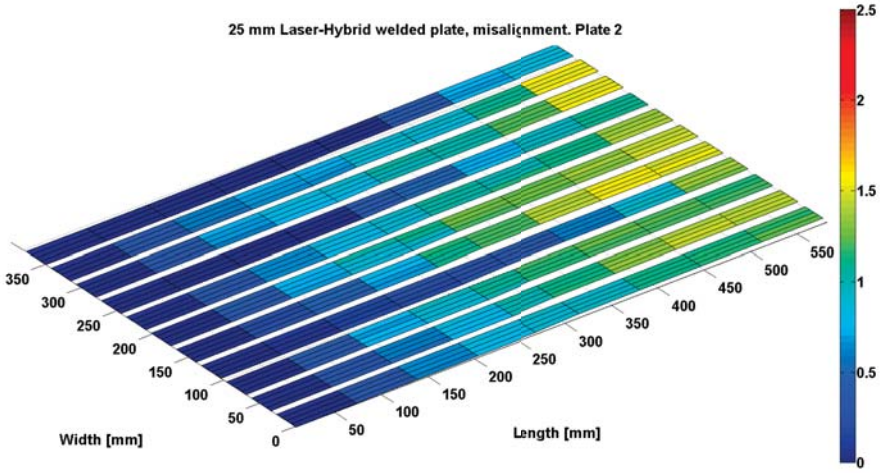

Figure 6.4: *Misalignment measurements of the 25 mm thick laser hybrid welded joints, plate 2. The figure shows individual measured surfaces for each specimen which are thereafter aligned together in their original location*

The maximum end-to-end misalignment of the joints measured were 1.69 mm, 2,16 mm and 1.85 mm with the corresponding minimum misalignment measured to be 0.33 mm, 0.97 mm and 1.06 mm and lastly the measured average misalignment was 0.95 mm, 1.53 mm and 1.53 mm for plate 1, plate 2 and plate 3 respectively.

The maximum axial misalignment, e, was measured to be 0.49 mm, 0.09 mm and 0.38 mm with the corresponding minimum axial misalignment equalling 0.03 mm, 5.96e-4 mm and 0.01 mm for plate 1, plate 2 and plate 3 respectively.

The maximum angular misalignment, α, was measured to be 0.26°, 0.27° and 0.34° with the corresponding minimum angle measured to be 0.08°, 0.03° and 0.02° for plate 1, plate 2 and plate 3 respectively.

The average axial misalignment, $\bar{e}$, was measured to be 0.23 mm, 0.04 mm and 0.15 mm and the resulting average angular misalignment, $\bar{\alpha}$, was 0.19°, 0.15° and 0.18° for plate 1, plate 2 and plate 3 respectively.

All these misalignment measurements lie well below the maximum limits recommended by the standards. The measurement results highlight that the laser-hybrid welding technique and the welding fit-up maintains results in low axial misalignment and angular distortion as the largest measured value of axial misalignment was, e = 0.49 mm, which

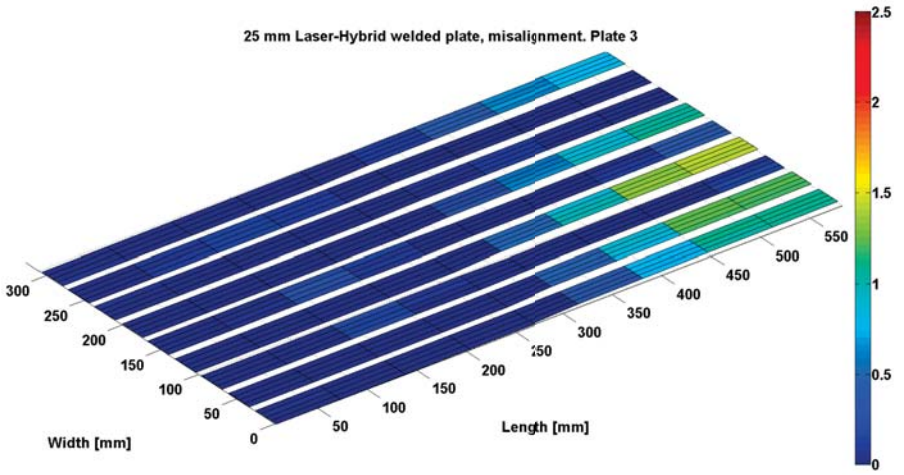

Figure 6.5: *Misalignment measurements of the 25 mm thick laser hybrid welded joints, plate 2. The figure shows individual measured surfaces for each specimen which are thereafter aligned together in their original location*

is 80% below the recommended limit of eccentricity over thickness, e/t = 10%. The same can be observed with the maximum measured angular distortion, $\alpha = 0.34°$, is well below the recommended limit of 1°.

6.3 Experimental testing

The following section describes the experimental test procedure and includes a brief discussion relating to the obtained results.

6.3.1 Static testing

The laser-hybrid welded joints were subjected to axial static testing in order to retrieve mechanical properties of the joints as well as to estimate a reference load level for the subsequent fatigue testing. The static tensile testing was performed in accordance to ASTM E8, ASTM E111 and DS/EN ISO 6892, [98], [99] and [100]. The applied

testing machines were described in section 6.2.1. Before initiating the test sequences all machines were calibrated and load cell readings verified.

The strain gauges applied were "general purpose", EP-08-250BG-120 ohm strain gauges from Vishay with an active gauge length of 6.35 mm. These strain gauges are meant for high elongation and post yield strain measurements. In addition extensometers were applied for the calculation of the elastic modulus whilst a digital image correlation system was applied in order to receive a full field three dimensional displacement field of the area of interest.

Six static tests were performed, two from each laser-hybrid welded plate. The rate of displacement was 2 mm/min. The data acquisition devices, i.e. MGCPlus and the DIC system, were synchronized with a common voltage load signal from the controller.

All statically loaded laser-hybrid specimens fractured in the base material, far from the weld and heat affected zone region. The mechanical properties derived from the static testing are listed in table 6.3. The joints yield strengths, σ_y, were estimated by applying a 0.2% offset curve. The computed yield strength, σ_y, was relatively consistent and resulted in an average yield strength of $\bar{\sigma}_y$ = 330.6 MPa, which is below the minimum required mechanical yield strength for the steel grade of S355 J2 + N. Further investigation demonstrated a slight difference between the two steel plates which were laser-hybrid welded together, e.g. one side of the weld the demonstrated a yield strength of, σ_y = 332.4 MPa while the other side resulted in σ_y = 344.5 MPa. This eventually affects the direct comparison with the traditional SAW butt joints, as they demonstrated higher yield strengths. The subsequent sequence of fatigue testing was

Table 6.3: *Laser-hybrid welded joints, engineering mechanical properties*

Test Series 3 - Laser-hybrid welded joints.							
Specimen #	Width [mm]	Thickness [mm]	Area [mm^2]	Length [mm]	σ_y [MPa]	σ_{ult} [MPa]	E modulus [GPa]
LH 1_1	20.21	25.01	505.33	600	334.72	437.06	207.76
LH 13_1	20.27	25.01	506.85	600	328.43	427.63	201.82
LH 1_2	20.07	24.96	500.72	600	328.22	429.56	203.08
LH 13_2*	20.41	25.03	510.13	600	334.06	424.99	204.64
LH 1_3	20.02	25.17	503.68	600	332.38	431.23	203.11
LH 13_3*	20.13	24.95	502.14	600	325.78	427.50	205.62

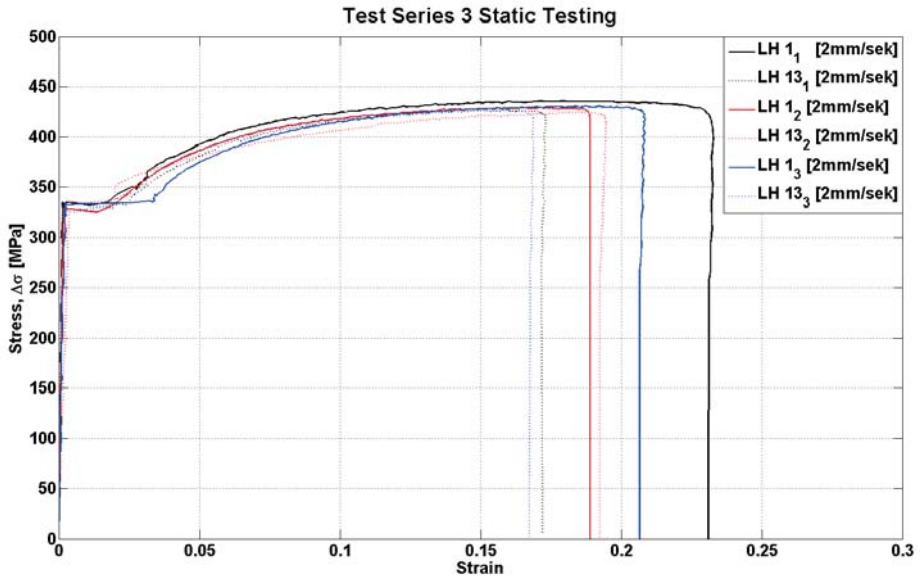

Figure 6.6: *Test series 3: Stress-strain curves obtained from the static testing of the laser-hybrid welded joints*

dependent on the specimen's yield strength and the fatigue load levels and corresponding stress ranges were determined as a percentage of the specimens yield strength. However, as previously mentioned, the welded joints lower yield strengths were consistent for all specimens subjected to static testing and thus the reference load level for the subsequent fatigue test series was computed from $\bar{\sigma}_y$ = 330.6 MPa.

Figure 6.6 illustrates the obtained yield strengths determined from the static testing. All six static tests are shown, where LH 1_1 is the first specimen from plate 1 and LH 13_3 is the last specimen from plate 3.

6.3.2 Fatigue testing

Axially loaded tension-tension fatigue tests were performed in the aforementioned SHMs, located in building 119 at the Technical University of Denmark, DTU. All tests were carried out in laboratory air conditions at room temperature, +20°C.

All laser-hybrid welded joints were subjected to fatigue loading in the as-welded condition, i.e. no post weld treatment was applied. All tests specimens were subjected to

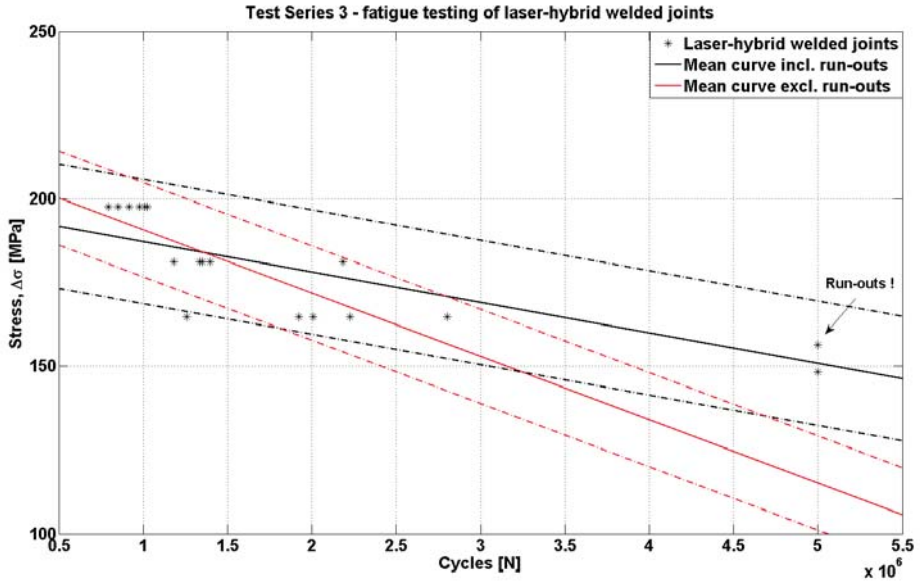

Figure 6.7: *Fatigue results for the laser-hybrid welded joints. Stress range* $\Delta\sigma$*, as a function of cycles to failure, N*

constant amplitude sinusoidal waveform at a frequency of 8Hz. The cyclic loading was performed at a stress ratio of R = 0.5, with stress levels computed as a percentage of the specimens average yield strength, $\bar{\sigma}_y$. The stress ratio, R = 0.5, was maintained constant throughout the test sequence in order to achieve direct comparison to the SAW specimens, from test series 1, see Chapter 4. Additionally, in order to generate an experimental S-N curve, the welded joints were tested at five different stress levels with a minimum of five specimens tested at each stress level. The maximum applied stress, σ_{max}, in the test series equalled 120% of the yield strength of the welded joints while the minimum stress applied, σ_{min}, equalled 90% of the respective average yield strength.

N.B. The definition of failure in all fatigue tests was complete rupture.

All test data was acquired from the relevant machine controllers and the tests were monitored by a high resolution camera in order to follow the crack propagation and failure location.

The fatigue test sequence of the laser-hybrid welded joints started with performing tests with the maximum stress level equalling the specimen's respective yield strength, $\sigma_{max} = \sigma_y$. The corresponding maximum and minimum applied load levels at the

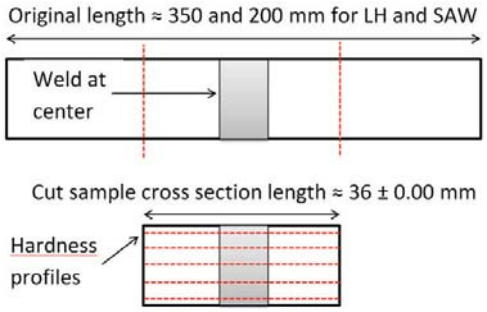

(a) Sample cutting procedure.

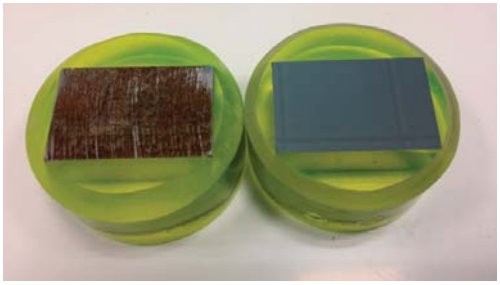

(b) Ready made samples, pre and post polishing.

Figure 6.8: *Laser-hybrid and SAW sample preparation for SEM analysis and hardness testing*

welded joint's yield strength were approximately 330 kN and 165 kN respectively. The subsequent stress levels were reduced in order to reach the fatigue threshold stress level, i.e. an endurance limit for the test series. Thereafter, the stress level was increased as a function of yield strength to build up the S-N curve with short cycle, high stress level fatigue testing. The results from the fatigue testing are illustrated in Figure 6.7.

Figure 6.7 demonstrates the fatigue strength of the laser-hybrid welded joints as a function of cycles to failure. This figure also illustrates the mean $\pm$ two standard deviation from the test population. The black curve is the mean including the fatigue run-outs, whilst the lower red curve is the mean computed solely from the fractured specimens.

6.3.3 SEM-EDS analysis

Sample preparation

Test specimens, cut out with a waterjet cutting machine, were additionally sectioned into smaller test samples that would be applicable for microscopic evaluation, illustrated in Figure 6.8. Three samples from the laser-hybrid welding technique and three samples from the 20 mm thick SAW samples from batch 2 were prepared.

The specimens were machined in order to fit the largest available molding cup, 50 mm in diameter. The applied resin was epoxy, SpeciFix, applicable for cold mounting. The samples were subjected to grinding with abrasive grits from 80 to 600 and thereafter

the samples were fine polished with polishing cloths 1200 to 4000, median diameter 15.3 to 2.5 μm. The applied diamond polishing paste was Mol B3, 3 μm, and Nap B1, 1 μm. All grinding and polishing was applied with a fixed 60 N force for six minutes. Lastly, the samples were etched in 2% Nital for three seconds. A maximum of five samples could fit the grinding-polishing machine's holder and thus one laser-hybrid sample was left behind.

SEM-EDS testing

A scanning electron microscope, SEM, was used to perform an energy dispersive x-ray spectroscopy, EDS, from the cross section of the two welding techniques, laser-hybrid and SAW. The specimens were carbon coated with a 15nm layer for five minutes.

6.3.4 Hardness testing

The two welding techniques, laser-hybrid and SAW, were additionally subjected to hardness testing. The applied hardness testing machine, Wolpert Lestor, is capable of both Vickers and Brinell hardness testing. Vickers pyramid hardness was preferred. Every sample had five hardness profiles across the welded region created at varying locations with respect to the samples height, illustrated in 6.8 (left). The indentations were made by a 3 kg force for 10 seconds and the distance between indentations was 2.5 times the diagonals length, i.e. 2.5 * D apart.

A certified Vickers hardness testing procedure according to DS/EN ISO 6507-1, was performed by Force Technology on similar welded joints to those that were applied in this test series. Obtained hardness values in the base material were measured to be 149 HV10 while the laser welded seam at the sample's center had hardness values measured up to a maximum of 336 HV10.

6.4 Test results & comparison to the traditional SAW technique

This section will provide and analyse the relevant results from the laser-hybrid welding and subsequent experimental testing. Additional investigation was performed by a

comparative study to the obtained results from SAW butt joints in test series 1, see Chapter 4.

6.4.1 Welding procedure

The applied SAW equipment used for welding the test specimens for test series 1 was able reach a welding speed of 40 cm per minute, while the laser welding technique had speeds up to 200 cm per minute. The two 20 mm thick SAW plates from test series 1, were both welded in four passes, while the laser-hybrid welding joined the 25 mm thick plates in two passes. Additionally, the two 30 mm thick SAW joints were welded in seven and eight passes. Thus, emphasizing purely on welding time, the laser technique could have a 10-fold efficiency.

6.4.2 Misalignment measurements

From the misalignment measurements the 20 mm thick SAW butt joints were demonstrating a average axial misalignment of 0.17 mm from batch 1 while batch 2 demonstrated 0.21 mm and 0.95 mm. The laser-hybrid welded joints showed an average of 0.23 mm, 0.04 mm and 0.15 mm for plate 1, plate 2 and plate 3 respectively.

The measured angular misalignment from the 20 mm thick SAW butt joints were 0.37°, 0.38° and 0.20° for the three plates respectively. The laser-hybrid welded joints demonstrated 0.19°, 0.15° and 0.18° for the three laser-hybrid welded plates respectively.

Figure 6.9, illustrates the misalignment of the laser-hybrid welded joints against the 20 mm and 30 mm thick SAW butt joints. The figure also illustrates the standards and guidelines recommended limits for axial and angular misalignment.

The figure shows that all the laser-hybrid welded joints are within the limits and demonstrate a slight improvement compared to the 20 mm thick SAW butt joints from batch 1. The level of misalignment for the laser-welded joints was in the same range as the 30 mm thick SAW butt joints from batch 1, where the average axial misalignment, e, was measured to be 0.15 mm and the average angular misalignment, α, approximately 0.19°. The 2nd batch of 20 mm thick SAW butt joints demonstrated the highest axial and angular misalignment, however all but two specimens lie within the recommended limits.

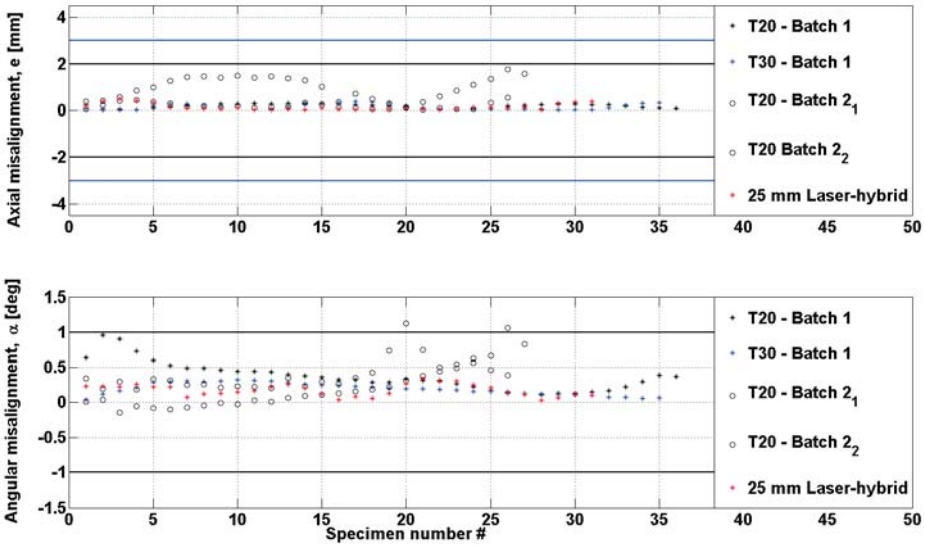

Figure 6.9: *Misalignment measurements from the laser-hybrid welded joints along with 20 mm and 30 mm thick SAW specimens from test series 1. The standards maximum allowable misalignment is additionally added as the horizontal lines. (Above) axial misalignment, e, and (below) angular misalignment* α

6.4.3 Static testing

As mentioned previously, all laser-hybrid welded specimens subjected to static loading fractured in the parent material, away from the weld and heat affected zone. The weld zone as well as the heat affected zone of the joints had been significantly reduced when compared to the 20 mm thick SAW butt joints, and even more when compared to the 30 mm thick SAW butt joints. This is illustrated in Figures 6.10 and 6.11.

In particular, figure 6.10 illustrates the strain along the vertical axis, ε_y, from the DIC measurements during the static testing of 25 mm thick laser-hybrid test specimen 13_1. The system measured at a 45° angle, thus enabling full field displacement views of the front and side surfaces. Two measurement sections have been implemented in the figure. Each point in the section is a measurement point and the corresponding reading from each point is illustrated in the graph in the lower right corner. The figure demonstrates how the weld and the heat affected zone demonstrate stronger mechanical properties than the parent material which has in the figure, started to yield in the upper

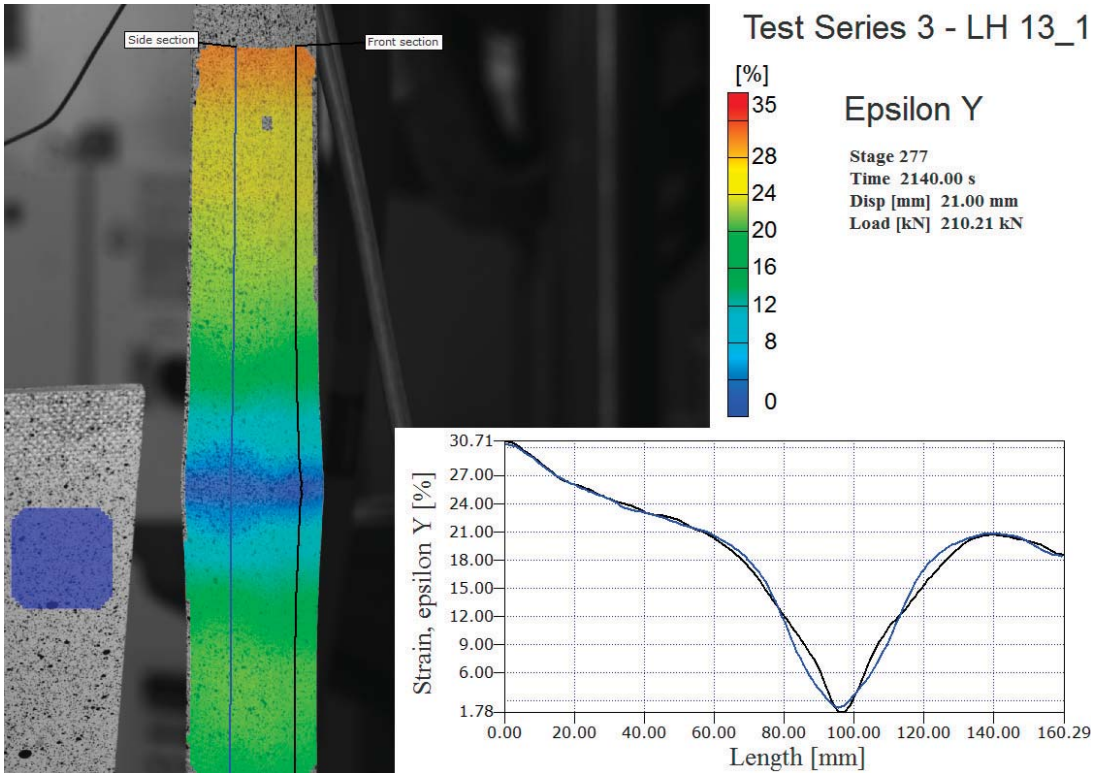

Figure 6.10: *DIC measurements during the static loading of the 25 mm thick laser-hybrid welded joint. The implemented graph illustrates the strain measurements from the sections created along the length of the joint. The blue (left) line goes along the side whilst the black (right) line goes along the front of the joint*

region.

Figure 6.11, illustrates a static test of a 20 mm thick SAW butt joint at an approximate same load level, with the same features, i.e. displaying ε_y along the vertical axis with two sections across the welded region. From both figures it is evident that the weld as well as the heat affected zone has been reduced extensively by the laser-hybrid welding technique or by a factor of more than 2.

6.4.4 Fatigue testing

Figure 6.7 illustrates the experimental fatigue testing of the laser-hybrid welded joints. The resulting fatigue strength threshold level, i.e. the endurance limit, was high com-

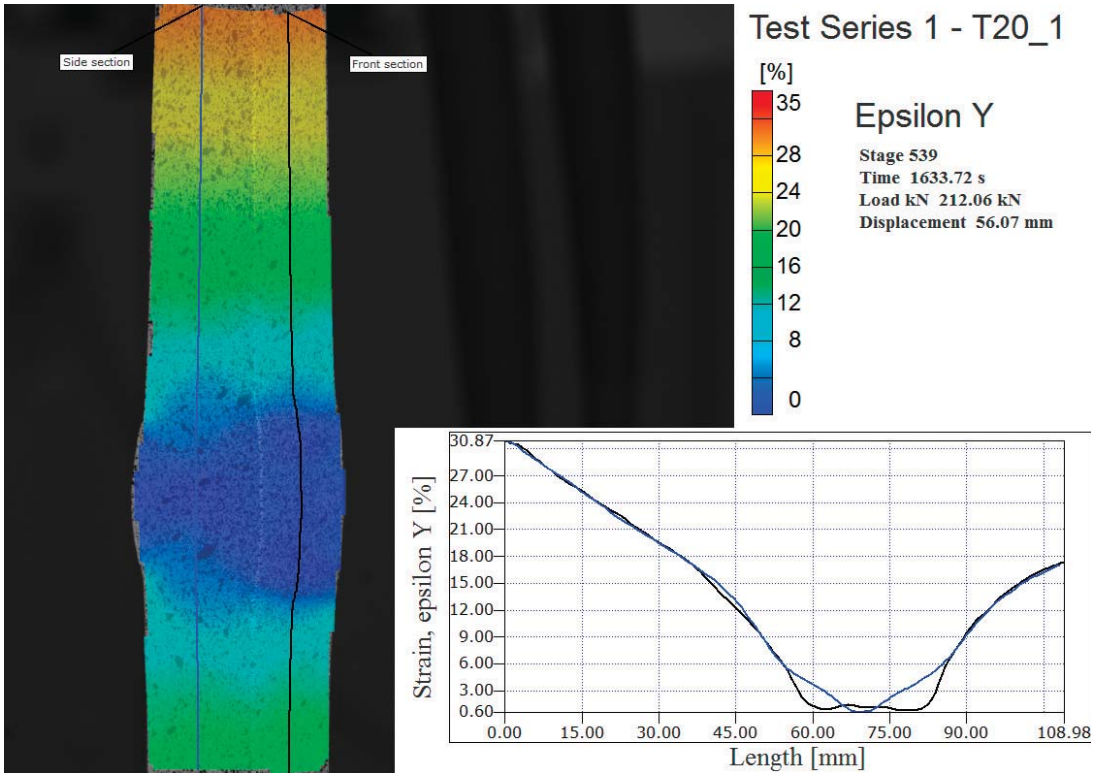

Figure 6.11: *DIC measurements during the static loading of the 20 mm thick SAW butt joint. The implemented graph illustrates the strain measurements from the sections created along the length of the joint. The blue (left) line goes along the side whilst the black (right) line goes along the front of the joint*

pared to the previously performed fatigue tests of SAW butt joints. The threshold level was already established at 97.7% of the specimens average yield strength, i.e. all test specimens tested at 90% and 95% of $\bar{\sigma}_y$, endured 5 million cycles of fatigue loading without fracture. Thus, the collection of fractured specimens in the experimental S-N curve represents test specimens subjected to loads at yield strength and higher.

Figure 6.12 illustrates a comparison of the laser-hybrid welded joints against the previously cyclically fatigue tested 20 mm thick SAW butt joints from batch 1, i.e. the welded joints that demonstrated the highest fatigue resistance from the thickness effect investigation, from Chapter 4. Figure 6.12 (left) shows the obtained results where the stress range, y-axis, is the level of stress applied to the specimens. However, as the yield strength of the specimens differed between the two test series another illus-

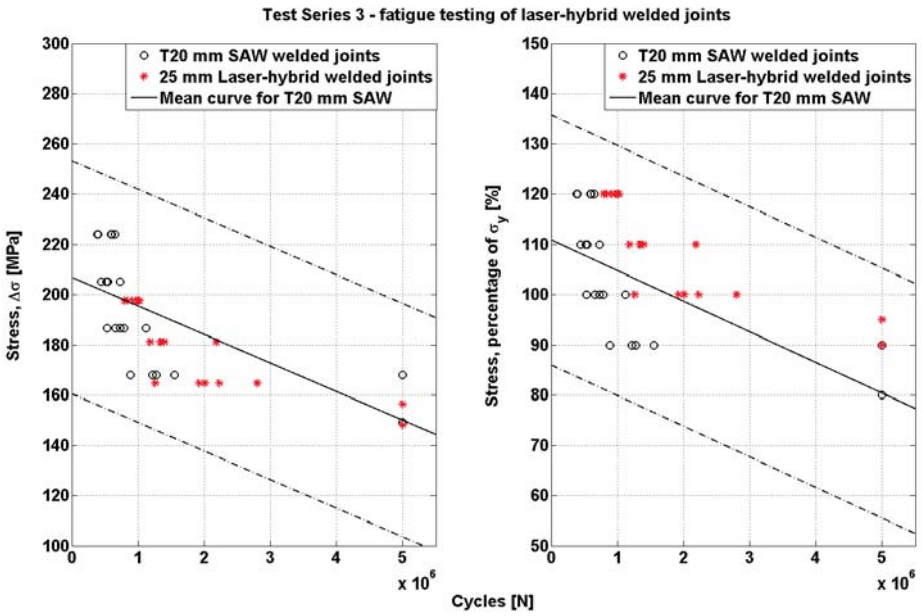

Figure 6.12: *Fatigue result comparison between 20 mm thick SAW butt joints and 25 mm thick laser-hybrid welded joints. (left) S-N data from subjected stress levels and (right) S-N data as a function of the specimens average yield strength*

tration was made, 6.12 (right), showing the fatigue resistance of the results with the stress range shown as a percentage of the specimens respective average yield strength, $\bar{\sigma}_y$.

From the figures it is clear that the laser-hybrid welded joints are demonstrating higher fatigue resistance than the 20 mm thick SAW butt joints, both in the applied stress range, $\Delta\sigma$, and in relation to the percentage of the specimens respective average yield strength, $\bar{\sigma}_y$. Figure 6.12 (right) also demonstrates that almost the entire collection of test specimens from the laser-hybrid welded joints lies in the upper scatter band of the $\pm$ 2 standard deviation from the mean of the 20 mm thick SAW butt joints.

Additionally it is worth re-iterating that laser-hybrid welded joints did not demonstrate failure below their respective yield strength at 5 million cycles. The 20 mm thick SAW butt joints from batch 1 fractured at 90% of σ_y. The 20 mm thick SAW butt joints from batch 2 fractured at 85% of σ_y. Finally the 30 mm thick SAW butt joints fractured at 80% and 60% σ_y from batch 1 and batch 2 respectively.

Moreover, figure 6.13 illustrates the fatigue results from the laser-hybrid welded joints plotted up against the recommended IIW fatigue design curve for butt welded joints in

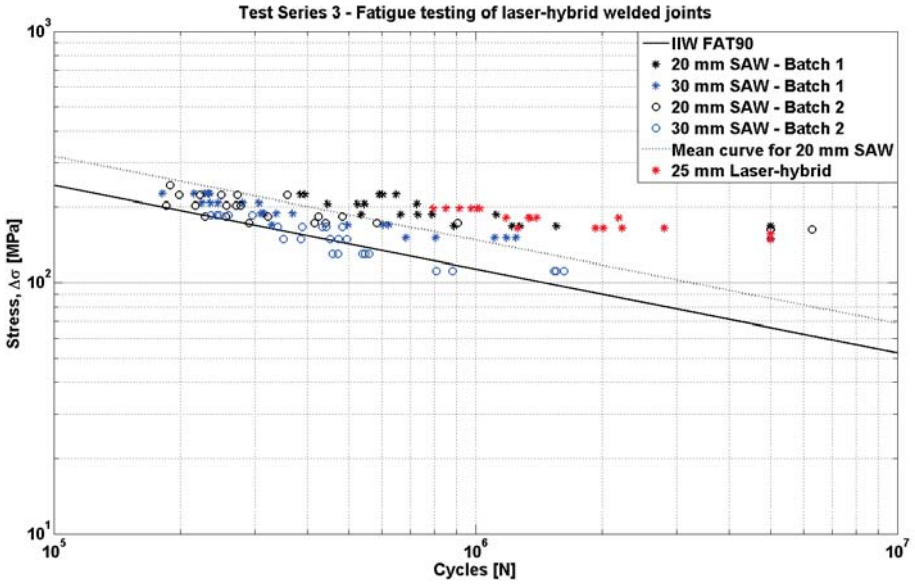

Figure 6.13: *S-N plot showing the fatigue resistance of the laser-hybrid welded joints against 20 mm and 30 mm thick SAW butt joints in addition to design curve FAT90 from IIW*

the as-welded condition, FAT90, which corresponds to DNV's fatigue design curve D. Additionally, the fatigue results from the 20 mm and 30 mm thick SAW butt specimens from batch 1 and batch 2 are presented along with the mean curve from the 20 mm thick joints.

Figure 6.13 shows that the laser-hybrid welded joints demonstrate higher fatigue resistance compared to the tested SAW butt joints. The laser-hybrid welded joints all lie above the mean curve generated from the 20 mm thick SAW butt joints. Furthermore, the recommended fixed slope of m = 3 might even be challenged. The computed fatigue strength of the laser-hybrid welded population, excluding the run-outs, at 2 million cycles with a recommended fixed slope of m = 3, was 159.39 MPa and the characteristic fatigue strength, i.e. the lower part of the scatter band with 95% survival probability, was 136.45 MPa at 2 million cycles. The test population is however small, and the number of fractured specimens even less, totalling 16 specimens, which could be leading to optimistic results. However, based on these results, design curve FAT112 recommended by the IIW or design curve C1 would be more appropriate and even conservative for the laser-hybrid welded joints. These design curves are recommended for butt welded joints that are transversely loaded, ground flushed and 100%

NDT results.

Together these results were compared to the total population of the 20 mm and 30 mm thick SAW butt joints from both welded batches to the aforementioned results. The outcome of this, was a calculated fatigue strength of 108.36 MPa with a characteristic fatigue strength of 79.88 MPa. These results are based on excluding the run-outs, at 2 million cycles with a recommended fixed slope of m = 3.

6.4.5 Secondary bending under axial loading

The presented fatigue data measurements from the laser-hybrid welded joints are based on the respective test machine's controller readings from a verified load cell mounted in an uni-axial SHM. The resulting acquired stresses are calculated from the applied load range, ΔF [kN], and the specimens cross sectional area [mm^2], which corresponds to the nominal stress, σ_{nom}, for the welded detail, not taking into account the stresses induced by secondary bending as a result of global geometrical misalignment.

Applying equations, 2.19, 2.25 and 2.26, a stress magnification factor, K_m, for axial and angular misalignment can be derived and subsequently the bending stress can be computed at the critical location, i.e. at the welded region. The stress magnification factors are computed separately and used in conjunction with the measured nominal stress to derive a modified nominal stress, σ_{nom_mod}, for the joint. By doing this, the secondary bending stress introduced by the joint's geometrical misalignment under axial loading is taken into consideration.

All the performed fatigue tests were subjected to this increase in stress due to secondary bending and thus the detrimental effects on the fatigue resistance is already implemented in the recorded failure cycle for each specimen.

Figure 6.14 illustrates the increase in stress due to the secondary bending under axial loading derived by the application of the computed axial and angular magnification factors for each of the respective laser-hybrid welded joints tested.

Table 6.4 lists the computed average axial, $\bar{e}$, and angular, $\bar{\alpha}$, misalignments derived from the measured coordinate values for the laser-hybrid welded joints. Additionally, the average stress magnification factors for angular and axial misalignment, $\bar{K}_{ang\_m}$ and $\bar{K}_{ax\_m}$ are presented along with the combined stress magnification factor, $\bar{K}_m$ and the maximum and minimum computed values for the three laser-hybrid welded plates. The derived values for the 20 mm thick SAW butt joints are included for comparison.

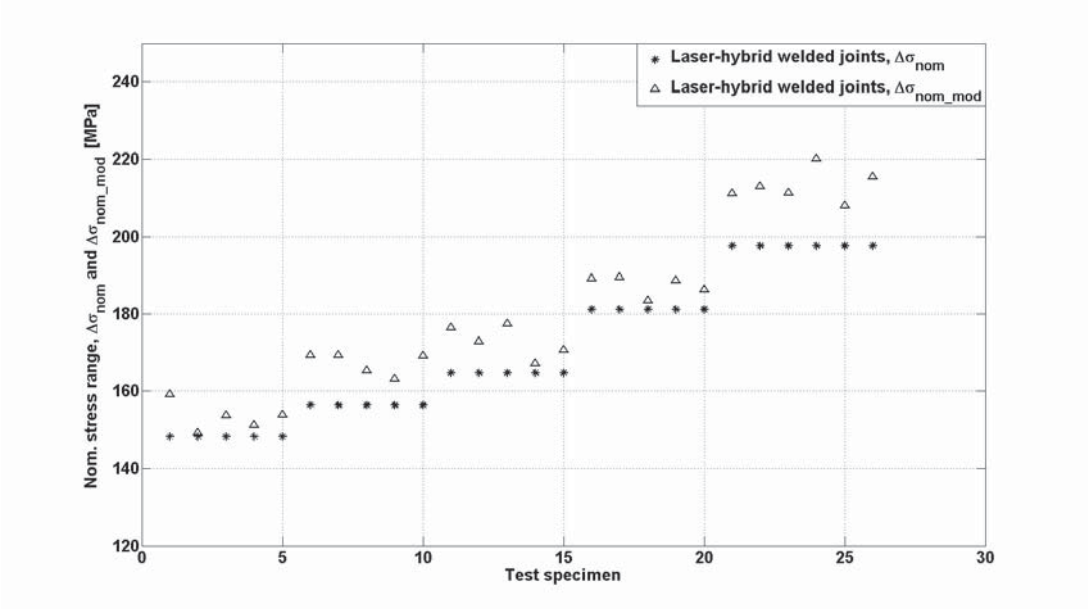

Figure 6.14: *Test series 3. Influence of the secondary bending stresses under axial loading, computed modified nominal stress* $\Delta\sigma_{nom\_mod}$

Table 6.4: *Stress magnification factors due to misalignment under axial loading*

Test Series 3 - Laser-hybrid and SAW welded butt joints							
Plate #	$\bar{\alpha}$ [deg]	$\bar{e}$ $[mm]$	$\bar{K}_{ang\_m}$	$\bar{K}_{ax\_m}$	Combined, $\bar{K}_m$	Max. K_m	Min. K_m
T25 LH plate 1	0.1905	0.2294	1.0399	1.0202	1.0602	1.1145	1.0285
T25 LH plate 2	0.1517	0.0385	1.0388	1.0040	1.0428	1.0778	1.0128
T25 LH plate 3	0.1811	0.1451	1.0459	1.0174	1.0633	1.0904	1.0077
T20 Batch 1	0.3700	0.1718	1.0994	1.0250	1.1244	1.1929	1.0589
T20_1 Batch 2	0.3819	0.2099	1.1024	1.0335	1.1359	1.3248	1.0720
T20_2 Batch 2	0.2061	0.9452	1.0539	1.1417	1.1956	1.5410	1.0106

Moreover, table 6.4 shows that the angular misalignment for all three laser-hybrid welded plates are less than the measured values for the 20 mm thick SAW butt joints. In consideration to the axial misalignments, the welding technique's setup, steel plates fit-up and clamping are significant factors. The second laser-hybrid welded plate demonstrates the lowest axial misalignment, e = 0.0385 mm, while the second SAW butt plate from batch 2 resulted in the highest measured axial misalignment or e = 0.9452 mm.

The combined stress magnification factor, $\bar{K}_m$, due to geometrical misalignments is relatively consistent for the laser-hybrid welded joints, ranging from $\bar{K}_m$ = 1.0428 to 1.0633. The corresponding stress magnification factors for the 20 mm thick SAW butt joints are however somewhat higher or ranging from $\bar{K}_m$ = 1.1244 to 1.1956. Additionally, the scatter in the derived average K_m factors is relatively consistent for the laser-hybrid welded joints, while the SAW butt joints demonstrate much larger variation between the derived maximum and minimum values.

6.4.6 Hot spot stress analysis

The computed magnification factors from the specimen's global geometrical misalignments can be utilized to estimate the stress magnification at the critical location, i.e. the center or the welded region in this case. However, this does not take into consideration the sudden local geometrical effects of the weld reinforcement parameters nor the weld notch and the corresponding stress concentrations as well as non-linear stress distributions towards the stress peak at the weld toe.

In order to take into consideration the sudden change in the structural geometry due to the weld and the corresponding increase in stress a hot spot stress analysis, σ_{HS}, was performed. According to IIW recommendations, [7], the structural hot spot stress can be determined by strain measurements, i.e. strain gauges were mounted on the specimen's surface at specific known reference points away from the weld toe. The location of the gauges is dependent on the specimen's thickness. From the resulting strain gauge readings the structural hot spot stress at the weld toe can be determined by extrapolation. The reference point closest to the weld toe has to be positioned at a sufficient distance from the weld to avoid any influences of the weld notch. The structural hot spot stress analysis does not include the non-linear effects of the weld notch.

Applying the IIW recommendations for surface stress extrapolation, equations 2.9 and 2.10 are used for determining the stresses at the welded joints hot spot for a polyno-

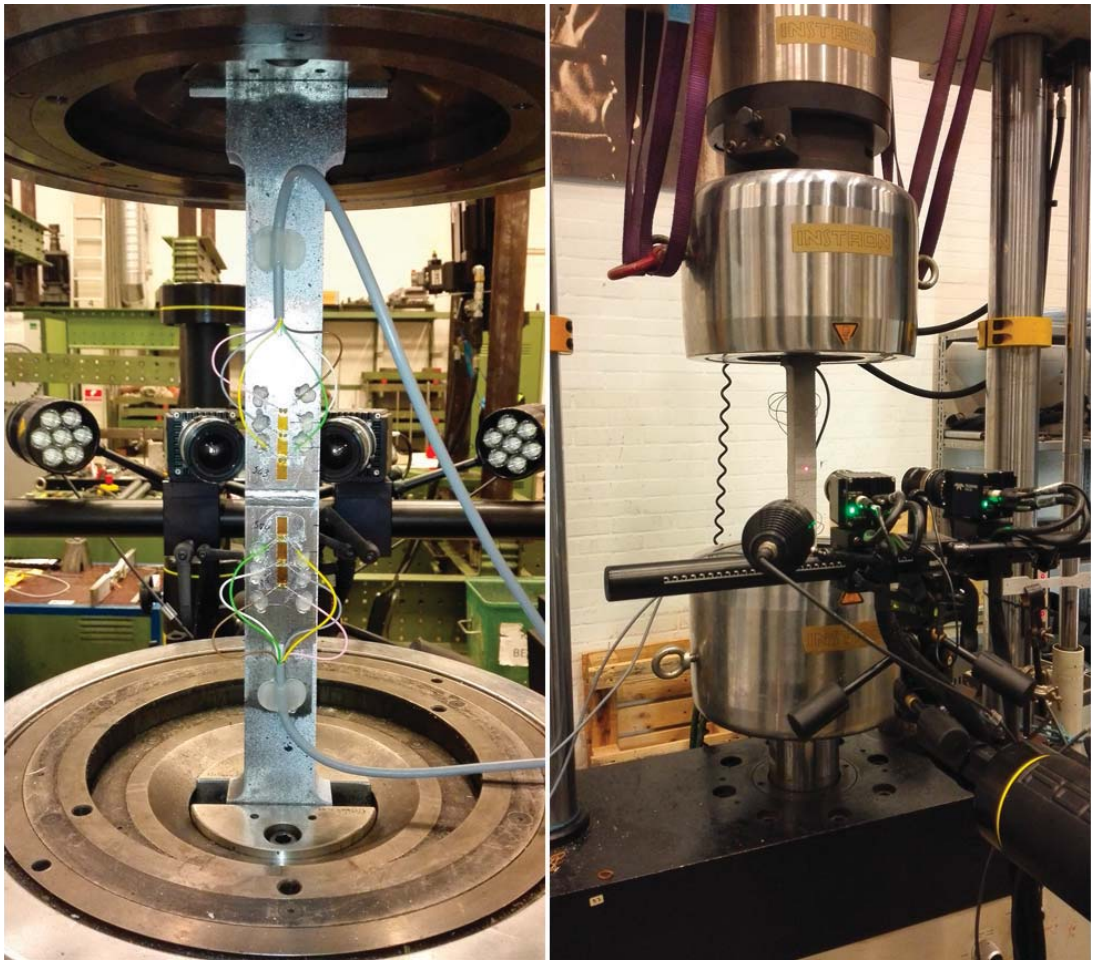

Figure 6.15: *Measurement equipment applied in order to determine the hot spot stresses, (left) strain gauges above and below the weld, (right) 3D DIC system*

mial and linear extrapolation. Three different laser-hybrid test specimens were statically tested with six strain gauges mounted, three on either side of the weld on the same surface, while a 3D digital image correlation system was used to track the full field displacements within the defined measuring volume on the opposite surface of the welded joint, i.e. the backside.

Figure 6.16 illustrates the measured strains from the static testing plotted up against the distance from the weld toe. The three measurement points on the opposite sides of the weld center are exact measurements and the last measurement point for each specimen is derived from the extrapolated polynomial curve towards the weld hot spot.

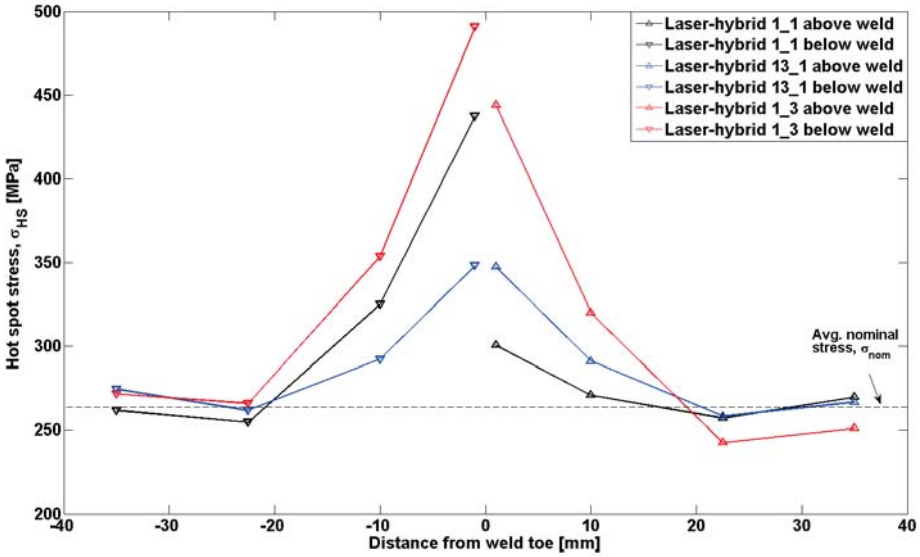

Figure 6.16: *Hot spot stress analysis for the laser-hybrid welded joints as a function of the distance from weld*

All strains have been converted into stresses by the application of the average computed E-modulus from all static tests, as the assumed stress state is close to uniaxial [7].

Figure 6.16 illustrates the obtained stresses from the strain gauges and their relative increase in stress as they approach the geometrical discontinuity, i.e. the weld. The rise in stress values is quite significant although the nominal load is at 80% of the welded joints yield strength, σ_y. In addition to the stress increase as the strain gauges approach the weld reinforcement and local geometrical changes, local plastic deformation and the welded joints straightening due to secondary bending stresses is a plausible cause for the high obtained stress values amongst other factors. There is also a noticeable inconsistency on the opposite sides of the weld, which indicates the mechanical strength differences of the applied steel. As previously mentioned, there were observed deviation in the yield strength between the two steel plates. However, the computed and applied yield strength was the obtained lower yield strength.

The ratio of the maximum obtained hot spot stresses at the weld by surface strain extrapolation from the experimental tests with respect to the nominal stress was σ_{HS}/σ_{nom} = 1.86, 1.66 and 1.32 for specimen LH 1_1, LH 1_3 and LH 13_1 respectively.

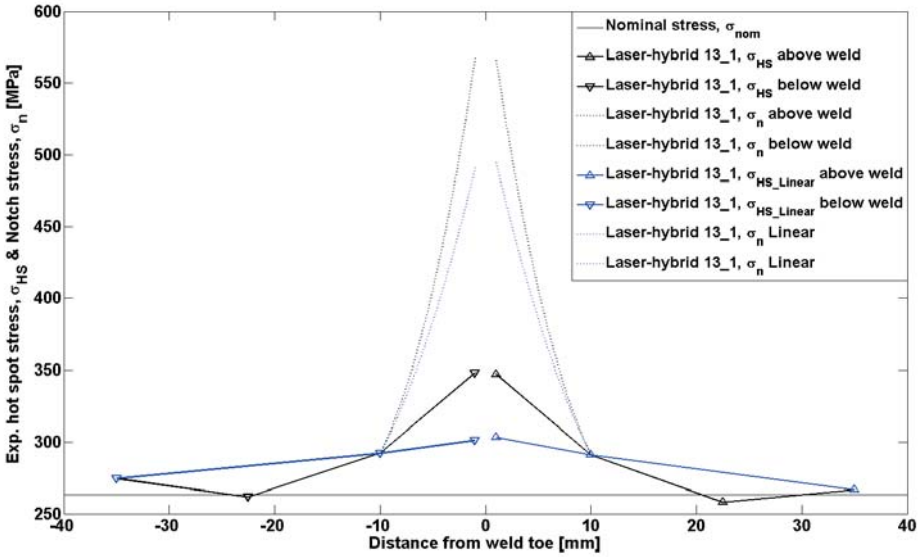

Figure 6.17: *HSS analysis for the specific case of laser-hybrid welded specimen 13_1 along with the nominal stress, modified nominal stress and notch stress according to stress magnification and concentration factors*

Figure 6.17 shows the specific case for test specimen 13_1, i.e. the specimen with the lowest measured hot spot stresses and a relative consistency from the opposite sides of the weld reinforcement. The applied nominal stress, σ_{nom}, is shown at the bottom as a solid black line and the measurement points are as well located at their respective distances from the weld toe. An additional linear extrapolation was performed between the first and last measurement points and derived towards the weld toe, illustrated in the figure as the straight blue line.

With the knowledge of the respective stress magnification factor K_m for the laser-hybrid welded joint from the global geometrical angular and axial misalignment magnification factors, K_{m_ang} and K_{m_ax}, the measured hot spot stress was decomposed into membrane, σ_{mem} and bending σ_{bend}, stresses, assuming a constant stress magnification factor K_m. Thus the peak stresses or notch stresses, σ_n, at the weld toe could be estimated according to the empirical expressions derived by Iida and Uemure, [47] and described in section 2.2.1. Equations 2.33 and 2.34 enable calculations of the axial and the bending peak stress concentration factors, $K_{t\_HS\_mem}$ and $K_{t\_HS\_bend}$ for butt welded joints by taking into account the weld reinforcement parameters as well as the notch radius. The required weld parameters were obtained from the 3D DIC system's

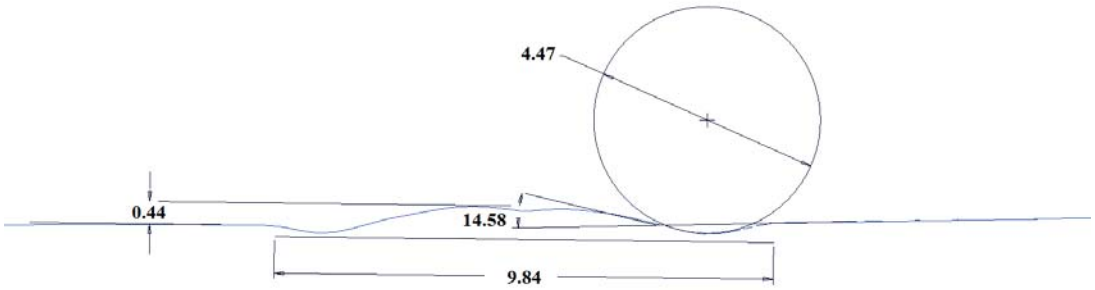

Figure 6.18: *Schematic illustration of the weld profile and weld parameter measurements for the laser-hybrid welded joint*

mapping of the test specimen's surface as illustrated in Figure 6.18. The parameters of the weld reinforcement for laser-hybrid welded joints are significantly lower than weld reinforcement parameters observed from the traditional SAW butt joints of all thicknesses as illustrated in Figure 4.35. The weld reinforcement height over the base material was 0.44 mm, the weld width approximately 9.84 mm and the weld flank angle was measured to be 14.58°. The measurement of the notch radius was not applicable, as it requires very high resolution or the right equipment, thus the IIW recommended weld notch of 1 mm was applied.

In order to determine the peak stresses at the weld notch the following relation is applied:

$$\sigma_{peak} = \sigma_{HS\_mem} * K_{t\_HS\_mem} + \sigma_{HS\_bend} * K_{t\_HS\_bend} \tag{6.1}$$

where the acquired strain gauge readings are applied to determine the stresses at the hot spot by either polynomial or linear extrapolation. Knowing the specimen's respective stress magnification factor, K_m, from the coordinate measurements, the increase in stress due to the secondary bending load was determined by [35]:

$$K_m = 1 + \frac{\sigma_{bend}}{\sigma_{axial}} \tag{6.2}$$

The magnification factor K_m is assumed to be constant throughout the static test, thus the influence of the secondary bending at the hot spot can be determined by:

$$\sigma_{HS\_bend} = (1 - K_m) * \sigma_{HS} \tag{6.3}$$

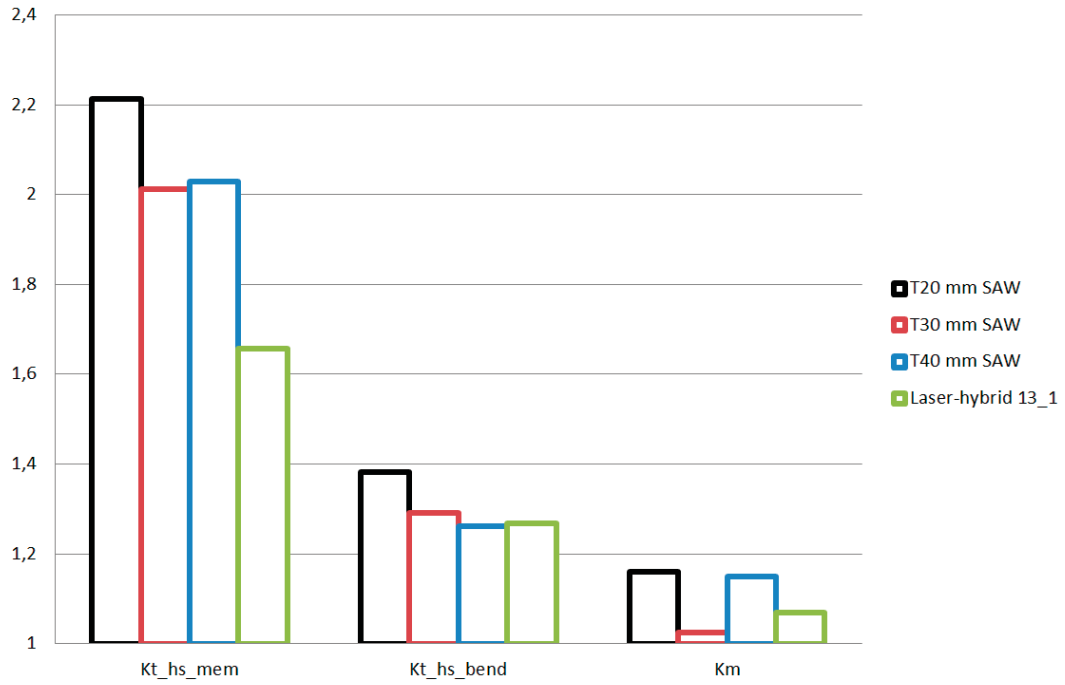

Figure 6.19: *Stress concentration factors for membrane and bending under axial loading as well as stress magnification factors due to axial and angular geometrical misalignments*

Using this information and with knowledge of the derived expressions for the peak stress concentration factors, $K_{t\_HS\_mem}$ and $K_{t\_HS\_bend}$, equation 6.1 was applied to derive the non-linear stress increase at the weld notch, i.e. the peak stress. The estimated peak stresses are illustrated in Figure 6.17 as the non-linear dotted lines approaching the weld center from opposite sides. The peak stresses were additionally estimated from a linear extrapolation, shown as the lower blue dotted lines. This was performed due to the reduction in measured strains from the gauges located in between the first and last gauges, which resulted in an increase of determined peak stresses from the three gauge polynomial extrapolation.

Figure 6.19, illustrates the derived axial and bending stress concentration factors by polynomial extrapolation, $K_{t\_HS\_mem}$ and $K_{t\_HS\_bend}$ as well as the stress magnification factor, K_m, for the laser-hybrid welded joints along with the corresponding factors resulting from the previously tested 20 mm, 30 mm and 40 mm thick SAW butt joints. The figure demonstrates the effect of the reduction in weld reinforcement parameters

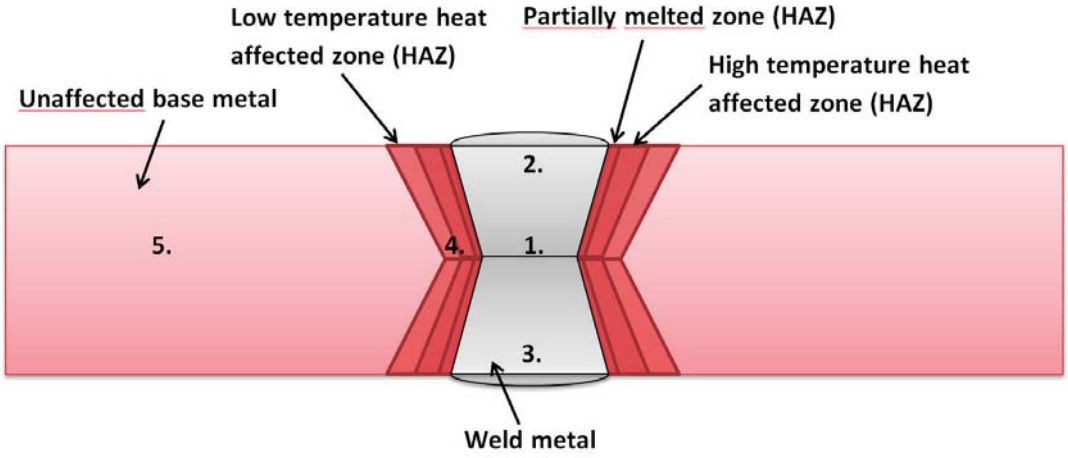

Figure 6.20: *The location of the SEM imaging and EDS regions on an ideally welded joint*

for the laser-hybrid welded joints. A direct comparison of the welding techniques is inappropriate, as the applied welded joints were subjected to different global axial and angular misalignments which results in different magnitudes of secondary bending, this is illustrated in Figure 6.19 as the columns extending from K_m. However, the most significant influence relating to the reduction of weld reinforcement parameters for the laser-hybrid welded joints is most apparent in the derived stress concentration factors for axial loading, $K_{t\_HS\_mem}$, where the laser-hybrid welded joint resulted in a $K_{t\_HS\_mem}$ = 1.66, while the 20 mm thick SAW butt joint demonstrates $K_{t\_HS\_mem}$ = 2.21.

The resulting derived peak stress to nominal stress ratio, $\sigma_{peak}/\sigma_{nom}$, equals 2.47, 2.94, 2.71 and 2.15 for the 20 mm, 30 mm, 40 mm thick SAW and laser-hybrid welded joints respectively, where the hot spot was extrapolated by a polynomial curve. The applied a linear extrapolation resulted in, $\sigma_{peak}/\sigma_{nom}$ ratios of 2.51, 2.79, 2.46 and 1.87 for the 20 mm, 30 mm, 40 mm thick SAW and laser-hybrid welded joints respectively.

6.4.7 SEM analysis

Figure 6.20, illustrates the regions where the SEM imaging and an EDS analysis was performed, with; 1) The weld center, 2) The weld's upper surface, 3) The weld's lower surface, 4) Within the heat affected zone, HAZ, and 5) In the base material.

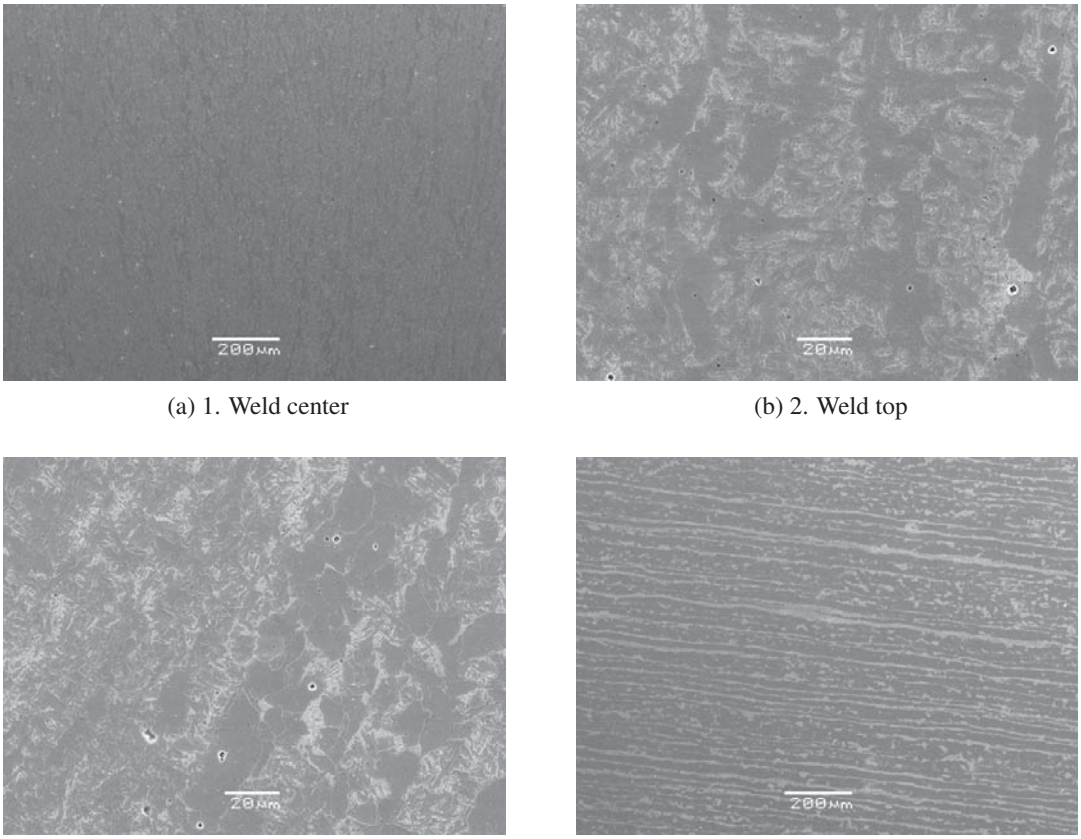

(a) 1. Weld center

(b) 2. Weld top

(c) 4. Weld HAZ

(d) 5. Base material

Figure 6.21: *SEM analysis of the SAW sample*

The EDS material compositions were consistent for every region measured, resulting in peaks for Fe (98 wt%), Mn (1.5 wt%) and Si (0.5 wt%). Figure 6.21, illustrates the SEM images for regions 1, 2, 4 and 5 for the SAW sample. In subfigure (a) at the weld center, directional columnar grains are observed and they become coarser at the weld top, as seen in subfigure (b). Subfigure (c) shows the heat affected zone on the left side of the weld where both coarse grains (high temperature) and finer grains (low temperature) are visible as faster cooling rates result in finer grains. Lastly, subfigure (d) illustrates the base material where the ferrite and small amounts of pearlite became visible along with the cold rolling direction.

For the purpose of this study, the emphasis was focused towards the weld defects within the weld zones. The defect density at the SAW samples at the center was unexpectedly

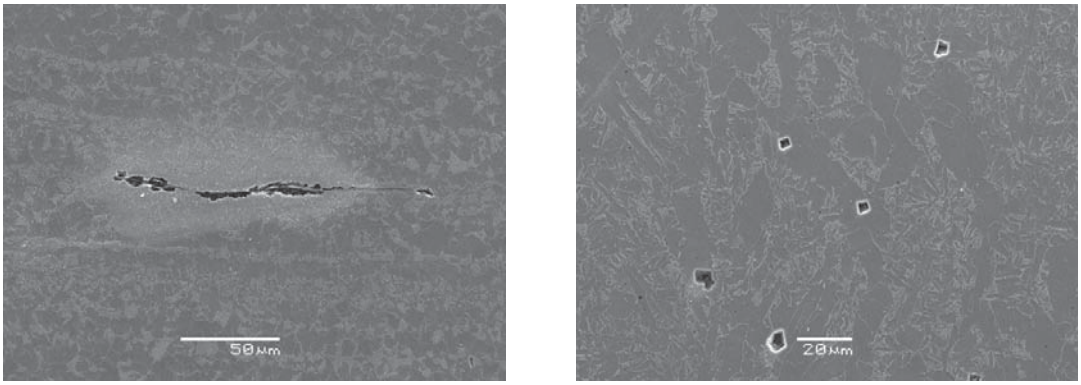

(a) HAZ large crack.

(b) HAZ large pores.

Figure 6.22: *Visible large defects within the HAZ in the SAW samples*

high, given that the specimen passed NDT according to all specifications. In addition, a number of large cracks and pores were quite visible. An illustration of weld solidification defects in the HAZ region, as shown in Figure 6.22.

Figure 6.23 illustrates the SEM images from the laser-hybrid welded samples with the respective regions specified in Figure 6.20. The EDS material compositions were consistent for every region measured, resulting in peaks for Fe (98.3 wt%), Mn (0.7 wt%), Cr (0.6 wt%) and Si (0.5 wt%). Subfigure (a) illustrates the laser-hybrid weld center with a lath martensitic microstructure and a single defect, pore, visible at the bottom. Subfigure (b) illustrates the GMA welded region at the top with a backscatter image, where a number of defects are visible. Subfigure (c) illustrates the coarse region of the heat affected zone close to the fusion line and subfigure (d) illustrates the transition from the fine grain / mixed grain heat affected zone into the base material consisting of mainly ferrite, with small amounts of pearlite.

From the SEM imaging and Figure 6.23 the reduction in defects was noticeable from within the pure laser seam welded region. In other words, the defects were infrequent and evasive where the GMA welding technique was not applied. However, in the GMA welded region a number of defects were visible.

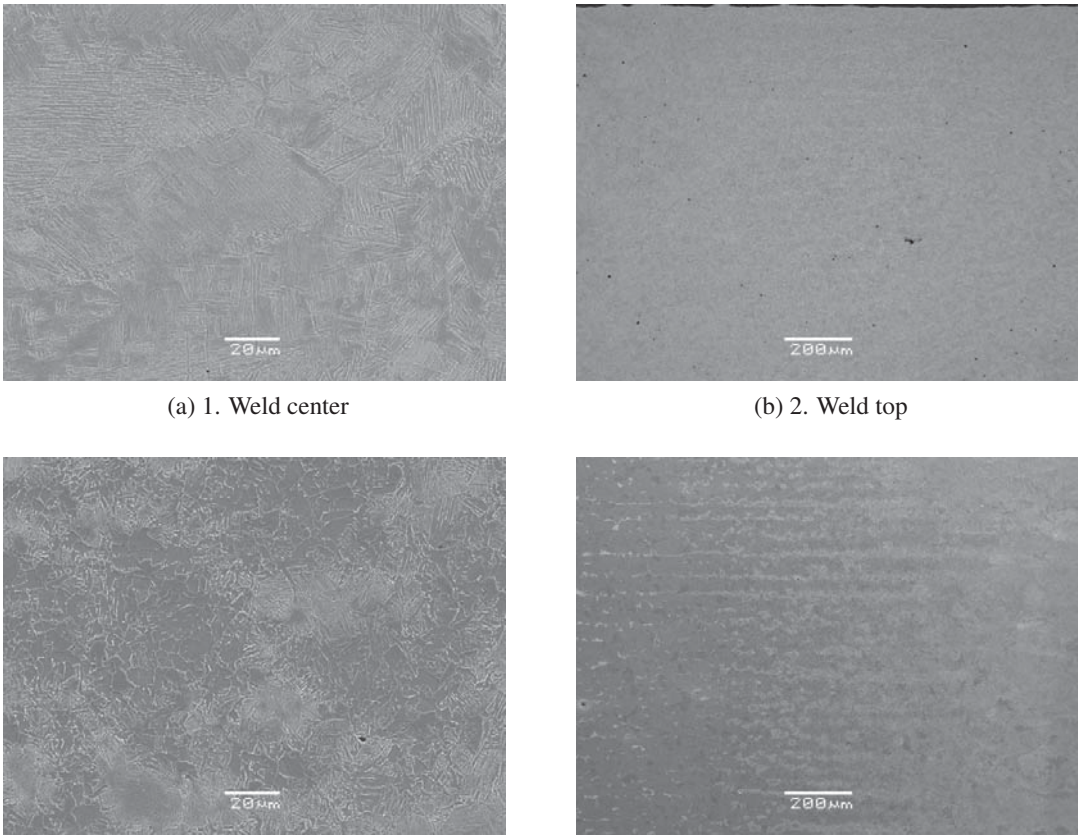

(a) 1. Weld center

(b) 2. Weld top

(c) 4. Weld HAZ

(d) "5". Transition from HAZ to the base material

Figure 6.23: *SEM analysis of the laser hybrid sample*

6.4.8 Hardness testing

Vickers hardness testing was performed on all 20 mm thick SAW samples and 25 mm thick laser-hybrid welded samples. Each sample was subjected to five indentation profiles across the welded region varying with the respective sample's height. The first profile was performed at a distance of 1 mm from the specimens upper edge and 2.5 indentation diagonals from the left edge of the sample. Following this, four subsequent profiles were made according to Figure 6.8.

The two welding techniques result in dissimilar cross sectional weld profiles, as illustrated in Figure 6.24. The laser-hybrid welded joints have a narrow through thickness seam with GMA arc welded region in the machined double-Y groove bevels on the top

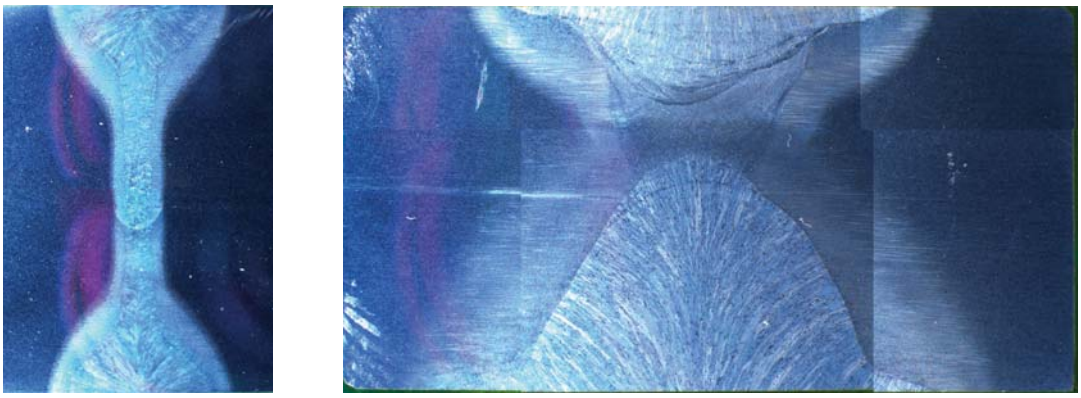

(a) Laser-hybrid welded sample

(b) SAW sample

Figure 6.24: *Leica microscopic images of (left) laser-hybrid and (right) SAW butt joints*

and bottom of the sample, and the specimen was joined in two welding passes. The SAW butt joints are welded in a machined X-groove bevel with five welding passes, with the applied filler and base material subjected to repetitive remelting and solidification processes. Additionally, as more material is required, the welded region becomes larger and the heat affected zone expands.

Figure 6.25 illustrates the resulting Vickers hardness values, HV, from the five hardness profiles for the three different SAW samples. The uppermost subfigure represents the hardness profile performed at the top of the sample while the bottom subfigures represent the hardness profiles at the samples bottom. The profile extends from the base material on the left side of the welded region progressing across the welded region towards the base material on the opposite side. The subfigures show an increase in hardness over the welded region from left to right. There are noticeable peak hardness values measured in the heat affected zone from the samples center towards the bottom.

The hardness peaks are considerably higher than the average hardness of the base material, i.e. approximately 270 HV10 compared to 175 HV10 respectively. These peaks are not observed in the upper half of the sample as the subsequent welding passes promote the tempering of prior welding passes as well as the neighbouring region of the heat affected zone. In this way, the last welding pass is not affected by any subsequent welding passes that would cause tempering of the material and lead to a reduction in hardness [112].

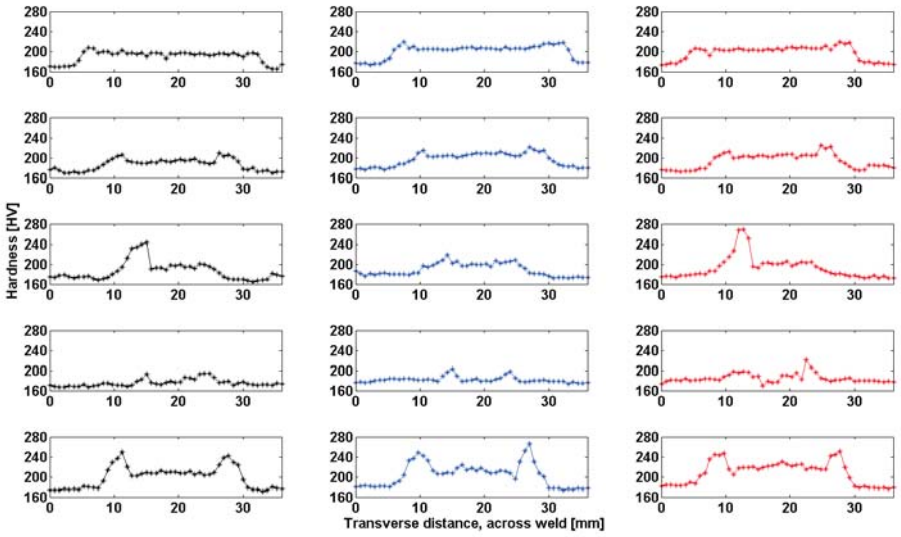

Figure 6.25: *SAW butt joints. Vickers hardness, HV, profiles across the weld*

Figure 6.26 illustrates the resulting Vickers hardness values, HV, from the five hardness profiles for the two different laser-hybrid welded samples. The subfigures show that there is a sharp increase in hardness over the welded region, where the base material approximate hardness was 150 HV10, while the welded region excluding the sample's center reaches approximately 250 HV10. The hardness values measured where only the laser welding took place, i.e. at the welded sample's center region, surpassed 300 HV10.

Additionally, the subfigures show the narrowness of the welded region from the laser-hybrid welded samples compared to the SAW samples, knowing that the SAW samples are 20% thinner.

There are expressions relating hardness to material tensile strength, σ_{ult}, and yield strength, σ_y, with quite satisfactory agreement. DS/EN ISO 18265, [113], shows conversion tables for hardness to tensile strength. However, emphasizing the involvement of considerable scatter and systematic errors where a major factor is the microstructural changes within as well as between specimens. Thus, the values recommended are only approximate values. Pavlina and Van Tyne compiled 20 years of work relating to hardness and strength values and estimated a correlation between Vickers hardness, yield strength ranging from 300 MPa to 1700 MPa, and tensile strength ranging from

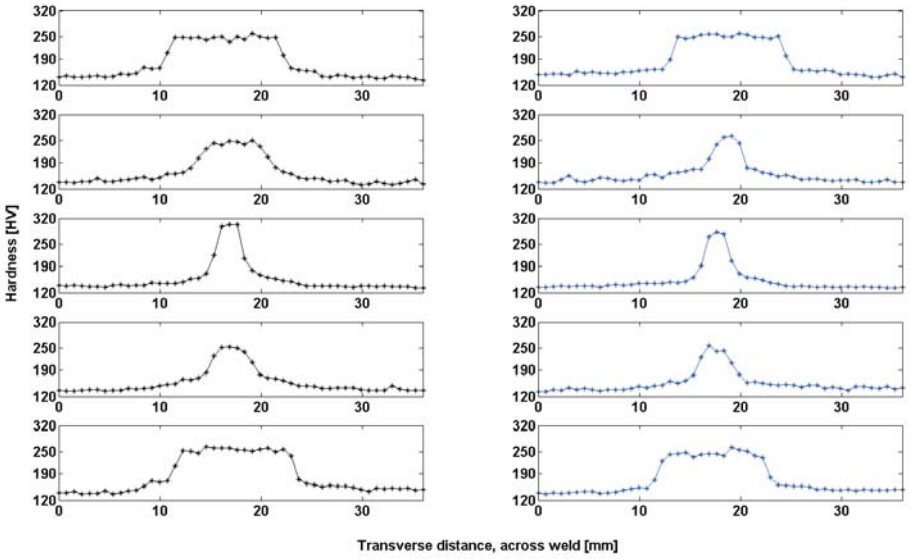

Figure 6.26: *Laser-hybrid welded joints. Vickers hardness, HV, profiles across the weld*

450 MPa to 2350 MPa [114]. According to the research a linear relationship was established between the Vickers hardness values, HV, and the entire strength range and a least square linear regression resulted in the following correlations for yield strength and tensile strength respectively:

$$\begin{aligned} \sigma_y &= -90.7 + 2.876 * HV \\ \sigma_{ult} &= -99.8 + 3.734 * HV \end{aligned} \tag{6.4}$$

Applying these expressions to the obtained hardness values for the laser-hybrid and SAW butt joints results in good agreement. The yield strength, σ_y, for the laser-hybrid welded base material results in approximately 340.7 MPa, whilst the yield strength, σ_y, for the SAW samples results in 412.6 MPa. These yield strengths were then compared to the calculated average yield strength from the static testing where $\bar{\sigma}_y$ = 330.6 MPa for the laser-hybrid welded joints and $\bar{\sigma}_y$ = 406.4 MPa for the 20 mm thick SAW samples.

Moreover, by applying these correlations to the obtained hardness results for all samples, yield strength values were derived and illustrated in a specific way in Figures

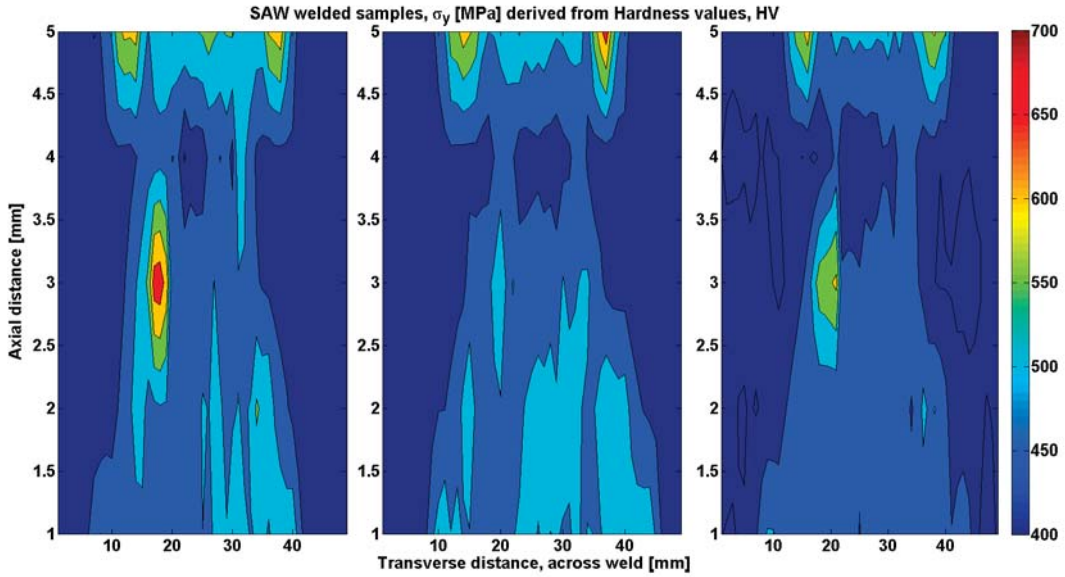

Figure 6.27: *Combined Vickers hardness profiles for the SAW samples*

6.27 and 6.28. In the figures the converted σ_y is illustrated with the respective colorbar ranging from 400 to 700 MPa and 300 to 700 MPa for the SAW and laser-hybrid welded samples respectively. The x-axis is the sample's respective length [mm] with strength values obtained transversely across the weld and the y-axis is the sample's height [mm].

The figures display the various yield strengths, σ_y, converted from hardness values within the welded region. In Figure 6.27 a consistent drop in σ_y in the SAW butt joints is noticed for all samples. This drop is located in the region of the first welding pass. This is a major concern due to all the observed defects and flaws within the welded region due to the repetitive melting and solidification of the neighbouring material.

Figure 6.28 shows the corresponding σ_y converted from hardness values for the laser-hybrid welded samples. The figure shows a much steeper gradient and the welded region is much harder and thus stronger than the base material. The laser-hybrid base material is weaker compared to the SAW samples, while the welded region on the other hand is much stronger, with the converted yield strengths of approximately 775 MPa.

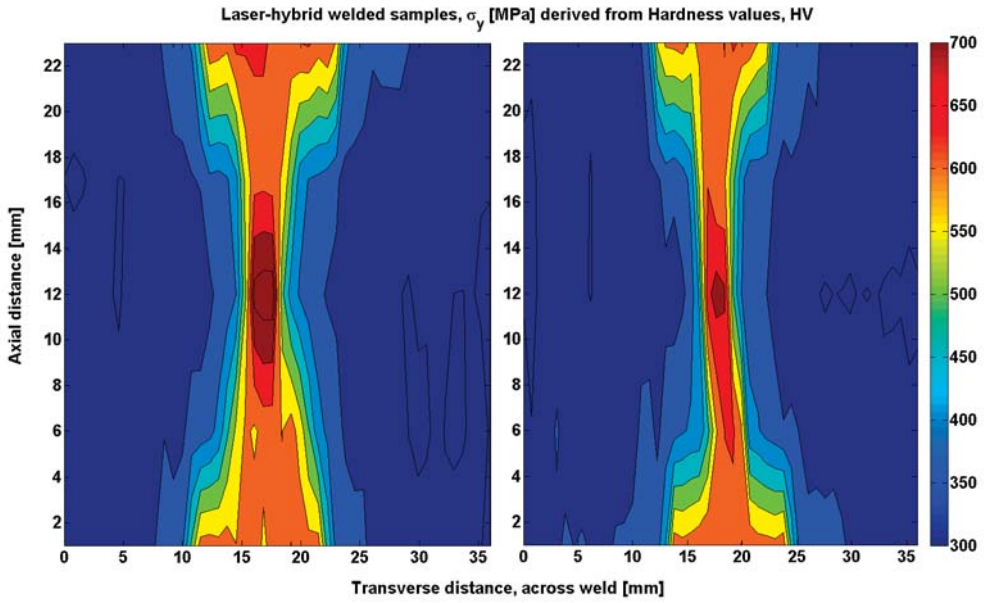

Figure 6.28: *Combined Vickers hardness profiles for the Laser-hybrid welded samples*

This page is intentionally left blank.

Chapter 7

Summary of experimental results

This chapter summarizes the main findings from each individual test series performed.

7.1 Test series 1: Experimental investigation of the thickness effect for submerged arc welded joints.

This experimental test series investigation was performed with the thickness effect as the main consideration. The thickness effect has been the topic of much debate, particularly in the recent years as structures are becoming increasingly larger and heavier. The thickness effect and the corresponding thickness correction factor used in design codes and recommendations play an influential role in those debates as it has been suggested that they might be too conservative, which leads to increased structural thicknesses if a certain fatigue strength of the structure is desired. Welding has been considered an established field where most of the experimental data and corresponding results have been presented and analysed. However, a large portion of those experiments and results were performed in the 60's and 70's. Since then there have been some major developments, changes and even breakthroughs in almost every aspect relating to the field, i.e. material, manufacturing, joining techniques, computations, etc. Thus, a motivation for further research relating to this topic was established.

The results from the performed literature review gave a basis for further investigation of the thickness effect of SAW butt joints. From the acquired collection of data, the larger welded joints, $\geq$ 25 mm, were located within the $\pm$ two standard deviations of the scatter bands from the mean results calculated for the under 25 mm thick welded joints, the thickness which is not subjected to a thickness correction. However, the thicker joints did collect in the lower half of the scatter band. From the entire dataset only two test specimens were lying outside the lower scatter band, which coincidentally coincided with the recommended design curve for this specific welded detail, i.e. butt welded joints. Another particularly interesting observation was that the extremely thick welded joints had similar fatigue strengths compared to the lower thicknesses. Thus, an indication of the thickness effect was observed, however the magnitude of the fatigue strength reduction due to thickness was not as severe as the standards and guidelines recommend.

The performed experimental fatigue testing of SAW butt joints demonstrated a similar tendency. The 20 mm thick joints demonstrated the highest fatigue resistance when compared directly to the 30 mm and 40 mm thick joints. However, almost the entire population of the larger joints tested until fracture were located within the lower scatter band of the $\pm$ two standard deviations calculated from the mean results from the 20 mm thick joints. Furthermore, the 40 mm thick joints demonstrated improved fatigue resistance when compared to the 30 mm thick joints.

After a statistical analysis of all the fatigue tests performed, a recommended homogenized population demonstrated a mean fatigue strength of 104.58 MPa with a characteristic fatigue strength of 91.24 MPa, i.e. the lower half of the scatter band. That is slightly higher than the recommended IIW FAT90 design curve for butt welded joints.

The influence of secondary bending due to axial and angular misalignments varied between the welded joints. The variation was noticeable between specimens of the same thickness as well as between thicknesses. The measured misalignments were however under the recommended limits from the standards and codes. The 20 mm thick butt welded batches demonstrated more misalignments and were therefore affected to a higher stress magnification factor, K_m. The 20 mm thick joints from the second plate manufactured from batch 2 demonstrated the largest measured misalignment and were thus affected by a corresponding stress magnification factor of $K_m = 1.20$. That is above the stress magnification factor already covered within the design FAT class in the IIW recommendations, i.e. $K_m = 1.15$.

The hot-spot stress and notch stress analysis demonstrated an increase in stress at the critical location. The increase in stress is due to the global geometrical misalignments,

weld detail discontinuities as well as the stress concentrations due to the weld reinforcement parameters and the weld notch. From the calculations, an indication of a very high notch stress for the 20 mm thick specimens from batch 2 was observed, due to a large weld profile angle. The height of the weld reinforcement was also highest for the 20 mm thick joints compared to the 30 mm and 40 mm thick SAW butt joints. The notch radius is hard to estimate, thus a fixed radius of, r = 1 mm, was assumed for all specimens. The calculated structural hot spot stresses demonstrated an increase of 18.7%, 47.2% and 41.6% in stresses for the 20 mm, 30 mm and 40 mm thick SAW joints respectively. The calculated non linear stress peak at the notch from the decomposition of the hot spot stresses, demonstrated an increase of 99%, 78% and 63% in stresses for the 20 mm, 30 mm and 40 mm thick SAW joints respectively. The peak stresses reduce with respect to thickness, contrary to what is expected. However, the large deviation in weld parameters measured between thicknesses have a considerable effect.

7.2 Test series 2: Corrosion fatigue resistance of large as-welded SAW joints in a circulating synthetic seawater environment with cathodic protection

This experimental test series related to establishing an operational corrosion testing environment in order to perform corrosion fatigue testing of large scale welded joints. Additionally, the corrosion environment was applied in order to investigate the influence of corrosion on fatigue resistance. The corrosion environment was implemented with a standardized ASTM synthetic seawater medium and an impressed current cathodic protection. The current setup enabled corrosion fatigue testing of 20 mm thick as-welded SAW butt joints. Furthermore, the obtained results from the corrosion fatigue testing was compared to identical specimens, selected from the same SAW batch, tested under in-air conditions.

The construction process of the corrosion environment was cumbersome and multiple predicaments were encountered before a working environment was functional. Initial problems concerning circulation loop leakage, slipping of the specimens and fractures in the gripping region were all accounted in the pilot testing of the environment, performed by MSc. student Laufey Gunnþórsdóttir [12].

The test specimens applied in this test series were manufactured along with the test specimens from test series 1, the thickness effect investigation. Thus all relevant data

concerning the welding procedure, non destructive testing, misalignments measurements and static testing were described in Chapter 4.

Initial corrosion tests were performed, without the corrosion environment, in order to gain knowledge and experience in working with corrosion and cathodic protection. Two SAW butt joints were submerged in ASTM synthetic seawater medium within a glass test cell, where one specimen was subjected to free corrosion while the other was cathodically protected with impressed current, ICCP. The potential changes from both specimens were monitored against a saturated calomel electrode, SCE. The test specimens were within the corrosive medium over a period of 3 days. The results demonstrated the effectiveness of the ICCP as the protected specimen did not show any signs of corrosion, while the other specimen subjected to free corrosion started corroding within the first day.

The fatigue testing of 20 mm thick SAW butt joints within the corrosion environment with ICCP applied, demonstrated fatigue resistance comparable to the welded joints tested under in-air conditions for the low cycle high stress range tests. The performance was slightly improved compared to the specimens tested under in-air conditions, with a upwards shift in the average mean stress S-N curve.

The calculated mean fatigue strength of the specimens tested in the corrosion environment at 2 million cycles was $\Delta\sigma$ = 126.67 MPa while the characteristic fatigue strength equalled $\Delta\sigma$ = 89.96 MPa, coinciding almost perfectly with the IIW recommended design curve FAT90, for butt welded structural details. This was expected as the frequency applied in the fatigue testing was 8 Hz and the corrosion is a time dependent process. Thus, any effects of corrosion along with other influences of testing within the corrosion environment were insignificant for these low cycle, high stress range tests. However, for the high cycle, low stress range tests an influence of the corrosion environment might have been identified.

The established fatigue threshold limit for the tests performed under in-air conditions was established at 80% of the respective average yield strength for the welded batch. The threshold limit was based on four specimens running out, i.e. subjected to 5 million cycles without failing, and one specimen running up till 6.3 million cycles without fracturing. The test specimens subjected to corrosion fatigue testing, within the corrosion environment with the ICCP implemented, were subjected to the same stress range, i.e. $\Delta\sigma = 0.8 * \sigma_y$, resulting in fracture for all test specimens. Furthermore, all test specimens tested at 70% of the average yield strength fractured. The corrosion fatigue test specimens tested at 60% of the average yield strength were able to run up to 5 million cycles without fracturing. Therefore, an obtained 20% reduction in fatigue strength between the tests performed in air and in a corrosion environment at 5 mil-

lion cycles. This could be an indication of stress corrosion cracking, where the effects of hydrogen embrittlement could be involved, as the steel material and weld are susceptible to hydrogen absorption in the presence of hydrogen gas and hydrogen ions. The formation of hydrogen gas in the corrosion environment was observed throughout this fatigue test series, where the potential of the specimens subjected to testing was lowered into the immune region, i.e. made more negative. The measured potential against a SCE electrode was -1.22 V corresponding to -0.98 V potential against a SHE reference electrode.

The test specimens subjected to corrosion fatigue testing with ICCP, demonstrated a thin layer of calcareous deposits on the surface. This layer was believed to be magnesium oxide, $Mg(OH)_2$, which was also indicated by FTIR and SEM analysis. This calcareous layer can be beneficial in protecting the specimen as it lowers the required current density and hinders the transport of oxygen to the specimen's surface. However, whether this surface layer is actually enhancing or limiting hydrogen uptake is receiving much attention in recent research [106].

7.3 Test series 3: Fatigue resistance of laser hybrid welded joints and a comparison to submerged arc welded joints

This experimental test series was performed in order to investigate the mechanical properties and fatigue resistance of 25 mm thick laser-hybrid welded joints. As mentioned previously, although laser and laser-hybrid welding has been around for decades, the application of laser and laser-hybrid welding has not been utilized for joining thick steel structures, i.e. thicknesses $\geq$ 20 mm. This joining technique with high powered lasers is still on the research and development stage.

The 25 mm thick laser hybrid welded steel butt joints were subjected to a variety of experimental testing and analysis. The obtained results were compared to the previously tested 20 mm thick butt joints, manufactured by the conventional and traditional SAW technique.

The 25 mm thick laser hybrid welded joints were joined in two welding passes, compared to the 4 and 7 passes which were required in welding the 20 mm and 30 mm thick SAW butt joints. The obtained welding speed of the laser welding was 200 cm/min while the maximum welding speed for the SAW technique was 40 cm/min. Together,

these factors lead to a possibility of more than 10 fold efficiency, in considering the welding speed.

The laser hybrid welded joints demonstrated low level of angular and axial misalignment and were within the recommended limits according to the standards. The laser hybrid welded joints demonstrated less misalignment compared to the 20 mm thick SAW joints. However, the level of misalignment was similar to the measured misalignments from the 30 mm thick SAW joints. The corresponding average combined stress magnification factors, calculated from the measured misalignments were, $\bar{K_m}$ = 1.0554, 1.1520 and 1.0567 for the 25 mm thick laser-hybrid welded, 20 mm and 30 mm thick SAW respectively.

The statically loaded laser-hybrid welded joints all fractured in the base material, far away from the welded region. The statically tested SAW butt joints demonstrated the same results. The laser-hybrid welded joints subjected to fatigue loading fractured in the weld region. The SAW butt joints subjected to fatigue loading demonstrated fractures in the grip region in some cases. However, all those tests were discarded in the comparison and only tests which fractured in the weld region applied.

In particular, the results from the fatigue testing of the laser-hybrid welded joints demonstrated high fatigue resistance. The entire population subjected to fatigue testing was considerably above the recommended fatigue design curve for butt welded joints in the as-welded condition. The laser-hybrid welded joints demonstrated fatigue strengths which are comparable to sound and high quality welded and post-treated butt joints from other welding techniques. The calculated fatigue strength of the laser-hybrid welded test population was 159.39 MPa, excluding the run-outs, with a recommended fixed slope of m = 3. The characteristic fatigue strength, i.e. the lower half of a $\pm$ two standard deviations of the mean strength, with 97.7% probability of survival, was 136.45 MPa. The increased fatigue resistance of the laser-hybrid welded joints could be associated with a much improved and narrower weld region, with reduced heat affected zone in addition to significantly improved weld profile parameters in the as-welded condition.

Comparing the fatigue results from the laser-hybrid welded joints to the 20 mm and 30 mm thick SAW butt joints shows considerable improvement of fatigue resistance. Additionally, the laser-hybrid welded joints had to be tested up to yield strength stress ranges, at a stress ratio of R = 0.5, in order to result in fracture. Fatigue tests with stress ranges at 90% and 95% of the calculated average yield strength were performed and resulted in test run-outs at 5 million cycles, i.e. demonstrated no signs of failure.

The laser hybrid welded joints had largely improved weld reinforcement parameters,

which led to a reduction in calculated stress concentrations at the weld toe, i.e. the weld notch. This reduction is most significant in the derived stress concentration relating to axial loading where $K_{t\_HS\_mem}$ = 1.66 for the laser-hybrid welded joints while $K_{t\_HS\_mem}$ = 2.21 for the 20 mm thick SAW joints. The stress ratio between the maximum calculated non linear peak stresses at the weld notch with respect to the specimens nominal stresses at 80% of the yield strength were, $\sigma_{peak}/\sigma_{nom}$ = 2.51, 2.79, 2.46 and 1.87 for the 20 mm, 30 mm, 40 mm thick SAW and laser hybrid welded butt joints respectively. The corresponding maximum stresses at the weld notch were equal to, σ_{peak} = 711.47 MPa, 793.64 MPa, 700.10 MPa and 494.35 MPa for the 20 mm, 30 mm, 40 mm thick SAW and laser hybrid welded butt joints respectively.

The laser-hybrid welded joints demonstrated defects and flaws when subjected to SEM-EDS analysis, though mostly in the arc welded region at the top and bottom of the samples cross section. The laser welded region in the center with a lath martensitic microstructure was almost defect free. By contrast, the SEM-EDS analysis of the SAW butt joints revealed a higher density of defects, with noticeable large pores and cracks, which would eventually allow for crack growth or propagation. This observed collection of defects identified in the weld region and HAZ of the 20 mm thick SAW butt joints could be ideal for crack initiation and would accelerate crack propagation.

The laser hybrid welded joints showed a significant increase in measured hardness values, HV, across the welded region. In the pure laser welded region, i.e. at the center, the hardness values are almost double the base material's hardness, 300 HV10 against 150 HV10. The obtained hardness values were comparable to certified hardness testing performed by Force Technology on similar test specimens. The results from the 20 mm thick SAW butt joints demonstrated an increase in hardness in the weld region compared to the base material. However, there were noticeable reductions and fluctuations in hardness values in the weld region and HAZ. These observations and corresponding hardness values indicate the effect caused by subsequent welding passes, which tempers, i.e. softens, the neighbouring material during welding and therefore influences the previously obtained hardness values.

Therefore, the combination of; 1) reduced hardness regions in the weld, 2) a high density of pores and cracks of various sizes and orientations, and 3) repetitive melting and solidification processes due to multiple welding passes, could be providing the explanation for the low fatigue resistance of the 20 mm thick SAW butt joints from batch 2.

Figure 7.1 illustrates a collection of all fatigue resistance data points acquired from the fatigue testing performed, i.e. those which failed in the weld region. The figure additionally shows the recommended design fatigue curve, IIW FAT90, for the structural

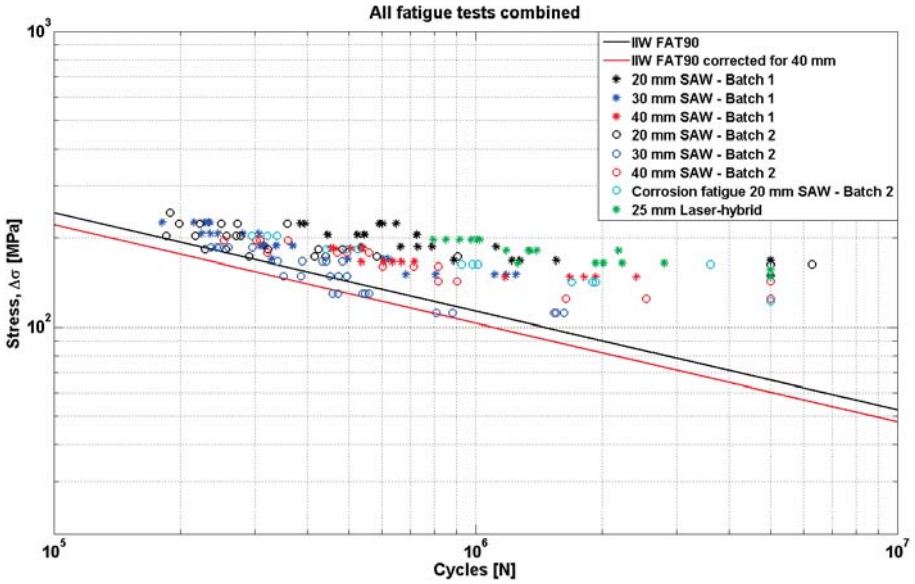

Figure 7.1: *Schematic illustration of all the performed fatigue tests along with IIW FAT90 recommended design curve*

detail of butt welded joints.

This page is intentionally left blank.

Chapter 8

Discussion

A brief description of the problem statement is reiterated, as the following section will combine the findings from the three fatigue test series performed. Thereafter address and discuss the achieved results in order to relate them to the main objectives of the overall project.

The main objectives for this project are comprehensive and vast. However, the research and experimental testing is much required in this field as previously stated. The industry is soaring and the offshore wind turbine market is becoming extremely competitive.

As mentioned in the Introduction, the two main objectives for the EUDP project were by definition:

- Drive down the cost of energy from monopile based offshore wind turbine generators.
- Monopile foundation stretch to deeper waters and/or bigger wind turbine generators.

Offshore wind turbines offer a huge potential to reduce the cost of energy by upscaling, i.e. making the wind turbines larger. Thus, increasing their capacity and the corresponding power output. Additionally, stretching further offshore, where winds are stronger. However, making the turbines larger results in much heavier structures with additional costs.

Offshore wind turbines are roughly two times more expensive than onshore wind tur-

bines. The additional cost is connected to; 1) increased raw material use and manufacturing costs associated with expensive foundations and transition structures required to construct wind turbines offshore, 2) transportation to site, 3) assembling and installing of the structure offshore, 4) connecting and placing cables offshore, 5) protecting the structure against the severe loading conditions, 6) protecting the structure from an aggressive corrosion environment, and 7) increased cost related to more demanding, challenging and weather dependent inspection and maintenance operations [2, 115].

The current project addresses the first cost factor mentioned above by providing experimental test data in order to improve the design basis for welded joints in seawater.

Thickness effect

The thickness effect investigation of welded joints, test series 1, demonstrated an indication that the current design recommendations concerning large welded joints might be on the conservative side.

This was first observed after conducting an extensive literature review which did not demonstrate the recommended large reduction in fatigue resistance of thicker welded joints. The thickness effect was evident as the thinner welded joints demonstrated an overall higher fatigue resistance. However, regarding a recommended 24.2% reduction of fatigue resistance of 100 mm thick welded joints was not observed. The majority of the thick welded joints resided within the lower scatter band of the $\pm$ two standard deviations calculated from the mean fatigue resistance of the under 25 mm thick welded joints which are applied as the reference thickness, i.e. not subjected to thickness correction.

The tendency observed in the literature review was validated by the performed experimental fatigue testing on welded joints of three different thicknesses. Two manufacturers produced the steel welded test plates, adding the influence of weld quality into the investigation. However, the 20 mm thick joints from batch 1 demonstrated the highest fatigue resistance. The 30 mm thick joints from batch 1 demonstrated a 21.4% reduction in fatigue resistance compared to the 20 mm thick joints. The 40 mm thick joints from batch 1 on the other hand demonstrated an increase in fatigue resistance when compared to the 30 mm thick joints.

This was additionally observed for the joints tested from the second welded plate, batch 2. Furthermore, the 40 mm thick welded joints from batch 2 demonstrated the highest fatigue resistance from batch 2, performing slightly better than the 20 mm thick

welded joints. The mean fatigue resistance for all fatigue tests performed, based on the nominal stress range, 50% probability of survival, are listed in Table 8.1, along with the calculated characteristic fatigue strength, 97.7% probability of survival.

The 40 mm thick joints should be subjected to a thickness correction according to recommendations from standards. The thickness correction reduces the fatigue resistance of the 40 mm thick joints by approximately 9%. Thus, lowering the recommended fatigue design curve for a 40 mm thick butt welded detail from FAT90 to FAT80 according to IIW, or from design curve D to curve E according to DNV.

The thickness effect recommendations can have considerable influences on the structural dimension on the design stage, if they are applied according to recommendations. The thickness reduction factor has no upper limit, thus the reduction in fatigue strength becomes truly significant when considering very large welded joints. New design concepts for extra large offshore wind turbine foundations, termed XXL monopiles, are estimated to have wall thicknesses up to 125 mm. Applying the thickness correction in its current form would reduce the fatigue strength of these thick joints by 27.5%.

Figure 8.1 illustrates the thickness effect, red curve, for butt welded joints in the as-welded condition. The figure shows the recommended reduction in fatigue strength as a function of wall thicknesses. Additionally, the experimental fatigue results are implemented, where the black triangles (upper) represent the joints from batch 1 and

Table 8.1: *Average fatigue resistance for all tests, mean and characteristic fatigue strength presented.*

All fatigue tests - Nominal stress range [MPa]		
thickness [mm]	PoS = 50% [mean strength]	PoS = 97.7% [Charact. strength]
T20 SAW - Batch 1	137.72	117.66
T30 SAW - Batch 1	108.32	93.19
T40 SAW - Batch 1	122.87	96.74
T20 SAW - Batch 2	105.32	85.56
T30 SAW - Batch 2	91.52	77.43
T40 SAW - Batch 2	106.57	90.06
Corrosion fatigue SAW	126.67	89.96
T25 Laser-hybrid	159.39	136.45

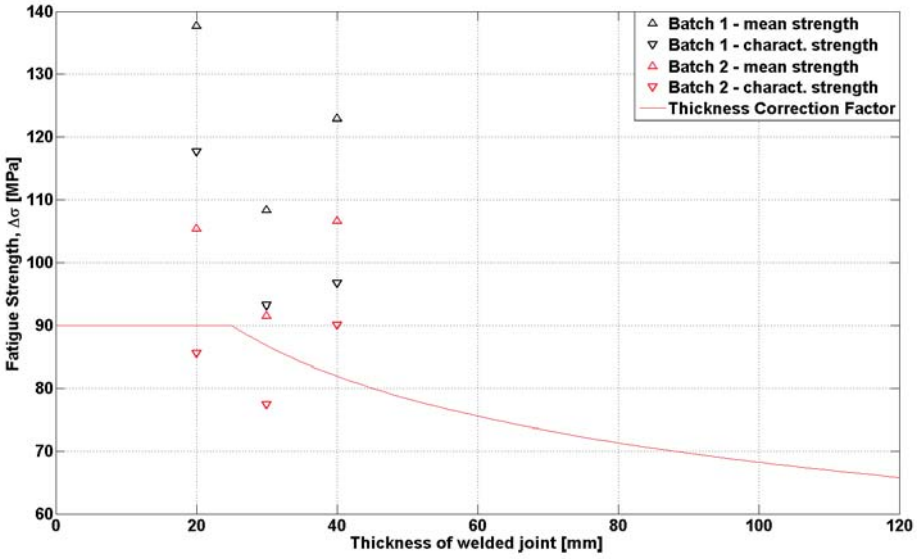

Figure 8.1: *Schematic illustration of the thickness effect. Recommended fatigue strength reduction as a function of wall thickness*

the red triangles (lower) represent the joints from batch 2.

Figure 8.1 illustrates additionally the corresponding mean, $\triangle$, and characteristic, $\bigtriangledown$, fatigue strengths from the fatigue tests performed. The figure shows the thickness effect from the performed fatigue tests with a slight downward tend. However, the 40 mm thick joints show higher fatigue resistance than the 30 mm thick joints. Furthermore, the 40 mm thick joints show a characteristic fatigue strength, with a 97.7% probability of survival, above the original recommended FAT90 curve.

Additional findings from test series 1 which are applicable for design basis of welded joints relates to the structural hot spot and peak stress analysis. The results emphasized the importance of post weld treatments in order to reduce the stress concentrations at the critical region. Reducing the weld reinforcement parameters will have beneficial effect on the welded joints fatigue resistance. The major weld reinforcement parameters which act as significant stress raisers are the weld flank angle and the weld toe radius.

Corrosion fatigue

Relating to test series 2, fatigue resistance of SAW joints in a corrosion environment, then a functional, circulating, and controlled corrosion environment with cathodic protection with the capacity to subject high loads was established. Performing corrosion fatigue tests on large welded joints is a significant step in achieving and determining reliable recommendations for structures that are subjected to high loads in an aggressive environment.

In order to simulate actual seawater conditions the experimental corrosion fatigue testing would have to be performed at seawater load frequencies which range from 0.17 Hz to 1 Hz. This was not applicable for the current project as the required test duration would span over a considerable amount of time.

The corrosion fatigue tests were performed on 20 mm thick SAW butt joints at a frequency of 8 Hz, i.e. the same frequency as the fatigue tests performed under in-air conditions. The welded joints subjected to corrosion fatigue testing did not demonstrate any reduction in fatigue resistance in the low cycle, high stress range region. However, in the high cycle, low stress range region the corrosion fatigue specimens demonstrated fatigue failures at low stress ranges. The corrosion fatigue test joints were fracturing at stress levels below the established fatigue threshold level for identical joints subjected to fatigue testing under in-air conditions.

The welded joints were protected from corrosion by cathodic protection, the ICCP technique, currently being promoted as an offshore wind turbine corrosion protection. Post test inspection and examination confirmed that the welded joints did not corrode, instead a thin layer of calcareous deposits had formed on the welded joint's surface. Material analysis of the calcareous layer deposited on the samples surface indicated after a database search a possible match with the formation of magnesium oxide, $Mg(OH)_2$, also known as Brucite. Brucite coating is beneficial in protecting the joint from corrosion by preventing oxygen and other species from accessing the joint's surface. Additionally, the calcareous layer lowers the required current density to protect the specimen.

Suggestions have been made relating to the use of this beneficial corrosion protection layer as a basis for improved corrosion protection. The proposal is to apply high initial cathodic current densities to form a thin and compact layer of beneficial deposits on the surface which would protect the structure from corrosion. Thereafter, maintaining this dense protective layer by applying the necessary lower current requirements throughout the lifetime of the structure. However, there is a great lack of experimental and real life results to verify these statements [10].

However, ongoing studies performed recently, in 2015 [106], are investigating whether the Brucite layer is actually reducing or increasing hydrogen uptake.

The hydrogen uptake, hydrogen embrittlement, of steel and welded joints invites the probability of potential catastrophic consequences. The hydrogen uptake is detrimental to the fatigue resistance of structures, especially consisting of welded joints. The hydrogen uptake reduces the ductility severely and thus makes the steel brittle. This becomes more a severe risk when considering welded joints, where discontinuities and stress raisers are already present. Additionally, the welding procedure itself can result in the presence of hydrogen and other detrimental elements in the welded region, which increases the uncertainty. Furthermore, the offshore wind turbine industry has been turning to high strength steel in order to reduce structural dimensions. This adds further complications and considerations towards the potential uptake of hydrogen, as high strength steel has less weldability and more susceptible to hydrogen embrittlement. Lastly, higher strength steels could result in higher residual stresses in the weld region.

Standard recommendations concerning fatigue resistance of welded joints in seawater with or without cathodic protection vary when compared to each other. Additionally, some recommendations do not provide any recommended fatigue resistance design curves relating to joints in a corrosion environment. The special case of free corrosion is commonly accounted for in many standards by a reduction of fatigue strength by the application of a multiplication factor of 2 or higher. The differences observed in recommendations relate to alterations in slopes, thickness correction exponents, and applied reference thicknesses. The only observed recommendation where all standards agree relates to the removal of a fatigue endurance limit.

A.R. Black et al, [56], published an article concerning on site measurements of offshore wind turbines. Their findings demonstrated a large variation in measured potential in critical regions, where the standards assume an even distribution. Additionally, they observed coating damages on several wind turbines and state that 30% of offshore foundations lack protection and fail to comply with standard specifications. The conservatism observed in standards might be a significant factor in saving many of the offshore wind turbines as owners have been very conservative on the design stage.

Laser hybrid welding

Test series 3, concerning fatigue resistance of laser hybrid welded joints, demonstrated results of superior fatigue resistance of the laser hybrid welding technique. The laser

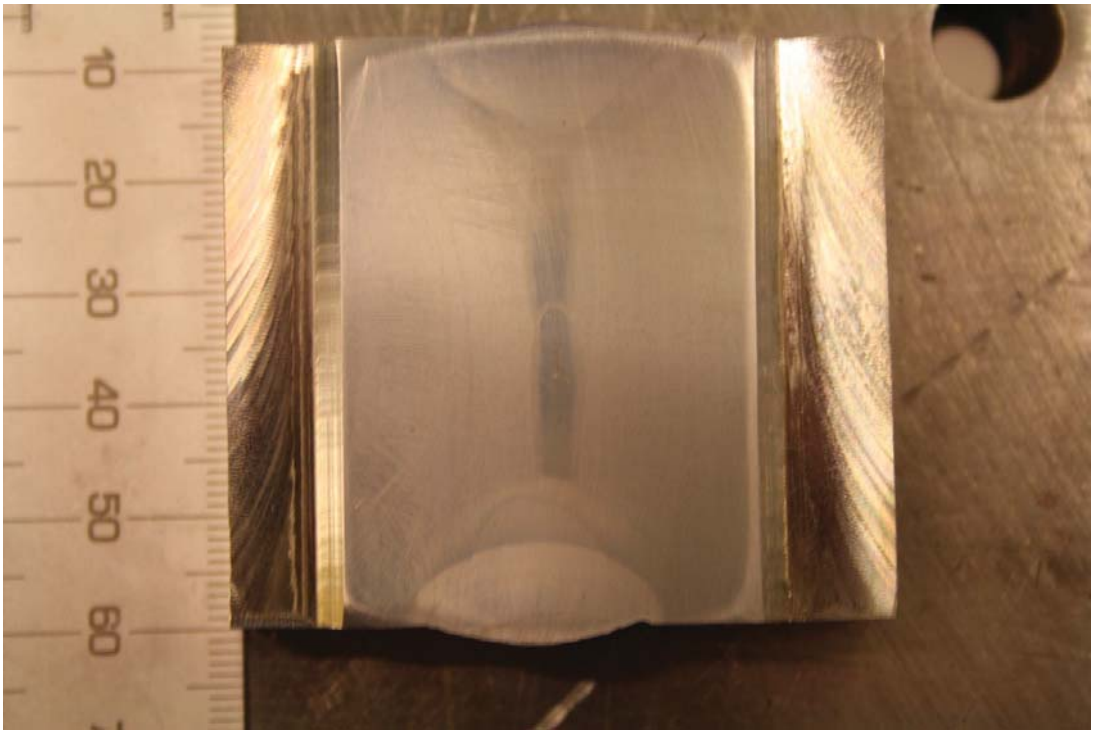

Figure 8.2: *50 mm laser hybrid welded joint, courtesy of LWT/Force Technology*

hybrid welded joints also demonstrated much improved weld region and weld reinforcement parameters. Therefore, the corresponding stress concentrations are reduced.

There is a great potential to lower the cost of energy associated with manufacturing monopiles with the laser hybrid welding technique. The major challenge is the technique's capability to produce sound and good welds for truly large steel components. The main disadvantages related to the welding technique are associated with high initial capital cost as well as the time required to setup and tune the system for a specific desired weld situation. On the contrary the benefits of the welding technique are numerous. The technique could become a significant factor or even a possible industrial breakthrough, in achieving faster, more consistent, higher quality, fully or semi-automatic production of welded monopile structures, i.e. mass production.

The laser welding technique is currently in the research and development phase. However, this technique is growing rapidly. In order to add some additional weight to that statement, then Figure 8.2, with courtesy of LWT and Force Technology, illus-

trates a 50 mm thick laser hybrid welded steel butt joint, welded from two sides in six passes.

This page is intentionally left blank.

Chapter 9

Conclusion

In this project multiple fatigue tests were performed on structural steel SAW butt joints in order to determine their fatigue resistance. Additionally, the fatigue resistance of laser hybrid welded joints of large thicknesses was determined, followed by a more detailed analysis. The fatigue testing was divided into three different test series where each test series emphasized on the influence of a particular effect concerning fatigue resistance.

The first test series investigated the effect of thickness on SAW butt joints fatigue resistance. The experimental testing was performed on three different thicknesses. The results demonstrated the presence of a thickness effect as the thicker SAW joints had a reduced fatigue resistance. However, the significance of the observed thickness effect was not as detrimental as the current standards and guidelines recommend for the design of welded structures. Therefore, the results indicate a possibility of revising the current recommendations concerning the thickness effect correction factor.

Additional results from an analysis of the structural hot spot stresses and notch stresses, demonstrated a considerable increase in stress at the welded joints critical region. The increase is due to global, and local stress raising effects of the butt welded joints including the stress concentrations due to the weld reinforcement parameters. Thus, en emphasis is made on post weld treatments in order to reduce the stress raising effects of the structural detail.

The second test series involved performing corrosion fatigue testing of 20 mm thick SAW butt joints within a corrosion environment with impressed current cathodic protection. The corrosion protection ensured that the welded joints did not corrode. How-

ever, the results demonstrated the effects of the corrosion environment by lowering the obtained fatigue threshold level, i.e. endurance limit, of the joints by 20% with respect to the calculated yield strength. This reduction is linked to observed hydrogen evolution within the test cell. The hydrogen can penetrate the steel as well as the more vulnerable weld region, causing brittleness or a less ductile behaviour.

The third test series considered validating the fatigue resistance of 25 mm thick laser hybrid welded butt joints. The laser hybrid welding technique has not been applied in the large steel construction industry, but rapid developments and breakthroughs in laser technology have cleared the path for laser welding and laser hybrid welding of thick steel joints. The results from the fatigue testing demonstrated a superior fatigue resistance of the laser hybrid welded butt joints compared to the traditional SAW butt joints. This is due to a significantly improved weld region and impressing weld reinforcement parameters, which can reduce the stress raising effects at the weld notch considerably.

Additional results from a SEM-EDS analysis demonstrated on a magnified scale that the welded region has been improved significantly. The number of noticeable discontinuities was limited in the pure laser welded region, while the arc welded region demonstrated a higher amount of discontinuities. The same analysis was performed on a SAW butt joint sample where the observed amount of discontinuities was considerably higher in addition to several noticeable large cracks.

Lastly, Vickers hardness testing was performed on the laser hybrid and SAW butt joints. The obtained hardness values for the laser hybrid welded butt joints demonstrated hardness values almost double compared to the base material and a good consistency of hardness in the weld region. The SAW butt joints demonstrated increased hardness values in the weld region. However, the hardness values were significantly lower compared to the laser hybrid welded butt joints. Furthermore, the SAW butt joints demonstrated varying hardness values in the weld region, with some hardness values showing similar hardness as in the base material. Additionally, observed hardness peaks were measured in the SAW butt joint, which indicates the last performed weld pass and thus material which has not been tempered by all subsequent welding passes.

Overall this project, motivated by personal perseverance, demonstrated the necessity to challenge suggested standard recommendations. This is particularly relevant when financially larger projects are being undertaken with an ideal target of both optimizing output and increasing longevity of these structures. This thesis undertook several challenging experimental setups and provides significant contributions into the general field of structural mechanics, with a renewed outlook in current practices and recommendations.

9.1 Further work recommendations

This project was quite comprehensive and touched upon various different fields of research. There are ample amount of future work possibilities related to each test series. In the following some recommendations are provided.

- A test series should be conducted on truly large welded joints which are currently applied in the industry, i.e. around up to 100 mm thick. Perhaps a joint venture could share the cost as it can amount to a significant figure. Establishing an experimental S-N curve for these truly large joints would help in the determination of the effect of thickness and give an increased weight to the proposition of a revised structural design recommendation from the standards.
- Performing a structural hot spot stress and notch stress analysis on an ideal post treated butt welded joint would result in useful reference data for subsequent testing on joints that are less post treated or not post treated at all. In addition to further peak stress analysis with the DIC method.
- Expanding the corrosion environment in order to perform corrosion fatigue testing in multiple installations simultaneously at the ocean level load frequency. Thus, enabling the the possibility of creating an experimental fatigue S-N curve within a corrosion environment. This is truly lacking in research and published literature. A corrosion environment expansion would also enable the following research topics.
  - This would enable corrosion fatigue testing of coatings that are applied in offshore industry.
  - This would enable testing of cathodic protection techniques, sacrificial anodes and impressed current, in a controlled environment.
  - This would enable testing of calcareous coatings and their beneficial/detrimental effects on cathodically protected steel joints under fatigue loading.
  - This would enable testing of hydrogen embrittlement for large welded joints subjected to high loading conditions and the corresponding fracture mechanisms within the base material and/or the weld region.
  - This would enable testing of various potential ranges and their efficiency or lack of efficiency in protecting the joint from corrosion. In addition to post examination of the resulting calcareous deposit formations.

  - This would enable testing of damaged/scratched/notched coating scenarios and the corresponding effects it has on the structures fatigue resistance and the effects of cathodic protection under these circumstances.
  - This would enable corrosion fatigue testing of high strength steel in a corrosion environment and the effects of cathodic protection on the steel's hydrogen uptake.
- Pursue further fatigue testing of laser hybrid and pure laser welded joints as the obtained results demonstrated great fatigue strength. Larger joints have to be tested in order for the welding technique to break into the offshore wind turbine industry.

This page is intentionally left blank.

Bibliography

[1] EWEA. The European Wind Energy Association. 2015 European Statistics. Wind in power.

[2] EWEA, The European Wind Energy Association. Deep water. The next step for offshore wind energy. July 2013.

[3] K. Weman. *Welding Processes Handbook, 2nd Edition.* Woodhead Publishing., 2012.

[4] D.R. Askeland, P.P. Fulay, and W.J. Wright. *The Science and Engineering of Materials. 6th Edition.* Cengage Learning, Inc., 2011.

[5] J. Schijve. *Fatigue of structures and materials.* Springer International Publishing., 2009.

[6] S.J. Maddox. *Fatigue strength of welded structures.* Abington Publishing, Cambridge, England, 2nd edition edition, 1991.

[7] A.F. Hobbacher. IIW (2016), Recommendations for Fatigue Design of Welded Joints and Components, IIW document IIW-2259-15., 2016.

[8] E. Niemi. *Stress Determination for Fatigue Analysis of Welded Components. IIW-1221-93 (ex doc XIII-1458-92, XV-797-92).* Abington Publishing, Cambridge, England., 1995.

[9] A. Chattopadhyay. The GR3 Method for the Stress Analysis of Weldments. Master's thesis, University of Waterloo, Waterloo, Ontario, Canada., 2009.

[10] V. Ashworth. *Shreir's Corrosion*. Elsevier Science & Technology, 4th edition. edition, 2010.

[11] M.M. Pedersen, J.G. Andersen, and O.M. Olafsson. Investigation of the thick-

ness effect for butt welded joints. *International Institute of Welding, Conference paper XIII-WG1-154-12*, 2012.

[12] L. Gunnthorsdottir. Fatigue and Fracture Testing of Welded Joints in a Corrosive Environment. Master's thesis, Technical University of Denmark, DTU, Department of Mechanical Engineering., September 2013.

[13] E. Bardal. *Corrosion and Protection.* Springer International Publishing., 2004.

[14] GWEC. Global Wind Energy Council. Global Wind Statistics. 2014. 10.02.2015.

[15] GWEC, Global Wind Energy Council. Global Wind Report. Annual Market Update 2013.

[16] EWEA, The European Wind Energy Association. The European offshore wind industry - key trends and statistics 2015. February 2016.

[17] EWEA. European Wind Energy Association. UpWind. Design limits and solutions for very large wind turbine.

[18] S. Anderson. Comparing offshore and onshore wind. *HSA 10-5 The Economics of oil and energy.*, 2013.

[19] T.R. Gurney. *Fatigue of welded structures, 2nd edition. London: Cambridge UP.* 1979.

[20] F. Brennan and I. Tavares. Fatigue design of offshore steel mono-pile wind substructures. *Energy, ICE Proceedings.*, Volume 167, Issue EN4:196–202, November 2014.

[21] S. Bhattacharya. Challenges in design of foundations for offshore wind tturbine. *IET, The Institution of Engineering and Technology.*, 2014.

[22] A.R. Tamboli. *Handbook of Structural Steel Connection Design and Details*. The McGraw-Hill Companies, Inc, 2nd edition. edition, 2010.

[23] R.L. Brockenbrough and F.S. Merritt. *Structural Steel Designer's Handbook*. McGraw-Hill, Inc, 3rd edition. edition, 1999.

[24] S. Kou. *Welding Metallurgy. 2nd Edition.* Wiley Interscience. John Wiley & Sons, Inc., 2003.

[25] R. Singh. *Applied Welding Engineering. Processes, Codes, and Standards. 2nd Edition.* Elsevier Inc., 2016.

[26] ESAB, Elektriska Svetsningsaktiebolaget. Submerged arc welding. 2008.

[27] The Lincoln Electric Company. Stick electrode. Welding Guide. Publication C2.410. 2014.

[28] *ASM Handbook. Vol. 6. Welding, Brazing and Soldering.* ASM International., 1993.

[29] W.D. Callister Jr and D.G. Rethwisch. *Materials Science and Engineering an Introduction. 8th Edition.* Jonh Wiley & Sons, Inc., 2010.

[30] American Welding Society. ANSI/AWS D1.1:2000, Structural Welding Code - Steel, 17th Ediition.

[31] S. Lampman. *Weld Integrity and Performance.* ASM International, The Materials Information Society., July, 1997.

[32] W. Schutz. A History of Fatigue. *Engineering Fracture Mechanics. Vol. 54. No. 2, pp. 263-300.*, 1996.

[33] *ASM Handbook. Vol. 19. Fatigue and Fracture.* ASM International., 1996.

[34] R.I. Stephens, A. Fatemi, R.R. Stephens, and H.O. Fuchs. *Metal Fatigue in Engineering. 2nd Edition.* John Wiley & Sons, Inc., 2001.

[35] S.J. Maddox. *Fitness-for-purpose assessment of misalignment in transverse butt welds subject to fatigue loading. IIW document XIII-1180-85.* The welding institute, Abington Hall, Cambridge CB1 6AL., 1985.

[36] DNVGL RP-C203. Det Norske Veritas - Germanischer Lloyd. DNVGL Recommended Practice, Fatigue Design of Offshore Steel Structures., June 2014.

[37] E. Niemi and G. Marquis. Introduction to the structural stress approach to fatigue analysis of plate structures. 2001.

[38] E. Niemi, W. Fricke, and S.J. Maddox. *Fatigue Analysis of Welded Components, Designer's guide to the structural hot-spot stress approach.* Woodhead Publishing, Abington Hall, Abington. Cambridge CB21 6AH, England., 2006.

[39] Ö. Örjasater. Effect of Plate Thickness on Fatigue of Welded Components. *IIW-XIII-1582-95. Internation Institute of Welding.*, 1995.

[40] F.R. Mashiri and X.L. Zhao. Thickness Effect in Welded Joints - A Review. *Proceedings of The Fifteenth International Offshore and Polar Engineering Conference.*, 2005.

[41] P.J. Haagensen, T. Slind, and Ö. Örjasaeter. Size Effects in Machine Components and Welded Joints. Technical report, The Royal Norwegian Council for Scientific and Industrial Research (NTNF)., 1988.

[42] D. Radaj., C.M. Sonsino, and W. Fricke. *Fatigue Assessment of Welded Joints by Local Approaches (Second edition).* Woodhead Publishing., 2006.

[43] S.J. Maddox. *Key Developments in the Fatigue Design of Welded Constructions. IIW Portvin Lecture.* Abington Publishing, Cambridge, England. TWI Ltd., 2003.

[44] G. Glinka, A. Chattopadhyay, M. El-Zein, and J. Qian. Stress analysis and fatigue life assessment of welded structures. iiw-xiii-2319-10. 2010.

[45] A. Chattopadhyay, G. Glinka, M. El-Zein, and J. Qian. Stress Analysis and Fatigue of Welded Structures. *Welding in the World, Vol. 55, Issue 7, pp 2-21.*, 2013.

[46] R. Goyal, M. El-Zein, and G. Glinka. A robust stress analysis method for fatigue life prediction of welded structures. *Weld World, 60:299-312.*, 2016.

[47] K. Iida and T. Uemura. Stress Concentration Factor Formulas Widely Used in Japan. *Fatigue and Fracture of Engineering Materials & Structures, Vol. 19, no.6, pp. 779-786.*, 1996.

[48] T. Palin-Luc, R. Perez-Mora, C. Bathias, G. Dominguez, P.C. Paris, and J.L. Arana. Fatigue crack initiation and growth on a steel in the very high cycle regime with sea water corrosion. *Engineering Fracture Mechanics, 77, 1953-1962.*, 2010.

[49] T.W. Thorpe, P.M. Scott, A. Rance, and D. Silvester. Corrosion fatigue of bs 4360:50d structural steel in seawater. *International Journal of Fatigue, Vol. 5, No. 3.*, 1983.

[50] W.J. Derrick Jones and A.P. Blackie. Cyclic Tension Corrosion Fatigue of High Strength Steels in Seawater. *Environmentally Assisted Cracking: Science and Engineering, ASTM STP 1049, W.B. Lisagor, T.W. Crooker, and B.N. Leis, Eds., American Society for Testing and Materials, Philadelphia, pp. 447-462.*, 1990.

[51] D.K. Mattlock, G.R. Edwards, D.L. Olson, and S. Ibarra. Effect of Sea Water on the Fatigue Crack Propagation Characteristics of Weld for Offshore Structures. *Journal of Materials Engineering, Vol. 9, No. 1.*, 1987.

[52] D.H. Kang, J.K. Lee, and T.W. Kim. Corrosion fatigue crack propagation in a

heat affected zone of high performance steel in an underunder sea environment. *Engineering Failure Analysis, 18, 557-563.*, 2011.

[53] D.H. Kang, S. Kim, C. Lee, J.K. Lee, and T.W. Kim. Corrosion fatigue behaviors of HSB800 and its HAZ in air and seawater environments. *Materials Science & Engineering, A 559, 751-758.*, 2013.

[54] C.M. Sonsino, K. Lipp, and E. Lachmann. Corrosion Fatigue of Welded High Strength Cast and Structural Steel Joints Under Constant and Variable Amplitude Loading. *Proceedings of the Fifth International Offshore and Polar Engineering Conference.*, 1995.

[55] I. Lotsberg and P.K. Larsen. Developments in Fatigue Design Standards for Offshore Structures. *Proceedings of the Eleventh International Offshore and Polar Engineering Conference.*, 2001.

[56] A.R. Black, T. Mathiesen, and L.R. Hilbert. Corrosion protection of offshore wind foundations.

[57] Det Norske Veritas. DNV-RP-B401. Recommended Practice. Cathodic Protection Design. October 2010.

[58] H. Davy. Philosophical Transactions Royal Society of London. pages 114, 151, 242, 328, 1824.

[59] R. Baboian. *Corrosion Tests and Standards. Application and Interpretation. 2nd Edition.* ASTM International., 2005.

[60] S. Berge. On the effect of plate thickness in fatigue of welds. *Engineering Fracture Mechanics, Vol. 21, No. 2, pp. 423-435.*, 1985.

[61] H. von Selle, O. Doerk, J.K. Kang, and J.H. Kim. Fatigue tests of butt welds and plates edges of 80 mm thick plates. *Advances in Marine Structures, G. Soares & Fricke (editors).*, pages 511–519, 2011.

[62] H. Polezhayeva and C. Badger. Effect of Plate Thickness on Fatigue Strength of Base Material and Butt Welded Specimen Made from EH40 Steel Thick Plates: Phase 1. *Proceedings of the Nineteenth International Offshore and Polar Engineering Conference.*, 2009.

[63] O. Doerk, W. Fricke, and H. von Selle. Validation of Different Fatigue Assessment Approaches for Thick Plate Structures Made of High Tensile Strength Steel YP47. *Proceedings of the Twenty-second (2012) International Offshore and Polar Engineering Conference.*, 2012.

[64] A. Ohta, T. Mawari, and N. Suzuki. Evaluation of effect of plate thickness on fatigue strength of butt welded joints by a test maintaining maximum stress at yield strength. *Engineering Fracture Mechanics.*, 37(5):987 – 993, 1990.

[65] H. Petershagen. IIW Guidance on Fatigue Testing of Large Scale Welded Components. *Welding in the World, Vol. 48, n 9/10.*, 2004.

[66] NACE International. The Corrosion Society. ANSI/NACE Standard TM0177-96. Item No. 21212. Standard Test Method. Laboratory Testing of Metals for Resistance to Sulfide Stress Cracking and Stress Corrosion Cracking in H2S Environments.

[67] NACE International / ASTM International. NACE TM0169/G31 - 12a. Standard Guide for Laboratory Immersion Corrosion Testing of Metals 2015.

[68] M.Z. Shah Khan, I.A. Burch, and B.J. Baxter. A Corrosion Fatigue/Stress Corrosion Testing Facility at Materials Research Laboratory. *DSTO Materials Research Laboratory.*, 1989.

[69] Y. Kumakura, M. Takanashi, A. Fuji, M. Kitagawa, M. Ojima, and Y. Kobayashi. Fatigue Strength of Coated Steel Plate in Seawater. *Proceedings of the Ninth Interanational Offshore and Polar Engineering Conference.*, 1999.

[70] Y. Kobayashi, Y. Tanaka, H. Goto, K. Matsuoka, and Y. Motohashi. Corrosion fatigue strength of ship structural steel butt welded joints in synthetic seawater. *Welding International. 13 (5), pp. 385-391.*, 1999.

[71] M.A. Wahab and M. Sakano. Experimental study of corrosion fatigue behaviour of welded steel structures. *Journal of Materials Processing Technology. 118, pp. 117-122.*, 2001.

[72] R. Perez-Mora, T. Palin-Luc, C. Bathias, and P.C. Paris. Very high cycle fatigue of a high strength steel under sea water corrosion: A strong corrosion and mechanical damage coupling. *Internation Journal of Fatigue. 74, 156-165.*, 2015.

[73] M. Grupp, K. Klinker, and S. Cattaneo. Welding of high thicknesses using a fibre optic laser up to 30 kW. *Welding International. Vol. 27, No. 2, 109-112.*, February 2013.

[74] S.E. Nielsen. High power laser hybrid welding - challenges and perspectives. *15th Nordic Laser Materials Processing Conference, Nolamp 15, 25-27, Lappeenranta, Finland.*, 2015.

[75] S. Katayama, M. Mizutani, and Y. Kawahito. Fundamental Research of 100 kW

Ultra-High Power Fiber Laser Welding. *IIW Doc. IV-1182-14. 67th IIW Annual Assembly. Commission IV. Seoul, Rep. of Korea.*, 2014.

[76] Q. Pna, M. Mizutani, Y. Kawahito, and S. Katayama. Laser-Arc Hybrid Welding Phenomena of Thick High Tensile Strength Steel Plates. *IIW Doc. XII-2245-15/IV-1236-15/212-1396-15/I-1234-15.*, 2015.

[77] C. Hojerslev. Welding of Thick Walled Steel Components with 32 kW Laser Power. 2014.

[78] F. Vollertsen, S. Grunenwald, M. Rethmeier, A. Gumenyuk, U. Reisgen, and S. Olschok. Welding Thick Steel Plates with Fibre Lasers and GMAW. *Welding in the World, Vol. 54.*, 2010.

[79] H. Remes and P. Varsta. Differences in Fatigue Strength Between Arc and Laser Hybrid Welded Joints. *Journal of Ship Production, Vol. 24, No. 3, pp. 139-146.*, August 2008.

[80] I. Huther, V. Minard, Y. Royer, and H.P. Lieurad. Burr Grinding Effect on the Fatigue Strength as Regard to Initial Weld Quality, IIW Doc. XIII-2038-04. 2004.

[81] O. Lagerqvist, M. Clarin, J. Gozzi, B. Volling, D. Pak, J. Stötzl, H.P. Lieurade, B. Depale, I. Huther, S. Herion, J. Bergers, R.M Martsch, M. Carlsson, A. Samuelsson, and C. Sonander. LiftHigh - Efficient Lifting Equipment with Extra High-Strength Steel, European Commission, EUR22569EN, Brussels. 2007.

[82] T. Wang, D. Wang, L. Huo, and Y. Zhang. Discussion on Fatigue Design of Welded Joints Enhanced by Ultrasonic Peening Treatment (UPT). *International Journal of Fatigue, 31, pp. 644-650*, 2009.

[83] T. Dickerson and C. Moura Branco. Weld Improvement Methods for Low Cycle Fatigue Applications. *EUR17823, European Commission, Brussels.*, 1997.

[84] A. Ohta, N. Suzuki, and Y. Maeda. Shift of S-N Curves with Stress Ratio. *Welding in the World, 47.*, 2003.

[85] A. Wolfenden, H. Nakamura, S. Nishijima, and I. Soya. A Method for Obtaining Conservative S-N Data for Weld Structures. *Journal of Testing and Evaluation, JTEVA, 16 (3), pp. 280-285.*, 1988.

[86] R. Oliver and W. Ritter. Wöhlerlinienkatalog für Schweissverbindungen aus Baustählen. *DVS GmbH, Düsseldorf.*, 1979.

[87] I. Weich. Ermüdungsverhalten mechanisch nachbehandelter Schweissverbindungen in Abhängigkeit des Randschichtzustands. *Ph.D. Thesis, Technischen Universität Braunschweig*, 2008.

[88] M. Kassner, M. Küppers, G. Bieker, C. Moser, and C.M. Sonsino. Fatigue design of welded components of railway vehicles - influence of manufacturing conditions and weld quality. *IIW Doc. XIII-2267-09 / XV-1313-09*, 2009.

[89] NRIM Fatigue data sheet no. 5, National Research Institute for Metals, Tokyo, Japan. 1978.

[90] J.K. Lee, T.Y. Yoon, and S.P. Chang. The Fatigue Performance of Butt-welded Joint with Thick Plates. *Research Institute of Industrial Science and Technology, RIST 17 (3), Korea*, 2003.

[91] S.W. Im. Fatigue Characteristics of EH40-TM Steel Plate. *Research Institute of Industrial Science and Technology, RIST 23 (1), Korea*, 2009.

[92] K.N. Kim, S.H. Lee, and K.S. Jung. Evaluation of Factors Affecting the Fatigue Behaviour of Butt Welded Joints using SM520C-TMC Steel. *International Journal of Steel Structures, 9 (3), pp. 185-193.*, 2009.

[93] Ö. Bucak, F. Mang, and L. Stammet. Fatigue Behaviour of Mis-matched Butt Welded Heavy I-beams and the Rotation Capacity of Joints Made of QST-steel. *Constructions in Steel Structures, 41, pp. 115-126.*, 1996.

[94] ASTM International. ASTM E1012-14, Standard Practice for Verification of Test Frame and Specimen Alignment under Tensile and Compressive Axial Force Application.

[95] Det Norske Veritas. DNV-OS-C401, Fabrication and Testing of Offshore Structures, April 2013.

[96] Dansk Standard. DS/EN ISO 5817. Welding - Fusion-welded joints in steel, nickel, titanium and their alloys (beam welding excluded) - Quality levels for imperfections. 2014.

[97] C. Fischer, W. Fricke, and C.M. Rizzo. Review of the fatigue strength of welded joints base on the notch stress intensity factor and SED approaches. *International Journal of Fatigue (84), pp. 59-66.*, 2016.

[98] ASTM International. ASTM E8/E8M - 15a. Standard Test Methods for Tension Testing of Metallic Materials.

[99] ASTM International. ASTM E111-04 (Reapproved 2010). Standard Test Method for Young's Modulus, Tangent Modulus, and Chord Modulus.

[100] DS, Dansk Standard. DS/EN ISO 6892-1. Metallic materials - Tensile testing - Part 1: Method of test at room temperature. 2009.

[101] British Petroleum. BP Statistical Review of World Energy, 64th edition. June 2015.

[102] Norsok, Standards Norway. N-004, Rev 2. Design of Steel Structures., 2004.

[103] Health and Safety Executive, HSE. Comparison of fatigue provisions in codes and standards. Offshore Technology Report 2001 / 083.

[104] ASTM International. Standard Practice for Corrosion Fatigue Testing of Metallic Implant. F1801-97 (Reapproved 2014).

[105] ASTM International. ASTM D1141-98 (Reapproved 2013). Standard Practice for the Preparation of Substitute Ocean Water.

[106] W.R. Smith and S. Paul. Natural Deposit Coatings on Steel during Cathodic Protection and Hydrogen Ingress. *Coatings. 5, 816-829; doi:10.3390/coatings504816.*, 2015.

[107] J. Cwiek. Hydrogen assisted cracking of high strength weldable steel in seawater. *Journal of Materials Processing Technology. 164-165. 1007-1013.*, 2005.

[108] N. Eliaz, A. Shachar, B. Tal, and D. Eliezer. Characteristics of hydrogen embrittlement, stress corrosion cracking and tempered martensite embrittlment in high strenght steel. *Engineering Failure Analysis, 9, 167-184.*, 2002.

[109] J. Woodtli and R. Kieselbach. Damage due to hydrogen embrittlement and stress corrosion cracking. *Engineering Failure Analysis, 7, 427-450.*, 2000.

[110] P.J. Cotterill and J.E. King. Hydrogen embrittlement contributions to fatigue crack growth in a structural steel. *International Journal of Fatigue. 13. No 6. pp 447-452.*, 1991.

[111] W.H. Hartt. 2012 Frank Newman Speller Award: Cathodic Protection of Offshore Structures - History and Current Status. *Corrosion. Vol. 68, No. 12.*, 2012.

[112] S.S.M. Tavares, C.R. Rodrigues, J.M. Pardal, E.S. Barbosa, and H.F.G. de Abreu. Effects of Post Weld Heat Treatments on the Microstructure and Mechanical Properties of Dissimilar Weld of Supermartensitic Strainless Steel. *Journal of Materials Research. 17(5): 1336-1343.*, 2014.

[113] European Committee for Standardization. Danish Standards Foundation. DS/EN ISO 18265. Metallic materials, Conversion of hardness values. 2013.

[114] E.J. Pavlina and C.J. Van Tyne. Correlation of Yield Strength and Tensile Strength with Hardness for Steel. *Journal of Materials Engineering and Performance 17:888-893. ASM International.*, 2008.

[115] IRENA. International Renewable Energy Agency. Renewable Energy Technologies: Cost analysis series. Wind Power. Vol. 1: Power Sector. Issue 5/5. June 2012.

This page is intentionally left blank.

A. Misalignment measurements, tabular data

In this Appendix all the tabular data values for the misalignment measurements are presented.

Test series 1	Batch 1	20 mm thickness						
	t [mm]	Angular [deg]	Axial [mm]	Beta_angular	Angular k_m	Axial k_m	K_mis	e / t
T20-1	20,65000	0,63594	0,23291	1,92741	1,17161	1,03384	1,20545	0,01128
T20-2	20,64000	0,95765	-0,00074	1,97203	1,25600	1,00011	1,25611	0,00004
T20-3	20,13000	0,90566	0,01520	2,02223	1,24546	1,00227	1,24772	0,00076
T20-4	20,60000	0,73048	-0,00707	2,05929	1,19185	1,00103	1,19288	0,00034
T20-5	20,60000	0,60442	-0,08874	2,05929	1,15874	1,01292	1,17167	0,00431
T20-6	20,58000	0,52805	-0,14215	2,06129	1,13876	1,02072	1,15948	0,00691
T20-7	20,60000	0,49189	-0,18060	2,05929	1,12919	1,02630	1,15549	0,00877
T20-8	20,59000	0,48970	-0,19733	1,86360	1,13441	1,02875	1,16316	0,00958
T20-9	20,62000	0,46478	0,25572	1,86089	1,12746	1,03720	1,16466	0,01240
T20-10	20,59000	0,44675	0,26847	1,86360	1,12262	1,03912	1,16173	0,01304
T20-11	20,60000	0,44111	0,29050	1,86270	1,12104	1,04231	1,16334	0,01410
T20-12	20,61000	0,43443	-0,26970	1,86179	1,11917	1,03926	1,15843	0,01309
T20-13	20,60000	0,39766	0,28645	1,86270	1,10912	1,04172	1,15083	0,01391
T20-14	20,57000	0,37933	-0,27950	1,86541	1,10417	1,04076	1,14494	0,01359
T20-15	20,57000	0,35726	-0,26230	1,86541	1,09811	1,03825	1,13637	0,01275
T20-16	20,61000	0,32671	-0,25401	1,96250	1,08765	1,03697	1,12462	0,01232
T20-17	20,55000	0,32523	0,23459	1,96823	1,08740	1,03425	1,12164	0,01142
T20-18	20,59000	0,28906	-0,20370	1,96441	1,07759	1,02968	1,10727	0,00989
T20-19	20,61000	0,28624	0,18276	1,96250	1,07679	1,02660	1,10339	0,00887
T20-20	20,58000	0,32766	-0,12084	1,96536	1,08798	1,01761	1,10559	0,00587
T20-21	20,59000	0,31305	0,08833	1,96441	1,08403	1,01287	1,09690	0,00429
T20-22	20,60000	0,30449	0,03033	1,96345	1,08171	1,00442	1,08613	0,00147
T20-23	20,60000	0,27101	-0,03345	2,05929	1,07118	1,00487	1,07605	0,00162
T20-24	20,60000	0,22043	-0,07241	2,05929	1,05789	1,01055	1,06844	0,00352
T20-25	20,60000	0,17762	-0,12836	2,05929	1,04665	1,01869	1,06534	0,00623
T20-26	20,64000	0,14544	-0,17304	2,05530	1,03816	1,02515	1,06331	0,00838
T20-27	20,62000	0,11342	0,20422	2,14877	1,02916	1,02971	1,05887	0,00990
T20-28	20,64000	0,11326	-0,23625	2,14669	1,02910	1,03434	1,06344	0,01145
T20-29	20,72000	0,12973	-0,25058	2,13840	1,03327	1,03628	1,06955	0,01209
T20-30	20,64000	0,12575	-0,25362	2,14669	1,03231	1,03686	1,06918	0,01229
T20-31	20,57000	0,14432	-0,24501	2,15399	1,03715	1,03573	1,07288	0,01191
T20-32	20,58000	0,16508	-0,23033	2,15295	1,04248	1,03358	1,07606	0,01119
T20-33	20,59000	0,21912	-0,17149	1,86360	1,06014	1,02499	1,08513	0,00833
T20-34	20,56000	0,29703	-0,12153	1,75958	1,08350	1,01773	1,10124	0,00591
T20-35	20,07000	0,38746	0,09979	2,02371	1,10529	1,01492	1,12021	0,00497
T20-36	20,13000	0,37282	0,07321	2,01086	1,10130	1,01091	1,11221	0,00364

Figure 1: *Measured misalignments on the 20 mm thick plate from batch 1*

Test series 1	Batch 1	30 mm thickness					
	t [mm]	Angular [deg]	Axial [mm]	Beta_angular	Angular k_m	Axial k_m	e / t
T30-1	30,29000			1,43047			0,00000
T30-2	30,35000	0,03870	-0,06024	1,47567	1,00781	1,00595	0,00198
T30-3	30,38000	0,11726	-0,08161	1,48137	1,02362	1,00806	0,00269
T30-4	30,43000	0,16393	-0,05275	1,40113	1,03348	1,00520	0,00173
T30-5	30,42000	0,21176	0,01320	1,47740	1,04263	1,00130	0,00043
T30-6	30,44000	0,28609	0,17332	1,47643	1,05757	1,01708	0,00569
T30-7	30,43000	0,29600	-0,26241	1,40113	1,06045	1,02587	0,00862
T30-8	30,45000	0,30269	-0,25975	1,40021	1,06179	1,02559	0,00853
T30-9	30,42000	0,29328	-0,21763	1,40159	1,05991	1,02146	0,00715
T30-10	30,33000	0,30804	-0,15235	1,40575	1,06306	1,01507	0,00502
T30-11	30,45500	0,32468	-0,08823	1,31991	1,06726	1,00869	0,00290
T30-12	30,44000	0,31237	-0,01294	1,32056	1,06473	1,00127	0,00042
T30-13	30,45000	0,30332	0,04566	1,32013	1,06284	1,00450	0,00150
T30-14	30,41000	0,28844	0,14470	1,32186	1,05982	1,01427	0,00476
T30-15	30,33000	0,25656	0,27043	1,32535	1,05331	1,02675	0,00892
T30-16	30,44000	0,25101	0,31874	1,47643	1,05051	1,03141	0,01047
T30-17	30,44000	0,23837	0,31196	1,47643	1,04797	1,03074	0,01025
T30-18	30,41000	0,23288	0,36741	1,47789	1,04689	1,03625	0,01208
T30-19		0,21944	0,35750				
T30-20	30,45000	0,20433	0,31497	1,54799	1,04052	1,03103	0,01034
T30-21	30,43000	0,19787	0,20942	1,54900	1,03926	1,02065	0,00688
T30-22	30,47000	0,19741	0,10147	1,54697	1,03913	1,00999	0,00333
T30-23	30,47000	0,18478	0,04601	1,54697	1,03663	1,00453	0,00151
T30-24	30,42000	0,17979	0,04072	1,61841	1,03519	1,00402	0,00134
T30-25	30,45000	0,15845	0,04121	1,54799	1,03142	1,00406	0,00135
T30-26	30,39000	0,15794	-0,04066	1,62001	1,03093	1,00401	0,00134
T30-27	30,40500	0,12967	-0,04283	1,61921	1,02539	1,00423	0,00141
T30-28	30,43000	0,12558	-0,03965	1,61788	1,02457	1,00391	0,00130
T30-29	30,42000	0,11557	-0,04575	1,61841	1,02262	1,00451	0,00150
T30-30	30,34500	0,10911	-0,01946	1,28718	1,02282	1,00192	0,00064
T30-31		0,10253	-0,01688				
T30-32		0,10059	0,02421				
T30-33		0,07337	0,10665				
T30-34		0,07130	0,21376				
T30-35	30,37000	0,05352	0,28938	1,48597	1,01077	1,02859	0,00953
T30-36	30,39000	0,06077	0,33047	1,47589	1,01225	1,03262	0,01087

Figure 2: *Measured misalignments on the 30 mm thick plate from batch 1*

Test series 1	Batch 1	40 mm thickness						
	t [mm]	Angular [deg]	Axial [mm]	Beta_angular	Angular k_m	Axial k_m	combined	e / T
T40-1	40,52000	0,22091	0,74242	0,99789	1,03629	1,05497	1,09126	0,01832
T40-2	40,58000	0,15512	0,63583	1,01396	1,02538	1,04701	1,07239	0,01567
T40-3	40,52000	0,13871	0,59255	1,02042	1,02271	1,04387	1,06658	0,01462
T40-4	40,46000	0,13139	0,57752	1,01870	1,02155	1,04282	1,06437	0,01427
T40-5	40,63000	0,17008	0,60620	1,01444	1,02779	1,04476	1,07255	0,01492
T40-6	40,51000	0,15906	0,54107	1,01744	1,02606	1,04007	1,06613	0,01336
T40-7	40,73500	0,14021	0,54313	1,01182	1,02286	1,04000	1,06286	0,01333
T40-8	40,50500	0,17223	0,51717	1,01757	1,02822	1,03830	1,06652	0,01277
T40-9	40,53000	0,16473	0,43891	1,01694	1,02698	1,03249	1,05946	0,01083
T40-10	40,59000	0,16474	0,42034	1,01543	1,02694	1,03107	1,05801	0,01036
T40-11	40,49500	0,19610	0,53025	1,01782	1,03214	1,03928	1,07142	0,01309
T40-12	40,48500	0,19777	0,51207	1,01807	1,03242	1,03795	1,07036	0,01265
T40-13	40,54000	0,19589	0,55260	1,06631	1,03183	1,04089	1,07272	0,01363
T40-14	40,55000	0,19909	0,48000	1,06605	1,03234	1,03551	1,06785	0,01184
T40-15	40,63000	0,22266	0,20334	1,06395	1,03611	1,01501	1,05112	0,00500
T40-16	40,61000	0,24553	0,23811	0,96285	1,04045	1,01759	1,05804	0,00586
T40-17	40,51500	0,25655	0,27468	0,96511	1,04235	1,02034	1,06269	0,00678
T40-18	40,60000	0,25487	0,52086	0,96309	1,04200	1,03849	1,08049	0,01283
T40-19	40,55000	0,32035	0,33987	0,96428	1,05284	1,02514	1,07799	0,00838
T40-20	40,51500	0,33378	0,32666	0,96511	1,05510	1,02419	1,07929	0,00806
T40-21	40,54000	0,34383	0,37693	0,96451	1,05673	1,02789	1,08462	0,00930
T40-22	40,61000	0,33138	0,25200	0,90779	1,05502	1,01862	1,07364	0,00621
T40-23	40,59000	0,35577	0,27600	0,90823	1,05909	1,02040	1,07949	0,00680
T40-24	40,58000	0,36857	0,19067	0,90846	1,06123	1,01410	1,07533	0,00470
T40-25	40,53000	0,38032	0,25552	0,90958	1,06325	1,01891	1,08217	0,00630
T40-26	40,58500	0,38033	0,20476	0,90834	1,06318	1,01514	1,07832	0,00505
T40-27	40,58000	0,36952	0,13001	0,90846	1,06139	1,00961	1,07100	0,00320
T40-28	40,54000	0,37268	0,19710	0,90935	1,06197	1,01459	1,07656	0,00486
T40-29	40,57000	0,38389	0,26239	0,90868	1,06379	1,01940	1,08320	0,00647
T40-30	40,51000	0,34272	0,28172	0,91003	1,05703	1,02086	1,07789	0,00695
T40-31	40,53000	0,37087	0,35995	0,90958	1,06168	1,02664	1,08833	0,00888
T40-32		0,35827	0,31097					
T40-33		0,31823	0,25028					
T40-34	40,58000	0,33648	0,22235	0,90846	1,05590	1,01644	1,07234	0,00548
T40-35	40,53000	0,33865	0,38073	1,01542	1,05547	1,02818	1,08365	0,00939
T40-36	40,53000	0,38001	0,43274	0,98424	1,06253	1,03203	1,09456	0,01068

Figure 3: *Measured misalignments on the 40 mm thick plate from batch 1*

Test series 1	Batch 2	20 mm thickness	Plate 1					
	t [mm]	Angular [deg]	Axial [mm]	Beta_angular	Angular k_m	Axial k_m	combined	e / T
B2 T20-1	19,87000	0,33914	0,36655	2,34490	1,08647	1,05534	1,14181	0,01833
B2 T20-2	19,87500	0,03384	0,41481	1,95783	1,00943	1,06261	1,07204	0,02074
B2 T20-3	19,91000	0,29426	0,40396	2,08933	1,07942	1,06087	1,14029	0,02020
B2 T20-4	19,83500	0,18238	0,42057	1,96178	1,05085	1,06361	1,11446	0,02103
B2 T20-5	19,89500	0,33219	0,34667	2,33770	1,08473	1,05227	1,13701	0,01733
B2 T20-6	19,82500	0,31213	0,30013	2,34595	1,07975	1,04542	1,12516	0,01501
B2 T20-7	19,84500	0,25203	-0,15084	2,34359	1,06436	1,02280	1,08716	0,00754
B2 T20-8	19,86500	0,25922	0,17423	2,22109	1,06804	1,02631	1,09435	0,00871
B2 T20-9	19,82000	0,21448	-0,11514	2,22613	1,05636	1,01743	1,07378	0,00576
B2 T20-10	19,81500	0,23054	0,17193	2,22669	1,06058	1,02603	1,08661	0,00860
B2 T20-11	19,81000	0,22308	-0,08627	1,85969	1,06369	1,01307	1,07676	0,00431
B2 T20-12	19,79500	0,20072	-0,12507	1,81992	1,05785	1,01895	1,07681	0,00625
B2 T20-13	19,64000	0,35197	-0,15667	1,83429	1,10193	1,02393	1,12586	0,00783
B2 T20-14	19,82500	0,23268	0,32547	1,96277	1,06489	1,04925	1,11414	0,01627
B2 T20-15	19,75000	0,29452	-0,22227	1,97022	1,08231	1,03376	1,11607	0,01111
B2 T20-16	19,79500	0,26362	0,34388	1,96574	1,07358	1,05212	1,12570	0,01719
B2 T20-17	19,78000	0,35162	-0,10202	1,96723	1,09819	1,01547	1,11366	0,00510
B2 T20-18	19,83500	0,42656	0,02781	2,09723	1,11535	1,00421	1,11956	0,00139
B2 T20-19	19,66500	0,73466	0,04126	2,11536	1,19956	1,00629	1,20586	0,00206
B2 T20-20	19,77000	1,13000	0,12326	2,10412	1,30611	1,01870	1,32481	0,00616
B2 T20-21	19,80500	0,74716	-0,00230	2,10040	1,20221	1,00035	1,20256	0,00011
B2 T20-22	19,83500	0,49787	-0,08779	2,22445	1,13077	1,01328	1,14405	0,00439
B2 T20-23	19,81000	0,54469	-0,05379	1,96259	1,15203	1,00815	1,16017	0,00269
B2 T20-24	19,78500	0,63110	0,04690	2,23007	1,16597	1,00711	1,17308	0,00235
B2 T20-25	19,88000	0,46079	0,30560	2,21941	1,12090	1,04612	1,16701	0,01528
B2 T20-26	19,78000	0,38704	-0,54145	2,37933	1,09834	1,08212	1,18046	0,02707

Figure 4: *Measured misalignments on the 20 mm thick plate from batch 2 plate 1*

Test series 1	Batch 2	20 mm thickness	Plate 2					
	t [mm]	Angular [deg]	Axial [mm]	Beta_angular	Angular k_m	Axial k_m	combined	e / t
B2 T20-1	19,89000	0,00993	-0,05350	2,33791	1,00253	1,00807	1,01060	0,00267
B2 T20-2	19,80000	0,19549	0,21315	2,10093	1,05291	1,03230	1,08521	0,01066
B2 T20-3	19,72500	0,15088	0,56339	2,10892	1,04092	1,08569	1,12661	0,02817
B2 T20-4	19,78000	0,05122	0,85096	2,10306	1,01387	1,12906	1,14293	0,04255
B2 T20-5	19,74500	0,07986	0,99855	2,10679	1,02165	1,15172	1,17336	0,04993
B2 T20-6	19,75000	0,09750	1,27011	2,10625	1,02643	1,19293	1,21935	0,06351
B2 T20-7	19,74500	0,07706	1,42938	2,23458	1,02028	1,21718	1,23746	0,07147
B2 T20-8	19,70000	0,04703	1,45563	2,23969	1,01239	1,22167	1,23406	0,07278
B2 T20-9	19,75000	0,00764	-1,39866	2,17108	1,00204	1,21245	1,21449	0,06993
B2 T20-10	19,55000	0,02909	1,48986	2,19329	1,00781	1,22862	1,23643	0,07449
B2 T20-11	19,72000	0,02398	-1,39716	2,17438	1,00641	1,21255	1,21896	0,06986
B2 T20-12	19,70500	0,01356	1,44702	2,36024	1,00347	1,22030	1,22377	0,07235
B2 T20-13	19,72000	0,06590	1,38292	2,35845	1,01688	1,21038	1,22726	0,06915
B2 T20-14		0,09215	1,29908					0,06495
B2 T20-15	19,76000	0,11075	1,00620	2,35367	1,02834	1,15276	1,18110	0,05031
B2 T20-16	19,72500	0,13164	0,12113	2,35785	1,03371	1,01842	1,05213	0,00606
B2 T20-17	19,72500	0,15902	-0,69505	2,47293	1,03964	1,10571	1,14535	0,03475
B2 T20-18	19,69500	0,18278	-0,49297	2,47670	1,04559	1,07509	1,12068	0,02465
B2 T20-19	19,72000	0,22165	-0,30054	2,47356	1,05526	1,04572	1,10098	0,01503
B2 T20-20	19,72000	0,31226	0,10208	2,47356	1,07785	1,01553	1,09337	0,00510
B2 T20-21	19,69000	0,37431	0,33942	2,47733	1,09337	1,05172	1,14509	0,01697
B2 T20-22	19,69000	0,44378	0,58909	2,58748	1,10788	1,08976	1,19763	0,02945
B2 T20-23	19,68500	0,48516	0,84392	2,36264	1,12435	1,12861	1,25296	0,04220
B2 T20-24	19,68000	0,56152	1,10435	2,17880	1,15022	1,16835	1,31857	0,05522
B2 T20-25	19,68500	0,66439	1,35199	2,17825	1,17772	1,20604	1,38376	0,06760
B2 T20-26	19,78000	1,06516	1,75252	2,30746	1,27521	1,26580	1,54101	0,08763
B2 T20-27	19,79000	0,83081	1,57273	2,36135	1,21187	1,23841	1,45029	0,07864

Figure 5: *Measured misalignments on the 20 mm thick plate from batch 2 plate 2*

Test series 3	Laser hybrid	25 mm thickness						
	t [mm]	Angular [deg]	Axial [mm]	Beta_angular	Angular k_m	Axial k_m	combined	e / t
LH-2	25,05000	0,33820	-0,05410	1,82445	1,08395	1,00648	1,09043	0,00216
LH-3	25,07000	0,31457	0,01130	1,62202	1,08143	1,00135	1,08278	0,00045
LH-4	25,07000	0,30614	-0,02850	1,62202	1,07925	1,00341	1,08266	0,00114
LH-5	25,08000	0,25162	-0,13262	1,82226	1,06241	1,01586	1,07828	0,00530
LH-6	25,07000	0,21354	-0,12951	1,82299	1,05298	1,01550	1,06848	0,00518
LH-7	25,02000	0,13957	-0,09293	1,74889	1,03525	1,01114	1,04640	0,00372
LH-8	25,10000	0,11358	0,13130	1,74331	1,02863	1,01569	1,04432	0,00525
LH-9	25,01000	0,02319	0,01374	1,58254	1,00607	1,00165	1,00771	0,00055
LH-10	25,06000	0,06295	-0,28004	1,66483	1,01616	1,03352	1,04968	0,01120
LH-11	25,10000	0,12382	-0,34495	1,57687	1,03231	1,04123	1,07354	0,01380
LH-12	25,07000	0,10443	-0,37693	1,66416	1,02680	1,04510	1,07190	0,01508
LH-2		0,14708	-0,08882					0,00355
LH-3	24,96000	0,16341	-0,00644	1,63119	1,04241	1,00077	1,04318	0,00026
LH-4	24,92000	0,21844	0,00060	1,63381	1,05675	1,00007	1,05682	0,00002
LH-5	25,03000	0,25833	-0,04281	1,82817	1,06412	1,00513	1,06925	0,00171
LH-6	25,06000	0,19965	-0,02369	1,82598	1,04952	1,00284	1,05236	0,00095
LH-7	25,04000	0,12266	0,08755	1,74965	1,03095	1,01049	1,04144	0,00350
LH-8	24,97000	0,03283	-0,03750	1,75456	1,00830	1,00450	1,01280	0,00150
LH-9	25,01000	0,07947	0,00386	1,58450	1,02078	1,00046	1,02124	0,00015
LH-10	24,95000	0,05192	-0,01631	1,67424	1,01336	1,00196	1,01532	0,00065
LH-11	25,04000	0,12588	0,04308	1,58261	1,03289	1,00516	1,03805	0,00172
LH-12	24,99000	0,26897	-0,07250	1,67156	1,06914	1,00870	1,07784	0,00290
LH-2	25,05000	0,22938	0,18909	1,62163	1,05943	1,02265	1,08208	0,00756
LH-3		0,23254	0,36860					0,01474
LH-4	25,06000	0,22485	-0,49041	1,82183	1,05582	1,05871	1,11453	0,01962
LH-5		0,25771	0,40225					0,01609
LH-6		0,22476	-0,30925					0,01237
LH-7		0,21779	0,13640					0,00546
LH-8	25,05000	0,07652	0,07658	1,74498	1,01932	1,00917	1,02849	0,00306
LH-9	25,04000	0,12146	0,06354	1,57901	1,03176	1,00761	1,03937	0,00254
LH-10	25,11000	0,12929	0,02812	1,65979	1,03315	1,00336	1,03651	0,00112

Figure 6: *Measured misalignments on the 25 mm thick laser hybrid welded plate*

B. Calibration and load verification of testing machines

The following figures show information concerning the load calibration and verification of the applied servo hydraulic testing machines.

DTU Structural Lab

Test: Load Cell Calibration in Tension

Technical University of Denmark

DTU

Date:	13-02-2015
Name:	Ólafur Magnús Ólafsson
Place:	B119

Machine:	Instron 1343
Load cell:	500 kN load cell
Controller:	Instron 8500
Reference load cell:	900 kN
Validation load cell:	ESH - Ref No 4342
Comments:	Reference load Cell max capacity 900kN Conversion pieces used to fit the reference load cell in machine * Load cell unclamped and balanced before verification

Tension

Load Verification 1st

Load Command [kN]	Load Reference [kN]	Error [%]
0	0	
50	49,96	0,08%
100	100,1	-0,10%
150	150,2	-0,13%
200	200,5	-0,25%
250	250,6	-0,24%
300	300,7	-0,23%
350	350,8	-0,23%
400	400,9	-0,22%
450	451,1	-0,24%
500	500,7	-0,14%

Load Verification 2nd*

Controller Load Command [kN]	Reference load [kN]	Error [%]
0	0	
50	49,92	-0,16%
100	100,03	0,03%
150	150,12	0,08%
200	200,25	0,12%
250	250,35	0,14%
300	300,45	0,15%
350	350,6	0,17%
400	400,65	0,16%
450	450,7	0,16%
500	500,4	0,08%

Figure 7: *Calibration and load verification of the 500 kN Instron SHM*

DTU Structural Lab

Technical University of Denmark

DTU

Test: Load Cell Calibration in Tension

Date: 24-04-2015
Name: Ólafur Magnús Ólafsson
Place: B119

Machine: MTS 312.41
Load cell: 500 kN load cell
Controller: FlexTest
Reference load cell: 900 kN
Validation load cell: ESH - Ref No 4342
Comments: Reference load Cell max capacity 900kN
Conversion pieces used to fit the reference load cell in machine
* Load cell unclamped and balanced before verification

Tension

Load Verification 1st

Load Command [kN]	Load Reference [kN]	Error [%]
0,00	0,00	
25,00	25,05	-0,20
50,00	50,11	-0,22
75,00	75,12	-0,16
100,00	100,13	-0,13
125,00	125,13	-0,10
150,00	150,15	-0,10
175,00	175,16	-0,09
200,00	200,14	-0,07
225,00	225,13	-0,06
250,00	250,09	-0,04
275,00	275,10	-0,04
300,00	300,17	-0,06
325,00	325,27	-0,08
350,00	350,24	-0,07
375,00	375,18	-0,05
400,00	400,07	-0,02
425,00	424,84	0,04
450,00	449,65	0,08

Figure 8: *Calibration and load verification of the 500 kN MTS SHM*

DTU Structural Lab

Test: Load Cell Calibration

Technical University of Denmark

DTU

Date:	27-01-2014
Name:	Ólafur Magnús Ólafsson
Place:	B119
Machine:	Instron 4495
Load cell:	1,5 MN in static compression, 1 MN in fatigue
Controller:	Instron 8500
Reference load cell:	900 kN
Validation load cell:	ESH - Ref No 4342
Comments:	Reference load Cell max capacity 900kN Conversion pieces used to fit the reference load cell in machine * No indication of the gripping pressure for the Instron 4495

Tension

Load command [kN]	Reference reading	Reference load [kN]	Error %
0,000	0,0005	0,211	
50,000	0,1107	49,944	0,112
100,000	0,2208	99,654	0,346
150,000	0,3315	149,670	0,220
200,000	0,4424	199,799	0,100
250,000	0,5534	249,986	0,006
300,000	0,6643	300,130	-0,043
350,000	0,7756	350,445	-0,127
400,000	0,8866	400,605	-0,151
450,000	0,9975	450,689	-0,153
500,000	1,1084	500,731	-0,146
550,000	1,2180	550,135	-0,025
600,000	1,3296	600,377	-0,063
650,000	1,4414	650,633	-0,097
700,000	1,5528	700,623	-0,089
750,000	1,6634	750,159	-0,021
800,000	1,7723	798,829	0,146
850,000	1,8773	845,649	0,512
Max 900			
0,000	0,0047	2,104	

Figure 9: *Calibration and load verification of the 1000 kN Instron SHM*

DTU Structural Lab

Technical University of Denmark

DTU

Test: Load Cell Calibration

Date:	17-09-2013
Name:	Ólafur Magnús Ólafsson
Place:	B119
Machine:	Kyong Do
Load cell:	1,5 MN in static compression, 1 MN in fatigue
Controller:	Instron 8500
Reference load cell:	900 kN
Validation load cell:	ESH - Ref No 4342
Comments:	Reference load Cell max capacity 900kN
	Conversion pieces used to fit the reference load cell in machine
	* No indication of the gripping pressure for the Instron 4495

Tension

Readout	Load Command	True Load / readout	Error [%]			
0,000	0,000	0,0077				
0,111	50,000	50,0794	-0,002			
0,222	100,000	99,9705	0,000			
0,332	150,000	149,8957	0,001			
0,443	200,000	199,6182	0,002			
0,553	250,000	249,5793	0,002			
0,664	300,000	299,5422	0,002			
0,775	350,000	350,1743	0,000			
0,885	400,000	399,8825	0,000			
0,996	450,000	450,2377	-0,001			
1,107	500,000	500,0997	0,000			
		545,1341	max			

Figure 10: *Calibration and load verification of the 500 kN Korea, SHM. The corrosion environment*

C. Equipment documentation

The following figure is information concerning the applied strain gauges in this project.

General Purpose Strain Gages - Linear Patterns

GAGE PATTERN Actual size shown. Enlarged when necessary for definition. ES = Each section CP = Complete pattern S = Section (S1= Sec 1) M = Matrix inch millimeter	**GAGE DESIGNATION** Insert desired S-T-C number in spaces marked XX.	**RES. IN OHMS** Tolerance is increased when Option W, E, SE, LE, or P is specified.	**OPTIONS AVAILABLE**

250BF

General-purpose gage with high-resistance grid. Compact geometry. Similar to 250BG pattern except for resistance. See also 250BM and 250UW patterns. EK-Series gages are supplied with duplex copper pads (DP) when optional feature W or SE is not specified.

GAGE LENGTH	OVERALL LENGTH	GRID WIDTH	OVERALL WIDTH
0.250	0.375	0.125	0.125
6.35	9.53	3.18	3.18
MATRIX SIZE	0.52L x 0.22W		13.2L x 5.6W

EA-XX-250BF-350	350 ± 0.15%	W, E, L, LE, P
ED-DY-250BF-10C	1000 ± 0.3%	E, L*, LE*
EK-XX-250BF-10C	1000 ± 0.15%	W, SE
S2K-XX-250BF-10C	1000 ± 0.3%	W*
WA-XX-250BF-350	350 ± 0.3%	W*
WK-XX-250BF-10C	1000 ± 0.3%	
EP-08-250BF-350	350 ± 0.15%	
SA-XX-250BF-350	350 ± 0.3%	
SK-XX-250BF-10C	1000 ± 0.3%	
SD-DY-250BF-10C	1000 ± 0.6%	
WD-DY-250BF-10C	1000 ± 0.6%	

250BG

Widely used general-purpose gage. Compact geometry. See also 250BF and 250UN patterns.

GAGE LENGTH	OVERALL LENGTH	GRID WIDTH	OVERALL WIDTH
0.250	0.375	0.125	0.125
6.35	9.53	3.18	3.18
MATRIX SIZE	0.52L x 0.22W		13.2L x 5.6W

EA-XX-250BG-120	120 ± 0.15%	W, E, L, LE, P
ED-DY-250BG-350	350 ± 0.3%	E, L*, LE*
WA-XX-250BG-120	120 ± 0.3%	W*
WK-XX-250BG-350	350 ± 0.3%	W*
EA-XX-250BG-100	100 ± 0.15%	
EP-08-250BG-120	120 ± 0.15%	
SA-XX-250BG-120	120 ± 0.3%	
SK-XX-250BG-350	350 ± 0.3%	
SD-DY-250BG-350	350 ± 0.6%	
WD-DY-250BG-350	350 ± 0.6%	

Figure 11: *General purpose strain gauges - Linear patterns*

D. Non destructive test results

The following figures are non destructive test reports from the welded batches applied in this project.

DANAK
TEST Reg. nr. 30

FORCE TECHNOLOGY
Division for Inspection and Testing
Park Alle' 345, 2605, Brøndby, Denmark

Test Report - Ultrasonic Testing

DANAK Reg. No.	Rev. No.	FORCE Task No.	Report Id.		Report No.	Page of
30		113-24741.000203-10	thfUT4093			1 / 1
Requisition/ order No.		**Period of test/ Date**	**Technician (Init.)**	**Certificate No.**	**Assistant (Init.)**	**Certificate No.**
203-10		11-04-2013 - 11-04-2013	THF	0963-N2-U	-	-

Client	Address
LWT Lindø Welding Technology	Elektrikervej 5, 5330, Munkebo
Contractor	**Owner**
-	-

Test location
Elektrikervej 5 , 5330 , Munkebo

Job / Project (ident., dim., quantity)
Svejseprøve tykkelse 20 mm længde 1800 mm

Drawing No./ Rev. No./ Sketch / Other	Extent of testing	Material designation	Construction Standard
-	100%	Lavt legeret stål	-

Test specification (standard)	Quality requirements (standard, level)
ISO 17640-B	EN ISO 11666-2

Supplementary information (without liability, see footnote)

Welding process	Joint shape	Heat treated	Time of testing
121 Pulversvejsning	X	No information	Hours after weld -

Technical information regarding the test:

Object type	Joint type	Surface condition	Temperature °C (if outside 0 - 40°c)
Weld	Stumpsøm	Ubearbejdet, jævn	18

Equipment Type/ Reg. No.	Couplant	Calibration and reference blocks
USM35 ULXB42	Glycerin	☑ V1 Reg. No. utu117 ☑ V2 Reg. No. ut-v.39 ☑ TIF Reg. No. svc 20 ☐ Other

Straight probes			Angle probes			
Type	A: mseb 4	B:	Type	C: Siui71-2	D: swb60-2	E:
Reg. No. / Freq.	uae184 4 MHz	MHz	Reg. No. / Freq.	uifa21 2 MHz	uib19 2 MHz	MHz
Sensitivity setting			True angle	71 °	60 °	°
Basic sett. ~ ref.curve	44 dB	dB	**Sensitivity setting**			
Basic sett. ~ ref. BWE	dB	dB	Basic sett. ~ ref.curve	46 dB	54 dB	dB
Transfer correction	dB	dB	Transfer correction	2 dB	2 dB	dB
Extra when scanning	12 dB	dB	Extra when scanning	14 dB	14 dB	dB
Total	dB	dB	Total	62 dB	70 dB	dB
DGS (AVG): Disc diam. = 5 mm Range =		0-100 mm	DAC: Diam. =		Ø3 mm Range =	0-180 mm

Scanning for longitudinal defects and lamination

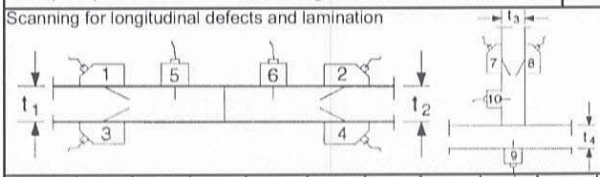

t1= 20 mm
t2= 20 mm
t3= mm
t4= mm

Position	1	2	3	4	5	6	7	8	9	10
Probe	cd	cd			a	a				

Scanning for transverse defects

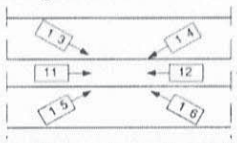

Position	11	12	13	14	15	16
Probe						

Specific information

100% UT af svejsning.
Der er en indikation i Dybde 10-13 mm Længde 40 mm DB -2 .Resten af svejsningen overholder kvalitets kravet.
Se bilag.

Test Result
Kvalitetskrav ikke opfyldt.

Repairs marked	Enclosures	Report approved by.	Technician (Signature)
	1		FORCE TECHNOLOGY Tommy Hansen Fabricius
Test object stamped	☐ Copy delivered to ch@lwt.dk		

Supplementary information : The grey fields supply available, relevant information for guidance only. The giving of such information in this Test Report should not be considered as verification of its accuracy

Bilag til Prøvningsrapport / Encl. to Test Report

Division for Inspektion og Prøvning / Division for Inspection and Testing

FORCE Task nr. / No.	Tekniker / Technician (init.)	Rapport id. / Report Id.	Rapport nr. og Rev. / Report No. and Rev.	Bilag nr. / Encl. No.
113-24741.000203-10	THF	thfUT4093		1

Rekvirent / Client	Bygherre / Owner
LWT Lindø Welding Technology	LWT Lindø Welding Technology
Entreprenør / Contractor	Prøvningssted / Test Location
LWT Lindø Welding Technology	Elektrikervej 5 , 5330 , Munkebo

Job / Projekt (Iden., dim., antal) / Job / Project (Ident., dim., quantity)

Svejseprøve tykkelse 20 mm længde 1800 mm

Non-destructive testing of welds - Magnetic particle testing

Submerged arc welded sample – 20 mm

Contact person:	Ólafur Magnús Ólafsson
Clients reference:	
LWT's reference:	203-00

Christian Højerslev
07-05-2013

Page 1/1

MAGNETIC PARTICLE TESTING OF FUSION WELD		Klik her for at angive tekst.
Specimen description	Submerged arc welded sample	
Specimen mark	20 mm	
Component manufacturer	Lindoe Welding Technology (LWT)	
Examining body	Lindoe Welding Technology (LWT)	
Extend of examination	100%	
Examination device(s) used	Magnavis WCP-2 White contrast paint Magnavis 7HF MPI Ink Tiede JWM220 230V; 50/60 Hz; 2.4/1.7A No. 9836278	
Test standard	DS/EN ISO 17638:2009	
Acceptance levels	DS/EN ISO 2378:2009	
Object examined		
Welding direction: Marked by yellow arrow in adjacent photo. Welding position: PA flat		
Test result	☒ Comply with acceptance levels	☐ Fails to comply with acceptance levels (for details see Enclosure 1)
Comments	NA	

Evaluator

Peter Østergaard Jørgensen

Welding Inspector

DANAK
TEST Reg. nr. 30

FORCE TECHNOLOGY
Division for Inspektion og Prøvning
Park Allé 345, 2605, Brøndby, Denmark

Prøvningsrapport - Ultralyd

DANAK Reg. nr.	Rev. nr.	FORCE Task nr.	Rapport id.		Rapport nr.	Side af
30		113-24741.000203-10	thfUT4083			1 / 1
Rekvisition / ordre nr.		**Prøvningsperiode / Dato**	**Tekniker (Init.)**	**Certifikat nr.**	**Assistent (Init.)**	**Certifikat nr.**
203-10		05-04-2013 - 05-04-2013	THF	0963-N2-U	-	-

Rekvirent	Adresse
LWT Lindø Welding Technology	Elektrikervej 5, 5330, Munkebo
Entreprenør	**Bygherre**
-	-

Prøvningssted
Elektrikervej 5 , 5330 , Munkebo

Job / Projekt (Iden., dim., antal)
Svejseprøve

Tegning nr. / Revision / Skitse / Andet	Prøvningsomfang	Materialebetegnelse	Konstruktionsstandard
-	100%	Lavt legeret stål	-

Prøvningsspecifikation (standard)	Kvalitetskrav (standard, niveau)
ISO 17640-B	EN ISO 11666-2

Supplerende oplysninger (Uden ansvar, se fodnote)

Svejsemetode	Fugeform	Varmebehandlet	Tidspunkt for prøvning
121 Pulversvejsning	X	No information	Timer efter sv. -

Prøvningstekniske oplysninger

Emnetype	Sømtype	Overflade	Temperatur °C (udover 0 - 40 °C)
Weld	Stumpsøm	Ubearbejdet, jævn	18

Apparat type / Reg. nr.	Koblingsmiddel	Justerings- og referenceblokke
USM35 ULXB42	Glycerin	☑ V1 Reg. nr. utu117 ☑ V2 Reg. nr. ut-v.39 ☑ TIF Reg. nr. svc 20 ☐ Andet

Normalhoved (Probe)			Vinkelhoved (Probe)			
Type	A: mseb 4	B:	Type	C: Siui71	D: swb60-2	E:
Reg. nr. / Frekvens	uae184 4 MHz	MHz	Reg. nr. / Frekvens	uifa21 MHz	uib19 MHz	MHz
Følsomhedsindstilling			Sand vinkel	71 °	60 °	°
Grundinds. ~ ref. kurve	44 dB	dB	**Følsomhedsindstilling**			
Grundinds. ~ ref. BVE	dB	dB	Grundinds. ~ ref. kurve	46 dB	54 dB	dB
Overføringskorrektion	dB	dB	Overføringskorrektion	2 dB	2 dB	dB
Afsøgningstillæg	12 dB	dB	Afsøgningstillæg	14 dB	14 dB	dB
Sum	dB	dB	Sum	62 dB	70 dB	dB

AVG: Skive ø = 5 mm Skalalængde 0-100 mm
DAC: Hul ø Ø3 mm Skalalængde 0-300 mm

Scanning for længdefejl og lagdeling

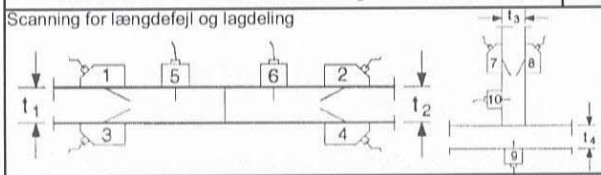

t1= 30 mm
t2= 30 mm
t3= mm
t4= mm

Position	1	2	3	4	5	6	7	8	9	10
Probe	cd	cd			a	a				

Scanning for tværfejl

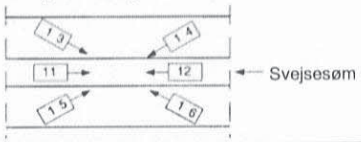

Position	11	12	13	14	15	16
Probe						

Specifikke oplysninger
100% af svejsning
Se bilag.

Prøvningsresultat
Kvalitetskrav opfyldt.

Rep. opmærkning	Bilag vedlagt	Rapport godkendt af	Tekniker (Underskrift)
	1		Tommy Hansen Fabricius
Emne stemplet	☐ Kopi afleveret til ch@lwt.dk		

Supplerende oplysninger : Oplysningerne i de grå felter er til information og angives kun i den udstrækning, de er tilgængelige og relevante. Deres angivelse på nærværende prøvningsrapport kan ikke betragtes som en verifikation af deres rigtighed

Bilag til Prøvningsrapport /
Encl. to Test Report

Division for Inspektion og Prøvning / Division for Inspection and Testing

FORCE Task nr. / No.	Tekniker / Technician (init.)	Rapport id. / Report Id.	Rapport nr. og Rev. / Report No. and Rev.	Bilag nr. / Encl. No.
113-24741.000203-10	THF	thfUT4083		1

Rekvirent / Client	Bygherre / Owner
LWT Lindø Welding Technology	-
Entreprenør / Contractor	Prøvningssted / Test Location
-	Elektrikervej 5 , 5330 , Munkebo

Job / Projekt (Iden., dim., antal) / Job / Project (Ident., dim., quantity)

Svejseprøve

Click here to enter text.

Non-destructive testing of welds - Magnetic particle testing

Submerged arc welded sample – 30 mm

Contact person:	Ólafur Magnús Ólafsson
Clients reference:	
LWT's reference:	203-00

Christian Højerslev
07-05-2013

Page 1/1

MAGNETIC PARTICLE TESTING OF FUSION WELD		Klik her for at angive tekst.
Specimen description	Submerged arc welded sample	
Specimen mark	30 mm	
Component manufacturer	Lindoe Welding Technology (LWT)	
Examining body	Lindoe Welding Technology (LWT)	
Extend of examination	100%	
Examination device(s) used	Magnavis WCP-2 White contrast paint Magnavis 7HF MPI Ink Tiede JWM220 230V; 50/60 Hz; 2.4/1.7A No. 9836278	
Test standard	DS/EN ISO 17638:2009	
Acceptance levels	DS/EN ISO 2378:2009	
Object examined		
Welding position: PA flat		
Test result	☒ Comply with acceptance levels	☐ Fails to comply with acceptance levels (for details see Enclosure 1)
Comments	NA	

Evaluator

Peter Østergaard Jørgensen

Welding Inspector

DANAK
TEST Reg. nr. 30

FORCE TECHNOLOGY
Division for Inspection and Testing
Park Alle' 345, 2605, Brøndby, Denmark

Test Report - Ultrasonic Testing

DANAK Reg. No.	Rev. No.	FORCE Task No.	Report Id.		Report No.	Page of
30		113-24741.000203-10	thfUT4092			1 / 1
Requisition/ order No.		**Period of test/ Date**	**Technician (Init.)**	**Certificate No.**	**Assistant (Init.)**	**Certificate No.**
203-10		11-04-2013 - 11-04-2013	THF	0963-N2-U	-	-

Client	Address
LWT Lindø Welding Technology	Elektrikervej 5, 5330, Munkebo
Contractor	**Owner**
-	-

Test location
Elektrikervej 5 , 5330 , Munkebo

Job / Project (ident., dim., quantity)
Svejseprøve tykkelse 40 mm længde 1800 mm

Drawing No./ Rev. No./ Sketch / Other	Extent of testing	Material designation	Construction Standard
-	100%	Lavt legeret stål	-

Test specification (standard)	Quality requirements (standard, level)
ISO 17640-B	EN ISO 11666-2

Supplementary information (without liability, see footnote)

Welding process	Joint shape	Heat treated	Time of testing
121 Pulversvejsning	X	No information	Hours after weld -

Technical information regarding the test:

Object type	Joint type	Surface condition	Temperature °C (if outside 0 - 40°c)
Weld	Stumpsøm	Ubearbejdet, jævn	18

Equipment Type/ Reg. No.	Couplant	Calibration and reference blocks
USM35 ULXB42	Glycerin	☑ V1 Reg. No. utu117 ☑ V2 Reg. No. ut-v.39 ☑ TIF Reg. No. svc 20 ☐ Other

Straight probes			Angle probes			
Type	A: mseb 4	B:	Type	C: Siui71-2	D: swb60-2	E: swb45-2
Reg. No. / Freq.	uae184 4 MHz	MHz	Reg. No. / Freq.	uifa21 2 MHz	uib19 MHz	uia64 2 MHz
Sensitivity setting			True angle	71 °	60 °	45 °
Basic sett. ~ ref.curve	44 dB	dB	**Sensitivity setting**			
Basic sett. ~ ref. BWE	dB	dB	Basic sett. ~ ref.curve	46 dB	54 dB	54 dB
Transfer correction	dB	dB	Transfer correction	2 dB	2 dB	2 dB
Extra when scanning	12 dB	dB	Extra when scanning	14 dB	14 dB	14 dB
Total	dB	dB	Total	62 dB	70 dB	70 dB

DGS (AVG): Disc diam. = 5 mm Range = 0-100 mm

DAC: Diam. = Ø3 mm Range = 0-300 mm

Scanning for longitudinal defects and lamination

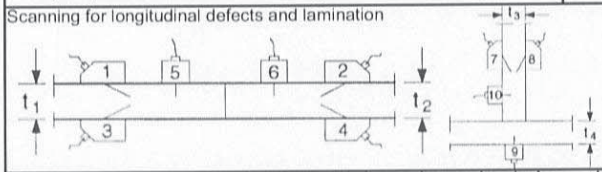

t1= 40 mm
t2= 40 mm
t3= mm
t4= mm

Position	1	2	3	4	5	6	7	8	9	10
Probe	cde	cde			a	a				

Scanning for transverse defects

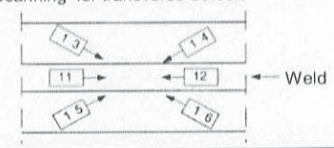

Position	11	12	13	14	15	16
Probe						

Specific information
100% af svejsning
Se bilag.

Test Result
Kvalitetskrav opfyldt.

Repairs marked	Enclosures	Report approved by.	Technician (Signature)
	1		Tommy Hansen Fabricius
Test object stamped	☐ Copy delivered to ch@lwt.dk		

Supplementary information : The grey fields supply available, relevant information for guidance only. The giving of such information in this Test Report should not be considered as verification of its accuracy

Bilag til Prøvningsrapport /
Encl. to Test Report

Division for Inspektion og Prøvning / Division for Inspection and Testing

FORCE Task nr. / No.	Tekniker / Technician (init.)	Rapport id. / Report Id.	Rapport nr. og Rev. / Report No. and Rev.	Bilag nr. / Encl. No.
113-24741.000203-10	THF	thfUT4092		1

Rekvirent / Client	Bygherre / Owner
LWT Lindø Welding Technology	LWT Lindø Welding Technology
Entreprenør / Contractor	**Prøvningssted / Test Location**
LWT Lindø Welding Technology	Elektrikervej 5 , 5330 , Munkebo

Job / Projekt (Iden., dim., antal) / Job / Project (Ident., dim., quantity)

Svejseprøve tykkelse 40 mm længde 1800 mm

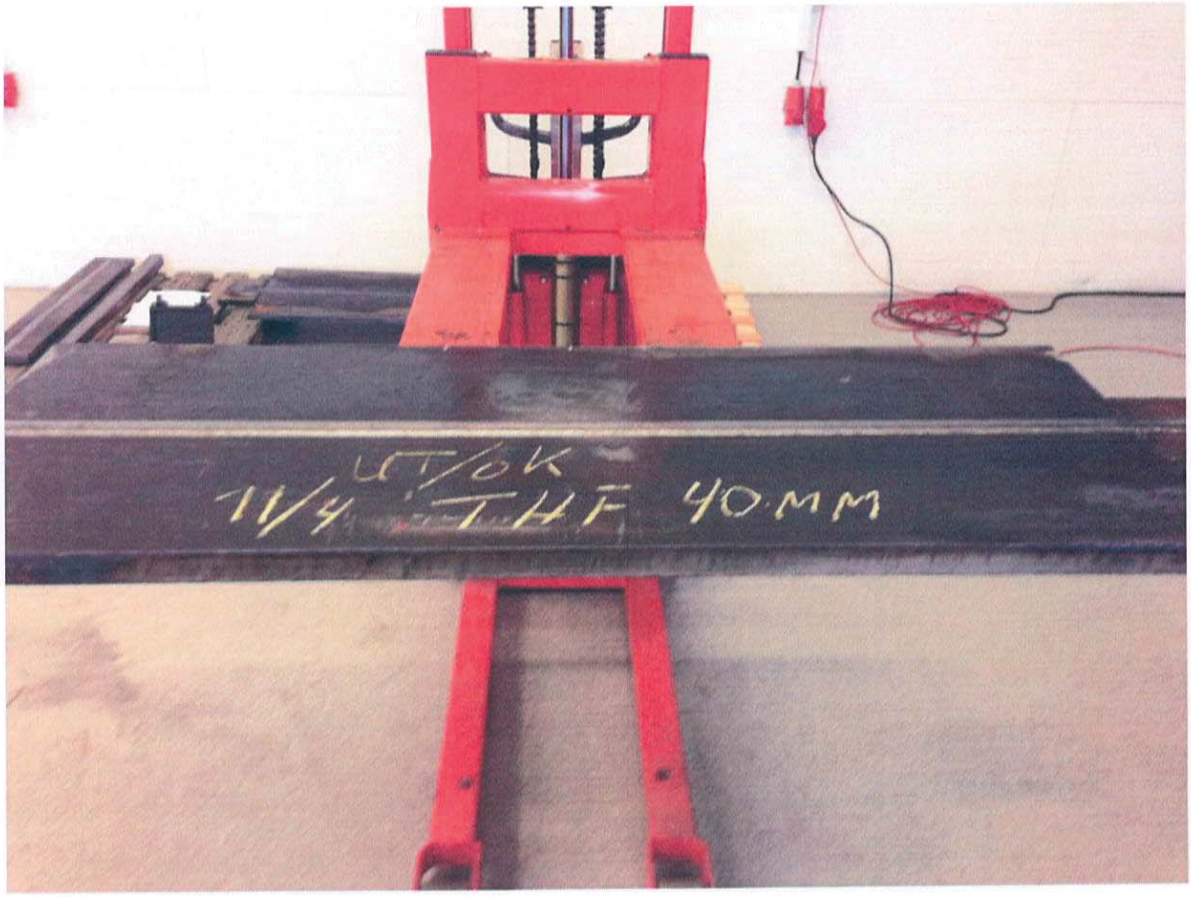

Click here to enter text.

Non-destructive testing of welds - Magnetic particle testing

Submerged arc welded sample – 40 mm

Contact person:	Ólafur Magnús Ólafsson
Clients reference:	
LWT's reference:	203-00

Christian Højerslev
07-05-2013

Page 1/1

MAGNETIC PARTICLE TESTING OF FUSION WELD		Klik her for at angive tekst.
Specimen description	Submerged arc welded sample	
Specimen mark	40 mm	
Component manufacturer	Lindoe Welding Technology (LWT)	
Examining body	Lindoe Welding Technology (LWT)	
Extend of examination	100%	
Examination device(s) used	Magnavis WCP-2 White contrast paint Magnavis 7HF MPI Ink Tiede JWM220 230V; 50/60 Hz; 2.4/1.7A No. 9836278	
Test standard	DS/EN ISO 17638:2009	
Acceptance levels	DS/EN ISO 2378:2009	
Object examined Welding direction: Marked by yellow arrow in adjacent photo. Welding position: PA flat		
Test result	☒ Comply with acceptance levels	☐ Fails to comply with acceptance levels (for details see Enclosure 1)
Comments	NA	

Evaluator

Peter Østergaard

Peter Østergaard Jørgensen

Welding Inspector

NSK Nordisk Svejse Kontrol a/s

DANAK TEST Reg.nr. 445

VISUAL EXAMINATION / VISUEL KONTROL

Client / Kunde **Bladt Industries**	File No. / Sag nr. **54641** Report No. / Rapport nr. **VT 01**
Contractor / Entreprenør **Bladt Industries**	Date / Dato **18/06-14** Page / Side **1** of / af **1**
Object / Objekt **Test series 2 pl. 30 mm 1 pcs.** **Test series 3 pl. 40 mm 1 pcs.** **NDT REKV: 02**	Drawing No. / Tegning nr. - Material / Materiale **Steel**

Supplementary information (without liability, see note) / **Supplerende oplysninger** (uden ansvar, se note)

Weld process / Svejseproces: ☐ 111 SMAW ☒ 121 SAW ☐ 141 GTAW ☐ 135/131 GMAW ☐ 136/138 FCAW ☐ 311 OFW ☐ Other / Andet

Weld preparation / Fugegeometri	PWHT / Varmebehandling	Time of examination / Tidsp. for unders.
Other / Andet ☒ X ☐ Y ☐ U ☐ V ☐ K ☐ I ☐ FW	☐ Yes / Ja ☒ No / Nej	24 Hours after welding / Timer efter svejsning

Reinforcement / Vulst højde	Surface condition / Overflade beskaffenhed
☒ As welded / Som svejst ☐ Ground / Slebet	☐ Ground / Slebet ☒ Smooth / Jævn ☐ Coarse / Grov

Examination procedure / Undersøgelses procedure: DS/EN ISO 17637

Accept criteria / Accept kriterier: DS/EN ISO 5817 /B

Extent / Omfang: ☐ 5% ☐ 10% ☐ 20% ☒ 100% ☐ %

Equipment / Udstyr: ☒ Weld gauge / Svejselære ☒ Torch / Lygte ☒ Sliding gauge / Skydelære Other / Andet

☒ Examination of finished welds / Kontrol af færdige svejsninger ☐ Examination during welding / Kontrol under svejsning

Extent of examination / Undersøgelsesomfang

100 % VT on test series 2 pl. 30 mm 1 pcs. and test series 3 pl. 40 mm 1 pcs.

Result of examination / Undersøgelsens resultat

Accepted to specifikation.

Rep. marked / Rep. mærket	Check of / Kontrol af	Enclosures / Bilag	Inspector / Inspektør	Cert. No. / nr.
☐ On object / På objekt ☐ On sketch / På skitse	☐ Grinding / Slibning ☐ Repair / Reparation	☐ None / Ingen ☐ No. / Antal	S.T.E. Nordisk Svejse Kontrol A/S	1523-VT-N2 Date / Dato 19/06-14
Remarks / Bemærkninger			Inspector / Inspektør STE	Cert. No. / nr. 1523-VT-N2
			Assistant / Assistent	Cert. No. / nr.

NSK VT 001 R3 07.01.11

Note: The grey fields supply available, relevant information for guidance only. The giving of such information in this Field Report should not be considered as verification of its accuracy.
Note: Oplysningerne i de grå felter er til information og angives kun i den udstrækning, de er tilgængelige og relevante. Deres angivelse på nærværende markrapport kan ikke betragtes som en verifikation af deres rigtighed.

NSK Nordisk Svejse Kontrol a/s

DANAK TEST Reg.nr. 445

VISUAL EXAMINATION / VISUEL KONTROL

Client / Kunde **Bladt Industies a/s**	File No. / Sag nr. **54641** Report No. / Rapport nr. **VT 02**
Contractor / Entreprenør **Bladt Industries a/s**	Date / Dato **25/06-14** Page / Side **1** of / af **1**
Object / Objekt **Test series 2 pl. 30 mm and Test series 3 pl. 40 mm.** **NDT REKV. 03**	Drawing No. / Tegning nr. - Material / Materiale **Steel**

Supplementary information (without liability, see note) / **Supplerende oplysninger** (uden ansvar, se note)

Weld process / Svejseproces: ☐ 111 SMAW ☒ 121 SAW ☐ 141 GTAW ☐ 135/131 GMAW ☐ 136/138 FCAW ☐ 311 OFW ☐ Other / Andet

Weld preparation / Fugegeometri: ☒ X ☐ Y ☐ U ☐ V ☐ K ☐ I ☐ FW — Other / Andet

PWHT / Varmebehandling: ☐ Yes / Ja ☒ No / Nej

Time of examination / Tidsp. for unders.: 24 Hours after welding / Timer efter svejsning

Reinforcement / Vulst højde: ☒ As welded / Som svejst ☐ Ground / Slebet

Surface condition / Overflade beskaffenhed: ☐ Ground / Slebet ☒ Smooth / Jævn ☐ Coarse / Grov

Examination procedure / Undersøgelses procedure: DS/EN ISO 17637

Accept criteria / Accept kriterier: DS/EN ISO 5817 /B

Extent / Omfang: ☐ 5% ☐ 10% ☐ 20% ☒ 100% ☐ %

Equipment / Udstyr: ☒ Weld gauge / Svejselære ☒ Torch / Lygte ☒ Sliding gauge / Skydelære Other / Andet

☒ Examination of finished welds / Kontrol af færdige svejsninger ☐ Examination during welding / Kontrol under svejsning

Extent of examination / Undersøgelsesomfang

100 % VT on test series 2 pl. 30 mm and test series 3 pl. 40 mm after repair from UT03.

Result of examination / Undersøgelsens resultat

Accepted to specifikation.

Rep. marked / Rep. mærket	Check of / Kontrol af	Enclosures / Bilag	Inspector / Inspektør	Cert. No. / nr.
☐ On object / På objekt ☐ On sketch / På skitse	☐ Grinding / Slibning ☐ Repair / Reparation	☐ None / Ingen ☐ No. / Antal	S.T.E. Nordisk Svejse Kontrol A/S	1523-VT-N2 Date / Dato 26/06-14
Remarks / Bemærkninger			Inspector / Inspektør STE	Cert. No. / nr. 1523-VT-N2
			Assistant / Assistent	Cert. No. / nr.

BLADT INDUSTRIES

NSK VT 001 R3 07.01.11

Note: The grey fields supply available, relevant information for guidance only. The giving of such information in this Field Report should not be considered as verification of its accuracy.
Note: Oplysningerne i de grå felter er til information og angives kun i den udstrækning, de er tilgængelige og relevante. Deres angivelse på nærværende markrapport kan ikke betragtes som en verifikation af deres rigtighed.

NSK Nordisk Svejse Kontrol a/s

DANAK TEST Reg.nr. 445

ULTRASONIC / ULTRALYD

Client / Kunde **Bladt Industries a/s**	File No. / Sag nr. **54641** Report No. / Rapport nr. **UT 02**
Contractor / Entreprenør **Bladt Industries a/s**	Date / Dato **1806 2014** Page / Side **1** of / af **1**
Object / Objekt **Test series 2 pl. 30mm 1 pcs.** **Test series 3 pl. 40mm 1 pcs.** **NDT REKV. 02**	Drawing No. / Tegning nr. - Material / Materiale **Steel**

Supplementary information (without liability, see note) / **Supplerende oplysninger** (uden ansvar, se note)

Weld process / Svejseproces: ☐ 111 SMAW ☒ 121 SAW ☐ 141 GTAW ☐ 135/131 GMAW ☐ 136/138 FCAW ☐ 311 OFW ☐ Other / Andet

Weld preparation / Fugegeometri: ☒ X ☐ Y ☐ U ☐ V ☐ K ☐ I ☐ FW — Other / Andet:

PWHT / Varmebehandling: ☐ Yes / Ja ☒ No / Nej

Time of examination / Tidsp. for unders.: >24 Hours after welding / Timer efter svejsning

Reinforcement / Vulst højde: ☒ As welded / Som svejst ☐ Ground / Slebet

Surface condition / Overflade beskaffenhed: ☐ Ground / Slebet ☒ Smooth / Jævn ☐ Coarse / Grov

Examination procedure / Undersøgelses procedure: DS/EN ISO 17640 B

Accept criteria / Accept kriterier: DS/EN ISO 11666 2

Extent / Omfang: ☐ 5% ☐ 10% ☐ 20% ☒ 100% ☐ %

Equipment type / Udstyr type: USM GO

Equipm. No. / Udstyr nr.: 30-53

Probe check performed / Prober kontrolleret: ☒

Straight beam probe / Normalhoved			Angle beam probe / Vinkelhoved			
NSK No./nr.	A: 55965	B:	NSK No./nr.	C: 3270	D: 653648	E:
Type / Freq.	SM / 4 MHz	/ MHz	Type / Freq.	70 / 2 MHz	60 / 2 MHz	/ MHz
Sensitivity setting / Følsomhedsindstilling			**Sensitivity setting / Følsomhedsindstilling**			
Basic sett. – ref. level	30 db	db	Basic sett. – ref. level Gr. indst. – ref. level	47 db	46 db	db
Transfer Correction Overføringskorrekti	0 db	db	Transfer Correction Overføringskorrektion	2 db	2 db	db
Extra db for scanning	>8 db	db	Extra db for scanning Ekstra db til scanning	10 db	10 db	db
Scanning level Scanningsniveau	>38 db	db	Scanning level Scanningsniveau	59 db	58 db	db

Reference / Reference: DAC: Hole / Hul Ø = 3 mm Range / Skala = 200 mm AVG: Disc / Skive Ø = mm Range / Skala = mm

Ref. block / Ref. blok	Ref. block / Ref. blok	Ref. block / Ref. blok	Ref. block / Ref. blok
☒ V1 NSK No./nr. 13-18	☒ V2 NSK No./nr. 72166	☒ NSK No./nr. 3351	☐ Other / Andet

Scanning for longitudinal defects and lamination / Scanning for længdefejl og lagdeling

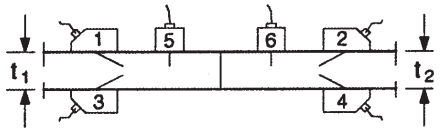

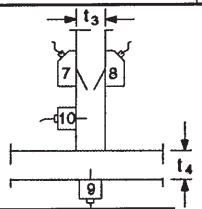

t1 = 30/40
t2 = 30/40
t3 =
t4 =

Position	1	2	3	4	5	6	7	8	9	10
Probe	cd	cd	cd	cd	a	a				

Scanning for transverse defects / Scanning for tværfejl

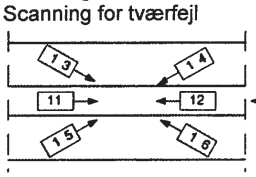

Position	11	12	13	14	15	16
Probe						

Extent of examination / Undersøgelsesomfang

100% UT Test series 2 pl. 30mm 1 pcs. and Test series 3 pl. 40mm 1 pcs.

Result of examination / Undersøgelsens resultat

Not accepted repair on Test series 2 pl. 30mm x:40 to 110 D: 17 and x:710 to 830 D: 14

Not accepted repair on Test series 3 pl. 40mm x:0 to 520 D: 20

Rep. marked / Rep. mærket	Check of / Kontrol af	Enclosures / Bilag	Inspector / Inspektør	Cert. No. / nr.
☒ On object / På objekt ☐ On sketch / På skitse	☐ Grinding / Slibning ☐ Repair / Reparation	☒ None / Ingen ☐ No. / Antal	R.E.N. NSK REN Nordisk Svejse Kontrol A/S	0408-N2-U Date / Dato 1906 2014
Remarks / Bemærkninger			Inspector / Inspektør REN	Cert. No. / nr. 0408-N2-U
			Assistant / Assistent	Cert. No. / nr.

BLADT INDUSTRIES A/S drgt. no.

NSK UT 001 R3 07.01.11

Note: The grey fields supply available, relevant information for guidance only. The giving of such information in this Field Report should not be considered as verification of its accuracy.
Note: Oplysningerne i de grå felter er til information og angives kun i den udstrækning, de er tilgængelige og relevante. Deres angivelse på nærværende markrapport kan ikke betragtes som en verifikation af deres rigtighed.

NSK Nordisk Svejse Kontrol a/s

DANAK TEST Reg.nr. 445

ULTRASONIC / ULTRALYD

Client / Kunde **Bladt Industries a/s**	File No. / Sag nr. **54641** Report No. / Rapport nr. **UT 03**
Contractor / Entreprenør **Bladt Industries a/s**	Date / Dato **2506 2014** Page / Side **1** of / af **1**
Object / Objekt **Test series 2 pl. 30mm 1 pcs. repair from UT 02** **Test series 3 pl. 40mm 1 pcs. repair from UT 02** **NDT REKV. 03**	Drawing No. / Tegning nr. - Material / Materiale **Steel**

Supplementary information (without liability, see note) / **Supplerende oplysninger** (uden ansvar, se note)

Weld process Svejseproces	☐ 111 SMAW	☒ 121 SAW	☐ 141 GTAW	☐ 135/131 GMAW	☐ 136/138 FCAW	☐ 311 OFW	☐ Other Andet	
Weld preparation / Fugegeometri	Other / Andet	PWHT / Varmebehandling		Time of examination / Tidsp. for unders.				
☒ X ☐ Y ☐ U ☐ V ☐ K ☐ I ☐ FW		☐ Yes Ja	☒ No Nej	>24 Hours after welding Timer efter svejsning				
Reinforcement Vulst højde	☒ As welded Som svejst	☐ Ground Slebet	Surface condition Overflade beskaffenhed	☐ Ground Slebet	☒ Smooth Jævn	☐ Coarse Grov		
Examination procedure Undersøgelses procedure	DS/EN ISO 17640 B		Equipment type Udstyr type	USM GO				
Accept criteria Accept kriterier	DS/EN ISO 11666 2		Equipm. No. Udstyr nr.	30-53				
Extent Omfang	☐ 5% ☐ 10% ☐ 20% ☒ 100% ☐ %		Probe check performed Prober kontrolleret	☒				

Straight beam probe / Normalhoved			**Angle beam probe / Vinkelhoved**			
NSK No./nr.	A: 55965	B:	NSK No./nr.	C: 3270	D: 653648	E:
Type / Freq.	SM / 4 MHz	/ MHz	Type / Freq.	70 / 2 MHz	60 / 2 MHz	/ MHz
Sensitivity setting / Følsomhedsindstilling			**Sensitivity setting / Følsomhedsindstilling**			
Basic sett. – ref. level	30 db	db	Basic sett. – ref. level Gr. indst. – ref. level	47 db	46 db	db
Transfer Correction Overføringskorrekti	0 db	db	Transfer Correction Overføringskorrektion	2 db	2 db	db
Extra db for scanning	>8 db	db	Extra db for scanning Ekstra db til scanning	10 db	10 db	db
Scanning level Scanningsniveau	>38 db	db	Scanning level Scanningsniveau	59 db	58 db	db

Reference / Reference DAC: Hole / Hul Ø = 3 mm Range / Skala = 200 mm AVG: Disc / Skive Ø = mm Range / Skala = mm

Ref. block / Ref. blok	Ref. block / Ref. blok	Ref. block / Ref. blok	Ref. block / Ref. blok
☒ V1 NSK No./nr. 13-18	☒ V2 NSK No./nr. 72166	☒ NSK No./nr. 3351	☐ Other / Andet

Scanning for longitudinal defects and lamination
Scanning for længdefejl og lagdeling

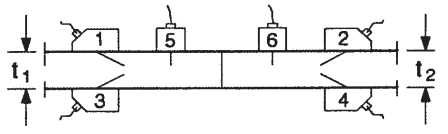

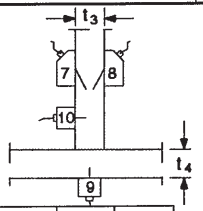

t1 = 30/40
t2 = 30/40
t3 =
t4 =

Position	1	2	3	4	5	6	7	8	9	10
Probe	cd	cd	cd	cd	a	a				

Scanning for transverse defects
Scanning for tværfejl

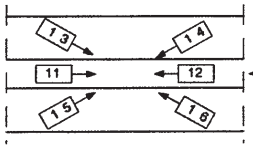

Position	11	12	13	14	15	16
Probe						

Extent of examination / Undersøgelsesomfang
100% UT of repair on Test series 2 pl. 30mm x:40 to 110 D: 17 and x:710 to 830 D: 14
100% UT of repair on Test series 3 pl. 40mm x:0 to 520 D: 20

Result of examination / Undersøgelsens resultat
All Accepted to spec

Rep. marked / Rep. mærket	Check of / Kontrol af	Enclosures / Bilag	Inspector / Inspektør	Cert. No. / nr.
☒ On object / På objekt ☐ On sketch / På skitse	☐ Grinding / Slibning ☐ Repair / Reparation	☒ None / Ingen ☐ No. / Antal	NSK REN R.E.N. Nordisk Svejse Kontrol A/S	0408-N2-U Date / Dato 1906 2014

Remarks / Bemærkninger

Inspector / Inspektør	Cert. No. / nr.
REN	0408-N2-U
Assistant / Assistent	Cert. No. / nr.

BLADT INDUSTRIES

NSK UT 001 R3 07.01.11

Note: The grey fields supply available, relevant information for guidance only. The giving of such information in this Field Report should not be considered as verification of its accuracy.
Note: Oplysningerne i de grå felter er til information og angives kun i den udstrækning, de er tilgængelige og relevante. Deres angivelse på nærværende markrapport kan ikke betragtes som en verifikation af deres rigtighed.

NSK Nordisk Svejse Kontrol a/s

DANAK TEST Reg.nr. 445

MAGNETIC TESTING / MAGNETPRØVNING

Client / Kunde **Bladt Industries a/s**	File No. / Sag nr. **54641** Report No. / Rapport nr. **MT 03**
Contractor / Entreprenør **Bladt Industries a/s**	Date / Dato **18-06-2014** Page / Side **1** of / af **1**
Object / Objekt **Test series 2 pl. 30m and Test series 3 pl. 40mm** **NDT REKV. 02**	Drawing No. / Tegning nr. - Material / Materiale **Cs.**

Supplementary information (without liability, see note) / **Supplerende oplysninger** (uden ansvar, se note)

Weld process / Svejseproces: ☐ 111 SMAW ☒ 121 SAW ☐ 141 GTAW ☐ 135/131 GMAW ☐ 136/138 FCAW ☐ 311 OFW ☐ Other / Andet

Weld preparation / Fugegeometri: ☐ X ☐ Y ☐ U ☒ V ☐ K ☐ I ☐ FW — Other / Andet

PWHT / Varmebehandling: ☐ Yes / Ja ☒ No / Nej

Time of examination / Tidsp. for unders.: >24 Hours after welding / Timer efter svejsning

Reinforcement / Vulst højde: ☒ As welded / Som svejst ☐ Ground / Slebet

Surface condition / Overflade beskaffenhed: ☐ Ground / Slebet ☒ Smooth / Jævn ☐ Coarse / Grov

Examination procedure / Undersøgelses procedure: DS/EN ISO 17638

Accept criteria / Accept kriterier: DS/EN ISO 23278 2x

Extent / Omfang: ☐ 5% ☐ 10% ☐ 20% ☒ 100% ☐ %

☒ Yoke / Magnet	☐ Direct contact / Direkte kontakt	☐ Coil / Spole	☐ Permanent magnet / Permanent magnet	☐ Test bench / Prøvebænk
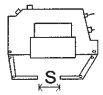		 Current/Strøm ☐ AC ☐ DC		Longit. / Langsg. Amp Circular / Rundg. Amp x turns/vind.
Type Yoke S max = 150 mm	S max = mm I eff. = Amp	K (turns/vind.) = I = Amp	S = mm Lift of power / Løftekraft = kg	
Equip. No. / Udstyr nr. MA 20-134	Equip. No. / Udstyr nr. MA	Equip. No. / Udstyr nr. MA	Equip. No. / Udstyr nr. MA	Equip. No. / Udstyr nr. MA

Probe material / Probe materiale	Probe marks grinded / Probemærke slebet	De-magnetized / Afmagnetiseret	Remaining magnetism / Rest magnetisme
	☐ Yes/Ja ☐ No/Nej	☐ Yes/Ja ☒ No/Nej	Gauss

Examination medium / Magnetvæske	Technique / Teknik	Background / Baggrund
27B	Black	White

Field strength / Feltstyrke: Oe 2-6 KA/m ☒ Castrol Silver

Light / Lys: ☒ White / Hvidt ☐ UV-light / UV lys — Lamp No. / Lampe nr.

Examined for / Undersøgt for: Indications in any direction — Other / Andet

Extent of examination / Undersøgelsesomfang

100% MPI test of welds on Test series 2 pl. 30mm and Test series 3 pl. 40mm

Result of examination / Undersøgelsens resultat

Accepted to specifikation.

Rep. marked / Rep. mærket	Check of / Kontrol af	Enclosures / Bilag	Inspector / Inspektør	Cert. No. / nr.
☐ On object / På objekt ☐ On sketch / På skitse	☐ Grinding / Slibning ☐ Repair / Reparation	☒ None / Ingen ☐ No. / Antal	NSK REN R.E.N. Nordisk Svejse Kontrol A/S	0408-N2-M Date / Dato 1906 2014
Remarks / Bemærkninger			Inspector / Inspektør: REN Assistant / Assistent	Cert. No. / nr.: 0408-N2-M Cert. No. / nr.

BLADT INDUSTRIES

NSK MT 001 R3 07.01.11

Note: The grey fields supply available, relevant information for guidance only. The giving of such information in this Field Report should not be considered as verification of its accuracy.
Note: Oplysningerne i de grå felter er til information og angives kun i den udstrækning, de er tilgængelige og relevante. Deres angivelse på nærværende markrapport kan ikke betragtes som en verifikation af deres rigtighed.

NSK Nordisk Svejse Kontrol a/s

DANAK TEST Reg.nr. 445

MAGNETIC TESTING / MAGNETPRØVNING

Client / Kunde **Bladt Industries a/s**	File No. / Sag nr. **54641** Report No. / Rapport nr. **MT 04**
Contractor / Entreprenør **Bladt Industries a/s**	Date / Dato **25-06-2014** Page / Side **1** of / af **1**
Object / Objekt **Test series 2 pl. 30m and Test series 3 pl. 40mm** **NDT REKV. 03**	Drawing No. / Tegning nr. - Material / Materiale **Cs.**

Supplementary information (without liability, see note) / **Supplerende oplysninger** (uden ansvar, se note)

Weld process / Svejseproces: ☐ 111 SMAW ☒ 121 SAW ☐ 141 GTAW ☐ 135/131 GMAW ☐ 136/138 FCAW ☐ 311 OFW ☐ Other / Andet

Weld preparation / Fugegeometri: ☐ X ☐ Y ☐ U ☒ V ☐ K ☐ I ☐ FW — Other / Andet

PWHT / Varmebehandling: ☐ Yes / Ja ☒ No / Nej

Time of examination / Tidsp. for unders.: >24 Hours after welding / Timer efter svejsning

Reinforcement / Vulst højde: ☒ As welded / Som svejst ☐ Ground / Slebet

Surface condition / Overflade beskaffenhed: ☐ Ground / Slebet ☒ Smooth / Jævn ☐ Coarse / Grov

Examination procedure / Undersøgelses procedure: DS/EN ISO 17638

Accept criteria / Accept kriterier: DS/EN ISO 23278 2x

Extent / Omfang: ☐ 5% ☐ 10% ☐ 20% ☒ 100% ☐ %

☒ Yoke / Magnet	☐ Direct contact / Direkte kontakt	☐ Coil / Spole	☐ Permanent magnet / Permanent magnet	☐ Test bench / Prøvebænk
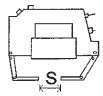	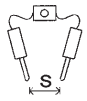	 Current/Strøm ☐ AC ☐ DC		Longit. / Langsg. Amp Circular / Rundg. Amp x turns/vind.
Type Yoke S max = 150 mm	S max = mm I eff. = Amp	K (turns/vind.) = I = Amp	S = mm Lift of power / Løftekraft = kg	
Equip. No. / Udstyr nr. MA 20-134	Equip. No. / Udstyr nr. MA	Equip. No. / Udstyr nr. MA	Equip. No. / Udstyr nr. MA	Equip. No. / Udstyr nr. MA

Probe material / Probe materiale	Probe marks grinded / Probemærke slebet	De-magnetized / Afmagnetiseret	Remaining magnetism / Rest magnetisme
	☐ Yes/Ja ☐ No/Nej	☐ Yes/Ja ☒ No/Nej	Gauss

Examination medium / Magnetvæske	Technique / Teknik	Background / Baggrund
27B	Black	White

Field strength / Feltstyrke: Oe 2-6 KA/m ☒ Castrol Silver

Light / Lys: ☒ White / Hvidt ☐ UV-light / UV lys — Lamp No. / Lampe nr.

Examined for / Undersøgt for: Indications in any direction — Other / Andet

Extent of examination / Undersøgelsesomfang

100% MPI test of welds on Test series 2 pl. 30mm and Test series 3 pl. 40mm after reapir from UT03

Result of examination / Undersøgelsens resultat

Accepted to specifikation.

Rep. marked / Rep. mærket	Check of / Kontrol af	Enclosures / Bilag	Inspector / Inspektør	Cert. No. / nr.
☐ On object / På objekt ☐ On sketch / På skitse	☐ Grinding / Slibning ☐ Repair / Reparation	☒ None / Ingen ☐ No. / Antal	NSK REN R.E.N. Nordisk Svejse Kontrol A/S	0408-N2-M Date / Dato: 2606 2014
Remarks / Bemærkninger			Inspector / Inspektør: REN	Cert. No. / nr.: 0408-N2-M
			Assistant / Assistent	Cert. No. / nr.

BLADT INDUSTRIES

NSK MT 001 R3 07.01.11

Note: The grey fields supply available, relevant information for guidance only. The giving of such information in this Field Report should not be considered as verification of its accuracy.
Note: Oplysningerne i de grå felter er til information og angives kun i den udstrækning, de er tilgængelige og relevante. Deres angivelse på nærværende markrapport kan ikke betragtes som en verifikation af deres rigtighed.

NDT undersøgelse af Svejse- / Procedureprøver

Division for Inspektion og Prøvning

DANAK Reg. nr.	FORCE TASK nr.	Working Area	Kontrolperiode/Dato	Side af
	114-20697/113-24705.20.5		**9-10-04-2014**	**1/2**

Rekvirent
MIH

Emne (Mrk., dim., antal)
2 stk stumpsømme i 25 mm plade, mærket 1 og 2
2 stk stumpsømme i 40 mm plade, mærket 3 og 4

VT - Visuel kontrol Emne nr.

Teknik
☐ EN 970 ☐ NS 10250 ☐ ASME V Andet ☐

Hjælpemidler
☐ A-målslære ☐ Skydelære ☐ Konturlære Andet ☐

Kvalitetskrav (Standard) for færdige svejsesømme
☐ EN ISO 5817 ☐ ASME Sect. ☐ ADM-HP 5/1 Andet ☐

Undersøgelsens omfang
☐ Side 1 (Dækside)
☐ Side 2 (Rodside)

Undersøgelsens resultat - Svejsefejl ifølge EN 26520
☐ Godkendt
☐ Kasseret

Att. af myndighed	Tekniker (Init.)	Certifikat nr.	Tekniker (Dato/underskrift)

RT - Radiografi Emne nr. **1+2+3+4**

Undersøgelsesprocedure
☐ EN 1435/ ☐ ASME V ☐ ADM-HP 5/3 Andet ☒ **ISO 15614**

Optageteknik A-E
☒ A. ☐ B. ☐ C. Eksp./Søm ☐ D. Ellipse + Direkte Eksp./Søm ☐ E. Eksp./Søm
Placer. af IQI ☒ IQI ☐ IQI

Filmfabr. **FOMA** / Type **R4** / Kl. 1) **C3** / Str.: **10** x **48** cm
☒ Vacuumpk. Folie: ☒ Pb / ☐ Ingen
Tykkelse: for: **0,027** mm bag: **0,027** mm

☐ Ir192 ☒ Rø.
☐ Se75
Andet: ☐

Rør reg. nr. **XRVA-1**
Brændplet **3** x **3** mm
Brændplet x mm

☐ Manuel / ☒ Automatisk fremkaldelse
Filmsværtning: **2,3 - 3,7**
Densitometer reg. nr. **PDE-28**
Lyskasse reg. nr. **VGI-1**

Exp.	kVP	SFD cm	mA/Ci	Min.
I	**225** /	**70** /	**5,3** /	**1,53**
II	**225** /	**70** /	**5,3** /	**10,00**
III	/	/	/	
IV	/	/	/	
V	/	/	/	

Kvalitetskrav
☐ EN 12517-1 niv. ☐ IIW (54-73) karakter
☐ EN ISO 5817 ☐ ASME VIII Div. 1. ☐ ASME IX ☐ API 1104 ☐ HP 5/3 Andet ☒ **ISO 12932:2013**

Tillægskrav

Omfang **100** %

☐ Film nr. ☒ Emne nr.	Filmplacering	Svejser mrk.	Tekn. A-E	Exp.d I-IV	Nominel tykkelse	MST	Svejsefejl EN 26520	Godk.	Kass.
1 B81	**0,00 - 0,35**		**A**	**I**	**25**	**13**		**X**	
2 B83	**0,00 - 0,35**		**A**	**I**	**25**	**13**		**X**	
3 B93	**0,00 - 0,35**		**A**	**II**	**40**	**11**		**X**	
4 B101-108	**0,00 - 0,35**		**A**	**II**	**40**	**11**		**X**	
---	---	---	---	---	---	---	---	---	---

Rep. opmrk.	Att. af myndighed	Tekniker (Init.)	Certifikat nr.	Tekniker (Dato/underskrift)
☐ På emne ☐ På skitse		**BUC**	**1118-N2-R**	**10-04-2014**

☒ Se bagside

MT - Magnetpulverprøvning Emne nr. 1+2+3+4

Undersøgelsesprocedure
☐ ASME V ☐ ADM-HP 5/3 ☐ EN 1290 Andet ☒ 15614

☒ Elektromagnet
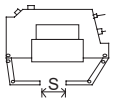

Type Magnaflux
Smax. = 120 mm
Apparat nr. EMM-106

☐ Prøvebænk
Langsg. ____ Amp.
Rundg. ____ Amp. vind.

Feltstyrke ____ kA/m
Ørstedmeterværdi: ____ Oe

Andet ☐ ____
Afmagnetisering ☐ Ja ☒ Nej
Belysning: ☒ Hvid ☐ UV-lampe Nr. ____

Kvalitetskrav
☐ EN ISO 5817 ☐ ADM-HP 5/3 ☐ ASME VIII.1 ☐ EN 1291 niv. Andet ☒ EN ISO 23278,1

Undersøgelsens omfang
☒ Side 1 (Dækside)
☒ Side 2 (Rodside) ☒ Fejl i alle retninger

Undersøgelsens resultat - Fejltype / nr. ifølge EN 26520
☒ Godkendt
☐ Kasseret

Rep. opmrk.	Att. af myndighed	Tekniker (Init.)	Certifikat nr.	Tekniker (Dato/underskrift)
☐ På emne ☐ På skitse		BUC	1118-N2-M	10-04-2014

PT - Penetrantprøvning Emne nr.

Undersøgelsesprocedure
☐ EN 571-1 ☐ ASME V, Art.6 ☐ ISO 3452 Andet ☐

Rensning før undersøgelse
☐ Ingen ☐ Rensevæske påført ☐ Neddypning i bad
Produktbetegnelse

Penetrantsystem
Fabrikat:

Penetranttype
☐ A. Fluoresc. ☐ B. Farve ☐ C. Kombin.
Produktbetegnelse/Batch nr.

Afrensning af overskudsvæske
☐ H. Opløsningsmiddel + aftørring ☐ I. Vandafskylning ☐ K. Emulgering + vand
Produktbetegnelse/Batch nr.

Fremkaldermetode
☐ Q. Tørpulver ☐ R. Pulver i vand ☐ S. Pulver i flygtig væske ☐ T. Opløsning i vand
Produktbetegnelse/Batch nr.

Indtrængningstid	Emulgeringstid	Fremkaldertid	Emnets temperatur
min.	min.	min.	° C

Belysning
☐ Hvid ☐ UV-lampe nr.

Kvalitetskrav (Standard)
☐ ASME VIII.1 ☐ ADM-HP 5/3 ☐ EN 1289, niv. ☐ EN ISO 5817 ☐ EN ISO 10042 Andet ☐

Undersøgelsens omfang
☐ Side 1 (Dækside)
☐ Side 2 (Rodside)

Undersøgelsens resultat - Fejltype / nr. ifølge EN 26520
☐ Godkendt
☐ Kasseret

Rep. opmrk.	Att. af myndighed	Tekniker (Init.)	Certifikat nr.	Tekniker (Dato/underskrift)
☐ På emne ☐ På skitse				

Supplerende bemærkninger
☐ **VT** ☐ **RT** ☐ **MT** ☐ **PT**

Bilag vedlagt	Teknisk sagkyndig	Sagsbehandler eller att. myndighed (Dato/underskrift)
☐ Stk.		

E. Fatigue test results

The following figures list individual fatigue results for all welded joints tested.

Test series 1 Batch 1 20 mm thickness

Test specimen	Area [mm2]	Percent yield [%]	Stress max [Mpa]	Stress min [Mpa]	Δσ [Mpa]	R - ratio	Frequency [Hz]	Machine	Cycles to failure	Failure description
T20 - 34	837,51	80,00	298,56	149,28	149,28	0,5	8	MTS 312.41	5000000	Run out
T20 - 15	833,09	90,00	335,88	167,94	167,94	0,5	8	MTS 312.41	1116793	Grip fracture
T20 - 14	830,21	90,00	335,88	167,94	167,94	0,5	8	MTS 312.41	1275457	Broke in Weld
T20 - 13	833,06	90,00	335,88	167,94	167,94	0,5	8	Instron 1343	889754	Broke in Weld
T20 - 12	834,50	90,00	335,88	167,94	167,94	0,5	8	MTS 312.41	4372412	Grip fracture
T20 - 11	832,86	90,00	335,88	167,94	167,94	0,5	8	Instron 1343	2416597	Grip fracture
T20 - 10	832,87	90,00	335,88	167,94	167,94	0,5	8	Instron 1343	1555263	Broke in Weld
T20 - 09	834,29	90,00	335,88	167,94	167,94	0,5	8	MTS 312.41	1220120	Broke in Weld
T20 - 08	832,25	90,00	335,88	167,94	167,94	0,5	8	MTS 312.41	5000000	Run out
T20 - 33	831,84	90,00	335,88	167,94	167,94	0,5	8	MTS 312.41	4592270	Grip fracture
T20 - 16	834,91	100,00	373,20	186,60	186,60	0,5	8	MTS 312.41	729306	Broke in Weld
T20 - 17	833,92	100,00	373,20	186,60	186,60	0,5	8	MTS 312.41	788778,5	Broke in Weld
T20 - 18	833,90	100,00	373,20	186,60	186,60	0,5	8	MTS 312.41	850626	Grip fracture
T20 - 19	837,59	100,00	373,20	186,60	186,60	0,5	8	MTS 312.41	1119794	Broke in Weld
T20 - 20	833,28	100,00	373,20	186,60	186,60	0,5	8	MTS 312.41	534886	Broke in Weld
T20 - 21	832,66	100,00	373,20	186,60	186,60	0,5	8	MTS 312.41	1162113	Grip fracture
T20 - 22	832,86	100,00	373,20	186,60	186,60	0,5	8	MTS 312.41	663568	Broke in Weld
T20 - 07	832,86	110,00	410,52	205,26	205,26	0,5	8	Instron 1343	726006	Broke in Weld
T20 - 06	831,43	110,00	410,52	205,26	205,26	0,5	8	Instron 1343	423891	Grip fracture
T20 - 05	831,62	110,00	410,52	205,26	205,26	0,5	8	Instron 1343	207876	Grip fracture
T20 - 04	831,83	110,00	410,52	205,26	205,26	0,5	8	Instron 1343	534024	Broke in specimen flaw (Indentation)
T20 - 23	832,24	110,00	410,52	205,26	205,26	0,5	8	MTS 312.41	545145	Broke in Weld
T20 - 24	832,24	110,00	410,52	205,26	205,26	0,5	8	MTS 312.41	525130	Broke in Weld
T20 - 25	832,86	110,00	410,52	205,26	205,26	0,5	8	MTS 312.41	446145	Broke in Weld
T20 - 26	833,65	110,00	410,52	205,26	205,26	0,5	8	MTS 312.41	545348	Broke in Weld
T20 - 27	832,64	120,00	447,84	223,92	223,92	0,5	8	MTS 312.41	384720	Broke in Weld
T20 - 28	833,44	120,00	447,84	223,92	223,92	0,5	8	MTS 312.41	394247	Broke in Weld
T20 - 29	836,47	120,00	447,84	223,92	223,92	0,5	8	MTS 312.41	591206	Broke in Weld
T20 - 30	833,86	120,00	447,84	223,92	223,92	0,5	8	MTS 312.41	830295	Grip fracture
T20 - 31	831,03	120,00	447,84	223,92	223,92	0,5	8	MTS 312.41	647360	Broke in Weld
T20 - 32	832,67	120,00	447,84	223,92	223,92	0,5	8	MTS 312.41	602732	Broke in Weld

Figure 12: *Test series 1: Fatigue test data for all 20 mm thick joints from batch 1*

Test series 1	Batch 1	30 mm thickness								
Test specimen	Area [mm2]	Percent yield [%]	Stress max [Mpa]	Stress min [Mpa]	Δσ [Mpa]	R - ratio	Frequency [Hz]	Machine	Cycles to failure	Failure description
T30 - 11	1227,64	80,00	301,44	150,72	150,72	0,50	8,00	Instron 1343	1109421	Broke in Weld
T30 - 12	1227,34	80,00	301,44	150,72	150,72	0,50	8,00	MTS 312.41	1246088	Broke in Weld
T30 - 13	1228,81	80,00	301,44	150,72	150,72	0,50	8,00	Instron 1343	1183833	Broke in Weld
T30 - 14	1226,59	80,00	301,44	150,72	150,72	0,50	8,00	Instron 1343	803934	Broke in Weld
T30 - 15	1223,51	80,00	301,44	150,72	150,72	0,50	8,00	Instron 1343	683003	Broke in Weld
T30 - 4	1226,94	90,00	339,12	169,56	169,56	0,50	8,00	Instron 1343	328235	Broke in Weld
T30 - 7	1226,79	90,00	339,12	169,56	169,56	0,50	8,00	Instron 1343	603130	Broke in Weld
T30 - 8	1227,59	90,00	339,12	169,56	169,56	0,50	8,00	Instron 1343	622385	Broke in Weld
T30 - 9	1226,23	90,00	339,12	169,56	169,56	0,50	8,00	Instron 1343	497692	Broke in Weld
T30 - 10	1223,36	90,00	339,12	169,56	169,56	0,50	8,00	MTS 312.41	604467	Broke in Weld
T30 - 5	1226,53	100,00	376,80	188,40	188,40	0,50	8,00	Instron 1343	316247	Broke in Weld
T30 - 6	1227,49	100,00	376,80	188,40	188,40	0,50	8,00	Instron 1343	368309	Broke in Weld
T30 - 16	1231,15	100,00	376,80	188,40	188,40	0,50	8,00	Instron 1343	336687	Broke in Weld
T30 - 17	1226,58	100,00	376,80	188,40	188,40	0,50	8,00	Instron 1343	309055	Broke in Weld
T30 - 18	1227,80	100,00	376,80	188,40	188,40	0,50	8,00	Instron 1343	313089	Broke in Weld
T30 - 20	1230,03	110,00	414,48	207,24	207,24	0,50	8,00	Instron 1343	224272	Broke in Weld
T30 - 21	1226,63	110,00	414,48	207,24	207,24	0,50	8,00	Instron 1343	234980	Broke in Weld
T30 - 22	1230,99	110,00	414,48	207,24	207,24	0,50	8,00	Instron 1343	244781	Broke in Weld
T30 - 23	1227,18	110,00	414,48	207,24	207,24	0,50	8,00	Instron 1343	280330	Broke in Weld
T30 - 25	1226,83	110,00	414,48	207,24	207,24	0,50	8,00	Instron 1343	306548	Broke in Weld
T30 - 24	1228,51	120,00	452,16	226,08	226,08	0,50	8,00	Instron 1343	180604	Broke in Weld
T30 - 26	1227,76	120,00	452,16	226,08	226,08	0,50	8,00	Instron 1343	214858	Broke in Weld
T30 - 27	1224,56	120,00	452,16	226,08	226,08	0,50	8,00	Instron 1343	234208	Broke in Weld
T30 - 28	1226,63	120,00	452,16	226,08	226,08	0,50	8,00	Instron 1343	232284	Broke in Weld
T30 - 29	1229,27	120,00	452,16	226,08	226,08	0,50	8,00	Instron 1343	228657	Broke in Weld

Figure 13: *Test series 1: Fatigue test data for all 30 mm thick joints from batch 1*

Test series 1	Batch 1	40 mm thickness								
Test specimen	Area [mm2]	Percent yield [%]	Stress max [Mpa]	Stress min [Mpa]	Δσ [Mpa]	R - ratio	Frequency [Hz]	Machine	Cycles to failure	Failure description
T40 - 22	1635,77	80,00	295,34	147,67	147,67	0,50	10,00	Instron 4495	1743101	Grip Fracture
T40 - 23	1634,97	80,00	295,34	147,67	147,67	0,50	10,00	Instron 4495	1808978	Broke in Weld
T40 - 26	1634,56	80,00	295,34	147,67	147,67	0,50	10,00	Instron 4495	1608600	Grip Fracture
T40 - 24	1634,56	80,00	295,34	147,67	147,67	0,50	10,00	Instron 4495	1176466	Broke in Weld
T40 - 25	1635,18	80,00	295,34	147,67	147,67	0,50	10,00	Instron 4495	1676702	Grip Fracture
T40 - 27	1634,56	80,00	295,34	147,67	147,67	0,50	10,00	Instron 4495	1405950	Grip Fracture
T40 - 28	1632,14	80,00	295,34	147,67	147,67	0,50	10,00	Instron 4495	718870	Grip Fracture
T40 - 29	1634,16	80,00	295,34	147,67	147,67	0,50	10,00	Instron 4495	2407330	Broke in Weld
T40 - 30	1632,96	80,00	295,34	147,67	147,67	0,50	10,00	Instron 4495	1686341	Grip Fracture
T40 - 31	1634,17	80,00	295,34	147,67	147,67	0,50	10,00	Instron 4495	1924216	Broke in Weld
T40 - 34	1649,50	80,00	295,34	147,67	147,67	0,50	10,00	Instron 4495	1674493	Broke in Weld
T40 - 16	1636,58	90,00	332,25	166,13	166,13	0,50	10,00	Instron 4495	536282	Broke in Weld
T40 - 17	1625,26	90,00	332,25	166,13	166,13	0,50	10,00	Instron 4495	576500	Grip Fracture
T40 - 18	1642,68	90,00	332,25	166,13	166,13	0,50	10,00	Instron 4495	667553	Broke in Weld
T40 - 19	1639,03	90,00	332,25	166,13	166,13	0,50	10,00	Instron 4495	635913	Broke in Weld
T40 - 20	1631,94	90,00	332,25	166,13	166,13	0,50	10,00	Instron 4495	605761	Broke in Weld
T40 - 21	1633,76	90,00	332,25	166,13	166,13	0,50	10,00	Instron 4495	715054	Broke in Weld
T40 - 4	1634,18	100,00	369,17	184,59	184,59	0,50	10,00	Instron 4495	462501	Broke in Weld
T40 - 5	1640,64	100,00	369,17	184,59	184,59	0,50	10,00	Instron 4495	540869	Broke in Weld
T40 - 6	1625,87	100,00	369,17	184,59	184,59	0,50	10,00	Instron 4495	346497	Grip Fracture
T40 - 7	1591,92	100,00	369,17	184,59	184,59	0,50	10,00	Instron 4495	388375	Grip Fracture
T40 - 8	1633,16	100,00	369,17	184,59	184,59	0,50	10,00	Instron 4495	506690	Broke in Weld
T40 - 9	1604,99	100,00	369,17	184,59	184,59	0,50	10,00	Instron 4495	377800	Grip Fracture
T40 - 10	1634,97	100,00	369,17	184,59	184,59	0,50	10,00	Instron 4495	536893	Broke in Weld
T40 - 11	1631,54	100,00	369,17	184,59	184,59	0,50	10,00	Instron 4495	394622	Grip Fracture
T40 - 12	1631,14	100,00	369,17	184,59	184,59	0,50	10,00	Instron 4495	453771	Broke in Weld
T40 - 13	1631,94	110,00	406,09	203,04	203,04	0,50	10,00	Instron 4495	293241	Grip Fracture
T40 - 14	1631,33	110,00	406,09	203,04	203,04	0,50	10,00	Instron 4495	225550	Grip Fracture
T40 - 15	1636,78	110,00	406,09	203,04	203,04	0,50	10,00	Instron 4495	51760	Grip Fracture

Figure 14: *Test series 1: Fatigue test data for all 40 mm thick joints from batch 1*

Test series 1	Batch 2	20 mm thickness								
Test specimen	Area [mm2]	Percent yield [%]	Stress [Mpa]	Stress min [Mpa]	Δσ [Mpa]	R - ratio	Frequency [Hz]	Machine	Cycles to failure	Failure description
T20 - 4_2	789,91	80,00	325,12	162,56	162,56	0,50	8,00	MTS 312.41	6270579	Run out
T20 - 2_2	795,76	80,00	325,12	162,56	162,56	0,50	8,00	Instron 1343	5000000	Run out
T20 - 3_2	790,78	80,00	325,12	162,56	162,56	0,50	8,00	Instron 1343	5000000	Run out
T20 - 5_2	788,42	80,00	325,12	162,56	162,56	0,50	8,00	Instron 1343	5000000	Run out
T20 - 6_2	788,52	80,00	325,12	162,56	162,56	0,50	8,00	Instron 1343	5000000	Run out
T20 - 24_2	787,40	85,00	345,44	172,72	172,72	0,50	8,00	MTS 312.41	907325	Broke in Weld
T20 - 25_2	787,01	85,00	345,44	172,72	172,72	0,50	8,00	MTS 312.41	583093	Broke in Weld
T20 - 11_2	787,32	85,00	345,44	172,72	172,72	0,50	8,00	MTS 312.41	291004	Broke in Weld
T20 - 10_2	780,83	85,00	345,44	172,72	172,72	0,50	8,00	MTS 312.41	441400	Broke in Weld
T20 - 9_2	789,41	85,00	345,44	172,72	172,72	0,50	8,00	MTS 312.41	414924	Broke in Weld
T20 - 8_2	785,64	90,00	365,76	182,88	182,88	0,50	8,00	Instron 1343	228010	Broke in Weld
T20 - 7_2	787,83	90,00	365,76	182,88	182,88	0,50	8,00	MTS 312.41	255551	Broke in Weld
T20 - 25_1	788,74	90,00	365,76	182,88	182,88	0,50	8,00	MTS 312.41	423851	Broke in Weld
T20 - 24_1	785,07	90,00	365,76	182,88	182,88	0,50	8,00	MTS 312.41	483480	Broke in Weld
T20 - 22_1	788,14	90,00	365,76	182,88	182,88	0,50	8,00	MTS 312.41	322403	Broke in Weld
T20 - 12_2	786,33	100,00	406,40	203,20	203,20	0,50	8,00	MTS 312.41	184433	Broke in Weld
T20 - 13_2	788,21	100,00	406,40	203,20	203,20	0,50	8,00	MTS 312.41	256347	Broke in Weld
T20 - 15_2	789,71	100,00	406,40	203,20	203,20	0,50	8,00	MTS 312.41	216400	Broke in Weld
T20 - 16_2	786,83	100,00	406,40	203,20	203,20	0,50	8,00	MTS 312.41	270590	Broke in Weld
T20 - 23_2	787,79	100,00	406,40	203,20	203,20	0,50	8,00	MTS 312.41	277507	Broke in Weld
T20 - 17_2	787,52	110,00	447,04	223,52	223,52	0,50	8,00	MTS 312.41	222302	Broke in Weld
T20 - 18_2	786,72	110,00	447,04	223,52	223,52	0,50	8,00	MTS 312.41	198270	Broke in Weld
T20 - 19_2	786,53	110,00	447,04	223,52	223,52	0,50	8,00	MTS 312.41	249409	Broke in Weld
T20 - 20_2	787,62	110,00	447,04	223,52	223,52	0,50	8,00	MTS 312.41	358530	Broke in Weld
T20 - 21_2	786,42	110,00	447,04	223,52	223,52	0,50	8,00	MTS 312.41	272243	Broke in Weld
T20 - 22_2	787,01	120,00	487,68	243,84	243,84	0,50	8,00	MTS 312.41	188628	Broke in Weld

Figure 15: *Test series 1: Fatigue test data for all 20 mm thick joints from batch 2*

Test series 1	Batch 2	30 mm thickness								
Test specimen	Area [mm2]	Percent yield [%]	Stress max [Mpa]	Stress min [Mpa]	Δσ [Mpa]	R - ratio	Frequency [Hz]	Machine	Cycles to failure	Failure description
T30 - 17_2	1200,48	60,00	222,84	111,42	111,42	0,50	8	MTS 312.41	1536450	Broke in Weld
T30 - 18_2	1202,58	60,00	222,84	111,42	111,42	0,50	8	Instron 1343	806739	Broke in Weld
T30 - 19_2	1197,38	60,00	222,84	111,42	111,42	0,50	8	Instron 1343	1554396	Broke in Weld
T30 - 20_2	1200,57	60,00	222,84	111,42	111,42	0,50	8	MTS 312.41	1623421	Broke in Weld
T30 - 21_2	1202,53	60,00	222,84	111,42	111,42	0,50	8	Instron 1343	882223	Broke in Weld
T30 - 22_2	1205,02	70,00	259,98	129,99	129,99	0,50	8	Instron 1343	546813	Broke in Weld
T30 - 23_2	1197,19	70,00	259,98	129,99	129,99	0,50	8	Instron 1343	539002	Broke in Weld
T30 - 24_2	1198,73	70,00	259,98	129,99	129,99	0,50	8	Instron 1343	458613	Broke in Weld
T30 - 25_2	1194,51	70,00	259,98	129,99	129,99	0,50	8	Instron 1343	471034	Broke in Weld
T30 - 26_2	1199,34	70,00	259,98	129,99	129,99	0,50	8	Instron 1343	558659	Broke in Weld
T30 - 2_2	1201,57	80,00	297,12	148,56	148,56	0,50	8	Instron 1343	350181	Broke in Weld
T30 - 3_2	1204,03	80,00	297,12	148,56	148,56	0,50	8	Instron 1343	452018	Broke in Weld
T30 - 4_2	1205,09	80,00	297,12	148,56	148,56	0,50	8	Instron 1343	385219	Broke in Weld
T30 - 5_2	1203,53	80,00	297,12	148,56	148,56	0,50	8	Instron 1343	494783	Broke in Weld
T30 - 6_2	1200,84	80,00	297,12	148,56	148,56	0,50	8	Instron 1343	473250	Broke in Weld
T30 - 7_2	1201,02	90,00	334,26	167,13	167,13	0,50	8	MTS 312.41	433421	Broke in Weld
T30 - 8_2	1201,83	90,00	334,26	167,13	167,13	0,50	8	MTS 312.41	339160	Broke in Weld
T30 - 9_2	1203,12	90,00	334,26	167,13	167,13	0,50	8	MTS 312.41	441920	Broke in Weld
T30 - 10_2	1205,69	90,00	334,26	167,13	167,13	0,50	8	MTS 312.41	483461	Broke in Weld
T30 - 11_2	1209,82	90,00	334,26	167,13	167,13	0,50	8	MTS 312.41	387589	Broke in Weld
T30 - 12_2	1210,92	100,00	371,40	185,70	185,70	0,50	8	MTS 312.41	235425	Broke in Weld
T30 - 13_2	1205,19	100,00	371,40	185,70	185,70	0,50	8	MTS 312.41	242985	Broke in Weld
T30 - 14_2	1205,60	100,00	371,40	185,70	185,70	0,50	8	MTS 312.41	259764	Broke in Weld
T30 - 15_2	1198,98	100,00	371,40	185,70	185,70	0,50	8	MTS 312.41	247309	Broke in Weld
T30 - 16_2	1196,64	100,00	371,40	185,70	185,70	0,50	8	MTS 312.41	296069	Broke in Weld

Figure 16: *Test series 1: Fatigue test data for all 30 mm thick joints from batch 2*

Test series 1	Batch 2	40 mm thickness								
Test specimen	Area [mm2]	Percent yield [%]	Stress max [Mpa]	Stress min [Mpa]	Δσ [Mpa]	R - ratio	Frequency [Hz]	Machine	Cycles to failure	Failure description
T40 - 1	1615,63	70,00	249,73	124,86	124,86	0,50	6,00	Instron 4495	5000000	Run out
T40 - 2	1612,81	70,00	249,73	124,86	124,86	0,50	6,00	Instron 4495	2543332	Broke in weld
T40 - 4	1605,56	70,00	249,73	124,86	124,86	0,50	6,00	Instron 4495	5000000	Run out
T40 - 11	1600,72	70,00	249,73	124,86	124,86	0,50	6,00	Instron 4495	1640186	Broke in weld
T40 - 12	1601,56	80,00	285,40	142,70	142,70	0,50	6,00	Instron 4495	712134	Broke in weld
T40 - 7	1600,33	80,00	285,40	142,70	142,70	0,50	6,00	Instron 4495	817198	Broke in weld
T40 - 16	1599,50	80,00	285,40	142,70	142,70	0,50	6,00	Instron 4495	905252	Broke in weld
T40 - 10	1605,11	80,00	285,40	142,70	142,70	0,50	6,00	Instron 4495	816239	Broke in weld
T40 - 13	1605,95	90,00	321,08	160,54	160,54	0,50	6,00	Instron 4495	495302	Broke in weld
T40 - 15	1604,37	90,00	321,08	160,54	160,54	0,50	6,00	Instron 4495	557922	Broke in weld
T40 - 14	1605,96	90,00	321,08	160,54	160,54	0,50	6,00	Instron 4495	602293	Broke in weld
T40 - 17	1606,37	100,00	356,75	178,38	178,38	0,50	6,00	Instron 4495	358784	Broke in weld
T40 - 18	1600,73	100,00	356,75	178,38	178,38	0,50	6,00	Instron 4495	321150	Broke in weld
T40 - 3	1615,22	100,00	356,75	178,38	178,38	0,50	6,00	Instron 4495	470184	Broke in weld
T40 - 5	1607,55	110,00	392,43	196,21	196,21	0,50	6,00	Instron 4495	302079	Broke in weld
T40 - 6	1603,94	110,00	392,43	196,21	196,21	0,50	6,00	Instron 4495	308386	Broke in weld
T40 - 9	1606,74	110,00	392,43	196,21	196,21	0,50	6,00	Instron 4495	252671	Broke in weld

Figure 17: *Test series 1: Fatigue test data for all 40 mm thick joints from batch 2*

Test series 2	Batch 2	20 mm thickness	Corrosion envrionment							
Test specimen	Area [mm2]	Percent yield [%]	Stress [Mpa]	Stress min [Mpa]	Δσ [Mpa]	R - ratio	Frequency [Hz]	Machine	Cycles to failure	Failure description
T3 - 13_1	783,34	60,00	243,84	121,92	121,92	0,50	8,00	Kyong Do	5000000	Run out
T3 - 12_1	788,83	60,00	243,84	121,92	121,92	0,50	8,00	Kyong Do	5000000	Run out
T3 - 2_1	791,82	70,00	284,48	142,24	142,24	0,50	8,00	Kyong Do	2655562	Fractured in rounding
T3 - 16_1	788,24	70,00	284,48	142,24	142,24	0,50	8,00	Kyong Do	1691186	Broke in weld
T3 - 17_1	787,24	70,00	284,48	142,24	142,24	0,50	8,00	Kyong Do	1893588	Broke in weld
T3 - 15_1	786,64	70,00	284,48	142,24	142,24	0,50	8,00	Kyong Do	1927360	Broke in weld
T3 - 14_1	788,14	70,00	284,48	142,24	142,24	0,50	8,00	Kyong Do	4912070	Fractured in rounding
T3 - 4_1	789,23	70,00	284,48	142,24	142,24	0,50	8,00	Kyong Do	3511868	Fractured in rounding
T3 - 18_1	789,43	80,00	325,12	162,56	162,56	0,50	8,00	Kyong Do	927996	Broke in weld
T3 - 19_1	781,59	80,00	325,12	162,56	162,56	0,50	8,00	Kyong Do	3602819	Broke in weld
T3 - 20_1	787,64	80,00	325,12	162,56	162,56	0,50	8,00	Kyong Do	1013356	Broke in weld
T3 - 21_1	787,84	80,00	325,12	162,56	162,56	0,50	8,00	Kyong Do	1340274	Fractured in rounding
T3 - 3_1	794,81	80,00	325,12	162,56	162,56	0,50	8,00	Kyong Do	984367	Broke in weld
T3 - 10_1	790,12	90,00	365,76	182,88	182,88	0,50	8,00	Kyong Do	493058	Broke in weld
T3 - 9_1	787,94	90,00	365,76	182,88	182,88	0,50	8,00	Kyong Do	442732	Broke in weld
T3 - 8_1	791,22	90,00	365,76	182,88	182,88	0,50	8,00	Kyong Do	526233	Broke in weld
T3 - 5_1	791,22	100,00	406,40	203,20	203,20	0,50	8,00	Kyong Do	294423	Broke in weld
T3 - 6_1	788,74	100,00	406,40	203,20	203,20	0,50	8,00	Kyong Do	320850	Broke in weld
T3 - 7_1	790,23	100,00	406,40	203,20	203,20	0,50	8,00	Kyong Do	337787	Broke in weld

Figure 18: *Test series 2: Corrosion fatigue test data for all 20 mm thick joints*

Test series 3	Laser hybrid	25 mm thickness								
Test specimen	Area [mm2]	Percent yield [%]	Stress max [Mpa]	Stress min [Mpa]	Δσ [Mpa]	R - ratio	Frequency [Hz]	Machine	Cycles to failure	Failure description
LH 11_3	1010,53	90,00	296,43	148,22	148,22	0,50	10,00	Instron 1343	5000000	Run out
LH 9_3	1003,68	90,00	296,43	148,22	148,22	0,50	10,00	Instron 1343	5000000	Run out
LH 11_2	1004,28	90,00	296,43	148,22	148,22	0,50	10,00	Instron 1343	5000000	Run out
LH 9_2	1002,65	90,00	296,43	148,22	148,22	0,50	10,00	Instron 1343	5000000	Run out
LH 11_1	1003,35	90,00	296,43	148,22	148,22	0,50	10,00	Instron 1343	5000000	Run out
LH 4_3	1007,69	95,00	312,90	156,45	156,45	0,50	10,00	MTS 312.41	5000000	Run out
LH 3_3	1006,18	95,00	312,90	156,45	156,45	0,50	10,00	Instron 1343	5000000	Run out
LH 4_2	999,47	95,00	312,90	156,45	156,45	0,50	10,00	MTS 312.41	5000000	Run out
LH 3_2	998,20	95,00	312,90	156,45	156,45	0,50	10,00	Instron 1343	5000000	Run out
LH 4_1	1003,75	95,00	312,90	156,45	156,45	0,50	10,00	MTS 312.41	5000000	Run out
LH 12_3	1009,87	100,00	329,37	164,69	164,69	0,50	10,00	MTS 312.41	2801993	Broke in Weld
LH 10_3	1005,78	100,00	329,37	164,69	164,69	0,50	10,00	MTS 312.41	2226760	Broke in Weld
LH 12_2	1003,15	100,00	329,37	164,69	164,69	0,50	10,00	MTS 312.41	1259179	Broke in Weld
LH 10_2	1000,54	100,00	329,37	164,69	164,69	0,50	10,00	MTS 312.41	1924324	Broke in Weld
LH 12_1	1007,21	100,00	329,37	164,69	164,69	0,50	10,00	MTS 312.41	2009060	Broke in Weld
LH 8_3	1006,06	110,00	362,31	181,15	181,15	0,50	10,00	MTS 312.41	1182202	Broke in Weld
LH 7_3	1003,73	110,00	362,31	181,15	181,15	0,50	10,00	MTS 312.41	1350088	Broke in Weld
LH 8_2	999,47	110,00	362,31	181,15	181,15	0,50	10,00	MTS 312.41	2184448	Broke in Weld
LH 7_2	1004,23	110,00	362,31	181,15	181,15	0,50	10,00	MTS 312.41	1396310	Broke in Weld
LH 8_1	1008,51	110,00	362,31	181,15	181,15	0,50	10,00	MTS 312.41	1335994	Broke in Weld
LH 6_3	1005,11	120,00	395,24	197,62	197,62	0,50	10,00	MTS 312.41	1007145	Broke in Weld
LH 5_3	1008,59	120,00	395,24	197,62	197,62	0,50	10,00	MTS 312.41	916212	Broke in Weld
LH 5_2	1003,20	120,00	395,24	197,62	197,62	0,50	10,00	MTS 312.41	850232	Broke in Weld
LH 6_1	1004,03	120,00	395,24	197,62	197,62	0,50	10,00	MTS 312.41	793294	Broke in Weld
LH 6_2	1003,30	120,00	395,24	197,62	197,62	0,50	10,00	MTS 312.41	976247	Grip Fracture
LH 2_3	1005,77	120,00	395,24	197,62	197,62	0,50	10,00	MTS 312.41	1023621	Broke in Weld

Figure 19: *Test series 3: Fatigue test data for all 25 mm thick Laser hybrid welded joints*

E. Corrosion

Figure 20, is a list of metals arranged with respect to their standard potentials against a hydrogen electrode, SHE.

Figure 21 illustrates a simplified pourbaix diagram for iron in water.

Electrode reaction	E_0^0 (V)
$Au^{3+} + 3e^- = Au$	1.50
$Cl_2 + 2e^- = 2Cl^-$	1.36
$O_2 + 4H^+ + 4e^- = 2H_2O$	1.23
$Pt^{2+} + 2e^- = Pt$	1.20
$Fe_3O_4 + 8H^+ + 2e^- = 3Fe^{2+} + 4H_2O$	0.98
$HNO_3 + 3H^+ + 3e^- = NO + 2H_2O$	0.96
$Ag^+ + e^- = Ag$	0.80
$Fe^{3+} + e^- = Fe^{2+}$	0.77
$Fe_2O_3 + 6H^+ + 2e^- = 2Fe^{2+} + 3H_2O$	0.73
$O_2 + 2H_2O + 4e^- = 4OH^-$	0.40
$Cu^{2+} + 2e^- = Cu$	0.34
$Hg^{2+} + 2e^- = 2Hg$	0.79
$AgCl + e^- = Ag + Cl^-$	0.22
$S + 2H^+ + 2e^- = H_2S$	0.14
$2H^+ + 2e^- = H_2$	0
$Fe_3O_4 + 8H^+ + 8e^- = 3Fe + 4H_2O$	–0.085
$Pb^{2+} + 2e^- = Pb$	–0.13
$Sn^{2+} + 2e^- = Sn$	–0.14
$Ni^{2+} + 2e^- = Ni$	–0.25
$Cd^{2+} + 2e^- = Cd$	–0.40
$Fe^{2+} + 2e^- = Fe$	–0.44
$Cr^{3+} + 3e^- = Cr$	–0.74
$Zn^{2+} + 2e^- = Zn$	–0.76
$2H_2O + 2e^- = 2OH^- + H_2$	–0.83
$Ti^{2+} + 2e^- = Ti$	–1.63
$Al^{3+} + 3e^- = Al$	–1.66

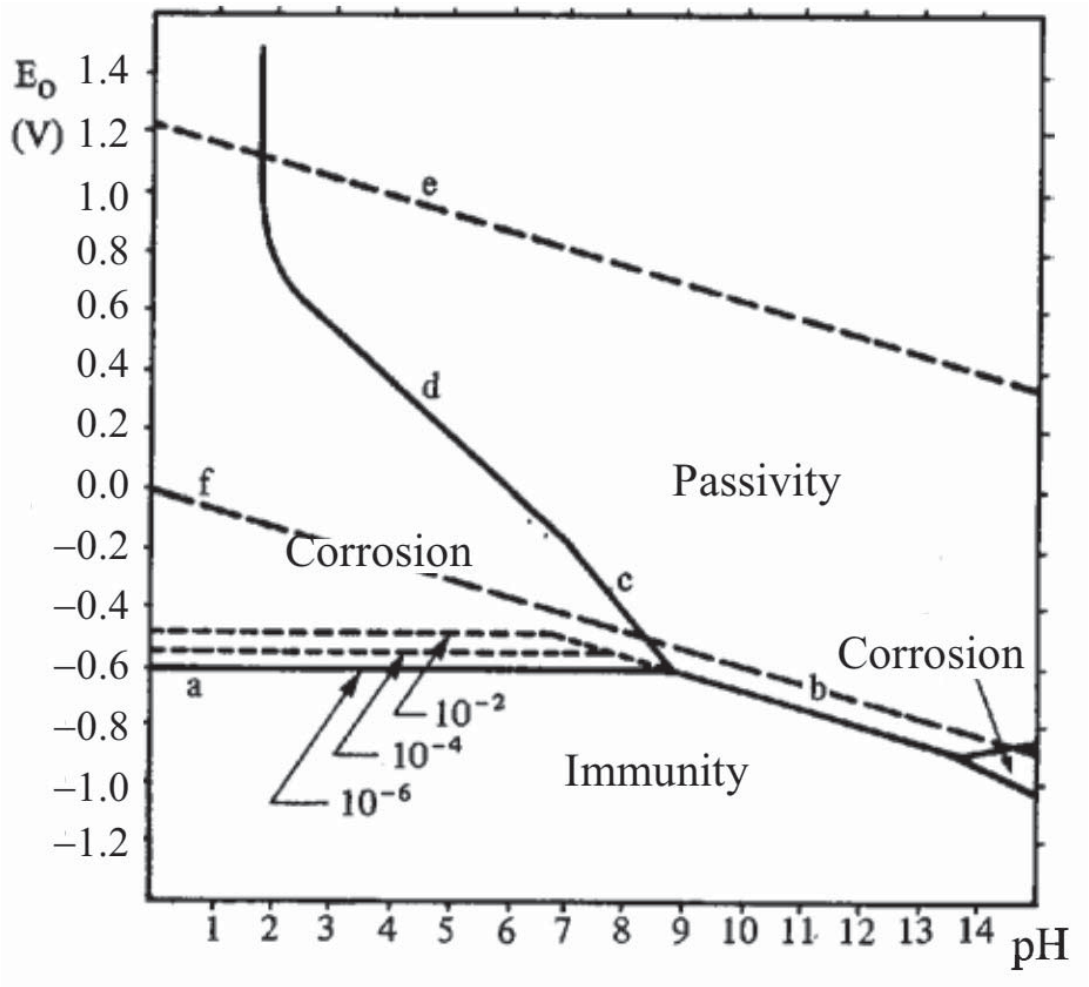

Figure 21: *Simplified Pourbaix diagram in water [13]*

DTU Mechanical Engineering
Section of Solid Mechanics
Technical University of Denmark

Nils Koppels Allé, Bld. 404
DK-2800 Kgs. Lyngby
Denmark
Phone (+45) 4525 4250
Fax (+45) 4593 1475
www.mek.dtu.dk
ISBN: 978-87-7475-446-6

DCAMM
Danish Center for Applied Mathematics and Mechanics

Nils Koppels Allé, Bld. 404
DK-2800 Kgs. Lyngby
Denmark
Phone (+45) 4525 4250
Fax (+45) 4593 1475
www.dcamm.dk
ISSN: 0903-1685